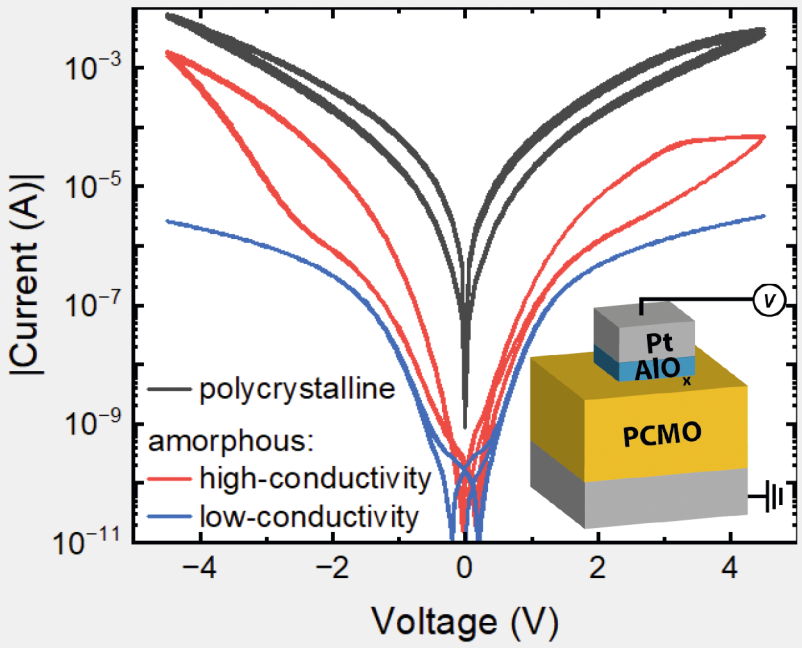

BEOL-Compatible Area-Dependent Memristive Devices from Wafer-Scale Pulsed Laser Deposited Amorphous $Pr_{0.7}Ca_{0.3}MnO_3$

Max Buczek

Schlüsseltechnologien / Key Technologies
Band / Volume 310
ISBN 978-3-69367-002-6

Mitglied der Helmholtz-Gemeinschaft

JÜLICH
Forschungszentrum

BEOL-Compatible Area-Dependent Memristive Devices from Wafer-Scale Pulsed Laser Deposited Amorphous $Pr_{0.7}Ca_{0.3}MnO_3$

Von der Fakultät für Elektrotechnik und Informationstechnik der
Rheinisch-Westfälischen Technischen Hochschule Aachen
zur Erlangung des akademischen Grades eines

Doktors der Naturwissenschaften

genehmigte Dissertation

vorgelegt von

Max, Buczek, M.Sc.

aus Uelzen

Berichter*innen: Univ.-Professorin Dr. Regina Dittmann

Univ.-Professor Dr. Christian Jooß

Tag der mündlichen Prüfung: 30.03.2026

Diese Dissertation ist auf den Internetseiten der Universitätsbibliothek online verfügbar.

Forschungszentrum Jülich GmbH
Peter Grünberg Institut (PGI)
Elektronische Materialien (PGI-7)

BEOL-Compatible Area-Dependent Memristive Devices from Wafer-Scale Pulsed Laser Deposited Amorphous $Pr_{0.7}Ca_{0.3}MnO_3$

Max Buczek

Schriften des Forschungszentrums Jülich
Reihe Schlüsseltechnologien / Key Technologies Band / Volume 310

ISSN 1866-1807 ISBN 978-3-69367-002-6

Bibliografische Information der Deutschen Nationalbibliothek.
Die Deutsche Nationalbibliothek verzeichnet diese Publikation in der
Deutschen Nationalbibliografie; detaillierte Bibliografische Daten
sind im Internet über http://dnb.d-nb.de abrufbar.

Herausgeber und Vertrieb:	Forschungszentrum Jülich GmbH Zentralbibliothek, Verlag 52425 Jülich Tel.: +49 2461 61-5368 Fax: +49 2461 61-6103 zb-publikation@fz-juelich.de www.fz-juelich.de/zb
Umschlaggestaltung:	Grafische Medien, Forschungszentrum Jülich GmbH
Druck:	Grafische Medien, Forschungszentrum Jülich GmbH
Copyright:	Forschungszentrum Jülich 2026

Schriften des Forschungszentrums Jülich
Reihe Schlüsseltechnologien / Key Technologies, Band / Volume 310

D 82 (Diss. RWTH Aachen University, 2026)

ISSN 1866-1807
ISBN 978-3-69367-002-6 (Print)
ISBN 978-3-69367-003-3 (E-Book)

Vollständig frei verfügbar über das Publikationsportal des Forschungszentrums Jülich (JuSER)
unter www.fz-juelich.de/zb/openaccess.



This is an Open Access publication distributed under the terms of the Creative Commons Attribution License 4.0, which permits unrestricted use, distribution, and reproduction in any medium, provided the original work is properly cited.

Curriculum Vitae

Max Buczek

1994	born in Uelzen, Germany
2004–2012	Abitur, Herzog-Ernst-Gymnasium Uelzen, Germany
10/2015	Bachelor of Science, Physics, University of Göttingen, Germany
2018–2019	ERASMUS Semester at Rijksuniversiteit Groningen, Netherlands
03/2020	Master of Science, Solid-State and Materials Physics, University of Göttingen, Germany
2020	Work at Warburg Invest AG in Investment Compliance
2020–2025	Research Assistant and Doctoral Candidate, Peter Grünberg Institut - Electronic Materials, Faculty of Electrical Engineering and Information Technology, RWTH Aachen University, Germany

I. Abstract

Motivation, goal and task of the dissertation: Memristive devices are considered promising non-volatile memory technology, particularly for use in neuromorphic computing architectures, which offer an alternative to conventional von Neumann architectures. Among the different types of memristive devices, area-dependent switching devices offer key advantages over filamentary types: their resistance scales with device area, enabling application-specific tuning; they exhibit gradual switching, especially during the SET, and their nonlinear $I - V$ characteristics make them suitable for selector-less memory arrays, all desirable traits for analog synaptic behavior in neuromorphic systems. A major material system of this switching class is heterostructures based on the material $Pr_{0.7}Ca_{0.3}MnO_3$ (PCMO). Pulsed laser deposition (PLD) enables the growth of complex oxides with precise stoichiometry; however, it is typically limited to small substrates. For industrial applications, scaling pulsed laser deposition (PLD) to wafer-level processes is essential. A major obstacle to CMOS integration is the high crystallization temperature of PCMO, which exceeds back-end-of-line (BEOL) thermal budgets and presents integration challenges for advanced memory applications. Therefore, deposition processes that remain within a temperature limit of 400 °C must be developed. In this context, amorphous PCMO is of particular interest, especially since its isotropic atomic structure could facilitate homogeneous vacancy transport across the entire interfacial switching region. However, its suitability for analog resistive switching and area-dependent behavior remains insufficiently explored.

The first goal of this dissertation is to develop a wafer-scale PLD process for integrating PCMO into CMOS-compatible, area-dependent memristive devices. A newly designed deposition system has been brought into operation to enable spatially homogeneous thin-film growth across an entire wafer. A PLD process had to be established that optimizes both film uniformity and stoichiometric control.

The second goal of this dissertation is to evaluate the potential of PCMO, grown at CMOS-compatible temperatures, for area-dependent resistive switching. This involves an investigation of the crystallization temperature of PCMO using in-situ X-ray diffraction. Comparisons are made between PCMO films deposited at room temperature, at the CMOS compatibility threshold of 400 °C, and after post-deposition crystallization. To understand structural evolution, X-ray diffraction and pair distribution function analysis are employed to reveal differences in long- and short-range order. Complementary measurements of electronic properties, including conductivity and band gap via UV/Vis spectroscopy and scanning tunneling spectroscopy, are conducted. Differences in work function between PCMO types are further assessed using photoelectron emission microscopy. The memristive properties are investigated in Pt/PCMO/AlO_x/Pt heterostructures. The $I - V$ characteristics are analyzed to elucidate the conduction mechanisms, which are interpreted in conjunction with energy band diagrams derived from the measured band gaps and work functions. Further, the $I - V$ loops are used to investigate the internal voltage division across the PCMO/AlO_x stack. Thus, the influence of the field distribution on the switching and the resulting on/off switching ratio is studied.

Major scientific contributions: This dissertation contributes to the development of CMOS-compatible, area-dependent memristive devices based on amorphous PCMO through the follow-

ing contributions:

1: Demonstration of wafer-scale pulsed laser deposition of PCMO: A central achievement of this work is the development of a wafer-scale pulsed laser deposition process that enables CMOS-compatible back-end-of-line integration of PCMO-based memristive devices. A newly designed deposition system was brought into operation. The process development achieved uniform layer thickness and stoichiometric control, supported by the use of simulation software.

2: Discovery of highly conductive amorphous PCMO with a CMOS-BEOL-compatible deposition process. PCMO deposited at the BEOL integration limit of 400 ℃ was found to exhibit up to four orders of magnitude higher conductivity than amorphous PCMO deposited at room temperature. X-ray diffraction, pair distribution function analysis, and in-situ studies of the crystallization temperature confirm that the highly conductive PCMO has an amorphous structure. The investigation of the short-range order indicates that MnO_6 octahedra form a local bonding unit, and a percolation-based model is proposed to explain the difference in conductivity.

3: Insights into the band alignment of memristive devices, depending on the PCMO type, and its connection to their conduction mechanisms: UV/Vis spectroscopy, scanning tunneling spectroscopy (STS), and photoelectron emission microscopy (PEEM) were employed to determine the band gap and the work function values. These parameters were used to calculate the band diagrams for Pt/ AlO_x/ PCMO/Pt devices, based on the different types of PCMO. The band diagrams are further used to interpret the conduction behavior observed in the I–V characteristics of the different devices.

4: Insight into the change of device resistance with PCMO type and AlO_x thickness, and its influence on the electric field distribution and the on/off ratio: Pt/ PCMO/ AlO_x/ Pt heterostructures were investigated regarding the influence of the AlO_x thickness and PCMO type on the memristive effect and the overall device resistance. The collected $I - V$ characteristics were subsequently used to fit the material parameters of a two-resistor model with non-linear voltage dependence. This model was employed to assess the internal division of the electric field through a finite-element simulation. The model revealed a correlation between the electric field strength in the tunnel oxide prior to switching and the resulting on/off ratio.

II. Kurzfassung der Promotion

Motivation, Ziel und Aufgabe der Dissertation: Memristive Bauelemente gelten als vielversprechende Kandidaten für nichtflüchtige Speicher, besonders für den Einsatz in neuromorphen Rechenarchitekturen, welche eine Alternative zu konventionellen von-Neumann-Architekturen bieten. Unter diesen bieten flächenabhängige Speicherbauelemente entscheidende Vorteile gegenüber filamentären. Ihr Widerstand skaliert mit der Bauelementfläche, was eine anwendungsspezifische Widerstandswahl ermöglicht; sie zeigen insbesondere während des SET-Vorgangs ein graduelles Schaltverhalten, und ihre nichtlinearen $I - V$-Charakteristiken machen sie geeignet für Speicherarrays ohne Selektoren. Das sind allesamt wünschenswerte Eigenschaften für analoges synaptisches Verhalten in neuromorphen Systemen. Ein wichtiges Materialsystem dieser Klasse schaltender Systeme sind Heterostrukturen basierend auf dem Material $Pr_{0.7}Ca_{0.3}MnO_3$ (PCMO). Die gepulste Laserabscheidung (PLD) ermöglicht das Wachstum komplexer Oxide mit präziser Stöchiometrie, ist jedoch typischerweise auf kleine Substrate beschränkt. Für industrielle Anwendungen ist daher eine Skalierung der PLD auf waferbasierte Prozesse unerlässlich. Ein wesentliches Hindernis für die CMOS-Integration ist die hohe Kristallisationstemperatur von PCMO, die das thermische Budget für Back-End-of-Line (BEOL) Prozesse übersteigt und die Integration in fortschrittliche Speicheranwendungen erschwert. Daher müssen Abscheidungsprozesse entwickelt werden, die innerhalb des Temperaturlimits von 400°C bleiben. In diesem Zusammenhang ist amorphes PCMO von besonderem Interesse, insbesondere, da seine statistisch homogene atomare Struktur für einen homogenen Leerstellentransport über die gesamte, für das Schalten relevante, Grenzflächenzone, sorgen könnte. Allerdings ist die Eignung von amorphen PCMO für graduelles flächenabhängiges resistives Schalten bislang unzureichend erforscht.

Das erste Ziel dieser Dissertation ist die Entwicklung eines wafer-skalierten PLD Prozesses zur CMOS-kompatiblen Abscheidung von PCMO für die Nutzung in flächig schaltenden memristiven Speicherzellen. Zu diesem Zweck wurde eine PLD-Anlage mit einem neuartigen Depositionskonzept in Betrieb genommen. Während des Promotionsprojekts musste ein PLD-Prozess entwickelt werden, der die Filmschichthomogenität auf dem Wafer optimiert und einen stöchiometrischen Transfer vom Target ermöglicht.

Das zweite Ziel dieser Dissertation ist die Untersuchung von PCMO, das bei CMOS-kompatiblen Temperaturen abgeschieden wurde, der Vergleich mit polykristallinem PCMO sowie die Untersuchung seiner Verwendung in resistiven Speicherzellen. Hierfür werden PCMO-Schichten verglichen, die entweder bei Raumtemperatur oder bei 400 °C, der CMOS-Kompatibilitätsgrenze, abgeschieden wurden, sowie bei Raumtemperatur abgeschiedene Schichten mit anschließender Kristallisation. Zur Analyse der Abhängigkeit der atomaren Nah- und Fernordnung von den Depositionsbedingungen wird die Paarverteilungsfunktion mittels Röntgenstreuexperimenten bestimmt und die Kristallisationstemperatur mit in-situ-Röntgendiffraktionsmessungen ermittelt. Des Weiteren werden Messungen der elektronischen Eigenschaften der verschiedenen PCMO-Schichten durchgeführt. Dies umfasst die Bestimmung der Leitfähigkeit, die Ermittlung der Bandlücke mittels UV/Vis-Spektroskopie und Rastertunnelspektroskopie sowie die Messung der Austrittsarbeit mit Photoelektronen-Emissionsspektroskopie. Zur Untersuchung der resistiven Eigenschaften werden die ver-

schiedenen PCMO-Schichten in Pt/PCMO/AlO_x/Pt Heterostrukturen intergirert und die $I-V$-Charakteristiken werden analysiert. Die dabei ermittelten Leiteigenschaften werden in Zusammenhang mit Energiebändermodellen interpretiert, die mit Hilfe der gemessenen Bandlücken und Austrittsarbeiten berechnet werden. Des Weiteren sollen die gemessenen $I-V$ Charakteristiken zur Parametrisierung einer Finite-Elemente-Simulation genutzt werden, mit deren Hilfe die Verteilung des elektrischen Feldes über den PCMO/AlO_x-Stapel untersucht werden kann. Auf diese Weise lässt sich der Einfluss des elektrischen Feldes vor dem Schaltvorgang auf das resultierende on/off-Widerstandsverhältnis ermitteln.

Wesentliche Wissenschaftliche Beiträge: Diese Dissertation leistet einen Beitrag zur Weiterentwicklung CMOS-kompatibler, flächenabhängiger memristiver Speicherzellen auf Basis von amorphem PCMO durch die folgenden Beiträge:

1: Demonstration der wafer-skalierten gepulsten Laserabscheidung von PCMO: Ein zentrales Ergebnis dieser Arbeit ist die Entwicklung eines wafer-skalierten Prozesses zur gepulsten Laserabscheidung (PLD) von PCMO für flächenabhängige memristive Heterostrukturen. Ein neu konzipiertes Abscheidungssystem wurde in Betrieb genommen, das ein flächig homogenes Dünnschichtwachstum über gesamte Wafer ermöglicht. Die Prozessentwicklung konzentrierte sich auf die Optimierung von Schichthomogenität und stöchiometrischer Kontrolle, unterstützt durch Simulationen.

2: Entdeckung von hochleitfähigem amorphem PCMO mit einem CMOS-BEOL kompatiblen Abscheidungsprozess: PCMO, das bei der CMOS Kompatibilitätsgrenze von 400 °C abgeschieden wurde, zeigt eine bis zu vier Größenordnungen höhere Leitfähigkeit als amorphes PCMO, das bei Raumtemperatur abgeschieden wurde. Röntgendiffraktion, Paarverteilungsfunktionsanalysen sowie in-situ-Untersuchungen der Kristallisationstemperatur belegen, dass das hochleitfähige PCMO amorph ist. Die Analyse der Nahordnung anhand der Paarverteilungsfunktion zeigt, dass die MnO_6-Oktaeder lokale Bindungseinheiten bilden. Ein perkolationsbasiertes Modell wird vorgeschlagen, um den Unterschied in der Leitfähigkeit zu erklären.

3: Erkenntnisse zur elektronischen Struktur der verschiedenen PCMO-Typen in memristiven Bauelementen und deren Leitmechanismen: Mittels UV/Vis-Spektroskopie, Rastertunnelspektroskopie (STS) und Photoelektronen-Emissionsmikroskopie (PEEM) wurden die Bandlücken und die Austrittsarbeiten bestimmt. Diese Parameter dienten zur Berechnung der Bandverbiegung der Pt/ AlO_x/ PCMO/ Pt Speicherzellen basierend auf den verschiedenen PCMO Schichten. Durch die Banddiagramme konnten die Leitmechanismen der I-V-Kennlinien interpretiert werden.

4: Verständnis der Widerstandsvariation durch Variation von PCMO-Typ und AlO_x Dicke sowie des daraus resultierenden Einflusses auf das on/off-Verhältnis über die Feldverteilung: Pt/ PCMO/ AlO_x/ Pt Heterostrukturen wurden untersucht, um den Einfluss der AlO_x Schichtdicke und des verwendeten PCMO-Typs auf den memristiven Effekt und den Gesamtwiderstand des Bauelements zu bewerten. Die $I-V$ Kennlinien wurden genutzt, um die Parameter eines Zweiwiderstandsmodells des memristiven Bauelements zu bestimmen. Dieses Modell wurde anschließend verwendet, um die interne Feldverteilung mittels Finite-Elemente-Simulation zu analysieren. Die Studie zeigt eine Korrelation zwischen der elektrischen Feldstärke im Tunneloxid vor dem Schaltvorgang und dem daraus resultierenden on/off Verhältnis der Speicherzelle.

III. List of publications

Most of the experimental findings are content of two separate publications.

1: The results related to large-area pulsed laser deposition were published in *Thin Solid Films*, 805 (2024), 140499, under the title 'Large Area Pulsed Laser Deposition of Memristive $Pr_{0.7}Ca_{0.3}$-MnO_3 Heterostructures for Neuromorphic Computing'.

2: The experimental findings on the highly conductive amorphous PCMO are published in *Advanced Electronic Materials* under the title 'Amorphous, Highly Conductive $Pr_{0.7}Ca_{0.3}$ for Area-Dependent Resistive Switching AlO_x Bilayer Devices'.

3: Furthermore, an in-depth review paper on the field, published in *Chemical Reviews* in June 2025 and titled '$Pr_{1-x}Ca_xMnO_3$-based Memristive Heterostructures: Basic Mechanisms and Applications,' serves as the theoretical background for this thesis.

Contents

I. Abstract v

II. Kurzfassung der Promotion vii

III. List of publications ix

1. Introduction 5
- 1.1. General introduction . . . 5
- 1.2. Motivation for the use of amorphous PCMO . . . 6
- 1.3. Structure of the thesis . . . 6

2. Theoretical background 9
- 2.1. Basics of PCMO . . . 9
  - 2.1.1. Crystal structure, phase diagram and magneto resistance . . . 9
  - 2.1.2. Electronic structure and the influence on conductivity . . . 11
  - 2.1.3. Detection of the charge carrier type . . . 13
  - 2.1.4. Polaronic model of PCMO and characterization by optical, vibrational and electric properties . . . 16
  - 2.1.5. PCMO defect chemistry and the influence of oxygen vacancies . . . 19
  - 2.1.6. Work function of PCMO . . . 24
  - 2.1.7. Relative permittivity of PCMO . . . 28
- 2.2. PCMO based memristive heterostructures . . . 28
  - 2.2.1. General consideration on PCMO based switching devices . . . 28
  - 2.2.2. Influence of the Gibbs energy on valve metal based memristive stacks . . . 29
  - 2.2.3. Space charge region in the MOP structure . . . 32
  - 2.2.4. Current transport across the MOP . . . 37
  - 2.2.5. Space-charge limited current . . . 40
- 2.3. Switching . . . 40
  - 2.3.1. Area-dependent switching . . . 40
  - 2.3.2. Switching mechanism overview . . . 44
  - 2.3.3. Switching mechanism based on changes of the tunnel oxide . . . 45
  - 2.3.4. Switching mechanisms based on the modification of PCMO . . . 51
  - 2.3.5. Switching kinetics . . . 52
- 2.4. CMOS co-integration . . . 59

3. Experimental methods 61
- 3.1. Deposition methods . . . 61
  - 3.1.1. Pulsed laser deposition . . . 61
  - 3.1.2. Sputter deposition . . . 62
- 3.2. Device structuring . . . 63
  - 3.2.1. Photo-Lithography . . . 64
  - 3.2.2. Ion beam etching . . . 64
- 3.3. Rapid thermal processing . . . 65
- 3.4. Process flow for device fabrication . . . 65

3.5. Scanning probe microscopy . . . 66
3.5.1. Atomic force microscope . . . 66
3.5.2. Scanning tunneling microscopy and spectroscopy . . . 67
3.6. X-rays based structural analysis . . . 69
3.6.1. X-ray reflectometry . . . 69
3.6.2. Grazing incident X-ray diffraction . . . 71
3.6.3. Grazing incident total X-ray scattering . . . 72
3.7. Photoemission based analysis . . . 73
3.7.1. (X-ray) photoelectron spectroscopy . . . 73
3.7.2. Photo electron emission microscopy . . . 75
3.8. Optical characterization . . . 76
3.8.1. Spectrophotometer . . . 76
3.9. Electrical characterization . . . 77
3.10. Elemental analysis . . . 77
3.10.1. Inductively Coupled Plasma Mass Spectrometry . . . 77

4. Large area pulsed laser deposition **79**
4.1. Consideration on the use of large-area PLD . . . 79
4.2. Details of the PLD system . . . 80
4.3. Influence of slit system and working pressure . . . 81
4.4. Parameterization of the simulation software . . . 82
4.5. Development of the simulation strategies for PCMO . . . 82
4.6. PCMO stoichiometry . . . 85

5. Devices based on low-conductivity amorphous PCMO **88**
5.1. Interfaces and PCMO Stoichiometry . . . 88
5.2. Aluminum oxide sub-stoichiometry . . . 90
5.3. Device characterization . . . 92

6. Devices based on highly conductive amorphous PCMO: a comparative study **97**
6.1. Overview . . . 97
6.2. Structural analysis and crystallinity . . . 97
6.2.1. Surface morphology and density change by crystallization of PCMO . . . 97
6.2.2. GI-XRD measurements and in-situ crystallization temperature . . . 98
6.2.3. Total X-ray scattering . . . 98
6.2.4. Calculation of the pair distribution function . . . 101
6.3. DC conductivity and atomic structure . . . 101
6.3.1. MnO_6 octahedron as local bonding unit and its network . . . 102
6.4. Electrical characterisation and conduction mechanism of the memristive devices . . . 105
6.4.1. *I-V* characteristics and resistive switching . . . 105
6.4.2. Conduction type and asymmetry . . . 107
6.5. Band alignment and asymmetry . . . 109
6.5.1. Work function determination by threshold emission spectroscopy . . . 109
6.5.2. Work function comparison . . . 110
6.5.3. Band gap determination by UV/Vis and STS . . . 111
6.5.4. Band alignment . . . 114
6.5.5. Density of states for the band alignment model . . . 116
6.5.6. Discussion of band alignment, conduction type and asymmetry . . . 117
6.5.7. Literature comparison . . . 118
6.6. Field distribution and on/off ratio . . . 120
6.6.1. Parametrization of non-linear resistance model . . . 122

6.7. Discussion of the PCMO and aluminum oxide interaction during switching 124

7. Conclusion and outlook **126**
7.1. Conclusion 126
7.2. Outlook 127

8. Acknowledgements **128**

References **130**

1. Introduction

The following introduction is based on the papers [1, 2] and [3].

1.1. General introduction

Due to their high scalability and simple structure, memristive devices are promising candidates as a storage class memory or as a competing technology to overcome the limitations of conventional non-volatile memories such as flash memory. They are already being used as embedded memory due to their ability to integrate BEOL and their low power consumption. The rapidly growing field of neuromorphic computing challenges the limitations of conventional computing based on the von Neumann architecture, especially in terms of energy efficiency [4]. In this context, resistive random-access memories (ReRAMs) based on the valence change mechanism have attracted considerable interest, especially for the use as synapse in neuromorphic circuits [5, 6, 7].

One of the most common types of memristive device is based on the valence change mechanism (VCM), which is caused by the movement of oxygen vacancies in mixed conducting oxide thin films or heterostructures. The switching behaviour of VCM devices can be distinguished between a resistance change along a filament or a resistance change across the entire device interface. Filamentary switching is stochastic because the movement of the vacancies is highly temperature accelerated by the Joule heating of the filament and due to the strong localization already few vacancies in the disc region of the filament can influence the device resistance. Compared to this, the kinetics in area-dependent devices can be controlled more gradually, which could be beneficial for use in neuromorphic systems [8].

Among the various types of memristive devices, area-dependent switching devices offer advantages over filamentary ones: First, their resistance scales with device area, allowing application-specific resistance tuning; second, their switching behavior is less affected by Joule heating during operation [9, 8], as it is the case in competing filamentary devices [10, 11]. This results in gradual and more symmetric switching characteristics, especially during the SET transition, which is essential for neuromorphic applications requiring gradual tunable conductance to emulate synaptic behavior [12]. Additionally, the inherent non-linearity of their current-voltage ($I-V$) characteristics supports their integration into passive selector-less memory arrays [13].

Stacks of the perovskite $Pr_{1-x}Ca_xMnO_3$ (PCMO) and an insulating oxide are an intensively studied material system for area-dependent switching. Among the various possible realizations of area-dependent devices, the combination of praseodymium calcium manganate (PCMO) and AlO_x is a promising memristive heterostructure [12, 14, 15].

Since the first observation of a voltage-induced resistance change in PCMO by Asamitu et al. [16] in 1997, based on an electronic phase transition at low temperatures, and today's array integration of PCMO-based ReRAM, hundreds of research papers have been written on PCMO from the material side and on PCMO in switching device stacks.

Fully CMOS integrated arrays based on PCMO-TO stacks could potentially outperform filamentary switching arrays in cycle-to-cycle and read-to-read variability and endurance. The high resistance values of PCMO-based devices, even in the LRS, could enable large crossbar arrays by avoiding the parasitic effects caused by the line resistances that dominate the arrays of their filamentary counterparts. With the ability to provide incremental resistance tuning and associated multi-level states, they could serve as synaptic weights for memristor-based AI hardware

accelerators in the growing field of AI technology and neuromorphic computing. New market opportunities for memristors in hardware-based AI accelerators are created by the rapid growth of AI technologies and their excessive need for computational resources and power consumption [6]. Low switching energies, together with higher endurance and high switching speed, may be an opportunity for PCMO-based memristor technology for in-memory computing in low-power edge devices [7].

1.2. Motivation for the use of amorphous PCMO

Switching in PCMO-based devices is driven by the electric-field-induced movement of oxygen vacancies between the PCMO and a tunnel oxide [13, 2]. A homogeneous distribution of this vacancy movement across the cross-section of the memristive microstructure is ideal for enabling area-scaled switching. To this end, an amorphous material could be beneficial, owing to its homogeneous vacancy mobility and concentration. In contrast, defects in polycrystalline PCMO can affect both vacancy mobility and spatial distribution, which has been particularly well studied in the case of grain boundaries [8, 17], and can potentially lead to non-uniform oxygen vacancy migration during switching. The use of amorphous PCMO may therefore support more reliable scaling of memory cells from the microscale down to the nanoscale, due to the absence of crystallographic defects, especially grain boundaries. Additionally, the amorphous structure may offer improved resilience against defect generation during fabrication processes, because there is no longer an atomic lattice structure whose damage could cause strong inhomogeneities across the surface.

However, most research on PCMO-based memristive devices has focused on polycrystalline PCMO films [8, 2, 9, 18, 19]. 4DS, a publicly traded company, claims on its website [20] to have developed a complementary metal-oxide-semiconductor (CMOS) integrated megabit array using crystalline PCMO devices with a size of 60 nm. Their technology offers dynamic random-access memory (DRAM) like persistent memory with nanosecond switching and over 10^9 endurance cycles, making PCMO one of the most advanced CMOS-integrated area-type switching material to date [20]. However, the downscaling of these memory cells to 20 nm, which is a major step toward industrial relevance, still remains challenging [20].

Amorphous PCMO-based devices are reported to exhibit lower on/off ratios and switch at higher voltages [1]. Nevertheless, the cause of their reduced switching performance remains unclear. Since the movement of oxygen vacancies, based on the Mott-Gurney law, is highly nonlinear with respect to the strength of the electric field [8, 2], the resistive switching strongly depends on the distribution of the electric field within the memristive device. Thus, an explanation for the less pronounced switching in a-PCMO could lie in changes to the electric field distribution, which are therefore investigated in this work. Since amorphous PCMO can exhibit significantly higher resistance compared to crystalline PCMO, deposition processes that reduce its resistance are needed to explore its potential advantages. These processes must be compatible with back-end-of-line (BEOL) integration into standard CMOS technology and, consequently, require temperatures limited to 400 °C. Furthermore, investigations into changes in the electric field distribution are also necessary. In addition, there is a general lack of literature addressing the electronic structure of amorphous PCMO, including properties such as the band gap and work function. These values are necessary to understand possible differences in the conduction mechanism due to variations in the band diagram of the device's heterostructure.

1.3. Structure of the thesis

This thesis begins with a comprehensive review of the field, based on the paper *"$Pr_{1-x}Ca_xMnO_3$-based memristive heterostructures: Basic mechanisms and applications."* This in-depth literature

review provides the theoretical foundation for the thesis. Afterwards, in Chapter 3, the different experimental methods used are presented.

The following Chapters presents the experimental results, which address the goals defined in Chapter I of this PhD project. Chapter 4 presents how a wafer-scale PLD process was developed, with a newly designed deposition system, to enable homogeneous thin-film growth. Thus achieving the first goal of this PhD project and delivering the first major scientific contribution.

Chapter 5 uses the developed PCMO deposition process at room temperature to ensure full CMOS compatibility, and evaluates the switching properties of the resulting PCMO/AlO_x devices, as well as the influence of a non-CMOS-compatible thermal crystallization treatment. This is part of the second goal of the PhD project.

To further optimize the switching properties within the limits of CMOS-compatible temperatures, Chapter 6 evaluates the switching properties of PCMO deposited at 400 °C and compares them with those of room-temperature-deposited and polycrystalline PCMO. This chapter investigates the differences in conductivity and relates them to X-ray scattering measurements of the short-range order, which provides the second major scientific contribution. Furthermore, the electronic structure of all three types of PCMO is investigated. The resulting band alignment in the device stack is studied and analyzed in coherence with the current-voltage characteristics. This analysis constitutes the third major scientific contribution. Finally, this chapter analyzes the distribution of the electric field within the devices and its impact on the on/off ratio as a function of the AlO_x thickness, which provides the fourth major scientific contribution of this thesis.

The last Chapter 7 presents the conclusions drawn from the experimental results and provides an outlook.

2. Theoretical background

The in this Chapter written text was perviously published in Chem. Rev., June 2025 with the title "$Pr_{1-x}Ca_xMnO_3$-based memristive heterostructures: Basic mechanisms and applications". Reprinted with permission from [2]. Copyright 2025 American Chemical Society.

2.1. Basics of PCMO

2.1.1. Crystal structure, phase diagram and magneto resistance

$Pr_{1-x}Ca_xMnO_3$ has an orthorhombic distorted perovskite ABO_3 structure with Pr and Ca sharing the A site and Manganese on the B site over the whole doping region. The ionic radii of Pr^{3+} (137 pm) and Ca^{2+} (134 pm) under 12-fold coordination [21] are similar, which leads to a stress-free homogenous distribution on the A side places. $Pr_{1-x}Ca_xMnO_3$ has a small bandwidth [22] compared to other rear earth manganites such as $La_{1-x}Sr_xMnO_3$, because of the small ion radii of Pr^{3+} and Ca^{2+} compared to other A-site atoms. For LSMO, Sr is larger than Ca since it is in period 5, compared to period 4 Ca, and La is larger since it has two atomic numbers less in the f-block as Pr [23]. The average small ion radius r_A on the A site, comparing to the B site r_B, leads to a decrease in the Goldschmidt tolerance factor

$$t = \frac{1}{\sqrt{2}} \frac{r_A + r_O}{(r_B + r_O)} \tag{2.1}$$

Here r_O is the radius of the oxygen anion. A Goldschmidt factor smaller 1 means the ionic distances in the Mn/O plane of the perovskite structure are larger than the distances in the Pr/Ca/O plane. Therefore, the crystal responds by a bending of the interplanar Mn-O-Mn bond angle away from 180°. The octahedral tilting changes the ideal cubic perovskite structure of PCMO to an orthorhombic symmetry over its entire doping range [21] and increases the unit cell to account for the octahedral tilting (Figure 2.1b). Reducing the bond angle reduces the transfer integral of the Manganese eg electron across the Mn-O-Mn bond [22, 23]. This localization causes a small bandwidth of PCMO. This strong influence of the A ion on the resistance can also be seen in Figure 2.11a. Experimentally, intense external hydrostatic pressure can reduce this buckling of the Mn-O-Mn bonds and increase the bandwidth [24].

Doping with Ca increases the amount of Mn^{4+} and decreases the ionic radius on the B site. The ionic radius of Mn in a 6-fold coordination is 64.5 pm, ranging from Mn^{3+} at high spin coordination to 53 pm for Mn^{4+} [25]. The small A-site radius of Ca is compensated by reducing the average B site radii. Therefore, the pseudocubic lattice parameters a, b, and c decrease linearly, as can be seen in Figure 2.1a for Ca content $x > 0.3$. This can be regarded as a solid solution according to a modified version of Vegard's law where, here, the linear combination of the lattice constant does not refer to the doping but to the doping controlled average ionic manganese radii. $CaMnO_3$ and PCMO have an orthorhombic symmetry of the space group *Pmna* up to a Ca doping of $x \geq 0.3$. For low Ca doping $x < 0.3$, the higher ratio of Mn^{3+} induces a symmetry reduction from *Pmna* towards *Pbnm* [21].

The manganite family has been the subject of extensive research due to its manifestation of colossal magnetoresistance (CMR)[22], an effect where the application of a magnetic field H in the order of a few Tesla leads to a substantial reduction of the resistance R, where $(R(H) -$

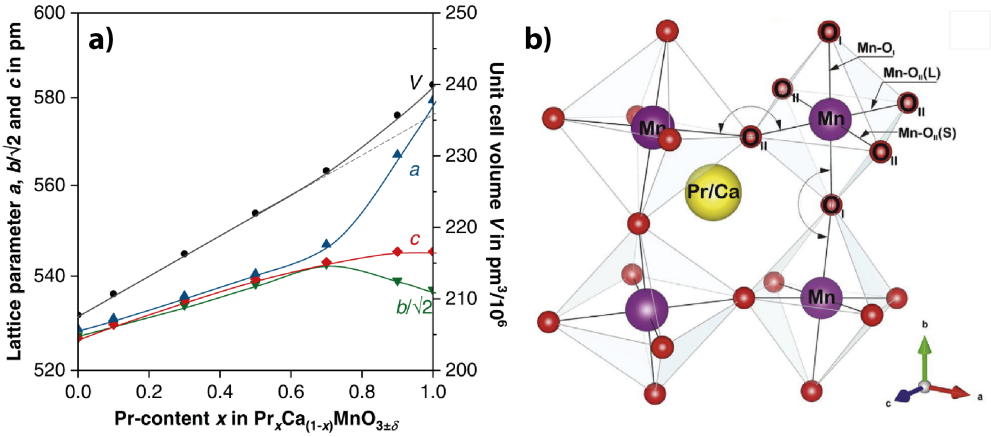

Figure 2.1.: a) Pseudo cubic lattice parameter of PCMO in dependence of the doping. Adapted and reprinted with permission from [21], © 2022 by Elsevier. b) Fragment of the PCMO unit cell to show the octahedral tilting. Adapted and reprinted with permission from [26], © 2018 by Elsevier.

$R(0))/(R(0)$ can approach 100%.

The manifestation of colossal magnetoresistance (CMR) in manganites is tightly connected with the double exchange, a mechanism according to an increase of the delocalization of the e_g electron for parallel spin alignment of neighboring mixed valence $Mn^{3+/4+}$ ions. The probability of electron transfer Mn^{3+}-O-Mn^{4+} goes by $\cos(\theta/2)$, where θ is the angle between the spins of the neighboring Mn ions under the assumption of strong Hund coupling [27]. This mechanism combines ferromagnetic ordering with metallic conduction, leading to a ferromagnetic metallic ground state at low temperatures for manganites with a large bandwidth [22]. The CMR effect is strongly pronounced near the Curie temperature, where the ferromagnetic spin ordering starts to become disordered. At this temperature, an external magnetic field can substantially affect the reordering of the spins, elevate the Curie temperature, and, thus, reduce the electrical resistance by the double exchange. The CMR in mixed-valence manganese oxides $(R_{1-x}D_x)MnO_3$ (R=trivalent cation, e.g. rare-earth, D= divalent cation, e.g. alkaline earth), like $Pr_{1-x}Ca_xMnO_3$, is particularly pronounced in the $x = (0.3 - 0.4)$ doping region (Figure 2.2a) [28], due to the destabilization of the charge ordering, which is most stable for a doping of 0.5 [29]. Hence, PCMO with the composition $Pr_{2/3}Ca_{1/3}MnO_3$ has been a primary focus in this context.

PCMO is characterized by low bandwidth [22], which leads to an insulating behavior over the entire Ca doping range (Figure 2.2b). It shows no ferromagnetic metallic ground state at low temperatures. Instead, it shows a charge-ordered state in a broad doping range around $x = 0.5$. Additional at lower temperatures an antiferromagnetic ordering forms [29, 30, 31, 32].

Applying a magnetic field, below the Néel temperature, can melt this charge-ordered state and introduce a ferromagnetic metallic state. This state is not considered to be a homogeneous phase, it is an electronic-magnetic percolation phase within the single-crystal [22]. The resistance difference to the ground state becomes enormous for a lower conducting small bandwidth manganite such as PCMO.

The charge-ordered state can also be melted by high currents or high fields, which lead to resistive switching in PCMO with noble ohmic contacts like Pt/PCMO/Pt at low temperatures [33, 34, 35, 36]. This effect is the called colossal electro-resistance effect (CER) and relates to a current-induced polaron solid-liquid transition [35].

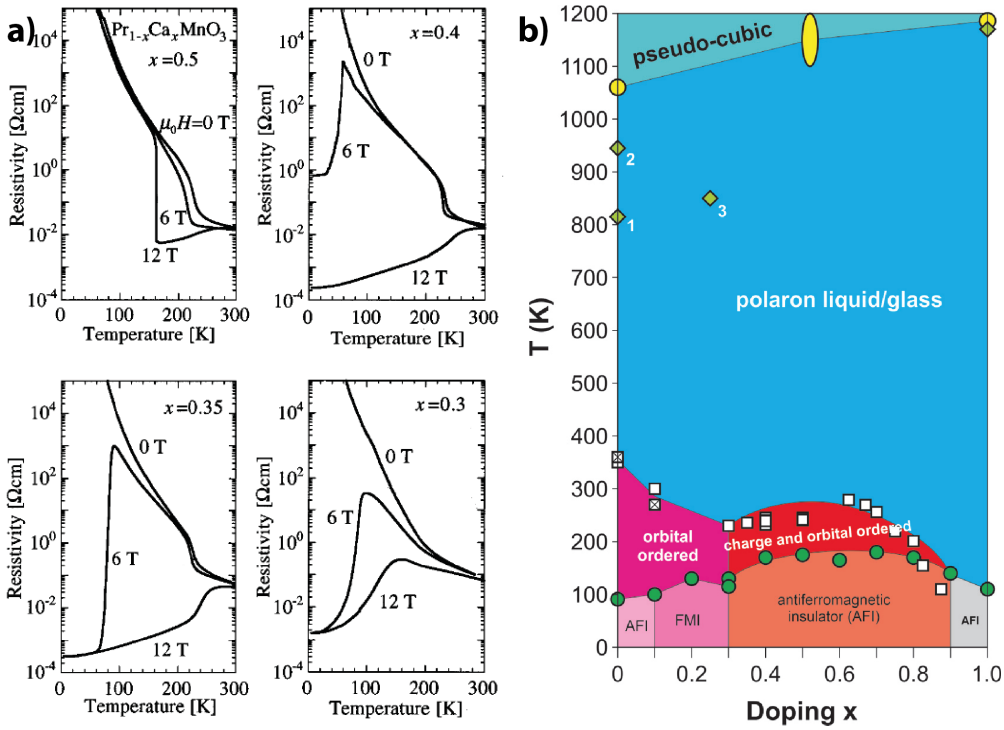

Figure 2.2.: a) CMR effect in PCMO for Ca doping from 0.3 to 0.5. The Resistance change is seen in the difference between the magnetic field applied, and the no-field applied cooling curves. Taken from [29], © 1996 by American Physical Society. b) Phase diagram of PCMO taken from [30], © 2021 by American Physical Society.

2.1.2. Electronic structure and the influence on conductivity

The electronic structure of PCMO is strongly influenced by the electronic state of the Mn ion and its hybridization with the oxygen ion. The electronic state of Pr^{3+} ([Xe] $4f^2$) can also contributions to the valence band and the higher energetic states of the conduction band (Figure 2.3a). Ca^{2+} is formally in the [Ar] noble gas configuration and can contribute to the higher-energy region of the conduction band. [37] [38]. However, around the Fermi level, the electronic structure mainly depends on manganese and oxygen.

The electronic configuration of the Mn^{3+} and the Mn^{4+} ions is [Ar]$3d^4$ and [Ar]$3d^3$, respectively, without occupation of the s-shell. Since an octahedral crystal field surrounds the Mn ion in the perovskite structure, the d states become split into the six t_{2g} and four e_g electronic states (Figure 2.3).

Hund's rule and Coulomb repulsion results in further spin-dependent splitting of the t_{2g} and e_g, states into spin-up and spin-down bands (Figure 2.3b). Therefore, the spin-split bands e_g and t_{2g} contain two and three remaining states, respectively [39].

For $CaMnO_3$, the $3d^3$ electron configuration of Mn^{4+} completely occupies the t_{2g} band, resulting in an insulator. The spin-dependent energy splitting of $t_{2g}\uparrow$ and $t_{2g}\downarrow$ is strong because of a high Coulomb repulsion described by U in the Hubbard Modell. Thus, the $t_{2g}\uparrow$ band lies lower than the oxygen p-band (Figure 2.3a), and CMO has to be regarded as a charge transfer insulator [40, 41, 42].

For pure Mn^{3+} as in the case of $PrMnO_3$, the two degenerated e_g states are filled with a single electron. According to the Jahn-Teller (JT) theorem, this degeneracy is lifted by a distortion of the ligand octahedron. There are two different ways of distortion. Compression in the xy plane and an extension along the z direction. This splits the e_g band by energetically lowering the d_{z^2} state

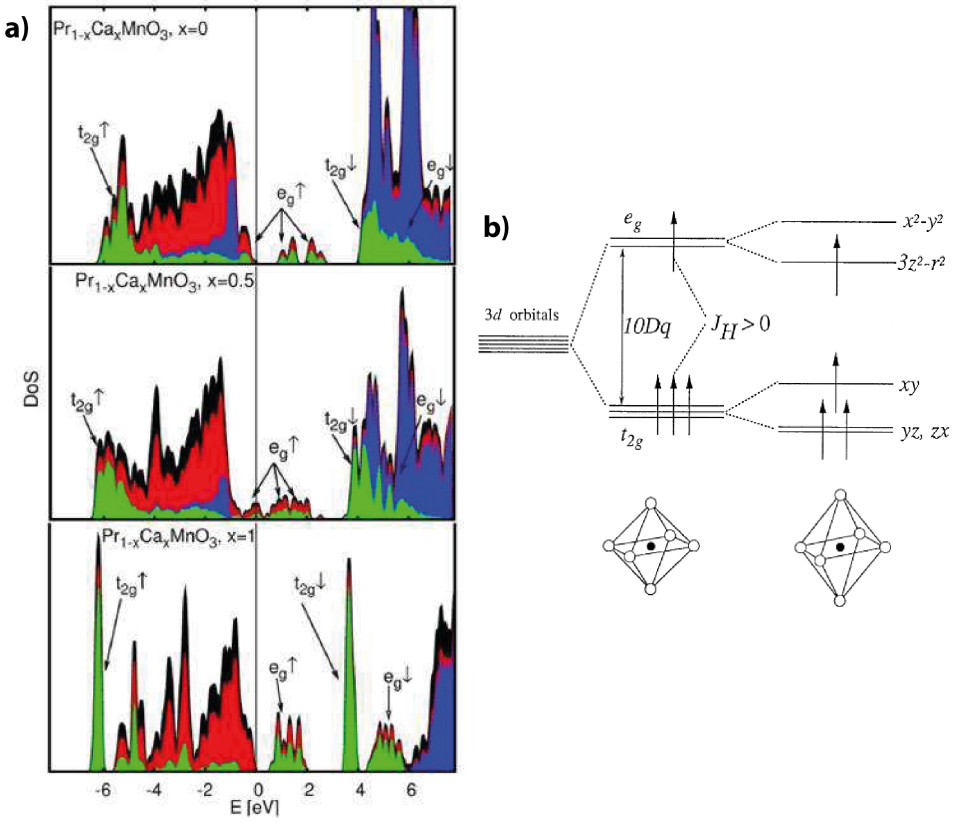

Figure 2.3.: a) The black enveloping area shows the density of states of PCMO with Calcium doping of 0, 0.5 and 1, calculated by DFT. The color represents the contributions from the atomic orbitals (red O 2p states, blues Pr d and f states, and green Mn d-states). Adapted and reprinted with permission from [37], © 2012 by John Wiley and Sons. b) Crystal field splitting for Mn^{3+} high spin configuration in an octahedral crystal field - caused by the O^{2-} ligands. Adapted and reprinted with permission from [22], © 2001 by Elsevier.

and increasing the $d_{x^2-y^2}$. Also, the t_{2g} band is split by lowering the d_{yz} state and increasing the d_{xy} and d_{xz} states. The opposite is the extension in the xy plane and the compression along the z axis. This increases d_{z^2}, d_{yz}, and d_{xz} in energy and lowers $d_{x^2-y^2}$ and d_{xz}.

If Mn^{3+}, the JT-splitting of the $e_g\uparrow$ band leads to a one electron band. For $PrMnO_3$ (PMO), this band is fully occupied, causing it to be an insulator (Figure 2.3a). Inge et al. [41] and Rosenberg et al. [43] have called PMO a Mott insulator. However, this label does not necessarily reflect the nature of the insulating state, since the $e_g\uparrow$ splitting is caused by the JT effect and the Coulomb interaction of the two e_{g1} and e_{g2} states is reduced due to their spin parallelism.

The substitution of Pr^{3+} by Ca^{2+} leads to a hole doping of the one electron e_g band of $PrMnO_3$ and causes formally a mixed valency of the Manganese in the ratio of $Mn^{3}{}_{+1-x}/Mn^{4+}{}_{x}$. From a perspective of simple band theory, $Pr_{1-x}Ca_xMnO_3$ should, therefore, be a conducting material since the band has unoccupied states and the charge carrier concentration is high with 10^{21}-10^{22} /cm^3 already for small Ca concentrations of a few atomic percentages.

Surprisingly, PCMO shows quite insulating behavior over its entire doping range. This can be explained by the low charge carrier mobility. A simple argument can be drawn from the connection of bandwidth and Fermi velocity from the simple tight-binding model. The narrow bandwidth, caused by the octahedral tilting, reduces the charge carrier's Fermi velocity and, therefore, increases the lattice's coupling. Further, each electron in the one-electron e_g band relates to a lattice distortion based on the Jahn-Teller effect. This couples the movement of an electron with the movement of a lattice distortion. Both factors lead to a polaronic description of the charge transport in PCMO, which results in a substantial increase in the effective mass and a strong reduction in charge carrier mobility [34]. The strong connection of the Jahn-Teller mode with the bandwidth has been shown by a metal-insulator phase transition from the CO phase caused by controlled stimulation of the Jahn-Teller mode in a pump-probe experiment [44].

2.1.3. Detection of the charge carrier type

The Hall and Seebeck measurements indicate that the carrier type in PCMO changes with the Ca doping [21, 45]. Besides from direct measurements, the charge carrier type in PCMO can also be determined indirectly by the interaction of PCMO in a junction [46]. From the perspective of a narrow e_g band, the charge carrier type can be described in dependence on the band filling c, which means the ratio of filled states n to the total amount of states n_c in the eg band $c = n/n_c$. In the context of mixed valence, this can also be described by

$$c \approx [\mathrm{Mn}^{3+}]/([\mathrm{Mn}^{3+}] + [\mathrm{Mn}^{4+}]) \tag{2.2}$$

or in the case of perfect oxygen stoichiometry

$$c \approx [\mathrm{Pr}^{3+}]/([\mathrm{Pr}^{3+}] + [\mathrm{Ca}^{2+}]) \tag{2.3}$$

If $c < 0.5$, then the e_g band is less than 50% filled with electrons. Therefore, it is an n-conductor. If $c > 0.5$, the filling is more than 50%, and thus, p-type. Interestingly, measurement data of the Seebeck coefficient indicate that the carrier type change happens between $Ca_{0.34}$ and $Ca_{0.37}$ and not as expected at $Ca_{0.5}$. The experimental determination by the Hall effect, caused by a magnetic field B_z, is difficult for PCMO. Since the Hall voltage [39]

$$V_y = \frac{B_z j_x}{ne} \tag{2.4}$$

decreases with high carrier density n and low current j_x it is difficult to measure the Hall effect on a material with high carrier density and low mobility. Nevertheless, Asanuma et al. [45] measured the Hall resistance R_H of $CaMnO_3$ and $Pr_{0.14}Ca_{0.86}MnO_3$, which showed n-type conductivity. Further,

they tried to measure the Hall resistance R_H at a Ca content of between 0.5 and 0.8 but were unable to obtain reliable measurements because of the high charge carrier density.

The highly rectifying character of a $Pr_{0.7}Ca_{0.3}MnO_3$/Nb:STO junction (highly rectifying because of the low n-type doping $SrTi_{0.9998}Nb_{0.0002}O_3$) showed that the description with a p-n type model fits better as the description with a Schottky junction model since the built-in voltage determined from the $1/C^2 - V$ characteristics is the same as the built-in voltage determined from the $J/T - 1/T$ characteristics. This can be regarded as verification for the description of $Pr_{0.7}Ca_{0.3}MnO_3$ as a p-type semiconductor.

The determination of the charge carrier type by the Seebeck effect is performed by measuring the sign of the Seebeck coefficient or thermopower S which relates to the thermoelectric voltage ΔV in a material with the temperature difference ΔT in a material by

$$\Delta V = S\Delta T. \tag{2.5}$$

The voltage is caused by the diffusion of the mobile carrier from the hot source to the cold sink. Therefore, the cold part of the material is charged according to the majority type of mobile charge carriers. S is negative ($S < 0$) for n-type materials and is positive ($S > 0$) for p-type materials. This consideration is true for doped semiconductors with clearly defined charge carrier characteristics but becomes more complicated for transition metal oxides.

The Heikes formula can be used [39, 47] to describe the Seebeck coefficient in materials with narrow band and localized charge carriers with hopping mobility. It describes with

$$S = \frac{k_B}{e} \log\left(\frac{c}{1-c}\right). \tag{2.6}$$

the dependence of the Seebeck coefficient from the filling state c of the narrow band. The term $\log(c/(1-c))$ describes the previously described sign change at $c = 0.5$. The term monotonously increases for both filling directions, $c \to 0$ and $c \to 1$, and diverges at $0/1$ to $-/+\infty$. Interestingly, the Heikes formula predicts that the Seebeck coefficient only depends on the band's filling and not on the temperature. Therefore, the Heikes formula should only be applied in cases where the Seebeck coefficient is temperature independent. Seebeck coefficient measurements from PCMO for different stoichiometries and temperatures are shown in Figure 2.4. PCMO shows no strong temperature dependence at room temperature over its whole stoichiometry range except for the stoichiometry $Pr_{0.9}Ca_{0.1}MnO_3$, as can be seen in Figure 2.4a.

Therefore, based on the interpretation of the sign of the Seebeck coefficient, Figure 2.4a shows n-type conductivity until a stoichiometry of $Pr_{0.5}Ca_{0.5}MnO_3$ and p conductivity at the stoichiometry of $Pr_{0.7}Ca_{0.3}MnO_3$. At stoichiometry between $Ca_{0.5}$ and $Ca_{0.3}$, the type of conductivity changes cannot be extracted from Figure 2.4a. However, since the absolute value of the Seebeck coefficient is smaller for $Ca_{0.3}$ than for $Ca_{0.5}$, the expected stoichiometry, which leads to the change of the carrier type, is probably closer to $Ca_{0.3}$.

A more precious measurement on the stoichiometry range between 0.5 and 0.4 can be found in Figure 2.4b. It shows the temperature independent negative Seebeck coefficient in the range from 250 to 300 K, continuously decreasing from $Ca_{0.5}$ to $Ca_{0.4}$. This data verifies the measurement from Figure 2.4a and further narrows the stoichiometric interval of sign change to the range between $Ca_{0.3}$ and $Ca_{0.4}$. This has also been shown by Kozakov et al. [26].

Figure 2.4c shows the Seebeck coefficient in the stoichiometric region $Ca_{0.33}$ to $Ca_{0.48}$. Most of the data stems from a temperature region with strong $S(T)$ dependence. The influence of T on S becomes particularly strong for temperatures below 230 K, when the CO phase begins to form. The data at the highest temperature of 270 K within the plateau region can be regarded as an approximation for room temperature for the change from p-type to n-type conduction in the stoichiometric region between $Ca_{0.37}$ and $Ca_{0.33}$.

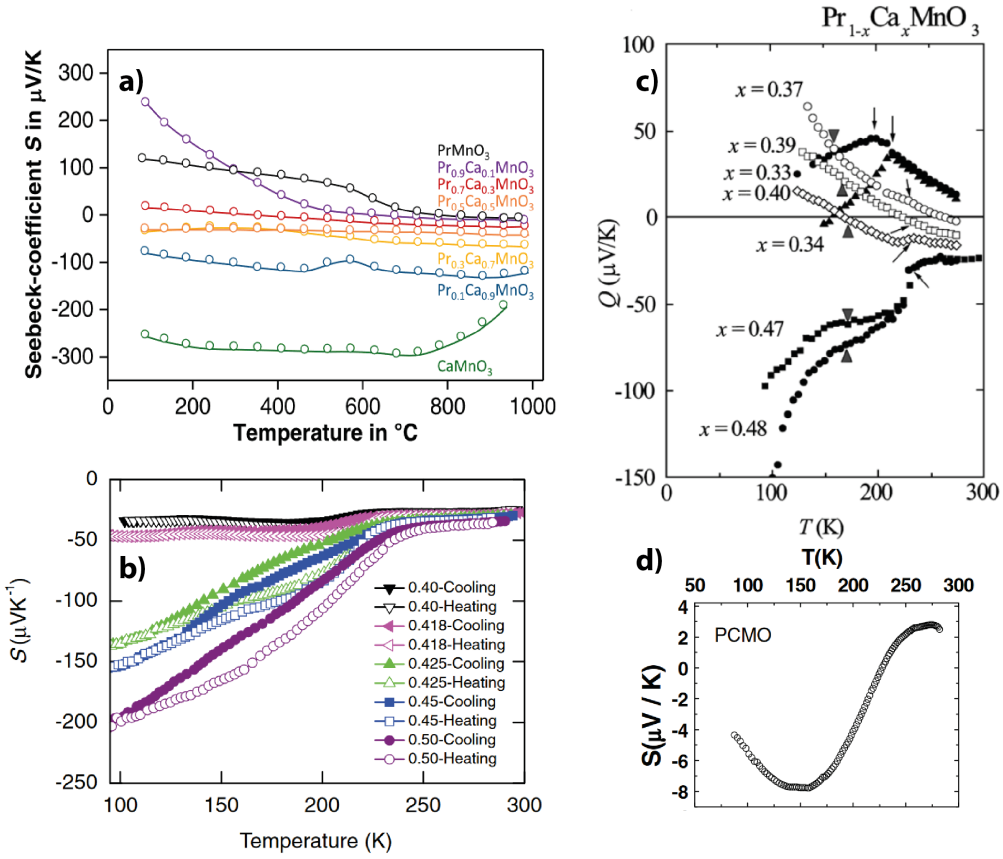

Figure 2.4.: a) Seebeck coefficient from PCMO measured for different stoichiometries measured on bulk, polycrystalline PCMO. Adapted and reprinted with permission from [21], © 2022 by Elsevier. b) Seebeck coefficient S from PCMO in the doping region $Ca_{0.4}$ till $Ca_{0.5}$, taken from [48]. c) Seebeck coefficient of PCMO in the doping range between $Ca_{0.48}$ and $Ca_{0.33}$. Adapted and reprinted with permission from [49]. © 2000 by the Physical Society of Japan. d) Temperature dependence of the Seebeck coefficient of $Pr_{0.67}Ca_{0.33}MnO_3$. Adapted and reprinted with permission from [50]. © 2007 by IOP Publishing Ltd.

The positive diminishing Seebeck coefficient at $Ca_{0.33}$ was also reported by Venkataiah et al. [50] and is depicted in Figure 2.4d. The behavior of PCMO does not fulfill the Heikes formula in the approximate temperature independent region at room temperature, since it would predict a change in sign at $Ca_{0.5}$. This deviation can be explained by considering the defect equilibria. Since metal vacancies dominate in the doping region of $x < 0.5$, as discussed in Chapter 2.2.5, and each metal vacancy causes 3 holes, the real hole concentration is higher than the formal doping by the Ca content [21]:

$$3O_2 \rightleftharpoons 4V_M''' + 12h_{VM} + 6O_O^x. \tag{2.7}$$

Defining the excess hole concentration caused by metal vacancies with h_{VM}, c could be corrected in the following way

$$c = \frac{n - h_{VM}}{n_c}. \tag{2.8}$$

Unfortunately, $h_{VM} \approx 0.15$ is needed for a correction, but according to Figure 2.7 only $h_{VM} \approx 0.02$ could be expected. An additional correction could result from the assumption that a relevant subset b of the e_g electrons are tightly bound and, therefore, do not play a role in the calculation of the configuration entropy. This would change c to

$$c = \frac{n - h_{VM} - b}{n_c - b}. \tag{2.9}$$

The Seebeck data shows that the carrier type in $Pr_{0.7}Ca_{0.3}MnO_3$, the most common stoichiometry for resistive switching devices, cannot simply be described as a p-type, as can be found in the literature. Further, the picture of a charge carrier type change at a certain doping is not consistent with the fact that the conduction mechanism in PCMO is based on a small polaron model, as will be described in the next section. In this model, the description of the charge carriers does not change at a certain stoichiometry.

2.1.4. Polaronic model of PCMO and characterization by optical, vibrational and electric properties

The polaronic nature of PCMO is not only based on the idea, that the polarization of the matter causes the localization of a charge carrier, as reflected in the word polaron. The polarization localization is based on the difference in the dielectric constant at different frequencies. The permittivity is much higher at static frequencies (ϵ_{static}) than at high frequencies ($\epsilon_{\text{high-}\omega}$), since the contributions of dipolar, molecular, and electronic polarization can be neglected. Therefore, for materials with high permittivity, a localized charge in a sphere of the radius r has a higher potential energy by polarization as a fast-moving (delocalized) charge, given in a simple electrostatic model [39] by:

$$\Delta E = \frac{-e^2}{8\pi\epsilon_0 r}\left(\frac{1}{\epsilon_{\text{static}}} - \frac{1}{\epsilon_{\text{high}-\omega}}\right). \tag{2.10}$$

This localization mechanism therefore competes with the delocalization energy represented by the kinetic energy D of the electron, which is half of the bandwidth. Since PCMO is a narrow-bandwidth manganite [22], mechanisms that provide potential energy gain from localization can easily compete with the energetic benefits of delocalization.

Polarization mechanisms can contribute, but the main mechanism of the polaronic trapping in PCMO is based on the Jahn Teller effect which causes a splitting of the degenerated, e_g band and as a result a local lattice distortion. Therefore, the polaronic model is not based on a continuum model as in the polarization-based description by the Fröhlich polaron. Instead, the model to describe PCMO requires a local configuration coordinate to parametrize the distortion as in the

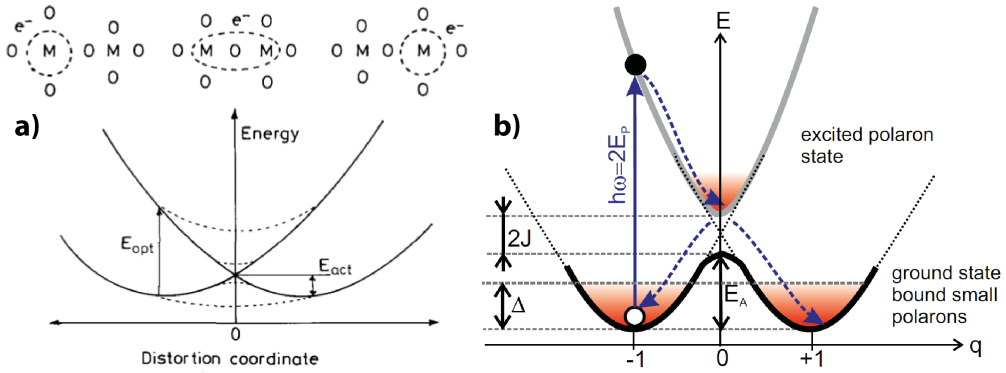

Figure 2.5.: a) General picture of a configuration coordinate model. Adapted and reprinted with permission from [39], © 2006 by John Wiley and Sons. b) Configuration coordinate model for PCMO. Adapted and reprinted with permission from [53], © 2015 by the American Physical Society.

Holstein model [51].

A common scheme for the graphical representation of a configuration coordinate q-based description of the energy landscape is seen in Figure 2.5a [39, 52]. The black line shows the energetic configuration of an electron on either the left or right cation of a two-atom model. The activation energy required to jump between these two states is shown by E_{act}, and a photonic absorption-activated change of the electronic configuration is shown by the absorption of energy E_{opt}. According to the Franck-Cordon principle, this is the most likely photonic absorption process.

The polaronic nature of the charge carrier of PCMO has been described in the literature by a small polaron within the framework of the Holstein model [53]. The Holstein model is described by a Hamiltonian [54, 55], which consists of a sum of three terms. Each term has an energy scaling factor, which scales the individual contribution to the system's total energy. The factors are the phonon energy $\hbar\omega$, the coupling energy g between the electron and the phonon, and the transfer integral J. The Holstein Hamiltonian can be simplified by imposing conditions on the ratio of the energy scales, leading to the model of the small polaron [55, 56]. Small means that the localization of the polaron is of the size of the lattice spacing, which refers to the lattice on which the Holstein model is based and, thus, to the bonding distance. The configuration coordinate model for PCMO is illustrated in Figure 2.5b.

The transfer integral J gives the delocalization energy of the electron over the bond and represents multiplied by the amount of its nearest neighbors Z (PCMO $Z = 6$, octahedral) with $ZJ = D$ the kinetic energy of the electron, which is half of the bandwidth [53]. For $Pr_{0.5}Ca_{0.5}MnO_3$ the bandwidth can, can be estimated by DFT calculations to be between 760 and 1300 meV, giving an estimate of J between 60 and 110 meV [57]. Experimentally, values can be derived from measurements of the thermally activated hopping conduction, leading to J between 90 and 110 meV [53], depending on the stoichiometry.

The energy of the Jahn-Teller involved phonon mode can be 42 or 71 meV [44]. The lower energetic modes are connected with octahedral tilting modes, while the higher energetic modes are considered to be connected with Jahn-Teller stretching and breathing modes [53, 58]. Thus, the higher energetic Jahn-Teller modes influence the hopping by influencing the tolerance factor and, therefore, indirectly, the octahedral tilting, while the lower energetic modes are bending modes of the bonding angle. The stimulation of the 71 meV mode can cause a phase transition from insulator to conductor in the CO phase by perturbating the tolerance factor and thus reducing the distortion of the Mn-O-Mn angle, as has been experimentally seen in pump-probe measurements [44].

Another experimental way to determine the energies of the involved phonon modes is by op-

tical investigation of two different optical excitations, shown in Figure 2.5b. PCMO shows two absorption features in the near-infrared region, which relate to the Frank-Condon on-site Jahn-Teller-excitation and the polaron hopping [53], respectively. The width of these photon absorption peaks is caused by the variance in the ground state Δ and, therefore, relates to the energy of the involved phonon modes. By fitting the peak width, phonon energies can be determined. The on-band Jahn-Teller-excitation gives energies of the involved phonon modes of 100-120 meV, while the hopping transition leads to phonon modes between 36 and 60 meV [53]. Interestingly, the phonon modes for hopping could be the tilting mode of the Mn-O-Mn angle. However, the mathematical calculation of the involved phonon energies from the peak width wrongly assumes $J = 0$, which could affect the precision of the determined energy value [53].

The strongest localization of the polaron occurs under the condition that the kinetic energy of the electron is smaller than the phonon-electron coupling $J \ll g$, and the kinetic energy of the electron is smaller than the energy of the involved phonon mode $J \ll \hbar\omega$ [55]. In the atomic limit $J = 0$, the simplified Hamiltonian can be transformed to a single oscillator picture, which describes the small polaron. It connects each phonon mode with a lattice distortion and has a defining parameter $\alpha = g/(\hbar\omega)$ [55], which gives the strength between the coupling of the lattice vibration and the electron. For high α, the electron is strongly coupled with the lattice vibration, and the polaron binding is high. The polaron bonding energy of this model is $E_p = g^2/(\hbar\omega)$ [55]. As can be seen in Figure 2.5, the polaron binding energy is directly connected to the Frank-Condon optical absorption peak and can be investigated by optical conductivity measurements. From the approximation of a local parabolic energy landscape, as drawn in the configurational coordinate model of Figure 2.5b the equation $E_p = E_{\mathrm{photon}}/2$ can be geometrically derived. It relates the polaron binding energy directly to the absorption energy of the involved photon, which is only valid when the kinetic energy of the electron D is smaller than the energy variance in the ground state Δ [53]. This is not the case for PCMO and therefore the photon energy of the connected absorption must be corrected by the term $E_{\mathrm{photon}}/2 + D^2/(4E_p) = E_p$ [53]. This allows the polaron binding energy to be determined from the frequency of the absorption peak if a correct value of the kinetic energy D is used.

In order to include hopping into the model, the transfer integral J cannot be zero. The parameter $\gamma = \hbar\omega/J$ can be defined for a mathematical description. For strong coupling $\alpha > 1$, the main guiding force of the movement of the electron is the electron-coupled lattice distortion. If the delocalization energy J dominates ($\gamma \to 0$), the lattice follows the electron, and an adiabatic description of the hopping process can be used [53, 55]. The opposite case is called anti-adiabatic and would lead to a substantial increase in the effective polaron mass [55]. Since for PCMO J and $\hbar\omega$ are of similar sizes, the adiabatic approximation is not strongly fulfilled, and PCMO is between adiabatic and anti-adiabatic regime [34, 53]. This gives a constraint to the equation for polaron hopping by an electric field, which was derived under adiabatic assumptions [34] and gives:

$$\frac{\sigma(E,T)}{\sigma_0(T)} = \frac{E_C(T)}{E}\sinh\left(\frac{E}{E_C(T)}\right) \tag{2.11}$$

where $\sigma_0(T)$ is the ohmic conductivity dominating at small fields and $E_C(T)$ the crossover field between ohmic and non-ohmic behavior

$$E_C(T) = \frac{2k_BT}{ea} \tag{2.12}$$

with the polaron hopping length a [34].

For a finite J, the ratio $\lambda = E_p/D$ of the previously defined polaron formation energy E_p and the kinetic energy D of the electron shows how stable the polaron is against delocalization. In the adiabatic limit λ and α are the two defining parameters for the polaronic model [55]. Strong coupling ($\lambda > 1$) is a requirement for the model of a small polaron [53]. In the case of strong

coupling, each jump of the electron relates to a localized jump of the lattice distortion and thus, to a Jahn-Teller-based rearrangement of the electronic structure. Therefore, the concept of the configuration coordination model can be specified for the polaron hopping in PCMO as shown in Figure 2.5b [53]. The broadening of the symmetric state of delocalization, given by $2J$, lowers the activation energy for hopping [52]. In the simple configuration model with the parabolic assumption [52] the necessary E_A activation energy for the polaron hopping in PCMO becomes

$$E_A = E_P/2 - J. \tag{2.13}$$

This equation has to be corrected for a strongly correlated manganite by an intersite Coulomb repulsion term E_C to

$$E_A = E_P/2 - J + E_C. \tag{2.14}$$

At small fields, the conductivity of the above-defined term is dominated by the conductivity $\sigma_0(T)$, which

$$\sigma_0(T) = \frac{A}{T} e^{-E_a/(k_b T)}. \tag{2.15}$$

which is thermally activated by the energy E_a of the small polaron hopping. The factor A consists of 22

$$A = \frac{n e^2 a^2 \omega_0}{2\pi k_B}. \tag{2.16}$$

the charge density n, the elementary charge e, the hopping length a and the frequency of the involved phonon mode ω_0. The conductivity increases with the temperature, as can be seen in Figure 2.6a and Figure 2.6b and can lead to the wrong assignment as semiconducting property. However, unlike in a semiconductor, the charge carrier density does not increase with temperature; instead, the mobility does. It is evident from Figure 2.6a and Figure 2.6b that the overall conductivity increase with the increase of Calcium doping for $x > 0.1$. This is probably caused by the decrease in the ratio of Mn^{3+} ions with a larger ionic radius, leading to an increase in the tolerance factor, a reduction in the tilting of the Mn-O-Mn angle, and higher hopping conductivity. Fitting the temperature dependence in Figure 2.6a shows that the activation energy is quite independent of the stoichiometry from $Ca_{0.2}$ to $Ca_{0.5}$ for temperatures higher than the CO phase, and that $Pr_{0.65}Ca_{0.35}MnO_3$ has an activation energy of 145 meV at room temperature. These values are varying in the literature, e.g. Figure 2.6b measured an activation energy of 128 meV for $Pr_{0.7}Ca_{0.3}MnO_3$. This can probably be explained by a difference in current densities, as Schramm et al. [34] showed for $Pr_{0.68}Ca_{0.32}MnO_3$ (Figure 2.6c) that the variation in the activation energy increases with lower current densities.

2.1.5. PCMO defect chemistry and the influence of oxygen vacancies

PCMO defect chemistry and the influence of oxygen vacancies point defects are part of the thermal equilibrium since they lower the Gibbs free energy by the increase of the configurational entropy. This can happen due to intrinsic defects, which are rearrangements of the existing material without changing stoichiometry. Examples for intrinsic defects are Schottky-defects (volume expanding vacancy generation), Anti-Schottky defects (volume-reducing pair of interstitials), Frenkel-defects (cation interstitial by cation vacancies generation), and Anti-Frenkel (anion interstitial by anion vacancy generation). For dense perovskites, the formation energy of interstitial is very high, and therefore, Schottky defects are particularly relevant [8], which form according to the following equation

$$2M_M^X + 3O_O^X \rightleftharpoons M_2O_3 + 3\ddot{V}_O + 2V_M'''. \tag{2.17}$$

PCMO is generalized by M_2O_3, where M stands for the metal cations. Point defects can also be caused extrinsically by exchange reactions with the surroundings. This causes non-stoichiometry

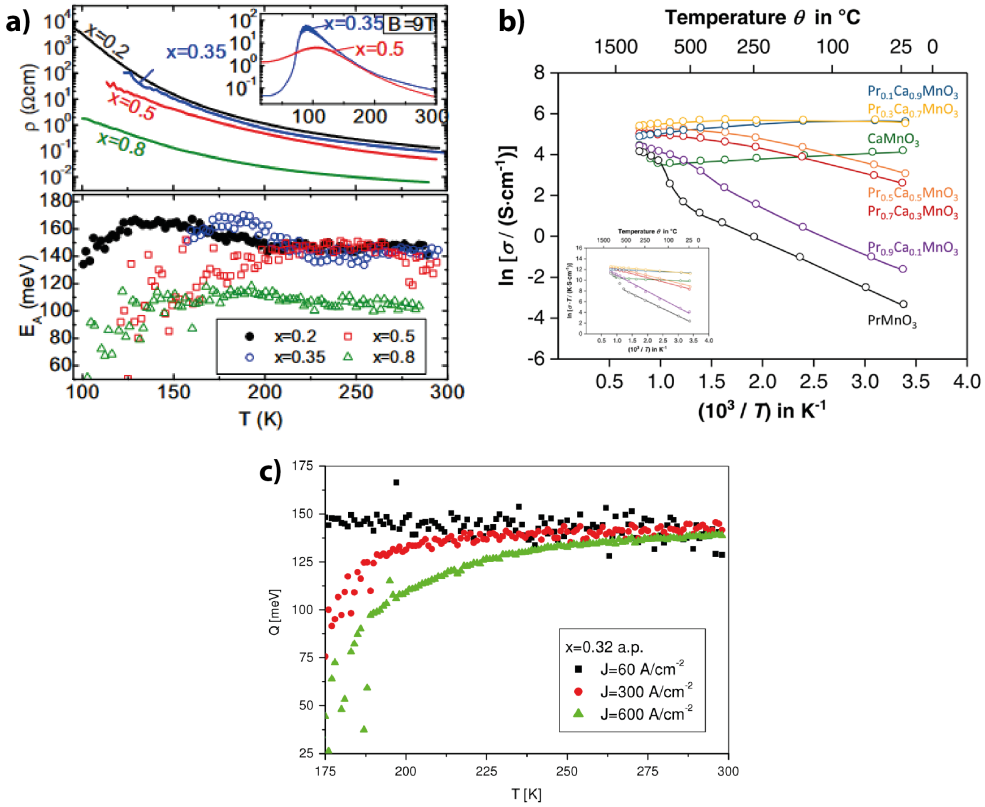

Figure 2.6.: a) Temperature dependence of the resistance and the fitted activation energy of PCMO with different doping concentrations x. The inserted graph verifies the CMR effect. Adapted and reprinted with permission from [53], © 2015 by the American Physical Society. b) Temperature dependency of conductivity for bulk polycrystalline $Pr_{1-x}Ca_xMnO_3$ with different stoichiometries. For $x < 0.7$, temperature-activated polaron hopping describes the dependency. The linear fit in the inset gives the following activation energies: $E_a(Pr_{0.3})$ = 43 meV, $E_a(Pr_{0.7})$ = 128 meV, and $E_a(Pr_{0.9})$ = 259 meV. Adapted and reprinted with permission from 9, © 2022 by Elsevier. c) Activation energy of the small polaron of $Pr_{0.68}Ca_{0.32}MnO_3$ for three different current densities in dependence of the temperature. Adapted and reprinted with permission from [34], © 2008 by IOP Publishing Ltd.

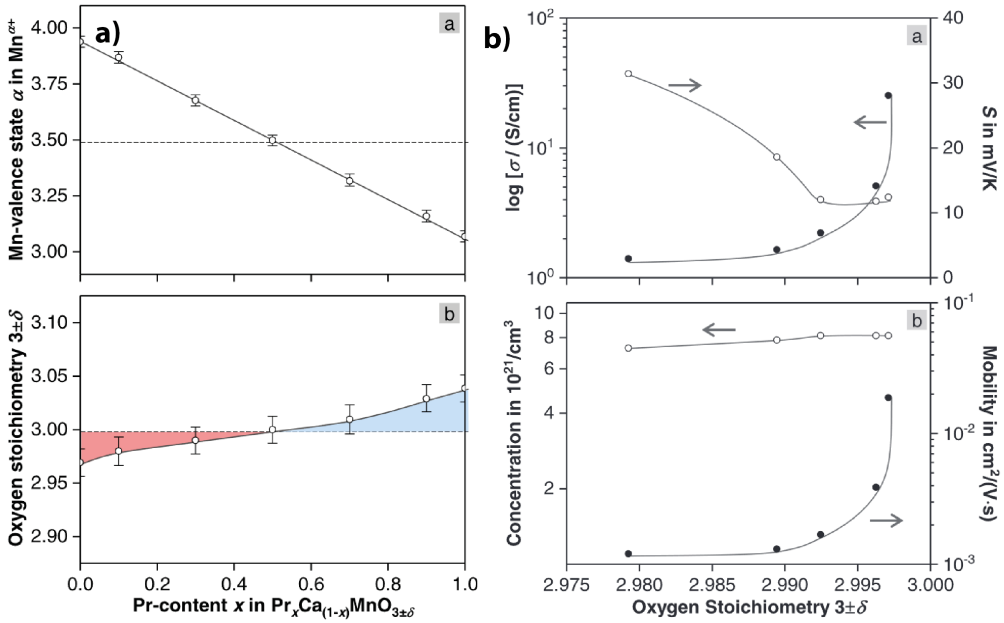

Figure 2.7.: a) Oxygen non-stoichiometry of PCMO, doping dependent. Measured on bulk polycrystalline samples by iodometric titration. Adapted and reprinted with permission from [21], © 2022 by Elsevier. b) Change of Seebeck coefficient, charge carrier density, and mobility by oxygen vacancy formation in $Pr_{0.7}Ca_{0.3}MnO_3$. Adapted and reprinted with permission from [21], © 2022 by Elsevier.

and electronic doping. Oxygen exchange reaction can also take place by field activation at cathode/anode interfaces which is the basis of resistive switching in the case of the valence change mechanism. For oxides in contact with the atmosphere, the exchange is especially the incorporation or release of oxygen as formalized below. The incorporation of oxygen leads to metal vacancy $V_M^{'''}$ formation and hole doping

$$3O_2 \rightleftharpoons 4V_M^{'''} + 12h^{\cdot} + 6O_O^x. \tag{2.18}$$

The release of oxygen leads to the formation of oxygen vacancies $\ddot{V}_O$ and electron $e^{'}$ doping

$$O_O^x \rightleftharpoons \ddot{V}_O + 2e^{'} + \frac{1}{2}O_2. \tag{2.19}$$

The oxygen stoichiometry, therefore, shows the type of vacancies generated by exchange with the atmosphere and the overall modification of the valence. For bulk PCMO [21] (sintered at 1350 °C and cooled slowly below 1 K/min in oxygen atmosphere) the dominating point defects are oxygen vacancies $\ddot{V}_O$ at a doping of $x > 0.5$ and metal vacancies $V_M^{'''}$ at a doping of $x < 0.5$ as can be seen from the measurement of the oxygen non-stoichiometry shown in Figure 2.7a. The relative amount of either metal or oxygen vacancies increases as $x \to 1/0$, thereby slightly compensating the doping deviation from $Mn_{0.5}$ through intrinsic oxygen non-stoichiometry.

Oxygen vacancies $\ddot{V}_O$ and metal vacancies $V_M^{'''}$ can compensate each other by

$$0 \rightleftharpoons 3\ddot{V}_O + 2V_M^{'''}. \tag{2.20}$$

The hole doping by Ca^{2+} can be formalized by the doping with a generalized acceptor AO into the generalized metal oxide M_2O_3 46[59]

$$AO + \frac{1}{2}O_2 \rightleftharpoons 2A_M^{'} + 2h^{\cdot} + 3O_O^x. \tag{2.21}$$

Since the metal vacancy contribution dominates in $Pr_{0.7}Ca_{0.3}MnO_3$ in the thermal equilibrium at room temperature, the actual hole doping level can be considered higher than the formal hole doping level given by the calcium content.

For resistive switching, the effect of oxygen vacancies on the resistance is essential. The conductivity

$$\sigma = en\mu \tag{2.22}$$

is the product of the charge carrier density n, and the mobility μ. The mobility is determined by the polaronic nature (eq. 2.11, 2.15, and 2.16). Oxygen vacancies are considered to increase the resistance due to a reduction in mobility μ. In case of hole conducting PCMO, oxygen vacancies are also considered to increase the resistance due to a reduction of the charge carrier density n. As can be seen in eq. 2.22, the reduction of the conduction is linear with a change in the charge carrier density and can be nonlinear if the effect of the vacancies on the mobility is nonlinear.

Figure 2.7b shows the impact of thermal reduction of $Pr_{0.7}Ca_{0.3}MnO_3$ on conductivity and the Seebeck coefficient. An increase in the Seebeck coefficient experimentally verifies the reduction of the hole charge carriers with decreasing oxygen content. Moreover, a non-linear decrease of the conductivity is measured. The strong non-linear change of the conductivity in PCMO cannot be explained by the small linear change of charge carrier density as expected from the iodometric measurements. Pithan et al. [21] further strengthen this argument by decomposing the conductivity into charge carrier density and mobility (Figure 2.7b) by calculating the carrier density from the Seebeck coefficient with the Heikes formula, which has some inaccuracy, as discussed in Chapter 2.1.3. It can be concluded that the change in mobility is the dominating effect of the conductivity change, observed during reduction. However, this raises the question of what causes the mobility change in PCMO. The activation energy of the polaron hopping depends strongly on the doping of the PCMO, as can be seen in Figure 2.6a+b. Over a broad doping range from $x = 0.2$ to $x = 1$, electron doping increases the activation energy and, therefore, the resistance.

Pithan et al. [21] or Nian et al. [60] assign the mobility reduction to the interruption of Mn-O-Mn chains, which are essential for polaron hopping (Chapter 2.1.4). However, this cannot be the only reason since a small change in vacancy concentration, like in Figure 2.7, does not broadly disturb the percolation network of Mn-O-Mn chains or severely increase the effective hopping path length but already causes a mobility reduction.

Besides the influence of the doping on the activation energy, also structural arrangements of the vacancies $\ddot{V}_O$ can play a role. Pithan et al. [21] analyzed neutron diffraction pattern and concluded that the vacancies preferably form in the manganese planes of the perovskite. This causes a stripe or superstructure formation in the TEM, which can be manipulated and moved by the application of an electric field, as shown by Liao et al. (Figure 2.8).

Jooß et al. [62] also observed this superstructure in the vicinity of the metal/oxide interface after a initializing process applied to a bulk PCMO by a Pt/Ir tip in a TEM, which is related to a resistance increase. They explained the structural change by a polaron order-disorder transition within the PCMO, which localizes the polarons. They further argued that this transition could be especially pronounced when a contact causes a down-bending of the bands in the PCMO because the hole depletion, similar to decrease of the Ca doping as can be seen in Figure 2.1, causes an increase in the octahedral tilting and therefore a stronger polaron localization.

Also, the increase of disorder in the Coulomb potential by high vacancy concentrations can lead to a mobility reduction as discussed in the framework of Anderson localization [28]. This effect can especially be considered for narrow bandwidth manganites such as PCMO. Particularly since the mixed valence doping already causes disorder on the A site. Further, the orthorhombic tilting leads to an extended unit cell within which the Mn-O-Mn bonding angles and distances show small variations [26]. This further increases the disorder in the electrostatic potential. The potential disorder can cause a separation of localized and delocalized charge carriers at the mobility edge, an energy level in the density of states [28, 39]. This idea is supported by DFT calculation can be

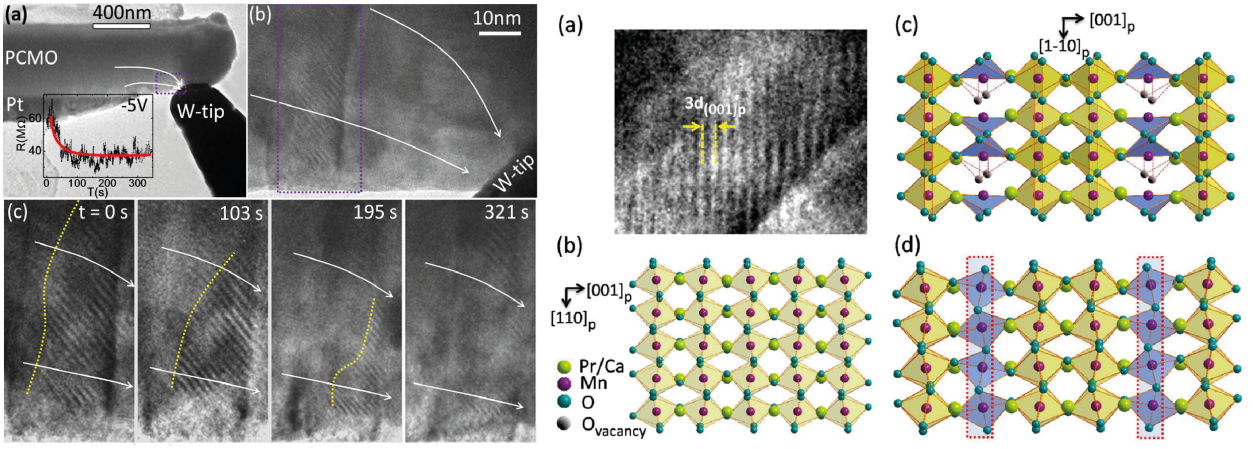

Figure 2.8.: The left series of images shows the time-dependent movement of the oxygen vacancy stripe pattern by application of -5 V on the W tip, in situ, observed in TEM. The right series of images shows the proposed alignment of the oxygen vacancies in PCMO in the Mn-based planes, forming stripes. Adapted and reprinted with permission from [61], © 2012 by AIP Publishing.

seen in Figure 2.10b [63].

To use this knowledge to gain deeper insights into the mechanism of resistive switching, it is important to know the concentration of oxygen vacancies in the interface region and its change during switching. If the field-driven vacancy concentrations in the interface regions are much higher than the $\ddot{V}_O$ concentrations achieved by thermal annealing in a bulk sample, it will be important to clarify if their impact on the conductivity remains the same.

For a strong thermal reduction, Pithan et al. [21] observed the appearance of additional phases $PrMnO_3$ and $Ca_2Mn_2O_4$ identified by additional Bragg reflections. The $Ca_2Mn_2O_4$ phase start to appear at an oxygen sub-stoichiometry of $O_{2.902}$ and the $PrMnO_3$ phase at an oxygen sub-stoichiometry of $O_{2.786}$. This shows that strong electrochemical reduction could even lead to phase separation.

Lee et al. [43] conducted spectroscopic measurements on PCMO before and after electrochemical reduction induced in a scanning force microscope by a grid scan with a tungsten tip. They applied +4 V to extract the oxygen from the interface region at each contact point with the surface. This area of higher resistance is called HRS in Figure 2.9. The reference virgin surface with lower resistance is named LRS. Since this type of performed reduction reaction is similar to the oxygen extraction within a switching device, the observed spectroscopic changes can be assumed to be similar to the vacancy concentrations relevant for resistive switching.

The influence of oxygen vacancies on the charge carrier density can be seen spectroscopically in ultraviolet photoelectron spectroscopy (UPS) and X-ray absorption spectroscopy (XAS) measurements (Figure 2.9). The UPS shows for the reduced (HRS) PCMO a clear drop in the peak b corresponding to the reduction of O 2p binding states and an increase in the edge energy, corresponding to a filling of the e_g band [43]. Further, the X-ray absorption near-edge structure (NEXAS) signal from the excitation from the O 1s state shows a decrease of the peak A with reduction. Since the peak A corresponds to the transition from O 1s into an empty e_g state, the decrease of peak A shows the filling of the holes by oxygen vacancy-induced n-type doping.

Lee et al. [43] conclude from the spectroscopic measurements that the decrease of the resistance due to the reduction is caused by a metal-insulator transition based on the filling of the e_g band.

They further observed an increase in the band gap between the e_{g1} and e_{g2} bands. Experimental evidence is the decrease of peak A and the increase of peak B. The increase of peak B is interpreted as an energetic increase of the e_{g2} levels. An increase of the band gap also has been

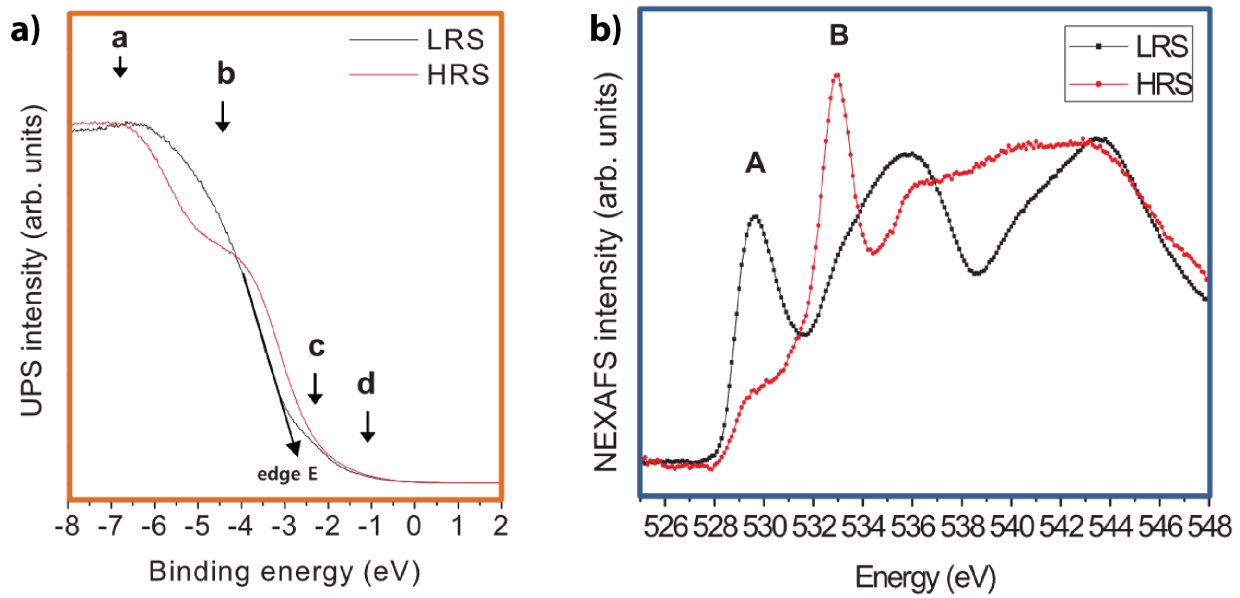

Figure 2.9.: Influence of oxygen vacancies on $Pr_{0.7}Ca_{0.3}MnO_3$ measured by UPS and XAS. LRS represents the as-deposited PCMO, and HRS represents the electronically reduced PCMO. a) shows the change in the UPS signal, and b) shows the change in the XAS signal. Adapted and reprinted with permission from [43], © 2013 by Springer Nature.

shown by UV/VIS studies of Asanuma et al..32 Figure 2.10a shows that the band gap increases for PMO (0.4 eV), CMO (0.4 eV), and $Pr_{0.5}Ca_{0.5}MnO_3$ (0.2 eV) after thermal reduction. Thus, a band gap increase by reduction happens for all filling levels of the e_{g1} band.

Lee et al. [43] claim further that an increase in energetic separation between the e_{g1} and e_{g2} can be considered as an increase in Coulomb interaction interpreted within the framework of the Hubbard model. They conclude that the low resistance caused by the band filling relates to a Mott metal-insulator transition based on strong correlation effects. This argumentation can be seen critical, since the separation of the e_{g1} and e_{g2} levels is caused by the Jahn-Teller-splitting and the occupying electrons of the e_{g1} and e_{g2} levels have the same spins because of the strong Hund's coupling. Therefore, their energetic separation cannot be connected to intersite Coulomb repulsion.

It can be summarized that oxygen vacancies increase the resistance and the band gap of the PCMO. Both can influence the heterojunction of a resistive device.

2.1.6. Work function of PCMO

Since the current transport within PCMO-based memristive devices is influenced by the band bending at the interfaces, the work function of PCMO is an important parameter. The literature values of work functions can differ for different measurement methods and between differently deposited PCMO layers. A direct method of measurement is UPS or Kelvin-Probe measurements. Indirect measurements are based on the transport characteristics of heterojunctions like MOS (metal/oxide/semiconductor), pn-junctions, or Schottky diodes and the fitting of the transport characteristics by a model. The work function values, which can be found in the literature, are summarized in Table 2.1.

As can be seen, the work function of PCMO depends on its doping. The MOS-characteristic measurement shows a higher value as expected from the other measurements, which is probably caused by a difference in growth conditions. The PCMO used for the MOS characteristics had been sputtered and post-annealed for crystallization while in the other papers the films were grown

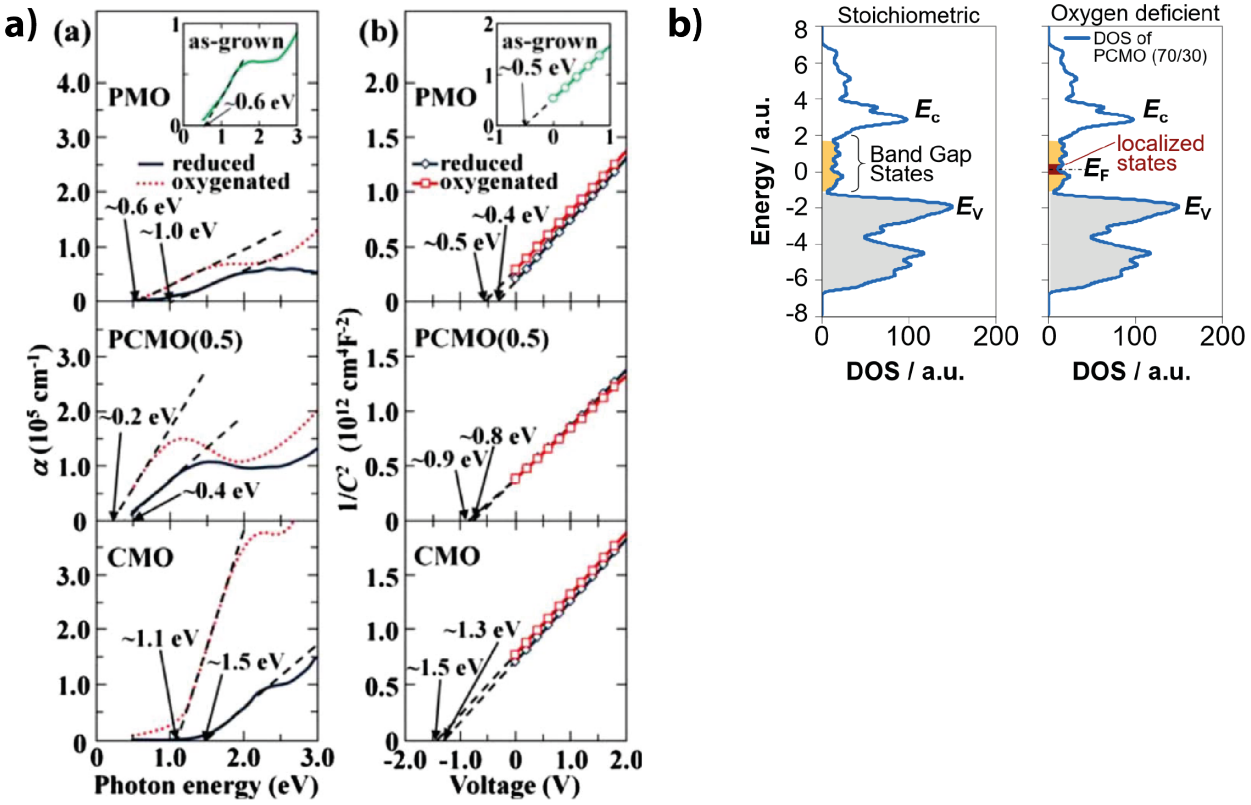

Figure 2.10.: a.a) Change of the bandgap and a.b) $1/C^2 - V$ characteristic of PMO, CMO, and $Pr_{0.5}Ca_{0.5}MnO_3$, oxygenated and reduced. Adapted and reprinted with permission from [45], © 2012 by AIP Publishing. b) Proposed localization of electrons by oxygen vacancies in PCMO. Based on unpublished but presented DFT calculations from Rene Meyer [63].

Method	Work Function in eV	Stoichiometry	Source
Kelvin-Probe	4.896	$Pr_{0.7}Ca_{0.3}MnO_3$	[64]
STO/PCMO pn-junction	4.4	$PrMnO_3$	[45]
	4.6	$Pr_{0.7}Ca_{0.3}MnO_3$	[46]
	4.8	$Pr_{0.5}Ca_{0.5}MnO_3$	[45]
	5.4	$CaMnO_3$	[45]
PCMO/ZrO_2/SiO_2/p-Si MOS	5.43	$Pr_{0.7}Ca_{0.3}MnO_3$	[65]

Table 2.1.: Literature values of PCMO work function.

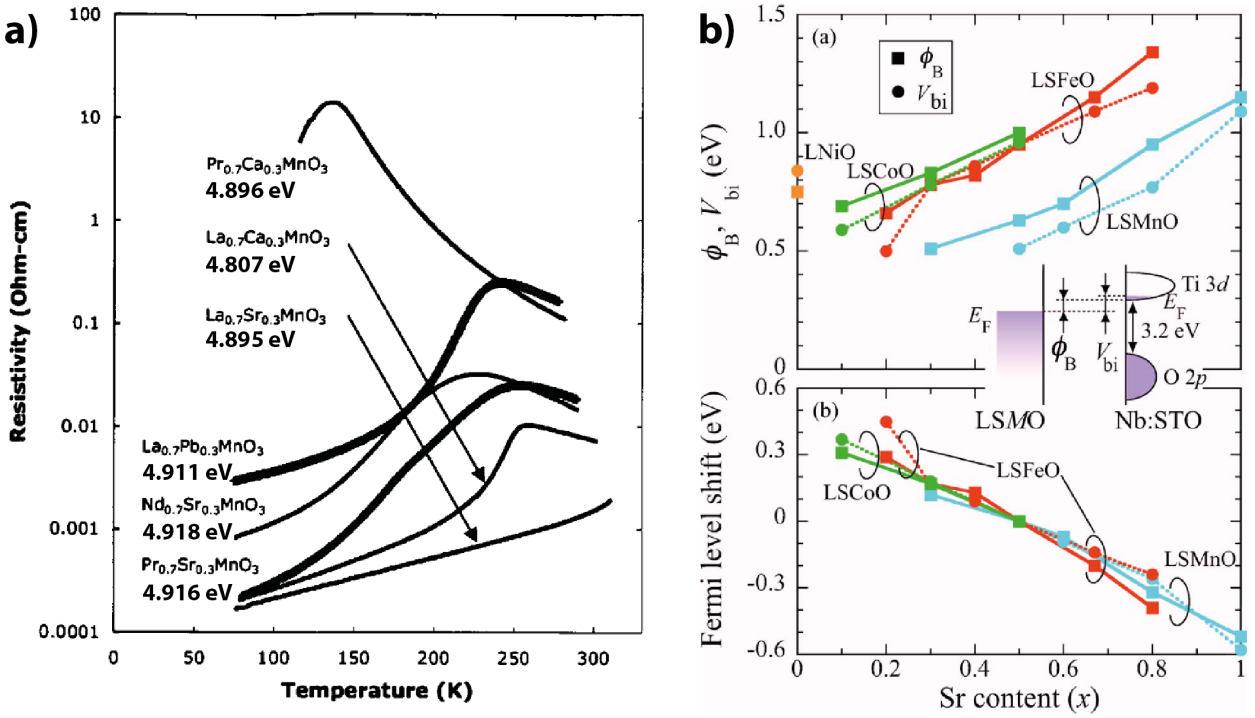

Figure 2.11.: a) Temperature dependence of the resistance of different manganites with the same doping but different lanthanides and divalent ions. The resistance shows many orders of magnitude of variation. Kelvin probe measurements of the work function show low variation. Adapted and reprinted with permission from [64], © 2004 by AIP Publishing. b) Shift of Fermi level in dependency of the doping in $La_{1-x}Sr_xMO_3$, with M=(Mn, Fe, and Co), determined by the Schottky junction with Nb:STO, from the $I-V$ (forward direction) characteristics and $1/C^2-V$ (reverse direction) characteristic. Adapted and reprinted with permission from [66], © 2007 by AIP Publishing.

by PLD directly at crystallizing temperatures. More details on the different work function measurements and the comparison of different valent manganites are discussed below. Direct work function measurements by the Kelvin probe method for the different mixed valent manganates with the same doping $Ln_{0.7}D_{0.3}MnO_3$ but with different Lanthanides La and divalent cations D with significant differences in the conductance show quite similar work functions (Figure 2.11a). All the combinations LaCa, LaSr, LaPb, PrCa, PrSr, and NdSr have work functions between 4.807 and 4.918 eV with $Pr_{0.7}Ca_{0.3}MnO_3$ at 4.896 eV [64].

Measurements of the interface between n-type doped $SrTi_{0.99}Nb_{0.01}O_3$ and high charge carrier $La_{1-x}Sr_xMO_3$ (where M is Mn, Fe, or Co) showed that it behaves like a Schottky junction [66]. Determination of the Schottky barrier from the forward bias behavior, as well as determination of the built-in voltage from the $1/C^2-V$ characteristic in the reverse direction, shows that the work function of all three transition metal oxides increases linearly with the hole doping x (Figure 2.11b). The linear increase demonstrates that no Fermi-level pinning takes place at the interface.

Sawa et al. [46] claims from the comparison between the junction of $Pr_{0.7}Ca_{0.3}MnO_3$ and $La_{0.7}Sr_{0.3}MnO_3$, respectively, with Nb:STO that the description of the highly rectifying junction with PCMO fits better to a description of a pn junction as to the description of a Schottky junction. Their main argument is that the PCMO junction does not show a temperature dependence of the leakage current up to an applied voltage of 100 V in the reverse direction compared to $La_{0.7}Sr_{0.3}MnO_3$, where the leakage current increases with decreasing temperature. Further, they determined the built-in voltage from the temperature dependence of the J_0 of the $J-V$ char-

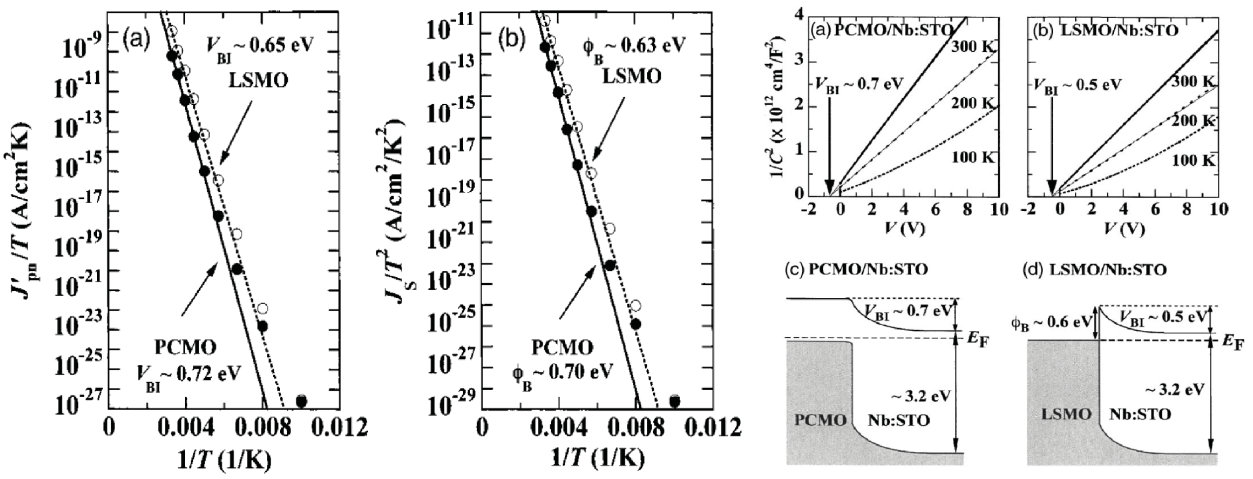

Figure 2.12.: Built-in voltage determination from the $Pr_{0.7}Ca_{0.3}MnO_3$ and $La_{0.7}Sr_{0.3}MnO_3$ junction. Analysis of the temperature dependency of the $J-V$ characteristics in the forward direction and of the temperature dependency of the $1/C^2-V$ characteristics. Adapted and reprinted with permission from [46], © 2005 by AIP Publishing.

acteristics in the forward direction. In a Schottky junction model, J_0 has a linear temperature dependence in a $J/T^2-1/T$ plot, and in the model of a pn-junction, the linear dependence was analyzed by $J/T-1/T$ plot. Since J_0 of PCMO and $La_{0.7}Sr_{0.3}MnO_3$ have a linear dependence (Figure 2.12) in both models and give with 0.70 V (PCMO), 0.63 V ($La_{0.7}Sr_{0.3}MnO_3$) (Schottky-model) and 0.72 V (PCMO), 0.65 V ($La_{0.7}Sr_{0.3}MnO_3$) (pn-model) similar results for the built-in voltage, the temperature dependence does not exclude the description with one of the models. This value was compared with the built-in potential determined from the $1/C^2-V$ dependence in the reverse direction (Figure 2.12), which is 0.7 V for PCMO and 0.5 V for $La_{0.7}Sr_{0.3}MnO_3$. Since both ways lead to the same built-in voltage of 0.7 V, a work function of 4.6 eV can be derived for $Pr_{0.7}Ca_{0.3}MnO_3$ while assuming 3.9 eV as the electron affinity of STO.

Based on the same analysis, Asanuma et al. [45] investigated the $1/C^2-V$ characteristics of the Nb:STO junction with $CaMnO_3$, $Pr_{0.5}Ca_{0.5}MnO_3$ and $PrMnO_3$ (Figure 2.10). The work function increase by Ca hole doping by represented by an increase of the built-in voltage. This behavior is the same as for for $La_{1-x}Sr_xMO_3$ (Figure 2.11b).

To investigate the influence of oxygen vacancies, the samples were first thermally reduced by annealing 1 hour at 600 °C in 10^{-7} Torr and subsequently measured after annealing 1 hour at 600 °C in 1 atm O_2. As a result, the work function decreases by the electron doping from oxygen vacancy formation during annealing in reducing atmospheres, which is the opposite effect of Ca hole doping. The built-in potential decreases from 0.5 V to 0.4 V ($PrMnO_3$), 0.9 V to 0.8 V ($Pr_{0.5}Ca_{0.5}MnO_3$), and 1.5 V to 1.3 V ($CaMnO_3$). Assuming 3.9 eV as electron affinity of STO leads to the following work functions: 4.4 eV/4.3 eV ($PrMnO_3$), 4.8 eV/4.7 eV ($Pr_{0.5}Ca_{0.5}MnO_3$), and 5.4 eV/ 5.2 eV ($CaMnO_3$) with oxygenated / reduced.

A value of 5.43 eV for the work function of $Pr_{0.7}Ca_{0.3}MnO_3$ was found by Bi et al. [65] analyzing the MOS capacitance characteristics of PCMO/ZrO_2/SiO_2/p-Si, where PCMO is serving as the metal. In this study, the flat band voltage of the MOS was determined for different SiO_2 and ZrO_2 thicknesses. It was shown that the influence of charges within ZrO_2 and especially within SiO_2 could be neglected. Further, the thickness dependence enabled Bi et al. [65] to separate the influence of the interface charges and determine the work function.

The calculated work function of 5.43 eV of $Pr_{0.7}Ca_{0.3}MnO_3$ and is much higher than the previously discussed work function of 4.896 eV from the Kelvin method [64] or 4.6 eV from the Nb:STO junction characteristics [46]. The authors discuss this issue using supportive DFT calculations,

which investigate the influence of oxygen enrichment in the interface region. Their DFT calculation shows that oxygen enrichment at the PCMO interface increases the work function. This fits the previously discussed observation that oxygen vacancies reduce the work function. Bi et al. [65], therefore, explain the high work function with an increase of oxygen at the PCMO/ZrO_2 interface.

An alternative explanation for the difference in work function could be the difference in crystalline quality at the measured interfaces caused by the difference in the growth conditions. In all three publications where lower work functions were found, PCMO was grown epitaxial by pulsed laser deposition on either $LaAlO_3$ or Nb:STO at high temperatures of 800 °C [64], 700 °C [46] and 760 °C [45] and with oxygen as the background gas. Bi et al. [65], in comparison, used RF-sputtering at 490 °C. Since the sputter deposition did not lead to full crystallinity, an additional thermal treatment of 5 minutes in a nitrogen atmosphere at 600 °C was used. However, it can be expected that the crystalline quality is better for epitaxial growth, causing a reduction of the work function.

2.1.7. Relative permittivity of PCMO

The relative permittivity ϵ_r of PCMO influences the effect that charge has on the electrical potential and is, therefore, an important material property for band bending considerations. The higher the permittivity, the more charge will be shielded, and the lower its effect on the potential. The typical way to measure the dielectric constant is by impedance spectroscopy. Since the capacitance

$$C = \epsilon_r \epsilon_0 \frac{A}{d} \tag{2.23}$$

of a parallel-plate capacitor with PCMO as dielectric increases with its relative permittivity, ϵ_r can be calculated by fitting the dielectric response with an equivalent circuit. The permittivity values of PCMO vary in the literature. Borgatti et al. [67] performed impedance spectroscopy of PCMO-based memristive devices before and after forming and used $\epsilon_r = 110$ for fitting the contribution from an oxygen-depleted $Pr_{0.5}Ca_{0.5}MnO_3$ layer. Sheng et al. [68] performed impedance measurements on $Pr_{0.5}Ca_{0.5}MnO_3$ - Nb:STO junctions and determined a static dielectric permittivity of $\epsilon_r = 39$ at room temperature. There exist several reports of a colossal dielectric response of 10^3 to 10^5 for PCMO at low temperatures. However, Biškup et al. [69] claim that, quite probably, these findings do not originate from a change of the bulk properties but are caused by a contact capacitance. According to their opinion, the permittivity of bulk PCMO can considered to be $\epsilon_r = 30$.

2.2. PCMO based memristive heterostructures

2.2.1. General consideration on PCMO based switching devices

Different types of stacks are used to fabricate PCMO-based memristive devices. This comprises epitaxial grown, polycrystalline, or amorphous PCMO. In memristive stacks, PCMO is sandwiched between an active switching interface and an ohmic contact. Noble metals, such as Pt, that do not oxidize at the PCMO interface are used for ohmic contact. For the epitaxial growth of PCMO, $SrRuO_3$ (SRO) can be used as a lattice-matched conductive bottom electrode.

The switching interface consists of an insulating, mixed conducting oxide and a reduced PCMO interface region. Some reports consider a space charge zone in the PCMO. The impact of the oxygen exchange on the current transport is most pronounced at the switching interface. Since the insulating oxides that are used have, as a result of the large band gap, no significant amount of electrons in the conduction band, this layer is called tunnel oxide (TO) for simplicity in this Chapter.

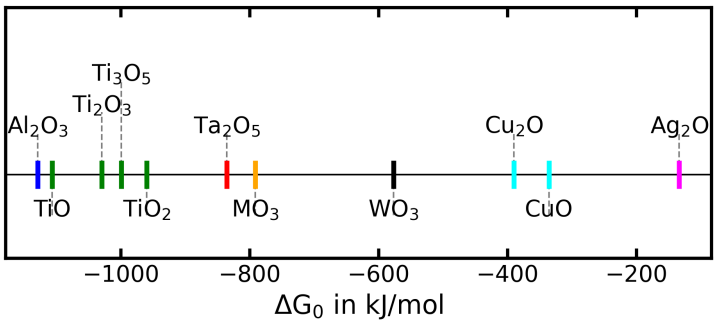

Figure 2.13.: Change of ΔG_0 of the metal during the oxidation reaction, normalized on the binding of one O_2 molecule. All data have been taken from [70].

A metal layer electrically addresses the tunnel oxide. Since the structure on the active side has some similarities with a MOS structure, it is further called MOP (metal/tunnel oxide/PCMO).

Different variants of MOP's can be found in the literature. The stacks can be divided into stacks where the tunnel oxide is a result of a redox-reaction between the metal and the PCMO and cases where the TO is grown by a vapor deposition technique. In the latter case, often noble metals are used to avoid the formation of an additional oxide layer at the metal/TO interface.

In order to make use of the interface reaction to form the TO, metals that are easy to oxidize are chosen. Typical metals for this stack are Al, W, Ti, or Ta, as will be discussed in Chapter 2.2.2. This stack can be prepared in two different ways. The oxidation of the metal by reduction of the PCMO can happen during the deposition, especially when the deposition happens at elevated temperatures. An electrical biasing step can further progress the interface oxide formation after the deposition, called the conditioning step, for which a positive bias is applied to the metal. The difference between the deposition of the TO and the formation of the TO by reduction of PCMO is that the amount of oxygen vacancies in the interface region of the PCMO is higher in the latter case. Further, the boundary between the tunnel oxide and the metal is due to the self-limitation of the interface reaction more continuous when the TO is formed by the interface reaction with PCMO.

2.2.2. Influence of the Gibbs energy on valve metal based memristive stacks

In this Chapter, the formation of an interface oxide and its necessity for switching will be discussed. Therefore, the investigated metal/PCMO stacks can be categorized according to their tendency to form an interfacial oxide layer. This tendency can be assessed by comparing the standard formation energy ΔG_0 of the different oxides, as shown in Figure 2.13. ΔG_0 is given by

$$\Delta G_0 = \Delta H_0 - T\Delta S_0. \tag{2.24}$$

while ΔH_0 is the change in enthalpy and ΔS_0 the change in entropy during the oxidation reaction. The temperature T is 298 K at standard temperature in the chosen literature [70]. ΔG_0 characterizes the change of the Gibbs free energy of a metal M during the oxidation reaction

$$xM(s) + O_2(g) \rightarrow M_xO_2(s). \tag{2.25}$$

To compare ΔG_0 of metal oxides with different stoichiometries, the ΔH_0 and ΔS_0, the values taken from [70] have been normalized according to equation 2.25 to the change of free Gibbs energy of a metal during oxidation by one mole of oxygen molecules O_2.

The redox reaction between PCMO and the metal can be divided into two partial reactions,

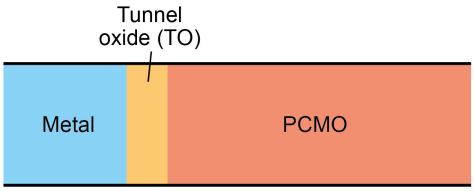

Figure 2.14.: Interfacial tunnel oxide formation resulting in a MOP stack.

namely, the reduction of the PCMO ΔG_{red} and the oxidation of the metal ΔG_0. If the sum of the change in free Gibbs energy $\Delta G_{red} + \Delta G_0 < 0$ is negative, the reaction can happen spontaneously. There are few papers that quantify ΔG_{red} of PCMO. Liao et al. [15] claim ΔG_{red} to be 366 kJ/mol, by estimating it from the formation enthalpy of an intrinsic oxygen vacancy generation in La-doped $BaTiO_3$ [71], which can only be seen as a rough estimation. This reasoning based on the thermodynamic potential, however, has limitations since kinetic limitations such as diffusion barriers are not considered. Kinetic limitations can be overcome during the deposition of the metal, for example, due to the high energetic impact of the plasma during sputtering. Moreover, the literature values of ΔG are measured on crystalline bulk materials. Therefore, these values do not necessarily apply to amorphous interfacial oxides in the order of nm. However, for all metals shown in Figure 2.13 where $\Delta G > 500$ kJ/mol, the formation of the interfacial oxides (Figure 2.14), has been shown experimentally, as will be discussed in the following text.

Gutsche et al. [72] showed by XPS measurements that the combination of Al with PCMO forms an interlayer of native AlO_x at the interface between the PCMO and the deposited Al metal. They compared the X-ray photoelectron spectroscopy (XPS) of PCMO before and after the deposition of 7 nm Al (Figure 2.15a). The existence of the AlO_x layer, caused by the oxidation of the Al by reduction of the PCMO, has been shown by the appearance of Mn^{2+} shake-up peaks in the Mn 2p region after deposition. Furthermore, the increased intensity of an Al 2p oxide peak at 75 eV for a higher take-off angle, corresponding to a higher depth sensitivity, shows the presence of the oxide layer.

Different papers report the formation of an interfacial oxide layer for oxidizable metals in contact with PCMO. Herpers et al. [74] confirmed the formation of TiO_x at the interface using HAXPES. They further claimed that the first application of a voltage to the device leads to a homogenization of the TiO_x interface layer. This homogenization during the first cycle can also be found for PCMO/Al by Gutsche et al. [12] . Beside this, Shono et al. [73] showed by TEM measurements the formation of a 10 nm amorphous-TiO_x layer between a PCMO and a Ti metal layer. Shono et al. [73] showed by electron energy loss spectroscopy that the oxygen in the a-TiO layer stems from the PCMO layer, as can be seen in Figure 2.15b.

The impact of the interface oxide on the switching ability of PCMO-metal devices was demonstrated by Liao et al. [15]. They showed that only metals that form, such as Al, Ti, and Ta, that form an oxide at the interface exhibit resistive switching. Other studies also reported that Mo and W form an oxide interface layer in between the PCMO and the metal [75]. In contrast, Laio et al. [15] reported that more noble metals like Pt, Ag, Au, and Cu do not form an oxide at the PCMO interface, which is consistent with Figure 2.13. Laio et al. [15] suggested that this native interface oxide is important for the resistive switching behavior of the PCMO/metal stack. They showed that without these oxide layers at the interface, no switching occurs, whereas the stacks with the native oxide layer show reliable resistive switching (Figure 2.15c). It can clearly be seen in Figure 2.16 that the PCMO/Ti, PCMO/Ta, and PCMO/Al stacks show a hysteresis, while the PCMO/Ag, PCMO/Au, PCMO/Pt, and PCMO/Cu stacks without the native oxide layer do not show any resistive switching hysteresis in the IV-curve. In Figure 2.17, it was shown that the initial resistance of the metal PCMO stack decreases with negative increasing free energy.

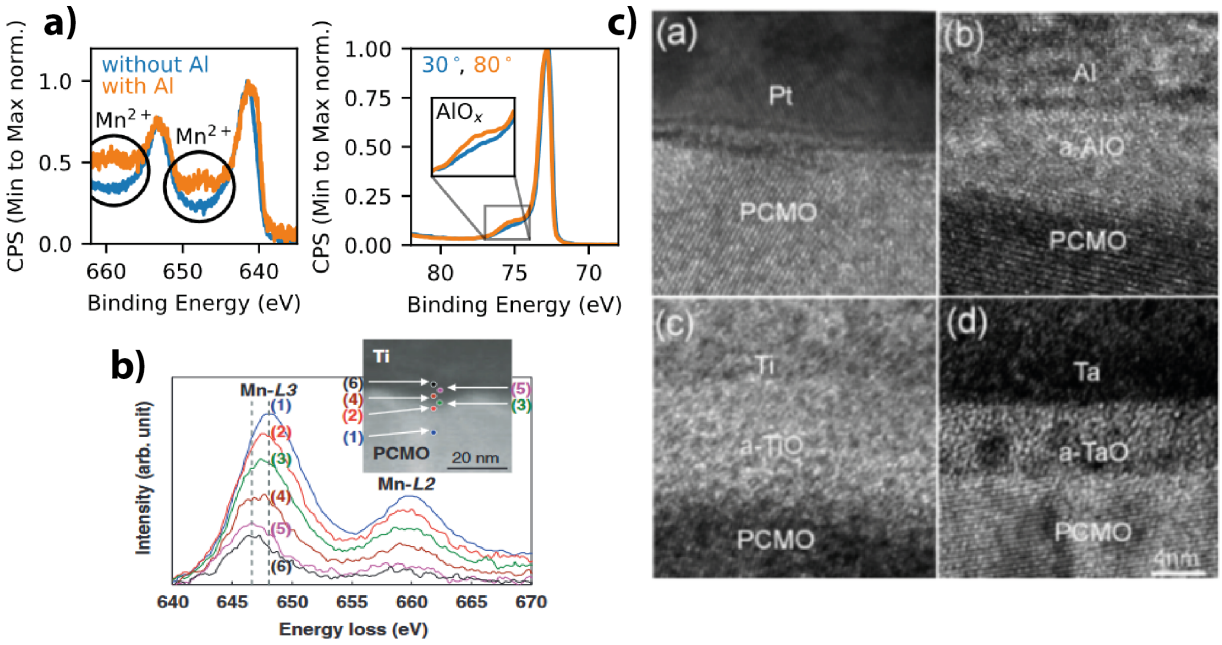

Figure 2.15.: a) Mn^{2+} shake-up peaks after Al deposition. Increased intensity of Al 2p oxide peak for higher take-off angle. Adapted and reprinted with permission from [72], © 2022 by the American Physical Society. b) Native TiO_x that has been formed by the deposition of Ti on top of a PCMO layer. Adapted and reprinted with permission from [73], © 2008 by IOP Publishing Ltd. c) HRTEM image of the native oxide at the interface between the PCMO and Al, Ti, and Ta. No native oxide can be seen for the PCMO/Pt interface. Adapted and reprinted with permission from [15], © 2009 by AIP Publishing.

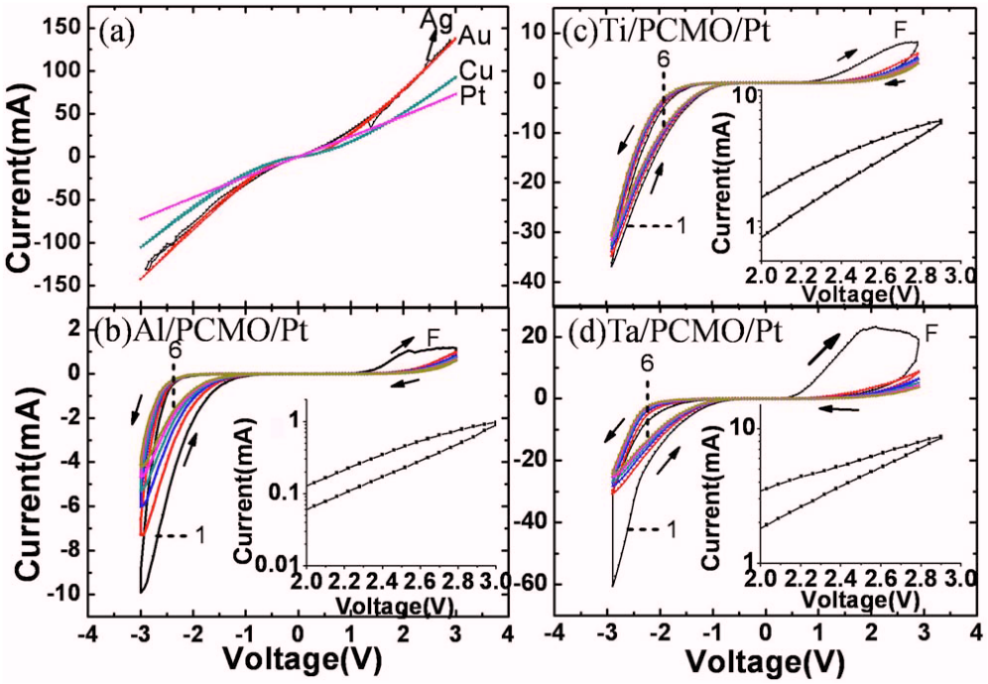

Figure 2.16.: $I-V$-characteristics of $Pr_{0.7}Ca_{0.3}MnO_3$ junction with different types of metals. a) noble metals and b) - d) non-noble metals. Adapted and reprinted with permission from [15], © 2009 by AIP Publishing.

This can be attributed to stronger oxidation at the interface. The by Liao et al. [15] assumed oxidation free energy of PCMO is marked with a dashed line and all the stacks that show resistive switching are at higher negative energy, see Figure 2.17. This further confirms that the oxidation of the metal at the interface and the reduction of the PCMO is crucial for the resistive switching process.

The question arises of whether the oxidation of the metal or the reduction of the PCMO is more important for the resistive switching process. Different studies show that a directly deposited oxide layer also leads to resistive switching behavior. For example, PCMO stacks with TaO_x, WO_x and Al_2O_3 show resistive switching [76]. In these cases, one can assume that the PCMO layer is not reduced during the deposition. We can, therefore, conclude that an oxide layer seems to be crucial for resistive switching and not the reduced PCMO interface layer. Furthermore, it was also shown that PCMO, in combination with TiN, shows resistive switching [77]. Also, here, an interfacial TiN_xO_y layer gets formed and modulated during switching [78]. The crucial role of the interface oxides will be discussed later in Chapter 2.2.4.

2.2.3. Space charge region in the MOP structure

Since the active switching MOPstructure (Figure 2.18) has similarities with an MOS, a similar band diagram can be expected.

A built-in potential $V_b = |\Phi_P - \Phi_M|$ is caused by the work function difference between the metal Φ_M and the PCMO Φ_P. Depending on the built-in potential, a space charge forms, with a narrow space region in the metal and a broader space charge region in the PCMO and, thus, a linearly tilted band in the tunnel oxide. The depth of the space charge region in PCMO is under discussion since it has a higher charge carrier density ρ than typical MOS. The thickness d of the space charge region can be estimated by the equation which is commonly used for the thickness of the depletion zone width in MOS [79]

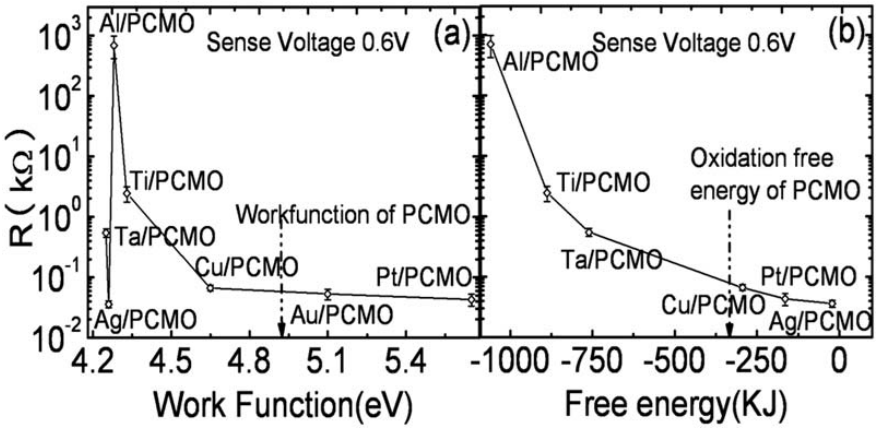

Figure 2.17.: Comparison of work function and Gibbs energy for oxidation between PCMO and different metal contacts. Adapted and reprinted with permission from [15], © 2009 by AIP Publishing.

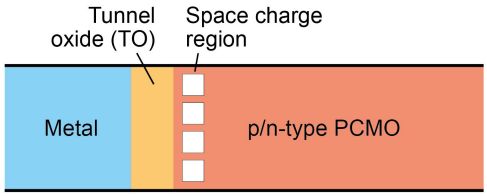

Figure 2.18.: MOP stack with significant space charge region.

$$d = \sqrt{\frac{2V_b\epsilon_P\epsilon_0}{e\rho}} \tag{2.26}$$

where ϵ_P is the permittivity of PCMO, ϵ_0 the vacuum permittivity and e the elementary charge. To estimate the thickness of the space charge region, the thickness is plotted in (Figure 2.19) in dependence on a work function difference V_b up to 2 eV. The density of states ρ_{eg} in the e_g band is formally

$$\rho_{eg}(x) = \frac{\rho_M(x)}{M(x)}N_A \tag{2.27}$$

given by the molar mass $M(x)$

$$M(x) = (1-x)M[Pr] + xM[Ca] + M[Mn] + 3M[O] \tag{2.28}$$

and the mass density $\rho_M(x)$ of PCMO in dependence on the Ca doping x. M[Pr]=141 u, M[Ca]=55 u, M[Mn]= 40 u, and M[O]=16 u are the used molar masses of the single elements. To get an estimation for different scenarios of doping, the density of states ρ_{eg} was calculated for $x = 0.1$, 0.5, and 0.9 using mass densities of $\rho_M(0.9) = 4.83\,\text{g/cm}^3$, $\rho_M(0.5) = 5.79\,\text{g/cm}^3$ and $\rho_M(0.1) = 6.59\,\text{g/cm}^3$ taken from Pithan et al. [21]. This results in density of states ρ_{eg} of $\rho_{eg}(0.1) = (1.7 \cdot 10^{22})/\text{cm}^3$, $\rho_{eg}(0.5) = (1.8 \cdot 10^{22})/\text{cm}^3$ and $\rho_{eg}(0.9) = (1.9 \cdot 10^{22})/\text{cm}^3$. Since the decrease of the molar mass with Ca doping is compensated by an increase in the mass density, the formal density of states remains fairly constant over the doping range. Multiplying with the amount of doping results in the formal carrier density of holes ρ_p and electrons ρ_e for the different doping with $\rho_p(0.1) = 1.7 \cdot 10^{21}/\text{cm}^3$, $\rho_{n/p}(0.5) = 9.0 \cdot 10^{21}/\text{cm}^3$ and $\rho_n(0.9) = 1.9 \cdot 10^{21}/\text{cm}^3$.

Since $\rho_p(0.1)$ and $\rho_n(0.9)$ are quite similar only $\rho_p(0.1)$ and $\rho_{n/p}(0.5)$ have been used for the calculations shown in Figure 2.19. The relative permittivity of PCMO had been chosen according

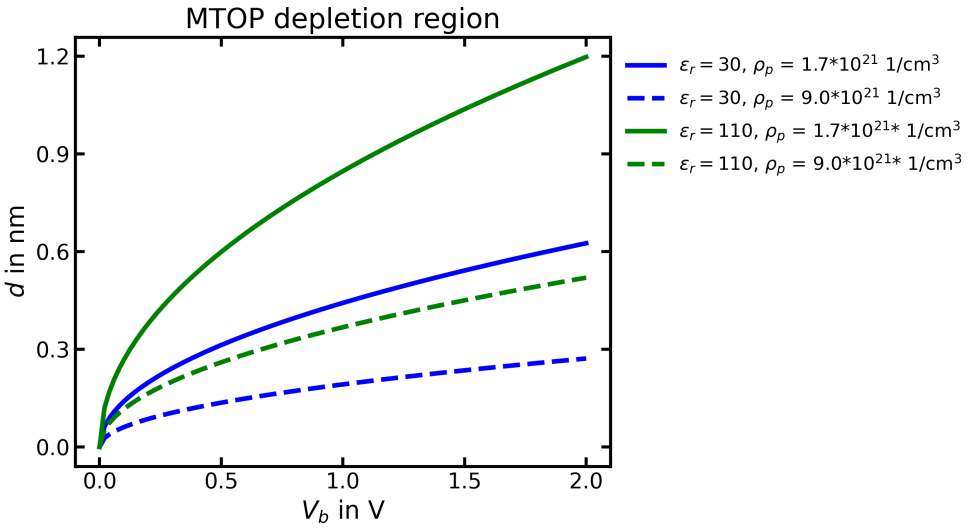

Figure 2.19.: Plotting of the approximated size of the depletion region in dependence on the work function difference for different permittivity values and charge carrier concentrations.

to Chapter 2.1.7, namely $\epsilon_r = 30$ is used to represent PCMO and $\epsilon_r = 110$ is used to consider a possible increase of permittivity after reduction in the interface layer.

The range of possible built-in potentials within MOP stacks can be considered by using the boundary values of the work function (Chapter 2.1.6) of 5.4 eV ($Pr_{0.7}Ca_{0.3}MnO_3$) for a junction with p-type PCMO and 4.8 eV ($Pr_{0.5}Ca_{0.5}MnO_3$) for a junction with n-type PCMO. For the case of p-type PCMO, a build-in potential of up to 1.2 eV can be achieved by combining it with a metal with a low work function, like Ag, with around 4.2 eV (Figure 2.17). For the case of n-type PCMO, one can achieve a difference of 0.9 eV by combining it with a metal with a high work function, like Pt, with around 5.7 eV (Figure 2.17). Therefore, in Figure 2.19 we used work function differences of up to 2 eV.

Considering Figure 2.19 for the more realistic value of $\epsilon_r = 30$, it is unlikely that the size of the space charge region exceeds a few Ångström. For the case of high permittivity $\epsilon_r = 110$ and low carrier charge densities the space charge region can spread up to 1 nm into the material (Figure 2.19).

The narrow width of the space charge region in $Pr_{0.66}Ca_{0.34}MnO_3$ due to the high charge carrier density has also been shown by simulations of the junction $Pr_{0.66}Ca_{0.34}MnO_3$/ $SrTi_{1-y}Nb_yO_3$ ($y = 0.002$), which results in a space charge region of around 0.2 nm in PCMO. Combined EBIC measurements confirmed the results of the simulation indirectly by measuring the simulated space charge region within STO. They excluded the space charge region in the PCMO as being of a few nm in size without giving a precise value in the single nm range because of the limit in the resolution [33] [80] [81] [82].

However, Gutsche et al. [72] measured the space charge region at the Al/AlO_x/$Pr_{0.7}Ca_{0.3}MnO_3$ interface by comparing X-ray photoelectron spectroscopy (XPS) measurements of PCMO before and after the deposition of 7 nm Al. As expected for the work function difference, the band down bending can be seen by a shift of 0.9 eV of the Pr 3d 5/2 region to higher binding energies after the deposition of Al (Figure 2.20a). The band diagram of the Al/AlO_x/PCMO MTOP structure is drawn in Figure 2.20. The negative space charge in the PCMO, with an electrostatic potential of 0.9 V, causes a linear field over the AlO_x with a total potential difference of 0.9 V. Interestingly, this increase in the binding energy of the Al 2p oxide was observed. The measured peak is around 75 eV (Figure 2.15a), while the literature value of the peak position for Al 2p 3/2 of corundum is around 74.1 eV [72].

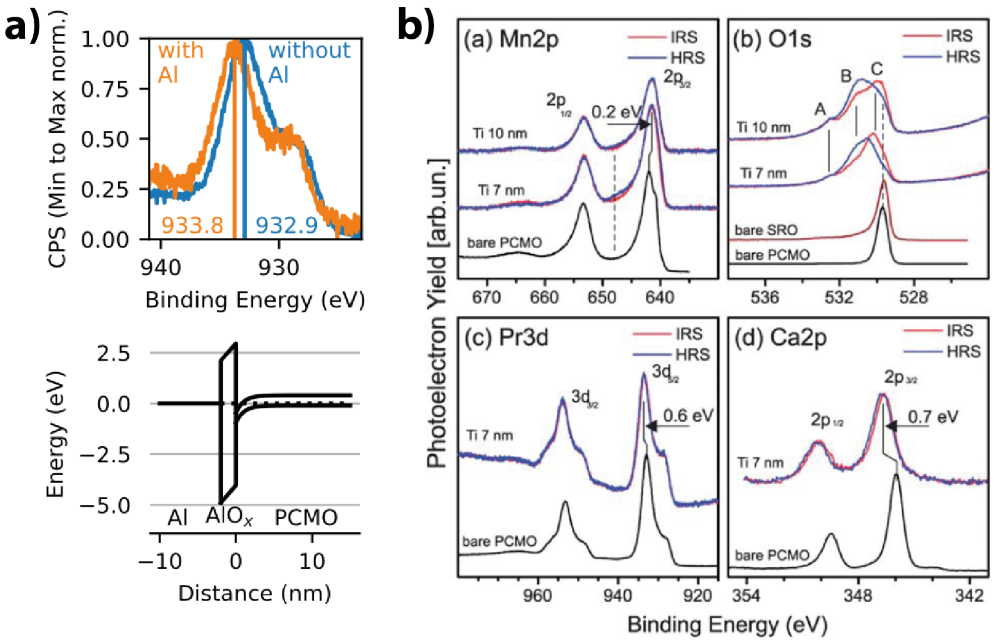

Figure 2.20.: a) Shift in the Pr 3d 5/2 peak from the band down bending and concluded band diagram for the PCMO/AlO$_x$/Al system. Adapted and reprinted with permission from [72], © 2022 by the American Physical Society. b) Core level shift in PCMO between bare PCMO and PCMO after Ti deposition. Adapted and reprinted with permission from [67], © 2009 by Royal Society of Chemistry.

Borgatti et al. [67] measured the space charge region for the system PCMO/TiO$_x$/Ti by the shift to higher binding energies of 0.7 eV and 0.6 eV in the Ca 2p and Pr 3d core level region, respectively (Figure 2.20b). This is expected for the combination of PCMO with the low work function metal Ti 4.3 eV (Figure 2.17).

Since in both publications Gutsche et al. [72] and Borgatti et al. [67] an interfacial oxide was created by the reduction of the PCMO, the measured space charge region could even be increased, by the combined change of band gap and work function of reduced PCMO as discussed in Chapter 2.3.4. Also a possible increase of permittivity and reduction of charge carrier density, as discussed in Chapter 2.1.5, 2.1.7, 2.3.3 and 2.3.4, could increase this effect.

It is evident, from spectroscopy, that the space charge region exists and can be measured, but since the region can be expected to be very narrow (Figure 2.19), the question arises if the space charge region has an influence on the current transport at the interface. A direct way to investigate the influence is to investigate metal/PCMO junctions (Figure 2.21), which form a rectifying Schottky junction, in the case of a significant space charge region. In contact with a noble metal with a lower work function than p-conducting PCMO, the forward direction of the Schottky junction would be at negative voltages with respect to the metal contact. The opposite (positive) voltage would be expected as the forward direction in the case of a high work function metal electrode and an n-conducting PCMO.

Borgatti et al. observed symmetric IV-curves for the contact between $Pr_{0.5}Ca_{0.5}MnO_3$ and the high work function metal Pt as well as for the contact with the low work function Ti before electronic forming (Figure 2.22a).

Interestingly, in contrast to Borgatti, Sawa et al. [13] (Figure 2.22b) observed a rectification in the $I-V$-curve of PCMO-Ti junction. Probably for Sawa's measurements a thicker interfacial oxide layer was formed and the measured asymmetry results from the current transport across a tunnel junction with different work functions of the contact electrodes, as explained in Chapter 2.2.4.

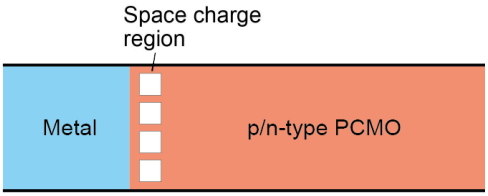

Figure 2.21.: Schottky junction at PCMO/metal contact, assuming a significant space charge region.

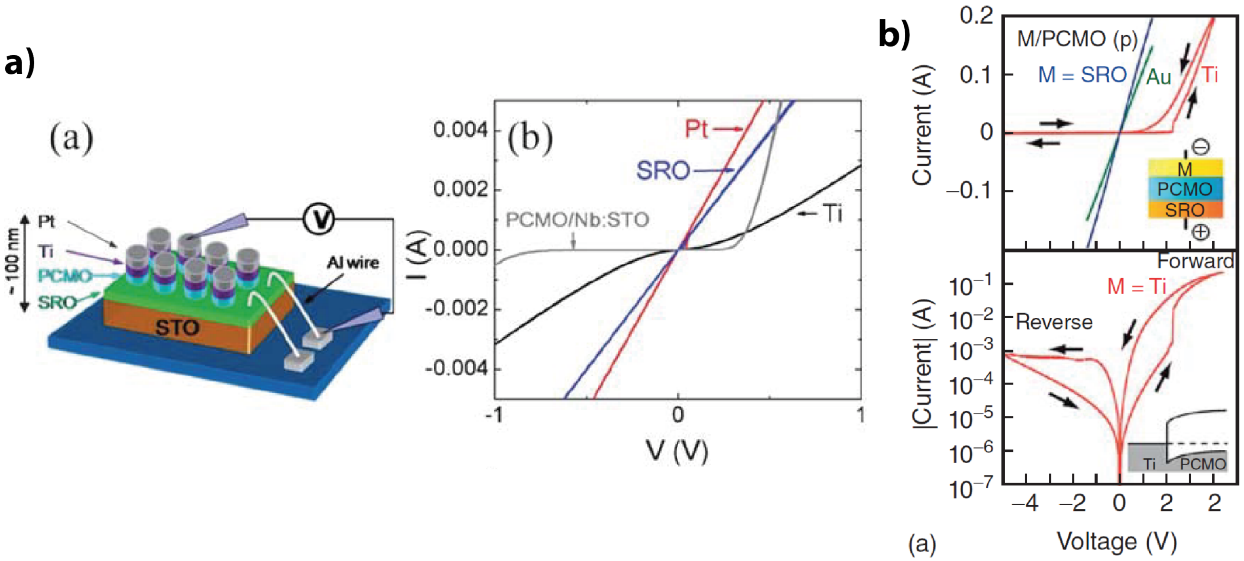

Figure 2.22.: a) IV curves for PCMO devices (structure shown in a) with different top electrodes. To analyze the junctions' characteristics, the shown voltage is the voltage applied to the top electrode. The junction with the Ti electrode is without previous forming treatment by electric biasing and has, therefore, an interfacial Ca-TiO_x oxide layer, which is less influential to the electric characteristic. Adapted and reprinted with permission from [67], © 2009 by Royal Society of Chemistry. b) Measurement of the M/PCMO/SRO junction for three different contacts M with different work functions (Ti 4.1 eV, Au 5.1 eV, and SRO 5.3 eV). Adapted and reprinted with permission from [13], © 2008 by Elsevier.

The same observations as Borgatti et al. was been made by Liao et al. [15] by combining PCMO with the metals Ag (4.26 eV), Au (5.1 eV), Cu (4.65 eV) and Pt (5.7 eV). All these junctions have symmetric $I - V$ characteristics (Figure 2.16).

It can, therefore, be concluded that the influence of the space charge region on the current transport of the metal/PCMO junction without an interfacial oxide layer can be neglected. This raises the question of whether this is also the case for transport over the MOP stack. Here, the charge transport over the tunnel oxide dominates the resistance, as can be clearly seen for PCMO/TO structures in which the tunnel oxide thickness is controlled by the deposition time (Figure 2.24a). There is a resistance difference of around one order of magnitude between the stack Pt/PCMO/ZrO_2/Pt with PCMO and the MIM stack with only the tunnel oxide (MIM). Meyer et al. assigned the resistance difference to the space charge region in PCMO [13]. How the current transport over the MOP stack can be described and what influence the space charge region has will be discussed in the next section.

2.2.4. Current transport across the MOP

Direct tunneling

The electronic conductivity of the PCMO based devices is dominated by the conductivity over the tunnel oxide, as is evident from Figure 2.24a [83]. To describe the conduction over the tunnel oxide, different models can be used.

Herpers et al. [74], as well as Arndt et al. [84] used the tunnel model of Simmons [85], which has been developed for direct tunneling through an insulating barrier (Figure 2.23). Simmons [85] describes the asymmetry of the tunneling current through an insulating current for two contact metals with different work functions.

The Simmons model distinguishes between low and high applied voltage regimes. Low means that the voltage drop across the tunnel oxide is lower than the average height of the tunnel barrier $\Phi = (\phi_2 - \Phi_1)/2$. In this voltage regime, the tunneling barrier is trapezoidal, and the tunneling current is higher for positive biasing at the low work function electrode (Figure 2.23 a+b). High voltage means that $V > \Phi$. In this case, the tunnel barrier becomes effectively triangular (Figure 2.23 c+d), and the tunneling current is controlled by the work function of the metal, which is negatively biased. Thus, the tunneling current is higher when the negative voltage is applied in the low work function metal.

This asymmetric behavior is similar as would be expected for the forward direction of a Schottky barrier with PCMO as p-conducting material and a low work function metal. This must be considered, if one wants to conclude from the asymmetry of the I-V-curves to the existence of space charge.

Simmons [85] developed two analytical descriptions to calculate the tunneling current. The simpler form does not include the barrier lowering by the image force effect. Herpers et al. [74], as well as Arndt et al. [84], used this form to describe the tunneling current across the TO. It converges to the Fowler-Nordheim tunneling when the voltage across the TO is larger than the difference between the two work functions. Then, the tunneling current is described by

$$J = \frac{BE^2}{\Phi} e^{-(\lambda \Phi^{3/2})/E} \tag{2.29}$$

where $E = V/d$ is the electric field, V the applied voltage, d the TO thickness, $B = 1.1e^3/(4\pi h)$ and $\lambda = (23\pi\sqrt{m^*}/(6he)$ with the effective mass m^* within the tunnel oxide.

Arndt et al. [84] described the current transport of $Pr_{0.48}Ca_{0.52}MnO_3$/YSZ/Pt devices and showed an exponential dependence of the tunnelling current on the tunnel oxide thickness (Figure 2.24b) as predicted by equation 2.29.

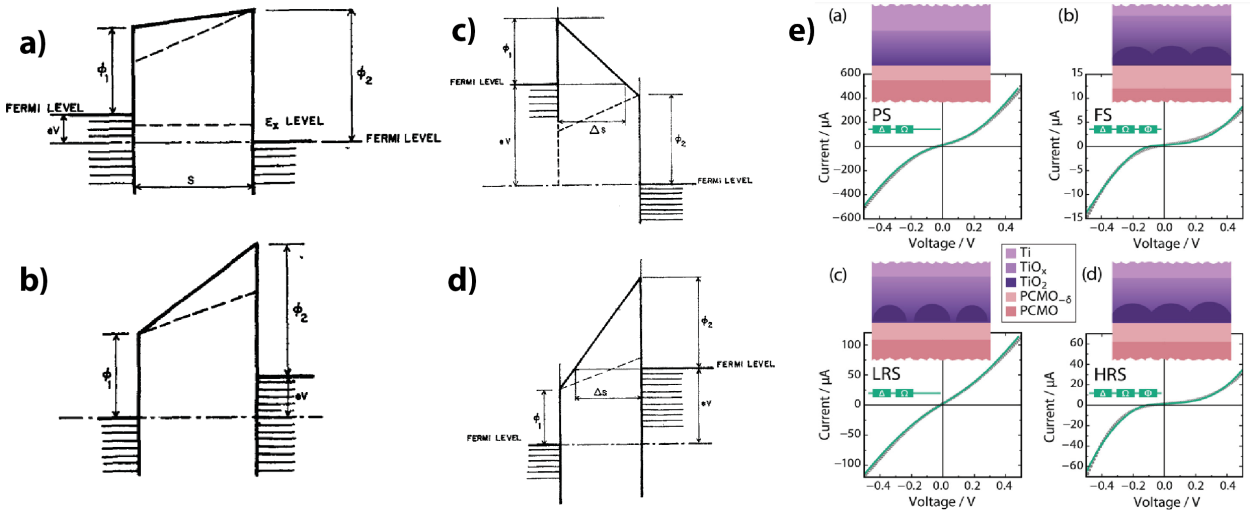

Figure 2.23.: In a) and b), the tunneling scenario relative to the tunnel barrier's low applied voltage is shown. Here, biasing the low work function metal with a positive bias b) leads to a higher tunneling current. The right figures c) and d) show the scenario for high applied voltages, which leads to an effective triangular barrier. Here, biasing the electrode with low work function negative c) gives the higher tunneling current. a) till d) all adapted and reprinted with permission from [85], © 2004 by AIP Publishing. e) Fitting of the current characteristic in the low readout voltage regime of the PCMO/TiO_x/Ti device by two circuit elements e.a) pristine device, e.c) device in LRS) and three circuit elements e.b) formed device and e.d) device in HRS). The two circuit elements are a constant resistance and the PCMO polaron hopping. The third resistance is the Simmons tunneling over the tunnel barrier. Adapted and reprinted with permission from [74], © 2014 by John Wiley and Sons.

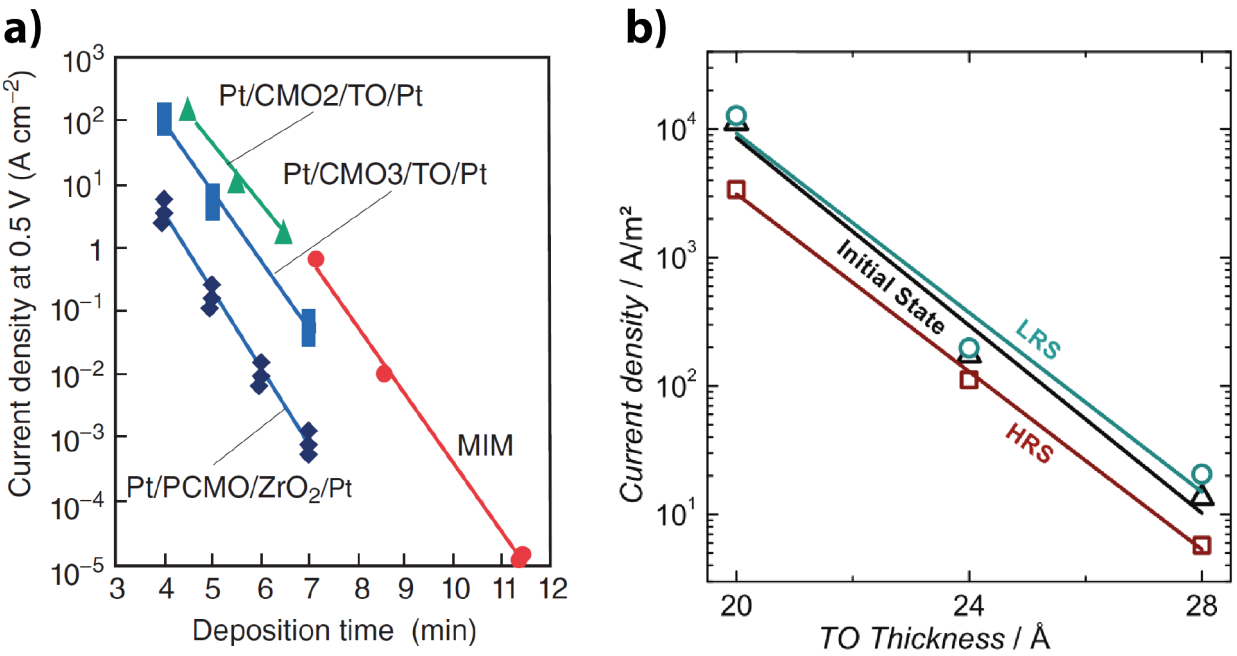

Figure 2.24.: a) Thickness dependence of the current transport of PCMO device with different ZrO_2 tunnel oxide thicknesses. In comparison with other higher conducting metal oxides (CMO2 and CMO3) and a stack without CMO. Adapted and reprinted with permission from [83], © 2016 by John Wiley and Sons. b) Exponential dependency of the current density of the PCMO/YSZ/Pt system from the YSZ thickness. Taken from [84].

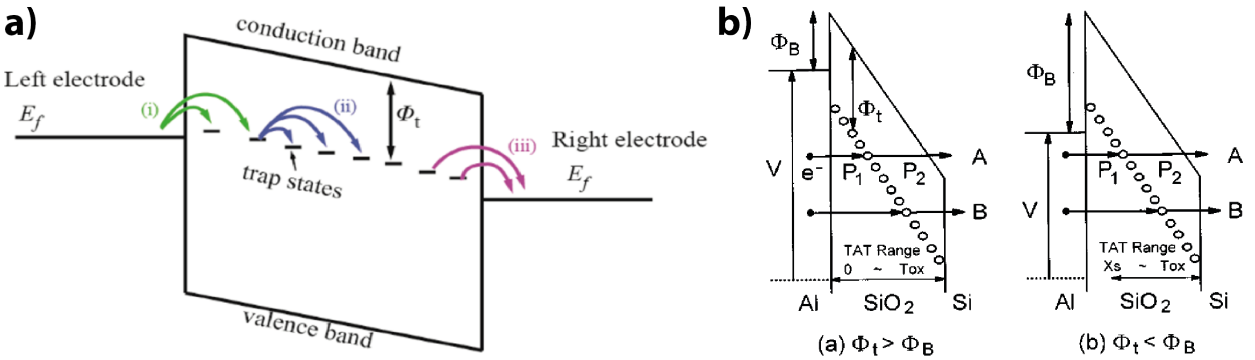

Figure 2.25.: a) Schematic drawing of the elementary tunneling steps during trap-assisted tunneling. Taken from [86]. b) Two scenarios of trap-assisted tunneling. b.a) if the tunnel barrier is smaller than the trap level depth. b.b) if the trap level depth is smaller than the tunnel barrier. In both scenarios, two different tunneling processes exist. A, which is tunneling through a triangular barrier and B tunneling through a trapezoidal barrier. Adapted and reprinted with permission from [87], © 1999 by AIP Publishing.

Herpers et al. [74], fitted the current-voltage curves of the PCMO/TiO_x/Ti stack in the readout voltage regime in four different states. In the pristine state (PS) and in the LRS, the TiO_x is assumed to be so leaky that a transport via the conduction band can be assumed, which results in symmetric I-V-curves (Figure 2.23 e.a+e.b). After the first biasing, which induces the formation of a TiO_2 tunnel barrier (FS) and in the HRS, the current transport can be described by the Simmons model, which causes asymmetric $I-V$ curves in both cases (Figure 2.23 e.b+e.d). The asymmetry in the HRS could even be more pronounced if the band gap and work function changes for reduced PCMO, as discussed in Chapter 2.3.4.

However, the application of the Simmons model for the transport over a MOP stack has several limitations. It completely ignores conduction through trap states in the band gap, and it incorrectly assumes PCMO is a metal. Therefore, it does not consider the influence of the density of states near the Fermi level or the impact of the influence of a space charge region. Further, direct tunneling cannot explain the high current levels often observed for tunnel oxide thicknesses above 3 nm.

Trap assisted tunneling in the TO

Oxygen vacancies can form defect states [72, 86] within the band gap of the tunnel oxide. If these defects states lie below the Fermi level, they are considered as trap states and must be included into the transport mechanisms across the tunnel oxide (Figure 2.25).

Funck et al. [86] compared different transport models and the role of defect states. Trap-assisted tunneling (TAT) can be described by up to 3 steps (Figure 2.25a) [86]. In the first step (i), the electron tunnels from the conduction band of one material into a trap or defect state within the band gap of the tunnel oxide. Then, depending on the thickness of the TO in an optional (ii) second step, the electron can tunnel between different trap states. In the final step (iii), the electron tunnels out of the tunnel oxide into the second material. The mathematical description of this process depends highly on the exact structure of the energetic landscape and is, therefore, not covered by a single analytical expression.

This process is considered e.g. by Mayer et al. [13, 83] for the transport across the Pt/ZrO_2/PCMO stack, for which an exponential dependence on the tunnel oxide thickness is observed (Figure 2.24a).

As reviewed by Funck et al. [86], an often-used equation for TAT is given by Phon et al. [87],

$$J \propto e^{-(k\Phi_t^{3/2})/E} \tag{2.30}$$

where Φ_t is the in Figure 2.25b shown defect level and $k = 4\sqrt{2em^*}/(3\hbar)$ with m^* as the effective mass in the tunnel oxide. This equation describes the simplified situation in which the tunneling takes place over only one trap state, with the trap depth Φ_t smaller than the tunneling barrier Φ_B scenario b in Figure 2.25b. Further, it is assumed that the field is high, so tunneling process A (depicted in Figure 2.25b) across the triangular barrier dominates. This equation shows the same exponential dependence with the tunnel oxide thickness of the Fowler-Nordheim equation for direct tunneling. Therefore, just from finding an exponential thickness dependence (e.g. Mayer et al. (Figure 2.24a) and Arndt et al. (Figure 2.24b)), it cannot be discriminated if the mechanism is trap-assisted or direct tunneling.

2.2.5. Space-charge limited current

Space-charge limited current (SCLC) is a conduction mechanism, which is based on the space charge distribution of the equilibrium flow of excess charge carrier in material. This model was first developed to explain the current flow in vacuum and was then adapted to describe electric transport in insulators with a certain electronic mobility by the so-called Mott-Gurney law for SCLC [86]. This transport in an insulator gives a $I \propto V^2$ characteristic, which is often used to identify SCLC as conduction mechanism in $I-V$ curves.

However, applying SCLC current to a material, certain requirements have to be fulfilled, such that the transport in the material happens by excess charge emitted by the electrodes. Only finding an interval with $I \propto V^2$ characteristic in the $I-V$ loop is not enough, as non-linearity of the $I-V$ characteristic can have multiple reasons.

The application of the SCLC model to PCMO, which is suggested in numerous papers in the literature [88] [89] [90] [91] [92], should be considered with caution, as the requirements are not fulfilled. The SCLC model assumes, as reviewed by Funck et al. [86], assumes a free excess electron in the material whose charge distribution limits the current. But PCMO does not require the injection of excess charge for electronic conduction, since it has due to the high doping concentration large charge carrier densities. In addition, the e_g electron does not behave like a free electron, as its mobility is severely restricted and field dependent, as discussed in Chapter 2.1.4. Non-linearities in the $I-V$ loop can be explained by the non-linearity of the polaron hopping.

The conduction based on SCLC can be further modified by the electronic traps in the material. There are several ways to respect them. Funk et al. reviewed, that traps can be reflect by a change to an $I \propto V^\alpha$ characteristic, where α varies with the trap density. However other approaches are to reflected traps by a factor θ to the current $I \propto \theta I_{\text{trap free}}$.

2.3. Switching

2.3.1. Area-dependent switching

In contrast to filamentary switching VCM devices, the current transport in area-dependent devices is homogeneous across the whole device area in both HRS and LRS. As a result of this, the current in both states scales with the device area. The difference to the filamentary type of devices is most pronounced in the LRS, where the current is dominated by transport within the filament [8]. A common way to validate the area dependence is to plot the device resistance in both resistive states against the device area A in a double logarithmic plot, as exemplary shown in Figure 2.26 for AlO_x/PCMO, TaO_x/PCMO and WO_x/PCMO. A linear fit of the device resistance with a slope of -1 verifies that the resistance is scaled by $1/A$. Moon et al. [93] showed for Mo/PCMO and Park

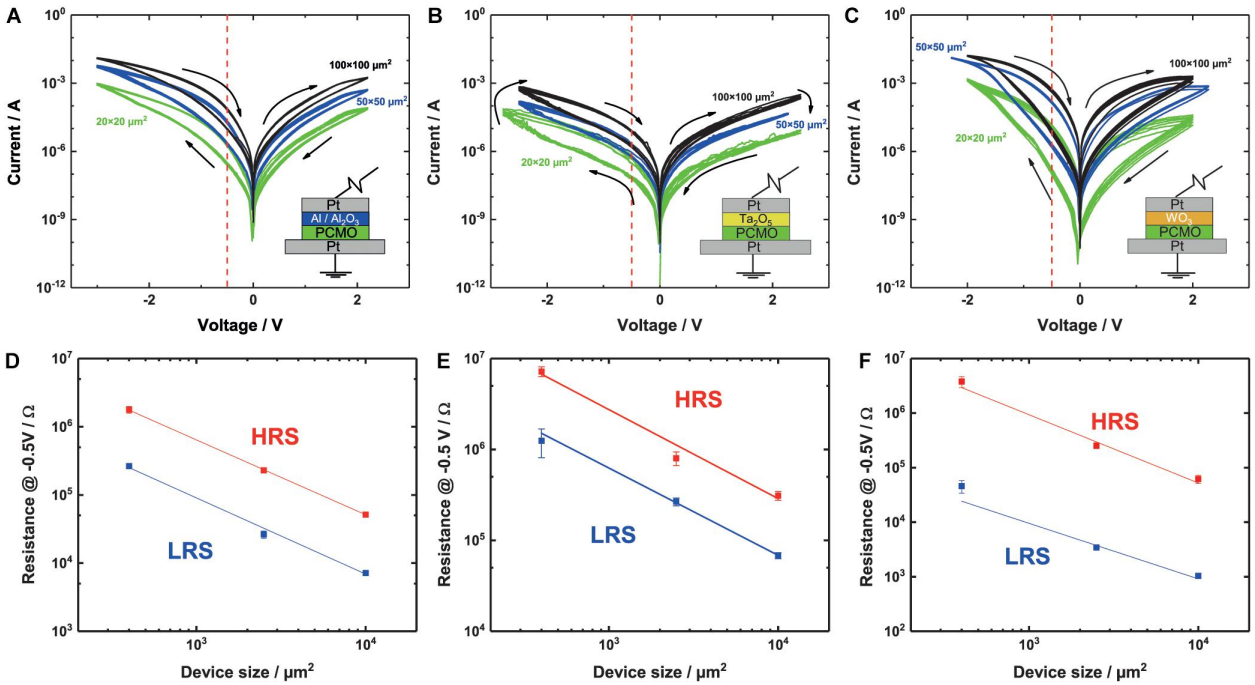

Figure 2.26.: Switching curves of PCMO based devices with A) AlO_x, B) TaO_x and c) WO_x and different pad sizes of 100 µm × 100 µm, 50 µm × 50 µm, and 20 µm × 20 µm. D) to F) show the area dependence of both resistive states, for a readout at -0.5 V, and their linear fit, with slopes close to -1 Ω/µm^2. The values for HRS/LRS are D) -1.09± 0.01/-1.12± 0.07, E) -0.98± 0.18/-0.95± 0.05 and F) -1.25± 0.18/-1.02± 0.22. All values and figures are taken from [12].

et al. [94] for TiN_x/PCMO that the area dependence scales down to devices of 150 nm diameter (Figure 2.27). A limit to the scaling behavior has not yet been shown. Public statements [20] of the company *4DS Memory*, which claim to have achieved 60 nm device sizes and are aiming for 20 nm device sizes, support that further scaling of PCMO-based devices may be possible.

Moon et al. [93] investigated the dependence of switching energy on conductance level for devices of different sizes and verified the expected decrease in switching energy with conductance (Figure 2.27a). They also verified the scaling of switching energy with device size by examining the dependence of switching energy density on conductance density (Figure 2.27b). Moon et al. [93] suggested that for 25 nm devices with 10 ns switching times, switching energies in the order of femtojoules may be possible. Achieving these low switching energies at small device sizes could give PCMO-based devices a advantage over filamentary devices. Moreover, the high resistance values of PCMO-based devices even in the LRS can be advantageous for the implementation in large crosss-bar arrays since parasitic effects caused by the line resistances might be circumvented.

In the ideal case of area-dependent switching, the atomic arrangement is homogeneous in every cross-section along the entire stack and does not change during the application of an electric field. Therefore, also the electric field and the resulting ionic processes are homogeneous across the entire interface. However, interfaces of deposited layers always have a certain degree of roughness and imperfection. The electric field might also be inhomogeneous, as can be seen in the simulation shown in Figure 2.28a. Here, the continuity equation for the electric current has been solved for a stack of 20 nm metal/ 5 nm tunnel oxide/ 30 nm PCMO/ 20 nm metal. The inhomogeneity simulated here is a general inhomogeneity in the resistance of the tunnel oxide. For that purpose, the TO is described by a checkerboard pattern with single fields of 20 nm x 20 nm size. The PCMO is included by an arbitrary conductivity of 10^3 S/m, and one subset of the tunnel

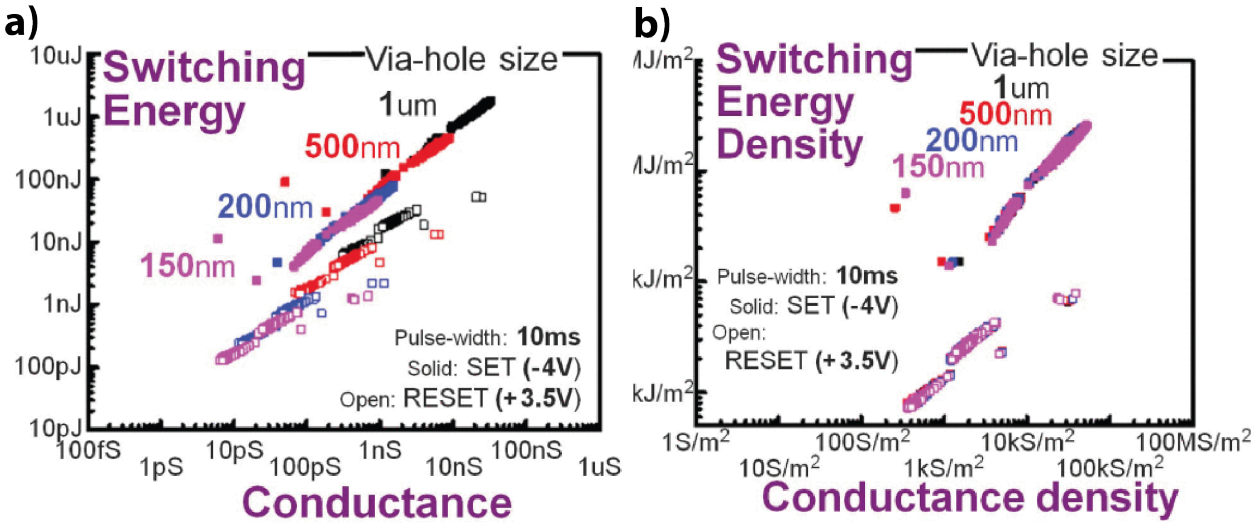

Figure 2.27.: a) Scaling of switching energy with conductance for devices of different sizes. b) Scaling of switching energy density with conductance density for devices of different sizes. Both figures are taken from [93].

oxide areas is considered by a fixed low conductivity of 1 S/m. The conductivity varies from Figure 2.28 a) to d) from the second subset of the TO pattern, with decreasing conductivity of a) 10^5 S/m, b) 10^3 S/m, c) 32 S/m, and d) 1 S/m. If the resistance of the TO dominates (seen c) and d)), the whole field is located in the tunnel oxide. As soon as the resistance of the TO becomes similar to the resistance of the PCMO b), or is even lower a), the field strays into the PCMO. This increase of resistance from a) to d) relates to the change from a metal to an oxide during the conditioning for metal/PCMO stacks, as discussed in Chapter 2.2.2.

The simulations further show that the stray of the field into the PCMO in the area where the TO is high conducting becomes shielded by the field confined in the low resistive areas of the TO because of the continuity of the field lines. Thus, it can be concluded that this effect is stronger if the area of low conductivity in the tunnel oxide is less granular.

Since both field and resistance inhomogeneities, as well as surface inhomogeneities, can result from the device fabrication, there has to be feedback mechanisms that compensate for the field inhomogeneities through the movement of oxygen. Otherwise, the area-dependent configuration would not remain stable over many switching cycles.

The most evident case of a feedback mechanism is the formation of the tunnel oxide at the valve metal-oxide interface during the conditioning process, as simulated by the resistance increase from a) to d) in Figure 2.28. Here, the formation of the tunnel oxide is caused by the movement of oxygen anions from PCMO into the non-noble metal. It is evident that in the area where the tunnel oxide has already been formed, the field drop across the PCMO is much lower as the voltage is divided between the high resistive oxide formed and the PCMO. Therefore, the growth rate of the tunnel oxide is increased in areas with less tunnel oxide if the resistance of the not fully formed tunnel oxide R_{TO} is lower than the resistance of the PCMO ($R_{TO} < R_{PCMO}$). Thus, the inhomogeneity of the electric field causes an oxygen movement, which equalizes the inhomogeneity in the electric field.

The field homogenizing movement of oxygen during switching cannot be explained by this simplified simulation because the resistance of the tunnel oxide dominates the voltage divider $R_{TO} \gg R_{PCMO}$ (Figure 2.28d). Therefore, a more detailed geometry of the interface region has to be studied. A successful model must include the non-linear field dependence of the resistance in the PCMO and in the tunnel oxide, the non-linear dependence of the oxygen drift velocity, and the spatial variation of oxygen within both PCMO and the TO.

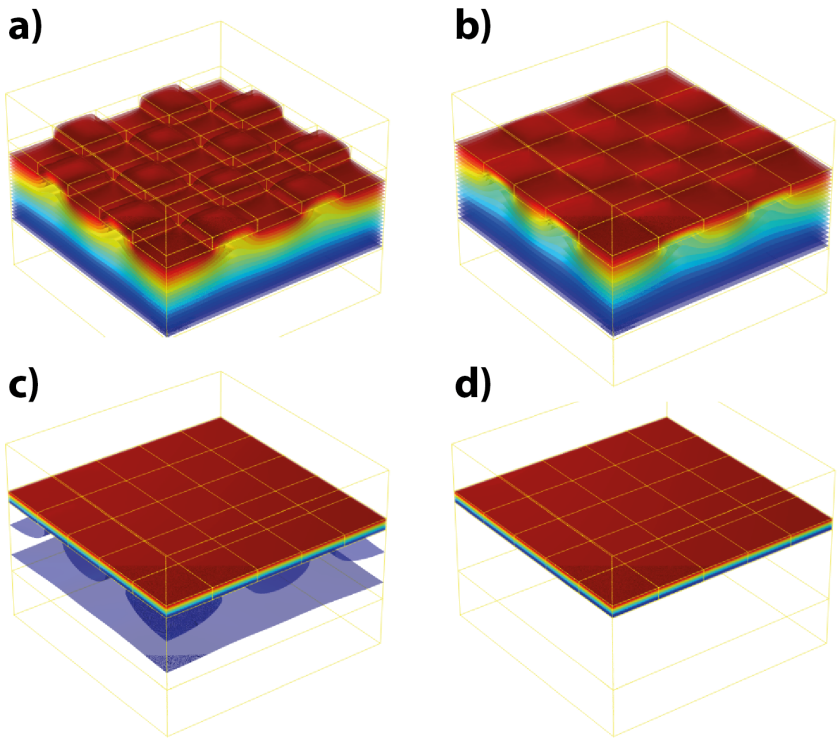

Figure 2.28.: Equipotential lines color-coded of the electric potential distribution (red 2 V two blue 0 V) for a tunnel oxide with inhomogeneous conductivity and PCMO with a fixed conductivity of 10^3 S/m. The inhomogeneities of the conductivities in the tunnel oxide are distributed in a checkerboard (20 nm x 20 nm) pattern. Where the insulation area has a constant conductivity of 1 S/m, and the variable area has a conductivity of a) 10^5 S/m, b) 10^3 S/m, c) 32 S/m, and d) 1 S/m. The conductivity of the metal contacts is 10^6 S/m, and the applied voltage is 2 V.

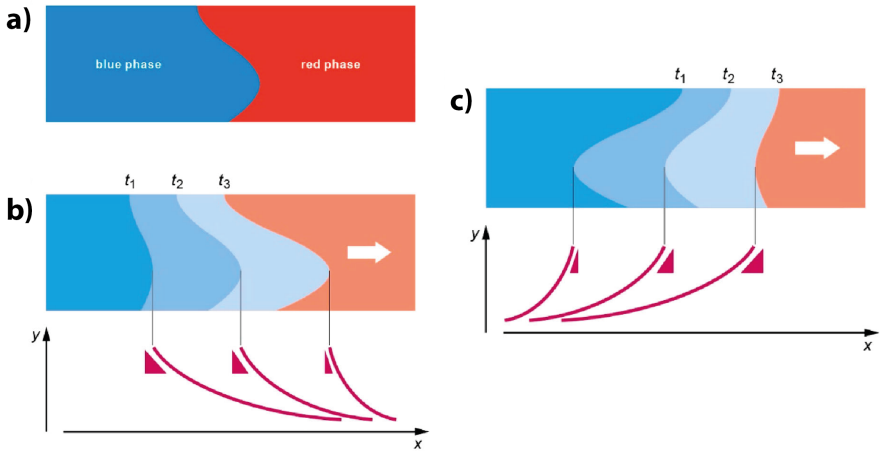

Figure 2.29.: Curvature increasing flux b) and reducing flux c) fluxes of phase growth in a matrix as depicted in a). Adapted and reprinted with permission from [8], © 2022 by Taylor & Francis.

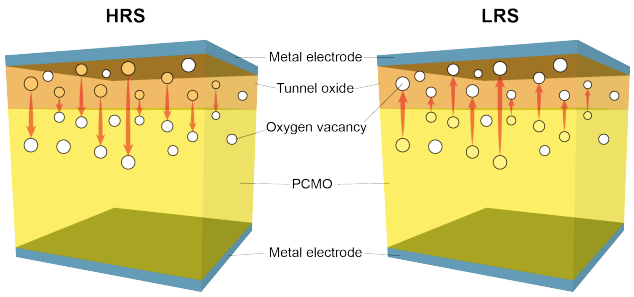

Figure 2.30.: VCM mechanism - field induced movement of oxygen vacancies, between PCMO and TO. The figures show the stack in two different resistive states, left HRS and right LRS. The arrows show the movement which the oxygen vacancies did, to reach the resistive state.. The filling of the white cycles symbolizes the refilling of the vacancy with oxygen.

The above considerations describe inhomogeneity-compensating fluxes through fixed static interfaces of different materials. Also, the movement of oxygen vacancies within one material might have an influence on homogeneity. A generalizing approach considering the curvatures of interfaces of phase growth within the same matrix material has been described by Dittmann et al. [8]. There, the phase growth is generalized to an arbitrary kind of phase growing through a generalized flux caused by a generalized thermodynamic potential. In order to obtain a roughness-reducing flux, the thermodynamic potential that drives the flux in the source phase has to be of the nature that its gradient decreases in the region of the convex phase boundary and increases in the region of the concave phase boundary (Figure 2.29c).

2.3.2. Switching mechanism overview

The switching mechanisms discussed in the following sections are based on the valence change mechanism (VCM) [8], which is caused by the movement of oxygen vacancies from the PCMO into the tunnel oxide during the SET and vice versa for the RESET, as depicted in Figure 2.30.

Several mechanisms have been proposed in the literature to explain the change in current transport with vacancy migration. The mechanism can be roughly divided into effects that the oxygen vacancies can have on the tunnel oxide and effects on the PCMO. Figure 2.31 gives an overview of the possible changes in the tunnel oxide, comprising a) the variation of thickness (Chapter 2.3.3), b) the variation in trap states (Chapter 2.3.3), c) the variation of space charge in the tunnel oxide

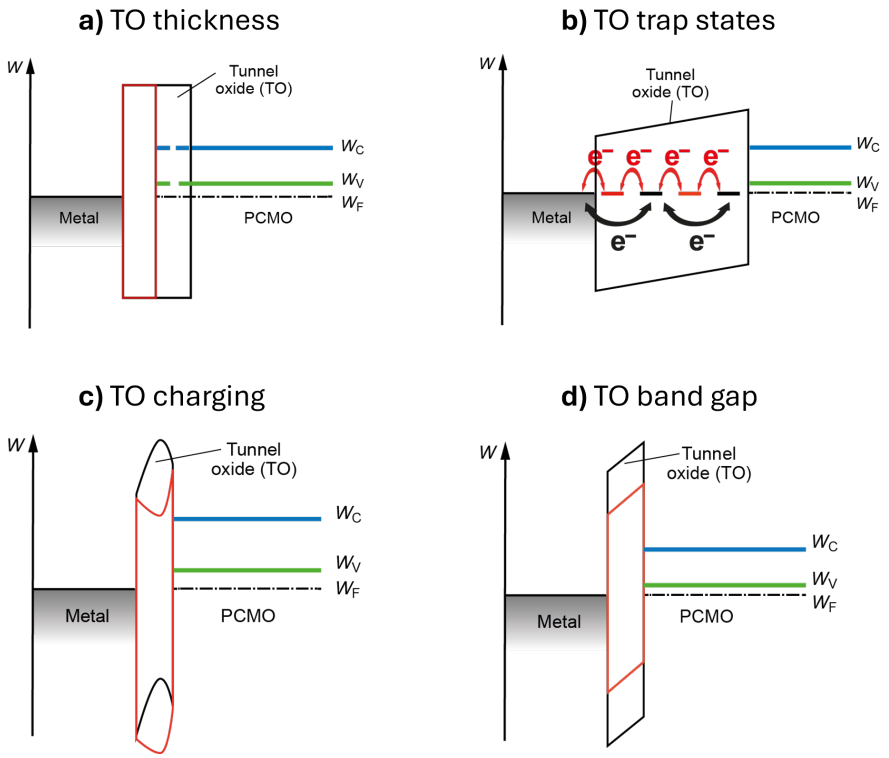

Figure 2.31.: Schematic overview of switching mechanisms based on the variation of the tunnel oxide barrier by oxygen vacancies. The LRS is depicted in red and the HRS in black.

(Chapter 2.3.3) and the d) variation of the band gap (Chapter 2.3.3). The variation of the dielectric constant (Chapter 2.3.3) can also be considered as a potential model, leading to a change in the band bending.

In addition Figure 2.32 gives an overview of the switching mechanism in the PCMO-TO devices. These are a) the reduction in electronic mobility (Chapter 2.3.4), b) the variation in carrier density and hence the broadening of the space charge region (Chapter 2.3.4), c) the change in the work function (Chapter 2.3.4) and d) the modification of the band gap (Chapter 2.3.4). All of these mechanisms have been proposed in the literature and are discussed in the corresponding Chapters.

2.3.3. Switching mechanism based on changes of the tunnel oxide

Resistance change by modifications of trap density and barrier thickness

As discussed in Chapter 2.2.4, the introduction of defect states in the TO can facilitate the charge transport by trap assisted tunneling and thus reduce the tunneling current. This mechanism depends highly on the location of the defect states in the band gap of the tunnel oxide and thus depends on the tunnel oxide material [86] [95]. Gutsche et al. [72] included this mechanism in their switching model for Al/PCMO-based devices.

Furthermore, as discussed in Chapter 2.2.4, the tunnel current is exponentially dependent on the tunnel oxide thickness. Thus, reducing the TO thickness by oxygen extraction during the set reduces the resistance. Baek et al. [78] showed by in-situ TEM observation that the growing and shrinking of an a-TiO_xN_y interlayer at the TiN/PCMO interface controls the area-dependent switching (Figure 2.33). Herpers et al. [74] also proposed the decrease of the interfacial oxide TiO_x oxide in PCMO/Ti devices as a switching mechanism (discussed in Chapter 2.2.4). Asanuma et

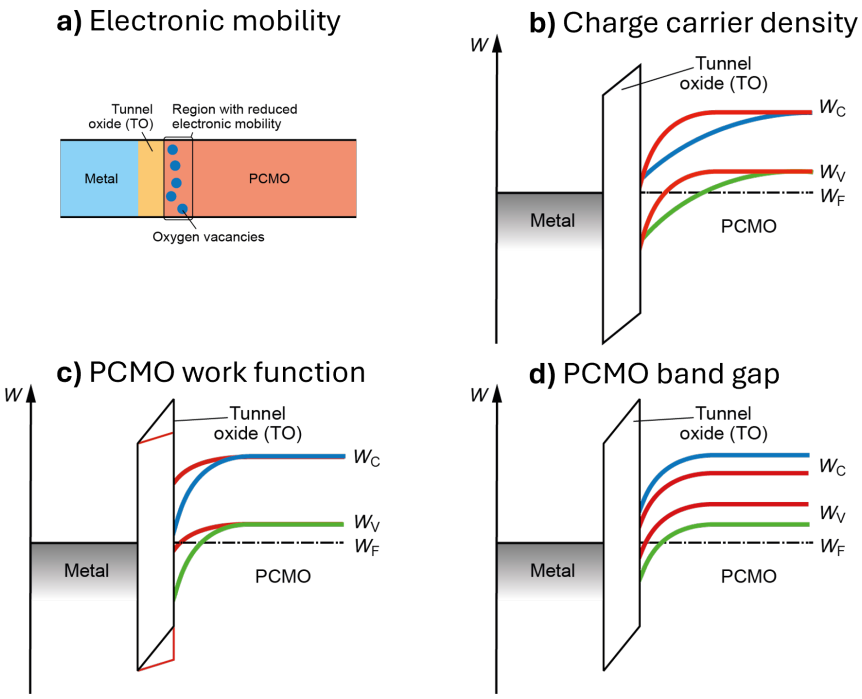

Figure 2.32.: Schematic overview of switching mechanisms based on the variation of the PCMO by oxygen vacancies. The LRS is depicted in red and the HRS in black.

al. [45] observed an interfacial TiO_x oxide layer for $PrMnO_3$/Ti, $Pr_{0.5}Ca_{0.5}MnO_3$/Ti and $CaMnO_3$/Ti devices after electronic biasing, however only the $PrMnO_3$/Ti and $Pr_{0.5}Ca_{0.5}MnO_3$/Ti exhibit hysteretic switching. Further, Arndt et al. [84], [96] found for PCMO/YSZ/Pt resistive switching without change of the oxide thickness. Therefore, the modulation of the TO thickness is not suitable to explain the switching in all kinds of PCMO-based stacks.

Charging of the tunnel oxide

There are ways in which the change in the oxygen content can alter the tunnel transport across the TO. The oxygen anion O^{2-} are considered as a mobile negative space charge, which bends both the valence and conduction band of the TO upwards and thus increases the effective height of the tunnel barrier (Figure 2.34). This model was used by Rene Meyer et al. to explain the switching behavior of TO/PCMO-based devices [8], [13], [83].

Arndt [96] experimentally showed that the electrostatic modulation of the Y-stabilized ZrO_2 (YSZ) tunnel barrier in the Rh/YSZ/PCMO structure does not explain the resistive switching in this structure as proposed by Meyer et al. [13] [83]. Arndt et al. [84] compared the peak level shift of the Rh3d and Zr3d core levels by hard x-ray photoelectron spectroscopy during the resistive switching cycle (Figure 2.35 b). They observed a remanent shift of around 0.34 eV of the Zr3d peak in the LRS to lower binding energy. Since the Rh3d level shows no shift, Arndt et al. [84] assigned the binding energy reduction to a change in the YSZ. The reduction of the binding energy in the LRS would be an experimental indication of an increase in negative space charge in YSZ. However, this contradicts the space charge model, as shown in (Figure 2.35), since a negative space charge would bend the tunnel barrier upwards and lead to the HRS. Arndt [96] assigned the reduction of the binding energy to a decrease of the YSZ band gap in the LRS and introduced a new switching mechanism, as will be discussed in the next section.

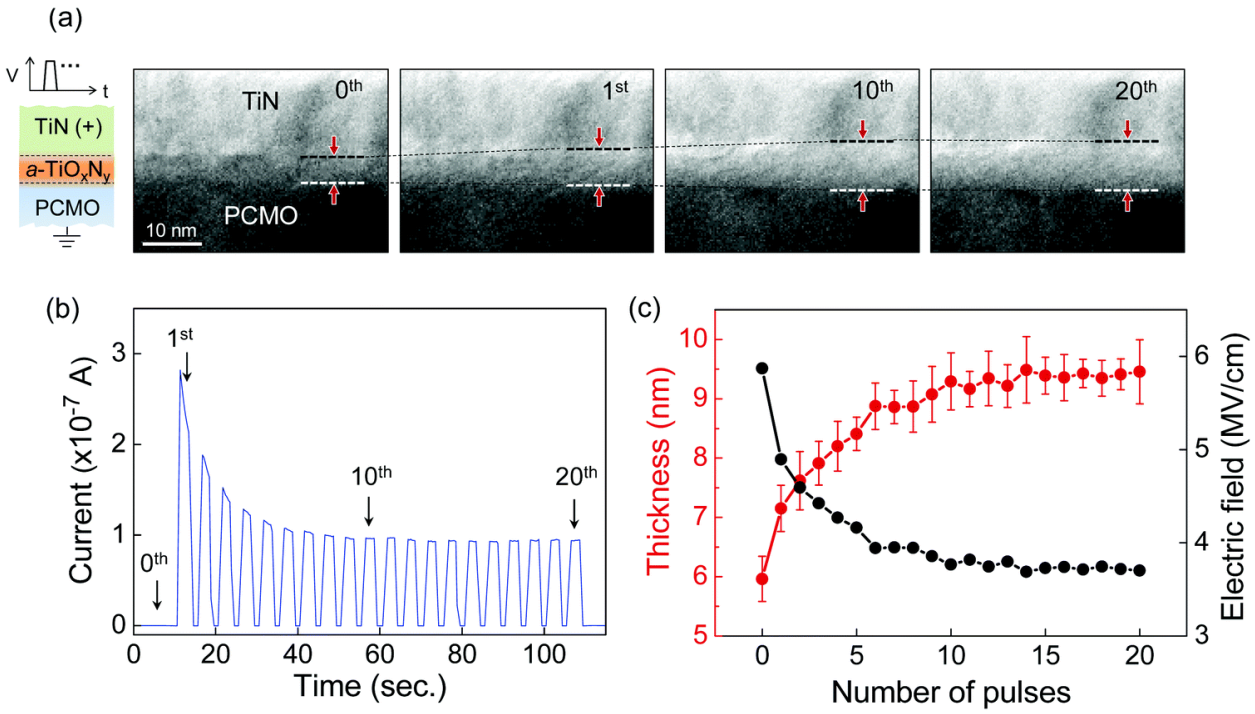

Figure 2.33.: In-situ observation of a-TiO_xN_y thickness variation with resistive states. Adapted and reprinted with permission from [78], © 2017 by American Chemical Society.

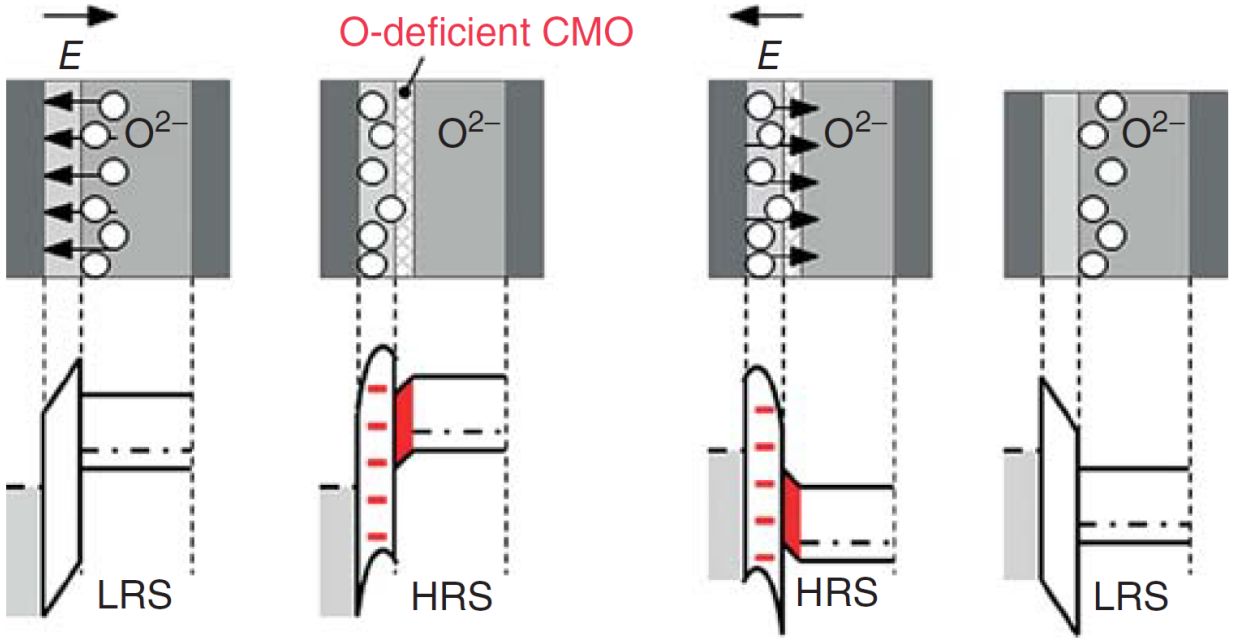

Figure 2.34.: Switching mechanism based on charging of the tunnel oxide. Adapted and reprinted with permission from [13], © 2016 by John Wiley and Sons.

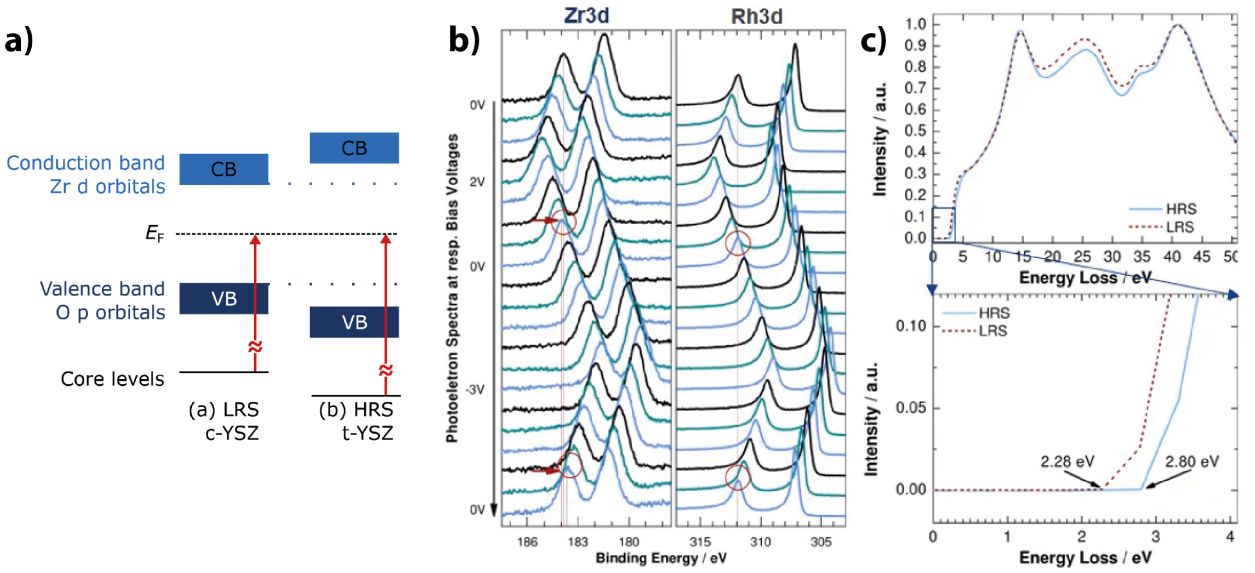

Figure 2.35.: a) Correlation of band gap change and core level change. The figure is inspired by [97]. b) Change of the Zr 3d and Rh 3d core level in in-situ HAXPES with the variation of the applied voltage. c) Variation of the EELS-spectra of YSZ in HRS and LRS. All Figures are taken from [96].

Change of the band gap of the tunnel oxide

The height of the tunnel barrier for direct tunneling is given on each site of the tunnel barrier by the difference between the work function of the metal or PCMO and the electron affinity of the TO. A decrease of the band gap of the TO caused by oxygen vacancies would increase the electron affinity of the tunnel oxide and thus reduce the tunnel barrier, as depicted in Figure 2.31.

Arndt [96] showed by XPS and EELS analysis a decrease of the YSZ band gap in the LRS compared to the HRS which will be explained in the following. XPS determines the binding energy in reference to the Fermi level. Assuming a constant position of the Fermi level in the middle of the band gap, a reduction of the band gap would be experimentally visible by a reduction of the binding energy, as can be seen in Figure 2.35a. This was observed by Arndt, for the binding energy of Zr3d5/2, which is lower in the LRS (181.24 eV) than in the HRS (181.58 eV). The band gap reduction is further supported by EELS data of the YSZ in LRS and HRS. This can be seen from the onset of the signal of electron energy loss in reference to the direct beam, which directly measures the band gap (Figure 2.35c). Arndt measured the onset of the energy loss signal at 2.28 eV for LRS and at 2.80 eV for the HRS.

Arndt assigned the band gap change of the local bonding configuration of the amorphous YSZ from a cubic configuration in the oxygen vacancy-rich LRS to a tetragonal configuration in the HRS. The fact that a cubic phase can be stabilized by oxygen vacancies was reported by Fabris et al. [98]. The relationship between band gap and phase was found by Jiang et al. [99] and Götsch et al. [100]. A change from cubic to the tetragonal phase relates to an increase of the shoulder around 530 eV in the Oxygen K edge, as shown by McComb [101] and Ostanin et al. [102]. This change is represented in the EELS data of Arndt (Figure 2.36). However, Arndt deposited YSZ with PLD at room temperature. Thus, the YSZ is amorphous and does not have a crystal symmetry, which could be assigned to name a phase cubic or tetragonal. The material change here can be seen as a change in the near order.

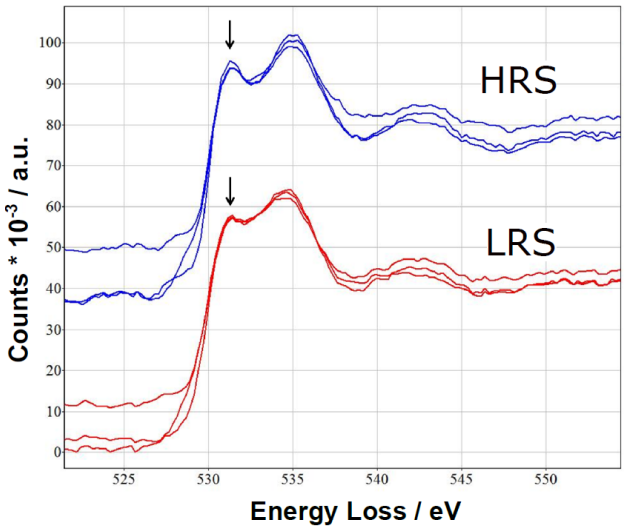

Figure 2.36.: Difference of the oxygen K-edge EELS data of amorphous YSZ in a metal/ YSZ/ PCMO/ SRO stack in HRS and LRS. Ni had been used as the top electrode. All Figures are taken from [96].

Influence of permittivity on the band bending and tunneling

As already discussed in Chapter 2.1.7, 2.2.3 and 2.3.4 the higher the permittivity, the more space charge is screened and thus the lower is the effect on the band bending. As the MOP stack contains two dielectric materials, the effect of the space charge depends on the relative permittivity between the PCMO and the tunnel oxide.

This has been considered by Sommer et al. [103] for a metal (high work function) / tunnel oxide / conducting oxide (low electron affinity - n-type) / metal (low work function) stack. In that case, the work function difference between the metal and the conducting oxide gives a negative built-in voltage and forms a Schottky barrier. The contact between the conducting oxide and the low work function metal is ohmic. The stack is shown in Figure 2.38a, and the two different oxygen vacancies profiles are plotted in red and blue in Figure 2.38b. The simulated stack deviates from the PCMO system due to several reasons. Firstly, the intrinsic charge carrier concentration of PCMO is larger than $10^{21}/\mathrm{cm}^3$ (see Chapter 2.2.3) and therefore much higher than the assumed $10^{18}/\mathrm{cm}^3$ in the simulation. Therefore, the effect of oxygen vacancy doping on the change of the carrier concentration is much less pronounced than in PCMO. Secondly, PCMO can be both n or p-type, as discussed in Chapter 2.1.3.

The three possible scenarios addressed in reference [103] and shown in Figure 2.38 are a) permittivity higher in the conduction oxide, b) equal permittivity, and c) higher permittivity in the tunnel oxide (Figure 2.38c). The red line indicates the scenario with high vacancy concentration in the tunnel oxide, as parametrized in Figure 2.37b. In the area of higher doping concentration, the conduction band is bent downwards because of the higher remaining space charge related to the doping. The lower the permittivity is in the TO, the less the remaining space charge is screened and the stronger its effect on the band bending. Sommer et al. found that the hysteresis in the $I-V$ curves (Figure 2.38a) is caused by the difference in band bending of the tunnel oxide if the relative permittivity is low and thus the band bending is pronounced. In the alternative scenario Figure 2.38c, a change in the switching polarity is observed, which is caused by an increase of electrons at the interface in the conducting oxide and thus an effective decrease of the tunneling distance for a positive applied bias and vice versa for an applied negative bias.

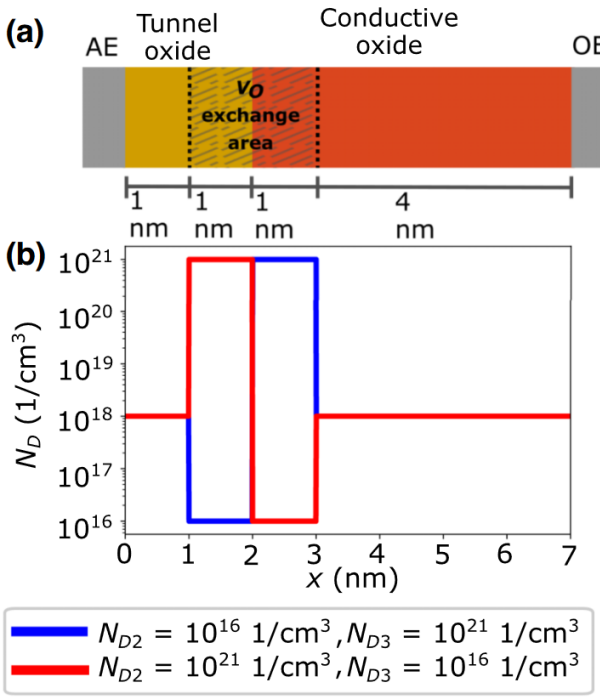

Figure 2.37.: a) shows the geometry of the simulated 1-dimensional model and b) shows the static donor concentration caused by oxygen vacancies. Taken from [103].

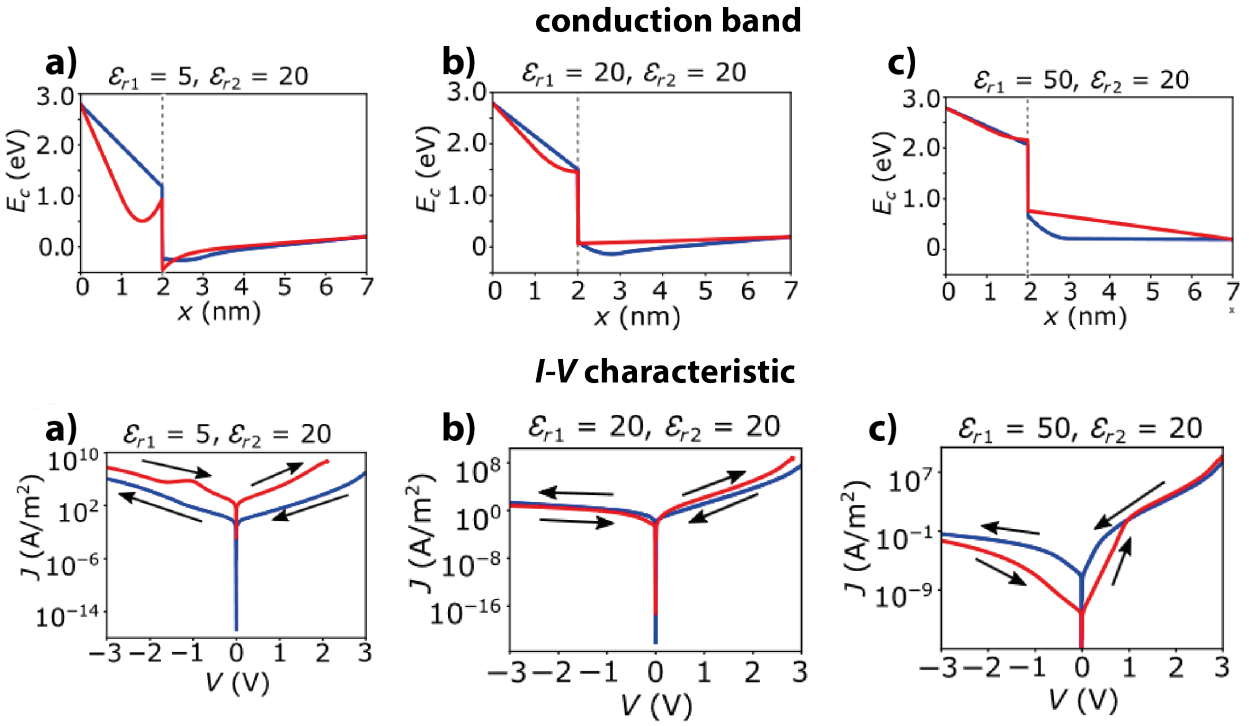

Figure 2.38.: The figures show the conduction band edge and the resulting $I - V$ loops for the two different oxygen vacancy distributions marked by red and blue, which corresponds to Figure 2.37b. Simulated are the possible scenarios with relative permittivity differences: a) permittivity higher in the conduction oxide, b) equal permittivity, and c) higher permittivity in the tunnel oxide. Taken from [103].

2.3.4. Switching mechanisms based on the modification of PCMO

Electron mobility and trap density changes

As discussed in Chapter 2.1.5 and illustrated in Figure 2.31, oxygen vacancies increase the resistance of PCMO and can therefore contribute to resistive switching. In particular, the increase is associated with a decrease in electrical mobility. It also allows the electric field to stray from the TO into the PCMO and facilitates the movement of the vacancies. The increase in resistance has also been referred to as a Mott transition by Lee et al. [43], a term also discussed in section 2.1.5.

Systems in which PCMO is sandwiched between two noble electrodes can, due to the absence of a tunnel oxide, be used to investigate the effect of oxygen vacancies in the PCMO layer. Several investigations of PCMO-devices with two noble electrodes assign the effect to the interface. In particular, Scherf et al. [104] investigated PCMO with Pt, Au, and Ag electrodes in different geometrical arrangements and located the switching process to the interfaces, which are competing in their dominance on the resistive change. Most importantly, Kramer et al. [105] proofed by in situ environmental TEM investigation that the switching in Pt/PCMO/Pt lamellae is connected to the electromigration of oxygen.

Although PCMO does not meet the requirements of SCLC (Section 2.2.5), some studies describe switching in PCMO-based devices by a variation of SCLC caused by changing the trap density in the material. For example, Chakraborty et al. [89] claimed for W/PCMO that the resistive state changes from LRS and HRS by increasing the trap density in the PCMO. This model was further developed by Saraswat et al. [106] into a quantitative reaction-drift model that includes ionic transport and describes PCMO switching based on variation of bulk defect states.

Influence of depletion zone variation on tunneling

The influence of oxygen vacancies on the tunnel current does not only depend on the change of the tunnel barrier height/bending or defect level concentration in the tunnel oxide as shown in Figure 2.32. The change in PCMO caused by oxygen vacancies can also affect the tunnel current. As shown in the simulation of the previous section, increasing the charge carrier density in the interfacial region can also increase the tunnel current. Charging the depth of the depletion region could also change the width of the tunnel barrier and, thus, the transport.

As discussed in Chapter 2.2.3, although the space charge region can be detected by photoelectron spectroscopy, it is too narrow to cause a rectification in the $I-V$ curves of the metal/PCMO Schottky junction. However, a strong reduction of the charge carrier concentration can reduce the depletion zone (as can be seen in Figure 2.19) and thus increase the tunnel current. As discussed in Chapter 2.1.5, switching can increase the oxygen vacancies and deplete the charge carrier density. For Ti/PCMO devices, Sawa [107] found that the capacity is increased in the LRS compared to the HRS (Figure 2.39) and concluded that the depletion zone is thinner in the LRS than in the HRS. As discussed in Chapter 2.1.7, also the permittivity of the oxygen-vacancy rich PCMO region could increase. This would further increase the depletion zone (Figure 2.19) and support this switching mechanism. However, a shortcoming of this model [46], [107] is that they did not include the TiO_x tunnel oxide at the interface [45]. Furthermore, the charge carrier due to oxygen vacancies causes the opposite effect for p-type and n-type PCMO. Therefore, the model predicts opposite switching directions. This cannot be seen when comparing devices based on $Pr_{0.5}Ca_{0.5}MnO_3$ (n-type) and devices based on $Pr_{0.7}Ca_{0.3}MnO_3$ (p-type), as both switches in counter-eightwise direction [46] [74] [67] [84] [107]. The switching direction is independent of the charge carrier type of PCMO if the change of the permittivity is considered solely.

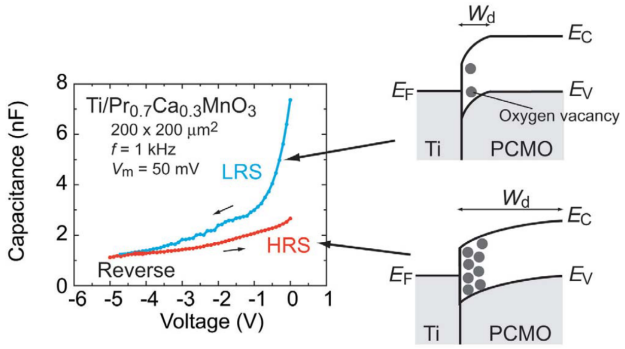

Figure 2.39.: Switching explanation for the PCMO/Ti structure based on the modulation of the space charge region by oxygen vacancies. Adapted and reprinted with permission from [107], © 2008 by Elsevier.

Change of band gap and work function

Besides the charge carrier density and the permittivity also, the work function and the band gap of PCMO can change by oxygen redistribution. As discussed in Chapter 2.1.6 2.6, the work function of PCMO can decrease after thermal reduction about 0.1 eV for $PrMnO_3$, 0.1 eV ($Pr_{0.5}Ca_{0.5}MnO_3$) and 0.2 eV ($CaMnO_3$). As discussed in Chapter 2.1.5, the bad gap of PCMO can also increase after thermal reduction around 0.4 eV for $PrMnO_3$, 0.4 eV for $CaMnO_3$, and 0.2 eV for $Pr_{0.5}Ca_{0.5}MnO_3$. As can be seen in Figure 2.40a, both effects add up and lift the bottom edge of the conduction band in the reduced PCMO. These effects counteract the shift of the valence band. If the change of the band gap dominates, the valence band edge effectively shifts down.

Asanuma et al. [45] used the band diagram-based description shown in Figure 2.40a to explain the resistive switching. They found that Ti/TiO_x devices based on $PrMnO_3$ and $Pr_{0.5}Ca_{0.5}MnO_3$ exhibit resistive switching and that devices based on $CaMnO_3$ do not switch. For the explanation, they assume that $PrMnO_3$ and $Pr_{0.5}Ca_{0.5}MnO_3$ are p-conducting and that $CaMnO_3$ is n-conducting. Therefore, Asanuma et al. [45] concluded from the band diagram that the change of the band bending by the oxygen redistribution only influences the transport within the valence band. Since the transport for n-type $CaMnO_3$ occurs within the conduction band and the work function is such that the bottom of the conduction band is below the Fermi level of the Ti, transport is unaffected by the change in band gap and work function (Figure 2.40b). For the transport within the valence band as relevant for p-type $PrMnO_3$ and $Pr_{0.5}Ca_{0.5}MnO_3$, the increase in band gap overcompensates the decrease in work function in the oxygen-deficient PCMO interface. As a result, the band bending increases, and the broadening of the tunneling barrier causes an HRS (Figure 2.40c). However, their assumptions regarding the positioning of the work function in the band diagram are not clearly explained. Further, their assumption of p-type $Pr_{0.5}Ca_{0.5}MnO_3$ is not covered by the Seebeck coefficient, as discussed in Chapter 2.1.3. Further restricting the switching model on variations in PCMO ignores the effect that oxygen vacancies have on the tunnel oxide. We must conclude that the relevant switching mechanism depends on the material selection in the MOP stacks. Further, different mechanisms can work in parallel; thus one does not necessarily have to dominate.

2.3.5. Switching kinetics

The switching kinetics of PCMO heterostructures is determined by the speed-limiting step for the field-accelerated movement of oxygen. It could either be limited by the drift within the tunnel oxide, within the PCMO, or across the PCMO/TO interface region. Furthermore, electron transfer can

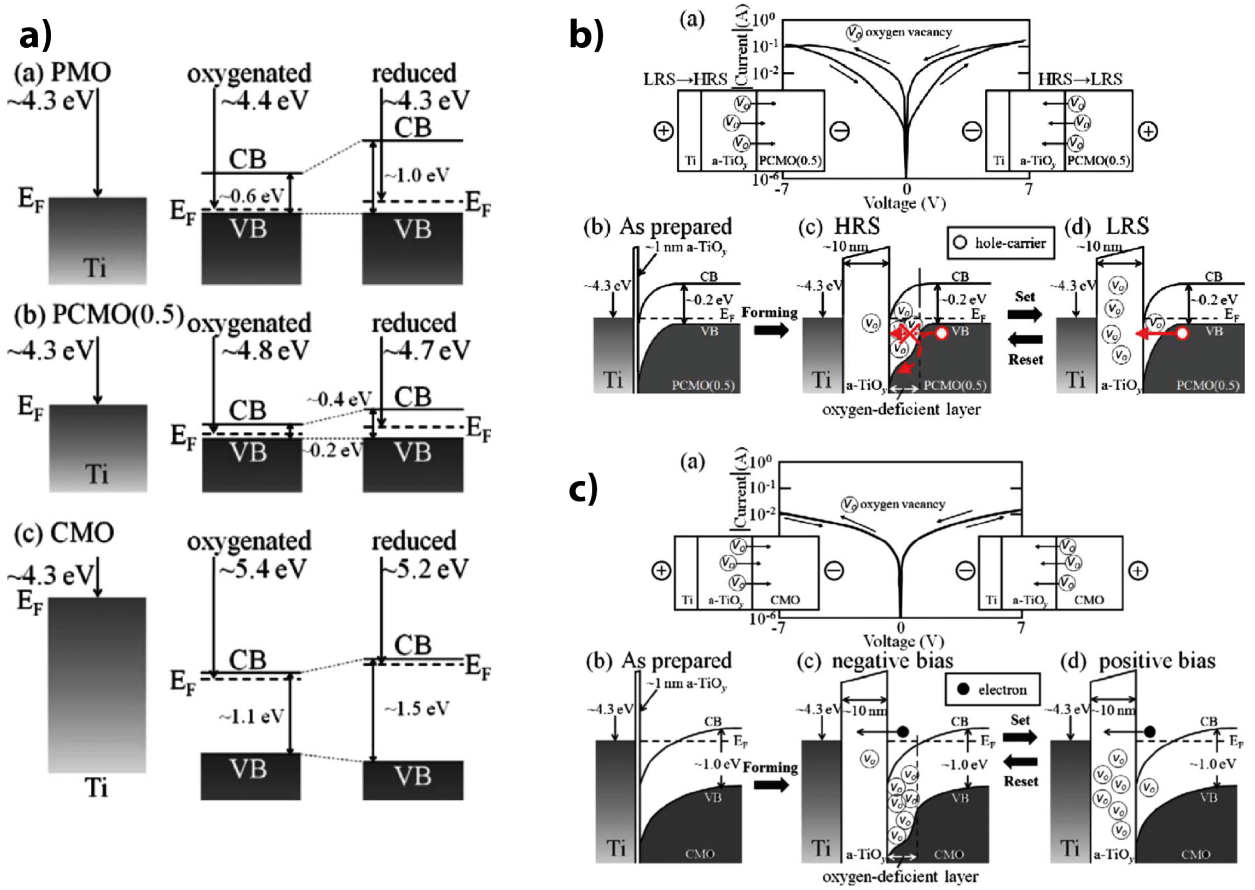

Figure 2.40.: Band diagram-based explanation for resistive switching of the Ti/TiO_x/PCMO structures. a)Shows the band structure of $PrMnO_3$, $Pr_{0.5}Ca_{0.5}MnO_3$ and $CaMnO_3$ oxidized and reduced in relation to Ti. b) Shows the resistive switching cycle of Ti/TiO_x/$Pr_{0.5}Ca_{0.5}MnO_3$ and the proposed band diagram change. c) It shows the missing resistive switching of $I-V$ cycles in Ti/TiO_x/$CaMnO_3$ structures and provides a band structure based explanation. Adapted and reprinted with permission from [45], © 2009 by American Physical Society.

be rate-limiting for redox reactions at the interfaces.99 The electrical field can be modulated as a result of changes in resistance, permittivity, and space charge caused by the oxygen exchange. An important difference between the kinetic of area-dependent and filamentary devices is that area-dependent devices are generally considered to be less dominated by Joule heating and the connected thermal acceleration during switching [8].

Kinetic considerations are important as a prerequisite for enabling resistive switching. Only if the electric field is sufficiently high ($E > E_c$) will oxygen movement be facilitated and resistive switching be induced. The critical field E_c required to facilitate the movement depends on the movement mechanism, as discussed in Chapter 2.3.5, and can be of the order of 1 MV/cm. The resistance of the materials and the resulting field drop within the stack is therefore important to the switching performance. As the switching takes place at the interface of PCMO/TO, it is particularly important that most of the field drops in this area. This is the case because the resistance of the tunnel oxide is usually higher than that of the PCMO. Further, in the interfacial region where the PCMO is reduced, the field can stray further into the PCMO and the space charge region could contribute. If the resistance of the PCMO becomes as high or higher than the tunnel oxide, this could lead to a field distribution whose main contribution is not within the active switching interface. This could lead to the kinetics prohibiting the ionic movement and could explain the poor or missing area-dependent switching of devices based on amorphous PCMO [1] [108] [109] [110] [111] [112] [113] [114], which has a much higher resistance than crystalline PCMO.

During set and reset, the vacancies must cross the interface in the opposite direction. Since the reset leads to further oxidation of the TO and the set to an oxygen extraction, the critical voltage to overcome the energy barrier may be different for set and reset. Lee et al. [115] showed that necessary voltage to do a set operation increases with the free energy of oxide formation of the TO oxide.

Diffusion and drift of oxygen

As described in Chapter 2.1.5 in detail, due to the densely packed perovskite lattice of PCMO, Frenkel defects are suppressed, and oxygen movement takes place via vacancies. Therefore, the vacancy can be described as the moving entity while using the same activation barrier ΔW as for the oxygen movement. The benefit of using the vacancy as a moving entity is that the vacancy usually has a neighboring oxygen anion since the number of vacancies N_V is usually much smaller than the number of oxygen anions N_O, and therefore, the average velocity v_D ($\ddot{V}_O = N_O/N_V \cdot v(O_O)$) during self-diffusion is not reduced due to the limited possibility of neighboring exchange partners [8]. The average drift velocity

$$v_D(\ddot{V}_O) = a\omega e^{-\Delta W/(k_B T)} \tag{2.31}$$

during self-diffusion can be determined by the Arrhenius law $\propto e^{-\Delta W/(k_B T)}$, the jumping distance a (usually interatomic distances of 0.2 nm - 0.5 nm [10]), and the attempt frequency ω. The attempt frequency is sometimes approximated by half of the Deby frequency [17], which would be $2 \cdot 10^{13}$ Hz for $Pr_{0.8}Ca_{0.2}MnO_3$ with a Debye Temperature of 325 K [116]. The activation barrier ΔW can experimentally be determined from self-diffusion profiles by oxygen tracer experiments. Fitting the time-dependent diffusion profiles results in the diffusion coefficient $D(O_O) = \frac{av(O_O)}{2}$, and the activation barrier ΔW can be determined from the temperature dependence. The application of an electric field E leads to the directionality of the drift velocity $v_D(\ddot{V}_O)$ because of the reduced activation barrier by $\Delta W - zeaE/2$, as sketched in Figure 2.41a. For the calculation of the effective drift velocity $v_D(\ddot{V}_O)$, the vacancy hopping in the opposite direction must be subtracted, resulting in the so-called Mott-Gurney law [117] of ion hopping

$$v_D(\ddot{V}_O) = a\omega e^{-\Delta W/(k_B T)} 2\sinh(zeaE/(2k_B T)) \tag{2.32}$$

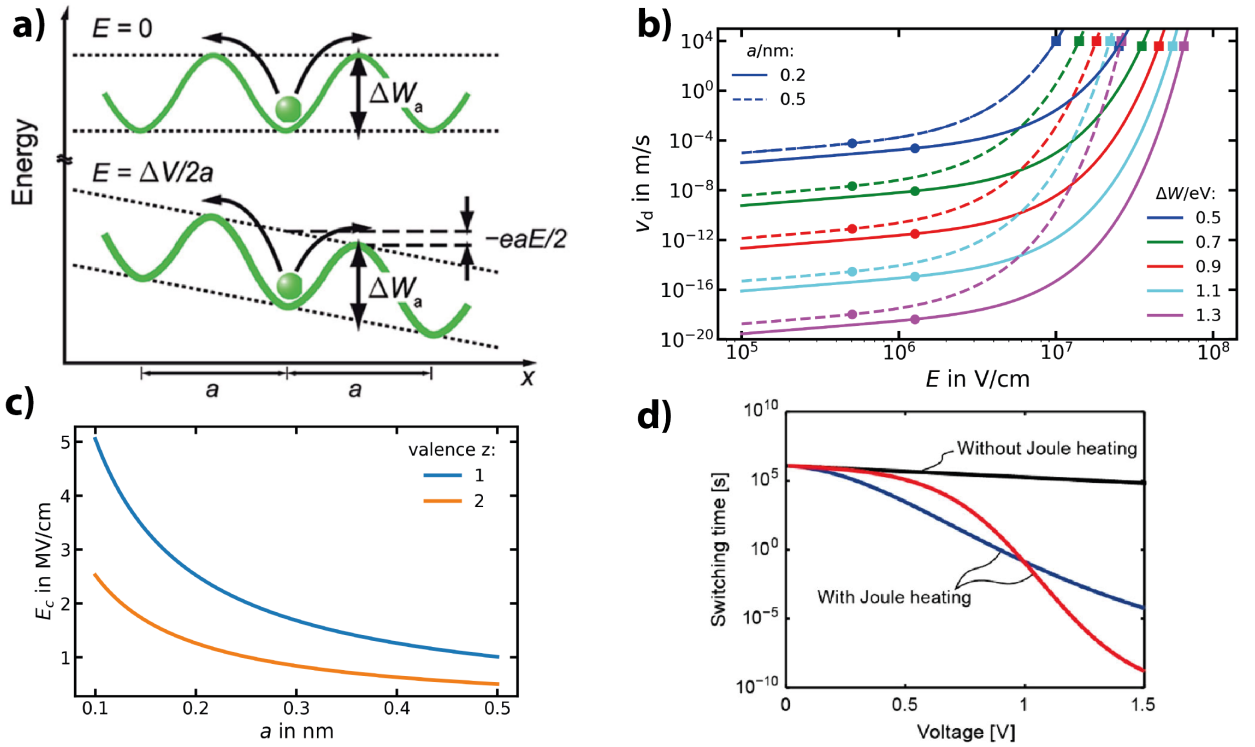

Figure 2.41.: a) Geometric argument for the activation barrier reduction for field enhanced diffusion, leading to the Mott-Gurney law. Adapted and reprinted with permission from [10], © 2015 by John Wiley and Sons. b) Drift velocity in dependence of the field according to equation 2.37 for different activation barriers ΔW and different jumping distances a at room temperatures for $z = 2$ and an attempt frequency of $\omega = 2 * 10^{13}$ Hz . E_c is marked by a dot and E_{max} is marked by a square. c) critical field (eq. 2.35) in dependence of valence and jumping distance. d) The influence of Joule heating on the switching was time calculated from Mott-Gurney based oxygen transport. The blue curve is for a linear current voltage relationship and the red for a diode like behavior. Adapted and reprinted with permission from [8], © 2022 by Taylor & Francis.

which is plotted in Figure 2.41b. It is often written in the form of ionic current density:

$$J(\ddot{V_O}) = zecv_D(\ddot{V_O}) \tag{2.33}$$

where c is the vacancy concentration and z the valence number. The Mott-Gurney law is only valid until the field E_{max}, shown by squares in Figure 2.41b. At this field strength, the electronic potential completely compensates the activation barrier ΔW

$$E_{max} = \frac{2\Delta W}{zea}. \tag{2.34}$$

The Mott-Gurney law converges at small fields in the linear regime of the sinh to the Einstein-Smoluchowski equation [117]. The difference between the dashed and the solid lines in Figure 2.41b also shows that the drift velocity increases for larger jumping distances a if the activation barrier ΔW remains the same.

At high fields $E > E_c$, with the critical field E_c

$$E_c = 2k_BT/(zea) \tag{2.35}$$

the field dependence of the ionic movement becomes exponential. E_c is dependent on the

jumping distance and the valence number and is usually in the order of few MV/cm, as can be seen in Figure 2.41c. Controlling the switching kinetics by a non-linear field dependence is important for the stability of the written state against decay over time (retention), for the stability against a reading voltage, and for fast writing speeds [10]. This non-linearity can be temperature accelerated by Joule heating [8]

$$T = T_0 + R_{th} I(V) V \tag{2.36}$$

by the electronic power $I(V)V$, especially when the current-voltage relationship is non-linear. R_{th} is thermal resistance and considers the material parameters. The non-linearity becomes particularly pronounced in cases of a non-linear $I-V$ relationship, as can be seen in the exemplary case of a diode with $I(V) = I_0(\exp(V/V_0) - 1)$ in Figure 2.41d. The ionic current density $J(\ddot{V_O})$ or the drift velocity $v_D(\ddot{V_O})$ can relate to the switching time t_{SET} by

$$J(\ddot{V_O}) \propto t_{set}^{-1}. \tag{2.37}$$

To investigate the switching kinetics, the switching time t_{SET} must be clearly defined. Therefore, it is defined as the time which is needed to switch between two defined resistive states $R_0(c_0)$ and $R_1(c_1)$. The resistive states are given by two oxygen concentration profiles c_0 and c_1. The redistribution $\Delta c = c_1 - c_0$ between both states is caused by the applied voltage. The same redistribution Δc takes place only within the same time t_{SET} if the initial distribution c_0 is the same. Therefore, controlling the initial resistance $R_0(c_0)$ is crucial for a reliable analysis of the switching kinetics. If the initial resistance $R_0(c_0)$ is experimentally well controlled, then a switching time can be defined as the time which is needed to achieve a certain arbitrary resistance ratio $R_1(c_1)/R_0(c_0)$.

For the investigation of the switching kinetics, t_{set} is plotted against the voltage (Figure 2.42b). If the kinetically limiting process is ion migration according to the Mott-Gurney law, the field strength is larger than E_c, and if Joule heating can be disregarded, than t_{set} should lie in the semi-logarithmic plot on a straight line [8] with a slope m of

$$m = -aze/(2k_B T w) \tag{2.38}$$

where w is the device thickness over which the voltage drops. In addition to ion migration, other mechanisms could also limit the kinetics, such as, the electronic transfer at the interface, which can be described by the Buttler-Volmer equation. For electrochemical metallization cells, the formation of a stable metallic nucleus prior to the filament growth could also become kinetically limiting [8], [10]. However, both competing processes result in an exponential field dependence and would result in a line in the semi-logarithmic plot. Menzel et al. [8], [10] compared the slopes under a span of physically reasonable parameters Figure 2.42a and concluded that the Mott-Gurney based ion migration has the lowest slope and thus is generally likely to be the dominating process at high voltages, as long as the Joule heating does not cause higher non-linearity (Figure 2.41d) as is the case of filamentary VCM devices.

Since PCMO/Al_2O_3/Pt based devices lie on a fairly straight line [118] at high voltages Figure 2.42b with a reasonable slope for the Mott-Gurney law, the kinetic of PCMO-based devices is likely controlled by ion migration without thermal acceleration. The slope m is given by [8]

$$\Delta V_{dec} = -1/m\ln(10) \tag{2.39}$$

the voltage which is necessary to increase the switching time by one order of magnitude. ΔV_dec is plotted in Figure 2.42c for different reasonable parameters in the case of a pure field dependent Mott-Gurney governed dynamic. As smaller ΔV_{dec} is favorable. The smaller ΔV_{dec} is, the shorter is the needed pulse to write a resistance state at high voltage. Further, the smaller ΔV_{dec} is, the longer can the resistance state be read at a low voltage without disturbing the state. However,

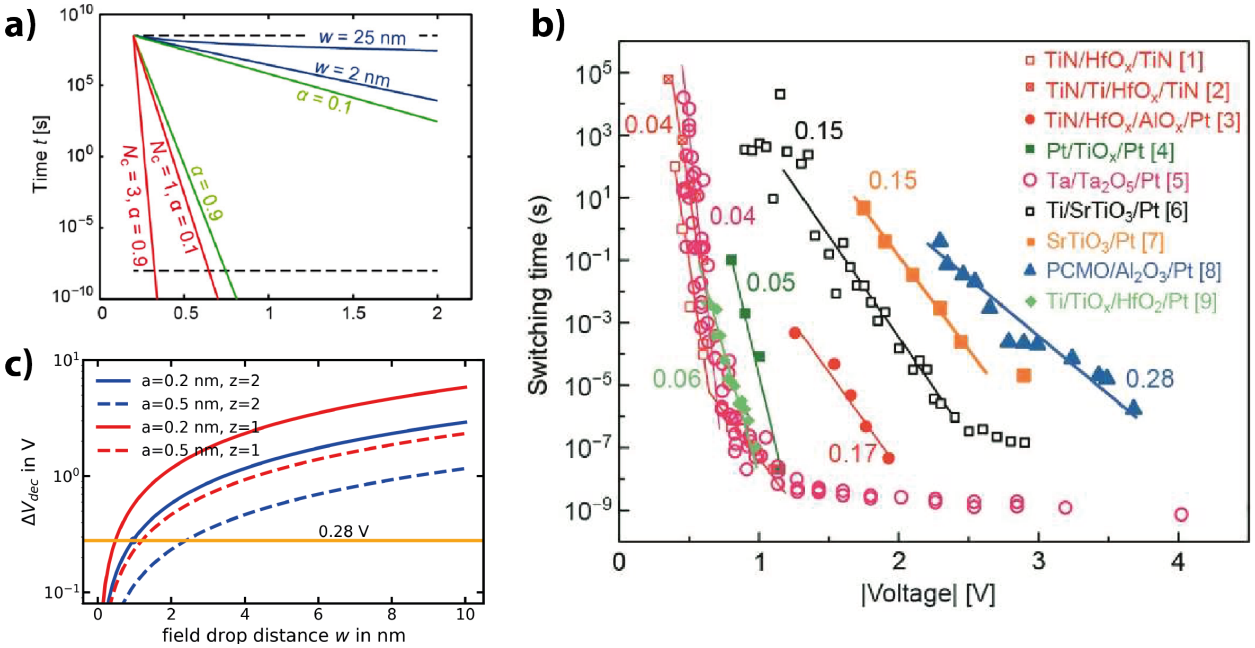

Figure 2.42.: a) Comparing the field dependency of different kinetic limiting processes (blue - ionic hopping, green - nucleation, red - electron transfer) under a span of different physical parameters. Adapted and reprinted with permission from [8], © 2022 by Taylor & Francis. b) Set time plotted against applied voltage for different VCM stacks. Adapted and reprinted with permission from [118], © 2023 by IEEE. The written numbers are ΔV_{dec} of the system. c) ΔV_{dec} in dependence of the field drop distance w for different parameters in the only field accelerated Mott-Gurney law with $E > E_c$. $\Delta V_{dec} = 0.28$ V of the PCMO/Al_2O_3/Pt devices is shown by the orange line.

this argumentation is only valid if the whole voltage range is dominated by one kinetic limiting mechanism.

Figure 2.42c shows possible ΔV_{dec} in dependence of the field drop distance w for the sole field accelerated Mott-Gurney law at $E > E_c$. It shows, on the one hand, that this mechanism is not able to achieve high nonlinearity for large time differences between reading and writing. It also shows that the nonlinearity can be improved by material stacks in which the voltages drop across very thin layers.

The $\Delta V_{dec} = 0.28$ V for PCMO/Al_2O_3/Pt devices (shown in Figure 2.42c by an orange line) leads to the conclusion that in the devices the voltage drops in the a region of around 1 nm (crossing lines with the different plotted ΔV_{dec}). Thus, it could be concluded that the active switching region of field drop including the AlO_x [118] reduced PCMO and the space charge region are very narrow.

The lack of temperature acceleration in the kinetics of TaO_x/PCMO devices is further indicated by the behavior of the potentiation and depression measurements performed by Gutsche et al. [12]. Here the change in resistive state depends only on the total applied time of a voltage pulse. The application of many short voltage pulses results in the same resistance changes as a long voltage pulse. This indicates that a longer voltage pulse does not further heat the device and thus thermally increase the vacancy mobility. This gradual switching property of PCMO-based devices makes them suitable for neuromorphic applications.

However, there are also studies that have found the effect of Joule heating on the kinetics of PCMO-based devices. These studies are based on the W/PCMO system, which exhibits a sharp SET transition in its IV loop and requires current compliance for SET, as is typical for filamentary systems. Although the group claims area dependence, [88] there is no clear experimental evidence for area scaling of the low resistance state. Therefore, Joule heating in these W/PCMO

stacks might be caused by a local confinement of the switching process within the interface oxide. A similar sharp SET behavior has been found for Ti/PCMO devices and has been attributed there to multi-filamentary switching within the interfacial oxide [74].

The experimental evidence for self-heating was found in the SET and RESET transients of W/PCMO devices, with timescales for self-heating between 50 and 100 ns [119]. This was further complemented by experimental studies of SET voltage versus SET time, which showed steep slopes and saturation at about 100 ns [106]. These results are accompanied by computational models simulating device temperature [106], [119]. However, these models include controversial approaches with SCLC for electrical transport (Chapter 2.2.5) and bulk trap variation as switching mechanisms (Chapter 2.3.4).

The switching time is an important quality parameter of PCMO-based devices, determining the possible memory applications. While it is obvious that the switching times speed up with higher voltages (Figure 2.42), high voltages can lead to poor endurance and difficulties in CMOS integration. However, the switching speed limit is still unknown. While Saraswat et al. [106] found a switching limit of 100 ns at around 2.5 V for their W/PCMO based devices, the commercial company *4DS Memory* publicly claims a switching speed of 4.7 ns for their PCMO based memory arrays [20].

Retention

Instabilities of the resistive states which limit the retention of memristive devices are induced by the redistributing diffusion of ions in a chemical gradient without applied voltage. The diffusion current can be considered as temperature accelerated by the activation energy ΔW as in equation 2.31, and the retention time t_{ret} can be assumed to be described by [8]

$$t_{ret} \simeq Ae^{-\Delta W/(k_B T)} \tag{2.40}$$

where A is a constant. Therefore, high activation energies are beneficial for high retention times [120].

Measurements of the temperature dependence of the retention times can, therefore, be used to determine the activation energy, which are called accelerated life testing. Kumbhare and Ganguly [121] analyzed the retention time of PCMO/W devices in dependence on the PCMO stoichiometry. They determined ΔW of $\Delta W(PrMnO_3)$ = 1.29 eV, $\Delta W(Pr_{0.9}Ca_{0.1}MnO_3)$ = 1.12 eV, $\Delta W(Pr_{0.8}Ca_{0.2}MnO_3)$ = 1.26 eV and , $\Delta W(CaMnO_3)$ = 0.61 eV. Lee et al. [122] derived an activation energy of 0.6 eV from retention measurements of $Pr_{0.7}Ca_{0.3}MnO_3$. Inge et al. [123] performed DFT calculations for $Pr_{0.5}Ca_{0.5}MnO_3$ and calculated the activation energy of vacancy migration in dependence of the migration path, ranging from 0.68 eV to 1.14 eV.

Since oxygen transport during decay consists of transport within the tunnel oxide, over the interface, and within the PCMO, this raises the question, of which activation energy must be considered. It is reasonable to assume that the highest activation energy will limit the kinetic. Since Kumbhare and Ganguly [121] observed a strong dependence on the retention of the PCMO/W devices from the PCMO stoichiometry, it is reasonable that for this device, the activation energy of oxygen movement in PCMO is the speed-limiting process for their devices. Moon et al. [120] compared $Pr_{0.7}Ca_{0.3}MnO_3$ devices with different top electrodes (Al, Ti, Ta and Mo). They saw the highest retention of the LRS for the devices with Mo as top electrode and concluded that the activation energy for the oxidation of the top electrode is controlling the retention. Moon et al. [93] further suggested an Al/Mo/PCMO based device as a compromise between improved retention due to MoO_x acting as an oxygen buffer layer and AlO_x to increase the on/off ratio.

However, the retention time of PCMO-based devices varies widely in the literature. In the same way as the measured activation energies of PCMO-based devices vary, also the measured retention times vary, from 10^{-2} s [120] over 10^8 s [122] to 10^{15} s [121]. This is, on the one hand, based

on the different activation energies for oxygen vacancy migration for different tunnel oxides and differences in the activation energies within PCMO between different stoichiometries and difference in layer growth. Further, retention values will also differ because of different SET or RESET pulse heights and lengths as well as read pulses. In addition, different definitions of retention time are used in relation to the resistance ratio, and a rigorous accelerated life study requires the use of different temperatures.118

Furthermore, these reports of retention are single device studies and therefore lack a high statistical base. An example of a statistical analysis of retention of a full memory block of filamentary devices was performed by Wiefels et al. [124] which shows that the whole statistical distribution changes during accelerated life testing, thus only considering the shift of the mean do reflect the reliability of the devices. To our knowledge, no such studies have been published for PCMO-based devices.

Compared to filamentary devices, area dependent devices are generally considered to have lower retention and more read disturbance than filamentary devices [7]. This could be due to less pronounced oxygen vacancy redistribution in the switching kinetics along the entire interface, as it is the case for highly temperature-accelerated switching of filamentary devices. However these limitations are not severe enough to stop the industrial interest in PCMO-based devices. Retention times can be controlled by engineering the ionic conductivities in the interfacial region, and the publicly traded company *4DS Memory* is advertising their devices with tunable retentions on the order of days to months [20].

2.4. CMOS co-integration

The required back-end of-the line (BEOL) integration of polycrytalline PCMO into CMOS technology circuits is challenging because PCMO must be deposited at elevated temperatures to grow in a crystalline phase. Temperatures above 400 ℃ are considered incompatible with the CMOS back-end of the line.

Crystalline growth below 400 ℃ by sputter deposition has been achieved by a special back-biased face-target sputtering process by the company *4DS Memory* [61], [15], [14], [125]. Normal RF sputter deposition at room temperature shows only a very low degree of crystallinity as shown by Kanegami et al. [109].

Pulsed laser deposition (PLD) has not been able to achieve high-crystallinity, which means significant strong Bragg reflections, at CMOS-compatible temperatures. Different crystallization temperatures have been reported depending on the substrate material. Yamamoto et al. [111] reported a low intensity of Bragg reflection for deposition at 600 ℃ on MgO (001) single crystal substrate and amorphous SiO_2 substrate, with a lower degree of crystallinity for deposition on amorphous SiO_2 compared to crystalline MgO. Kim et al. [126] showed that low intensity Bragg reflections are already visible when deposited on a crystalline Ag bottom electrode at 400 ℃. Seong et al. [112] saw no evidence of crystallinity for deposition on a polycrystalline Pt bottom electrode at 500 ℃ and below. Panwar et al. [127] also saw no evidence of crystallinity for deposition on a polycrystalline Pt electrode at 450 ℃.

So, to our knowledge, the best way to achieve BEOL integrated crystalline PCMO is a special sputtering process. The alternative is the use of amorphous PCMO, which is less studied. There are some studies showing area dependent switching for PCMO grown at room temperature by pulsed laser deposition (PLD), namely for ITO/PCMO [114], Ti/PCMO [110] and AlO_x/PCMO [1]. However, there are also studies showing different switching behavior with room temperature PLD grown PCMO, such as filamentary switching for ZnO [113], unipolar switching for W/PCMO [127] and a combination of filamentary and area dependent switching for Ti with room temperature sputtered PCMO [109].

3. Experimental methods

3.1. Deposition methods

3.1.1. Pulsed laser deposition

Pulsed Laser Deposition (PLD) is a thin-film deposition technique particularly suited for the growth of materials with complex stoichiometry, such as complex oxides. In this method, a high-energy laser pulse ablates a solid target at fluences exceeding the ablation threshold, resulting in the ejection of material. The laser fluence is therefore a critical parameter controlling the deposition process, with typical values on the order of 1 J/cm^2. KrF excimer lasers with a wavelength of 248 nm are commonly employed, with laser pulse lengths of few tens of ns. The interaction between the laser and the target is highly complex. The absorption of the laser pulse at the target surface generates a plasma plume that transports material toward the substrate [128]. The resulting plasma plume propagates approximately perpendicular to the target surface toward the substrate, as drawn in Figure 3.1.

One of the main advantages of Pulsed Laser Deposition (PLD) is that target ablation occurs in a largely non-selective manner with respect to the elements present in the target material. Consequently, the transfer of material from the solid target to the plasma plume typically preserves the stoichiometry, making PLD particularly well suited for the deposition of materials with complex compositions [128].

To enable propagation of the plasma plume from the target to the substrate, the process is carried out in a vacuum chamber, with the substrate typically positioned a few centimeters away and aligned orthogonally to the target surface. The plume propagates predominantly in the direction of the surface normal, driven by the high evaporation velocity resulting from the eruptive plasma formation. During propagation, internal electric fields generated by the charged plasma species influence the plume dynamics [128].

For oxide deposition, oxygen is commonly introduced as an active process gas. However, elevated pressures hinder plume propagation due to scattering with gas molecules; therefore, process pressures are typically maintained well below 1 mbar. Even at reduced pressures, interactions between the process gas and the plasma plume can still affect its propagation. At higher gas pressures, lighter elements are more easily scattered than heavier ones, which can lead to deviations in stoichiometry. Because the degree of interaction between the process gas and the plume depends on both the gas pressure and the target-substrate distance, these two parameters have similar effects on the transferred stoichiometry and are therefore critical for controlling the deposition process [128].

A certain kinetic energy of the plasma species is required for them to reach the substrate. Once adsorbed, the species can diffuse across the substrate surface, enabling nucleation and growth of crystalline phases. The extent of this surface diffusion, strongly depends on the kinetic energy of the adsorbed species, which is largely governed by the substrate temperature [128]. To promote crystalline or even epitaxial growth, depending on the material system and substrate morphology, substrate temperatures on the order of 1000 K are often required. Therefore, substrate temperature is a critical parameter in the deposition process. In the case of electronic materials for memory devices, compatibility with back-end-of-line CMOS processes imposes an upper temperature limit of approximately $400°$C, making it challenging to achieve high-quality crystalline layers while maintaining CMOS compatibility using PLD.

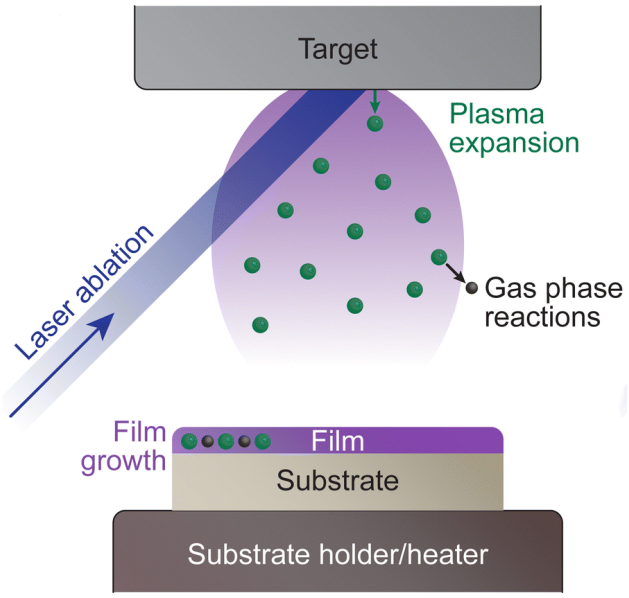

Figure 3.1.: Conceptual drawing of a pulsed laser deposition. Its shows the ablation of of target by the laser pulse, the expansion of the plume and the growth of the film on the substrate. The Figure was taken and adapted from [128].

An important field of application for PLD is the growth of epitaxial oxide layers. Since the deposition rate per laser pulse can be well below a single atomic layer, the method is highly suitable for the controlled growth of atomic layers and stacks of different metal oxides. A common approach for in situ monitoring of oxide growth is the use of Reflection High-Energy Electron Diffraction (RHEED). In particular, the intensity of the specular spot is tracked during growth, as changes in high-energy electron reflectivity correspond to changes in the surface structure of the layer and can therefore measure the growth on atomic-scale, especially in the case of layer-by-layer growth [128].

3.1.2. Sputter deposition

Sputter deposition is one of the most widely used industrial technologies for thin-film deposition. There are several technological variants of this technique, all based on the principle of sputtering, which is the physical vaporization of a target material by ions accelerated in an electric field. For this reason, sputter deposition is categorized as a Physical Vapor Deposition (PVD) process [129]. As the process gas, noble gases, such as argon, are typically used. For the deposition of oxides or nitrides, additional reactive gases such as O_2 or N_2 can be introduced, in which case the process is referred to as reactive sputter deposition. The pressure of the process gas, and in the case of reactive sputtering the mixture of the reactive gas and the sputter-active noble gas, are thus important process parameters.

The ionization of the noble gas is achieved by an electric discharge, initiated and sustained by electrically accelerated electrons. The resulting ions are then accelerated toward the target material, where their impact leads to the ejection of target atoms. To provide a sufficient mean free path for ionization, ion-acceleration and the transport of sputtered material, the deposition is carried out in a vacuum chamber with a low background pressure to minimize contamination and a controlled working gas pressure, typically well below $1\,\mathrm{mbar}$.

Sputtering can be performed using a direct current (DC) bias, referred to as DC sputtering, in which the target is negatively biased to attract the cations of the noble gas [129]. This technique is relatively simple and cost-effective, providing comparatively high sputtering rates [130]. However,

a DC bias can sustain plasma formation only when the target material is electrically conductive; therefore, DC sputtering is not suitable for targets which form surficial oxide layers or for generally insulating materials. Since the sputtering rate is mainly dependent on the applied DC power, the deposition process is typically conducted in constant-power mode, and the applied power is a major process parameter [130].

For insulating targets, RF sputtering is commonly employed. RF sputtering is based on the generation of an electric discharge using a 13.7 MHz RF power source with an impedance-matching capacitor connected between the target and the chamber [130]. The RF generator is directly coupled to the target, while the sample and the chamber are grounded. Owing to the large difference in electrode size between the small target and the large chamber, the electric field, and consequently the plasma, is strongly enhanced in front of the target. Since ions respond much more slowly to the electric field than electrons due to their higher mass, they cannot follow the high frequency of the commonly used 13.65 MHz power generator. As a result, more electrons are absorbed during the positive phase of the RF cycle than ions during the negative phase. This imbalance causes the target to acquire a net negative charge. The resulting self-bias accelerates argon ions toward the target, effectively making it act as a cathode and causing sputtering [129]. The deposition rate is controlled by the power applied to the RF generator; therefore, the deposition process is conducted in constant-power mode, making the applied power an important process parameter.

To further increase the ionization rate, the electron density in front of the target can be enhanced by controlling their trajectories with a magnetic field, a technique known as magnetron sputtering [131]. In this method, two magnetic poles are positioned behind a typically circular target: one at the center and one in a ring around the periphery. The resulting magnetic field lines confine the electron trajectories to a circular racetrack at the front of the target surface [129]. The increased ionization rate and sputter yield in this region lead to enhanced generation of secondary electrons, which further sustain the sputtering process. As a result, magnetron sputtering causes inhomogeneous erosion of the target. This technique can be employed to improve sputtering rates in DC and RF sputtering systems.

In this work, DC and RF magnetron sputtering were used, conducted in an ultra-high-vacuum (UHV) deposition system from *SURFACE systems + technology GmbH & Co. KG*. In this system, the SW-50-E-UHV-SH magnetron from *GENCOA* is used. For DC sputtering, a Maris GS10 DC power supply from *ADL* is employed, and for RF sputtering, a cito 136 RF generator with a agilo 1313a 7/16 matching unit, both from *Stolberg*, are used.

3.2. Device structuring

To laterally structure the material stack, photoresist is coated and patterned on the sample using photolithography. These photoresist structures either protect the underlying areas during a dry etching process or or inhibit material deposition in defined areas. In the latter case, the remaining photoresist can be removed in a subsequent step, known as the lift-off process. Since photoresists cannot withstand high deposition temperatures, photolithography followed by etching is the most common approach for structuring electronic materials.

As an alternative to structuring by photoresist and etching, a physical shadow mask was directly attached to the top of the sample for some samples that only had a Pt top electrode. This confines the deposition area to the openings of the shadow mask. This type of structuring has the benefit of being a very simple process, where the sample surface does not come into contact with the wet chemistry used during photolithography. However, this type of patterning is limited in resolution to a few tens of µm.

3.2.1. Photo-Lithography

To pattern the photoresist layer, the liquid photoresist is first coated onto the sample using a spin-coating process. During spin coating, the sample is held in place by vacuum suction on the back side of a rapidly rotating chuck, which typically operates at speeds of a few thousand rpm. The applied liquid photoresist is spread across the sample surface by centrifugal force. The combined effects of centrifugal force, surface tension, and the intrinsic viscosity of the photoresist produce a uniform film thickness over the entire sample [132, 133]. There are two types of photoresists, which respond differently to light exposure. In a positive photoresist, the illuminated areas become soluble during development, leaving those regions free of resist. Mostly in this work, the positive photoresist AZ MIR 701 from *Merck* was used. It forms a thin resist layer of a few µm after spin-coating at 4000 rpm. In a negative photoresist, the illuminated areas become insoluble and remain on the substrate after development.

After coating, the photoresist is partially solidified by evaporating part of its solvents through a heating step, commonly referred to as a soft bake. This solidification increases adhesion to the sample and is necessary to obtain a stable film for the subsequent processing steps.

During the subsequent lithography step, structured light exposure activates a photochemical reaction in the photosensitive resist to achieve the desired spatial pattern [132, 133, 134]. In this work, a shadow-mask process was used, in which illumination from a mercury lamp was selectively blocked by a chrome-coated glass plate. The shadow mask was designed so that the shadow pattern corresponded to the features to remain in the photoresist; therefore, a positive resist was used. The coated side of the mask was positioned in close proximity to the sample surface to define the desired pattern. The contact alignment of the mask and the subsequent illumination are performed with a manual MA6 mask aligner from *Karl Suss*.

After light exposure, a second thermal step, the so-called hard bake, can be applied to further evaporate the solvents in the photoresist. This hardens the resist and also improves its adhesion [133]. Depending on the photoresist used, a post-bake may also be necessary to promote the chemical reactions that were initiated by light exposure. In some cases, due to the interference, the light exposure can lead to non-uniform resist activation, which is called standing-wave effect. Post-bake can help to mitigate this effect.

To finalize the pattern in the resist the soluble regions of the photoresist get removed by the use of a specific chemical developer supported by ultrasonic treatment [132]. For the development of AZ MIR 701, the AZ 726 MIF Developer was used. It is a metal-ion-free (MIF) aqueous alkaline developer based on tetramethylammonium hydroxide (TMAH). The development get stopped and the samples get cleaned by the subsequent washing in deionized water.

3.2.2. Ion beam etching

Ion beam etching (IBE), also known as ion milling, is an etching method that belongs to the category of dry etching. Dry etching is based on plasma-assisted processes and can achieve much more directional etching profiles compared to wet etching, which relies on chemically active liquids with an isotropic etching effect [135, 136]. Dry etching methods can be categorized into processes where plasma is directly generated in the etch chamber, called plasma etching, and ion beam etching, where an ion beam is generated in an ion gun and directed towards the sample.

The etching process in both cases can consist of a physical and a chemical component. The physical component arises from sputtering caused by high-energy noble gas ions. The chemical component can be additionally introduced through chemically active species, such as CF_4, which, upon dissociation, form highly reactive radicals. These radicals can induce strong material-specific selectivity in the etching rates [135]. Because the radicals are electrically neutral, they are not accelerated by electric fields; instead, they move by diffusion and, in the case of an ion beam, additionally through the collective gas flow towards the sample. This process is referred to as

reactive ion beam etching (RIBE). In this work, however, only IBE using argon was employed, carried out with an Ionfab 300plus system from *Oxford Instruments*. To ensure a sufficient mean free path for ionic motion, the process is carried out in a vacuum chamber.

For IBE, the noble gas must first be ionized in the ion gun and then accelerated by an electric field to a defined kinetic energy. As the source of the ion beam, a radio-frequency inductively coupled plasma (RF ICP) was used. The ions are then extracted and accelerated by an accelerator grid. To prevent contamination of the ion beam with material from the accelerator grid, which is often made of graphite, the accelerator grid is further protected by a screen grid [136].

After exiting the acceleration stage, the ion beam is neutralized by a filament-less beam neutralizer, which emits electrons. This neutralization does not result in recombination of the ions with the electrons; rather, it primarily serves to maintain charge neutrality of the ion beam. Consequently, the beam profile does not deform due to space charge, and the impact of the ion beam remains charge-neutral, preventing charge buildup on the sample [136].

The ion beam then strikes the substrate, causing etch rates on the order of nanometers per minute. For homogeneous etching by the atomic beam, the substrate is continuously rotated during the process to compensate for beam inhomogeneities. Furthermore, to minimize temperature-related effects caused by etch-induced heating—particularly to prevent photoresist hardening or reflow, the sample holder is cooled from the backside. Efficient heat transfer between the water-cooled cooling block and the rotating sample holder in the vacuum chamber is achieved by introducing helium gas at the backside to fill the gap between the sample holder and the cooling block.

After the etch process the remaining photoresist has to be stripped. This happens by an ultrasonic treatment in a special remover chemical or in standard solvent like acetone, isopropanol or dimethylsulfoxid (DMSO). Subsequent mechanical swabbing can be used to reduce fences, which may form at the edges of the resist due to re-deposition during etching.

3.3. Rapid thermal processing

Thermal treatments for crystallization are carried out in an RTP-100 rapid thermal annealing process oven with vacuum system from *Unitemp*. This system is able to purge the processing chamber of ambient air by pumping it down to a vacuum of 1 mbar. Thermal processing can be conducted in a defined gas atmosphere consisting of different process gases, such as N_2, O_2 N_2+H_2. The gas mixture can be controlled using mass flow controllers.

Heating is provided by an array of infrared lamps with a total power of 20 kW, enabling heating ramps of up to 200 K/sec for 4 " wafers. Cooling after a thermal process can be achieved by water cooling of the chamber and nitrogen flushing of the sample, thus enabling cooling rates of 200 K/min in the temperature range from 1200 °C till 400 °C and 30 K/min from 400 °C till 100 °C.

For the crystallization of PCMO, the chamber is first flushed with nitrogen, then pumped down to 3 mbar, and subsequently filled with nitrogen up to atmospheric pressure. Using a heating ramp of 100 K/sec and continuous nitrogen flushing, the sample is heated to 650 °C. The temperature is then held for 120 sec. Afterwards, the sample is cooled by nitrogen flushing and chamber cooling at the maximum achievable cooling rate.

3.4. Process flow for device fabrication

The following device fabrication was used for the samples in chapter 5 and 6 and is based on the papers [1] and [3].

The substrates of the samples were either 4-inch Si wafers or 1 cm × 1 cm fused silica pieces. Before use, the 4-inch silicon wafers were thermally wet oxidized, resulting in an insulating layer

of approximately 430 nm SiO_2. When a bottom electrode was used, a 5 nm Ta adhesion layer was deposited by RF sputtering, followed by 25–40 nm Pt by DC sputtering.

For the PCMO deposition, PLD was used with a fluence of 2.5 J/cm^2 and an oxygen pressure of 1 Pa. For the samples in Chapter 5, PLD was conducted only at room temperature. For the samples in Chapter 6, PLD was performed at two different substrate temperatures: room temperature and 400 °C. Many of the PCMO depositions at 400 °C, along with the analysis of film thickness and surface morphology by AFM, as well as subsequent device fabrication, were carried out by Zhenhao Liu as part of his master's thesis, which was supervised as a direct part of this PhD project. After deposition, the samples grown on wafers were diced into 1 cm × 1 cm pieces.

If a memristive device was prepared, AlO_x was deposited on top of the PCMO by 200 W reactive magnetron RF sputtering of aluminum under a 1 Pa oxygen–argon atmosphere (3:2 Ar:O_2 flow rate mixture). The AlO_x layer was subsequently covered by a top electrode of approximately 20 nm Pt, deposited by DC magnetron sputtering. For the DC conductivity analysis or the PEEM investigation, the Pt top electrode was directly sputtered in a spatial pattern using a direct-contact shadow mask.

If a device stack was deposited, subsequent rectangular pad electrode structures were fabricated by patterning with a positive lithography process and dry etching with an argon beam . The pad sizes were 20 µm × 20 µm, 50 µm × 50 µm, and 100 µm × 100 µm.

To further electrically contact the devices, the shared Pt bottom electrode was accessed via wedge bonding using a tungsten wire to an external Pt-covered substrate. The structured pad top electrodes were contacted by flexible tungsten needles embedded in a micro-manipulator system equipped with an optical microscope. Electrical characterization was carried out using a Keithley 2611A source measurement unit.

3.5. Scanning probe microscopy

3.5.1. Atomic force microscope

To characterize surface morphology, particularly surface roughness, of deposited or processed layers, as well as to determine layer thickness at lift-off edges, Atomic Force Microscopy (AFM) was employed. The measurements were performed using a FlexAFM system from *Nanosurf*.

AFM determines the surface morphology by measuring the interaction between a sharp tip and the sample surface [137, 138]. The tip typically has the shape of a pyramid with a small triangular base and elongated lateral faces, two of which are usually slightly conical. The critical feature of the AFM tip is its apex, where interaction with the sample occurs; this apex has to be manufactured with nanometer precision. In this work, a PPP-NCHR-20 tip from *Nanosensors* was used, with a typical tip radius of less than 7 nm. The tip is mounted on the backside of a cantilever structure, which is attached to a support chip. Due to its long, thin, and narrow geometry, the cantilever behaves like a flexible spring. The spring properties of the cantilever have to be tailored for the specific measurement mode, for which the tip is used in the AFM.

The interaction between tip and sample surface can be broadly divided into two regimes: long-range attractive forces arising from van der Waals interactions and short-range repulsive forces due to Pauli repulsion [139]. These interactions between the tip and the sample surface are measured in the AFM by the cantilever deflection method, using an optical system. A laser beam is aligned to the backside of the cantilever and reflected toward an optical detector. Any bending of the cantilever changes the reflection angle, which is then detected. To measure spatial variations of the reflected beam, a position-sensitive photodetector is employed. Such detectors are typically segmented, and the relative signal differences between the segments provide information about the position of the reflected beam [140].

To systematically raster-scan the sample surface during measurement, actuators are employed for precise control of the lateral scanning motion, typically providing movement ranges from several hundred nanometers up to tens of micrometers. This can be achieved either with a tube piezo element, which allows large horizontal displacements through tube deflection, or with a flexure-based XY scanner. In this work, a flexure-based XY scanner was used. To control the tip-sample distance during approach, withdrawal, and fine adjustments, throughout the scan, piezoelectric actuators with sub-ångström precision are required. For this purpose, either the extension and contraction of a tube piezo element or a separate piezo-based Z actuator can be employed [141].

To measure surface topography, different measurement methods can be used, which are categorized into static and dynamic AFM. In static AFM, the force on the tip is measured directly through the cantilever deflection method. However, this approach was not employed here, as it can cause abrasion of both the sample surface and the tip apex, typically resulting in a short tip lifetime [142]. Instead, dynamic AFM was used, in which the cantilever is driven into forced oscillation by an oscillator. The tip-sample interaction is then probed through changes in the amplitude and phase of the cantilever oscillation, measured with a lock-in amplifier. The lock-in amplifier reads out the signal from the position-sensitive photo detector, using the oscillator signal as a reference [143].

Dynamic AFM can be conducted in two different modes, depending on the oscillation amplitude of the cantilever. In amplitude modulation mode, the oscillation amplitude of the cantilever is set to be small, on the order of the range of the tip-sample interaction forces. These forces can then be described as a secondary spring acting on the cantilever spring, thereby shifting its resonance frequency [143].

In tapping mode, the oscillation amplitude of the cantilever is set much higher than the range of the tip-sample interaction forces. As a result, the sample surface is probed by damping of the cantilever amplitude when the tip intermittently taps the surface [144]. Since this mode significantly reduces tip wear, all surface scans in this work were conducted in tapping mode. Tips designed for this method are typically stiff; their high spring constant and the resulting high resonant frequencies (around 300 kHz in this work) help reduce the influence of noise on the measurement.

During scanning, the tip-sample distance is adjusted so that the oscillation amplitude of the tip is damped to a defined value, corresponding to a specific tip-sample separation. A PID-based control unit continuously regulates the tip height to maintain this set amplitude. The resulting height variations required for this adjustment directly represent the surface topography and are used to construct the height profile from the raster scan.

3.5.2. Scanning tunneling microscopy and spectroscopy

Besides the mechanical interaction between a tip and a sample, electronic interactions can be investigated using Scanning Tunneling Microscopy (STM). This technique is based on measuring the tunneling current between an atomically sharp tip and the surface of a conducting sample. Since the tunneling probability through the vacuum barrier, determined by the work functions of the tip and sample, is highly sensitive to the tip-sample distance, the tunneling current primarily arises from the atoms of the tip closest to the sample. The tunneling current, arising from the overlap of the wavefunctions of the tip apex and the sample surface atoms, is effectively localized to these atoms, thereby enabling atomic-scale resolution [138]. Thus a STM can measure the surface of a conducting sample with higher accuracy than an AFM. For this work, a low-temperature (LT) STM from *Createc* was used.

The most common mode for scanning the sample surface is the constant-current mode. For a constant applied voltage V_T, a predefined tunneling current I_T is maintained by adjusting the tip-sample distance. To continuously adjust this distance throughout the raster scan, a piezoelectric actuator with a PID-based feedback loop, similar as in an AFM, is typically employed.

Models of varying complexity describe the tunneling current as a function of the applied voltage, the tip-sample distance, and the electronic structure of both the sample and the tip. The relative height adjustments required to maintain the tunneling current represent the sample's topography. The strong (exponential) dependence of the tunneling current on the tip-sample distance enables atomical vertical resolution [145]. Since the local conductivity respectively the local density of states, influences the tunneling current as well, the measurement is always a convolution of local conductivity and the actual topography.

Tunneling currents can be extremely low, down to the pA range; therefore, low-noise transimpedance amplifiers are typically used to convert the current into a measurable voltage [146]. Noise can be further reduced by minimizing mechanical vibrations through mechanical decoupling from the environment and by lowering thermal noise via low-temperature operation. In this work, the LT-STM chamber was cooled to approximately $5\,\mathrm{K}$ using liquid helium..

Tungsten was chosen as the tip material because it is a mechanically hard metal that can be electrochemically etched for tip fabrication. A 0.3 mm tungsten wire was electrochemically etched in a 2 mol/L NaOH solution with the DC drop-off method. The conical shape with a sharp apex forms at the NaOH/air interface due to the interplay of capillary wetting and etching processes, in a self-adjusted process [141]. After fabrication, the tip was cleaned and sharpened by applying short high-voltage pulses which promotes atomic rearrangement at the apex and removes contaminants. Reference scans on gold surfaces and surface electronic states were further used to ensure tip quality and to calibrate the STM voltage scale.

The exact shape of the voltage-current characteristic $I_T(V_T)$, and in particular its derivative $\mathrm{d}I_T/\mathrm{d}V_T$, can be used to investigate the electronic structure of the sample, a technique known as Scanning Tunneling Spectroscopy (STS). For STS measurements, the feedback loop for the height adjustment is typically disabled. The electronic structure is probed at a fixed point on the surface with at a constant tip-sample distance and the tunneling current and its derivative is recorded by voltage scanning. Instead of numerically deriving $\mathrm{d}I_T/\mathrm{d}V_T$ from the measured $I_T(V_T)$ data, which is highly sensitive to noise, the differential conductance can be measured directly by superimposing a small AC modulation on the bias voltage during the $I_T(V_T)$ sweep. The amplitude of the resulting current oscillation is proportional to $\mathrm{d}I_T/\mathrm{d}V_T$ and is extracted from the I_T signal using a lock-in amplifier [147].

To study the electronic structure of a sample through the voltage dependence of the tunneling current, and its differential conductance, a tunneling model must be employed that considers the exact form of the quantum-mechanical wave functions in both the sample and the tip. Typically, the Bardeen model is used for this purpose. It separates the system into two quantum-mechanical subsystems tip and sample and describes the tunneling current between them using a perturbative approach based on the time-dependent Schrödinger equation, including the application of Fermi's golden rule.

The dependence on the wave functions can be reduced to an energy dependence with respect to the Fermi level ϵ, which, under the low-temperature approximation, leads to the following expression for the tunneling current:

$$I_T = \frac{4\pi e}{\hbar} \int_0^{eV} \rho_{\mathrm{tip}}(\epsilon - eV)\, \rho_{\mathrm{sample}}(\epsilon)\, |M(\epsilon)|^2 \,\mathrm{d}\epsilon, \tag{3.1}$$

where $\rho_{\mathrm{tip/sample}}$ denotes the density of states and $M(\epsilon)$ the transition matrix element [145].

The transmission factor can be further simplified by approximating the matrix element for a rectangular tunneling barrier, characterized by the average work function $\frac{\Phi_{\mathrm{tip}}+\Phi_{\mathrm{sample}}}{2}$ of the tip and the sample. In this case, the participating wave functions of tip and sample decay exponentially

within the tunneling barrier, leading to the following expression for the transmission factor:

$$T(\epsilon, V, d) = |M(\epsilon)|^2 \propto \exp\left(-2d\sqrt{\tfrac{2m}{\hbar^2}\left(\tfrac{\Phi_{\mathrm{tip}}+\Phi_{\mathrm{sample}}}{2} + \tfrac{eV}{2} - \epsilon\right)}\right), \tag{3.2}$$

where d denotes the tip-sample distance [145].

Measuring the differential conductance thus probes

$$\frac{\mathrm{d}I}{\mathrm{d}V} = \frac{4\pi e^2}{\hbar}\,\rho_{\mathrm{tip}}(0)\,\rho_{\mathrm{sample}}(eV)\,T(eV, V, d), \tag{3.3}$$

which reflects the density of states of the sample and the tip, as well as the transmission function [147].

Assuming a constant density of states of the tip and only a weak variation of the transmission factor at low voltages leads to a further simplification:

$$\frac{\mathrm{d}I}{\mathrm{d}V} \propto \rho_{\mathrm{sample}}(eV), \tag{3.4}$$

so that the differential conductance can be considered a direct measurement of ρ_{sample} at eV, relative to the Fermi level [147]. However, since the transmission factor causes a significant increase in $\mathrm{d}I/\mathrm{d}V$ at higher voltages, analyzing the normalized differential conductance $(\mathrm{d}I/\mathrm{d}V)/(I/V)$ can help to separate ρ_{sample} from this background [147].

3.6. X-rays based structural analysis

3.6.1. X-ray reflectometry

X-ray reflectometry (XRR) is a standard method, used to measure the thickness of deposited thin layers. It was measured by the oscillation in the reflected X-ray intensity from a Cu source ($\lambda = 1.54$ Å) during a coupled 2θ-ω scan at small 2θ angles, up to around $5°$. The X-ray beam is parallelized (collimated) and mainly reduced to K_α radiation by a Göbel mirror and directed onto the sample at an angle ω, in a parallel beam geometry at a D8 diffractometer from *Bruker*.

After passing through the Göbel mirror, the beam is shaped into a rectangle by optical slits. The length of the rectangle lying within the plane of reflection is reduced to around 0.1 mm to minimize the footprint on the sample at small ω, while the length orthogonal to the plane of reflection is kept at approximately 1 cm, matching the sample size, in order to increase the signal-to-noise ratio.

Before the scan, the beam is aligned parallel to the surface of the sample. Consequently, the beam geometry at the sample can be described by Figure 3.2a, where $\omega = \theta$ due to the coupled scan.

The reflected X-ray beam at 2θ is measured by a silicon strip detector with a limited opening of 0.075 mm to improve the angular resolution. To adjust the intensity of the reflected X-ray beam to the detector's sensitivity, an automated absorber is placed in the beamline in front of the sample. Its absorption coefficient is known and is automatically accounted for in the measured intensity by the software.

The measurement profile $I(2\theta)$ contains various information about the material stack, such as the density of the individual layers, the interfacial roughness, and the thickness of each layer. This information can be extracted from the measurement data by fitting a material model using the program GenX, which implements the physical description of X-ray reflection based on the Parratt formalism [148]. To reduce the degrees of freedom and thus simplify the fitting process, usually only a single layer is deposited on a thick substrate with well-known density and low surface

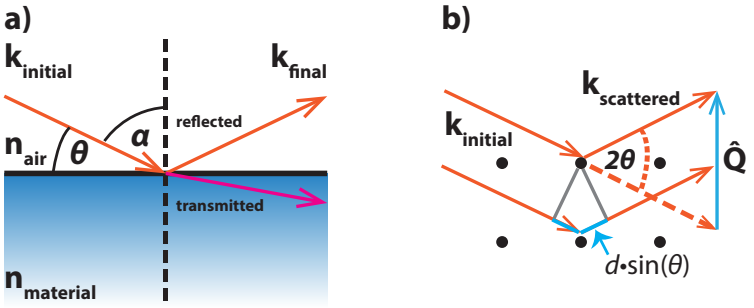

Figure 3.2.: a) Geometrical considerations for X-ray reflection at the sample's surface. b) Bragg reflection at the crystal lattice plane.

roughness. In this case, the density and thickness of the layer can be easily extracted from the XRR profile.

The information about the material density can be primarily obtained from the critical angle of total reflection, θ_c, which is the maximum angle up to which the X-ray reflection originates only from the sample surface. At angles below θ_c, the beam cannot penetrate the sample due to total external reflection, and only a non-energy-transmitting evanescent wave extends into the sample. The critical angle is approximately proportional to the square root of the electron density, $\theta_c \propto \sqrt{\rho_e}$, where ρ_e is the electron density of the material.

The angle of total reflection can be derived from Snell's law at the boundary, according to which the diffraction angle $\alpha_{\mathrm{air/material}}$, measured with respect to the surface normal, can be expressed as

$$n_{\mathrm{air}} \cdot \sin(\alpha_{\mathrm{air}}) = n_{\mathrm{material}} \cdot \sin(\alpha_{\mathrm{material}}) \tag{3.5}$$

where n_{air} and n_{material} are the respective refractive indices [149].

The angle of total reflection is the critical angle, $\theta_c = 90° - \alpha_{\mathrm{air}}$ (see Figure 3.2a), at which $\alpha_{\mathrm{material}}$ approaches $90°$. If α_{air} falls below this angle, Snell's law can no longer be satisfied with a real solution, and the resulting complex solution describes the properties of the evanescent wave.

Since $n_{\mathrm{air}} \approx 1$, n_{material} must be slightly smaller than 1 . The refractive index of the material can be approximated by a classical electromagnetic model, according to which the interaction of the electrons with the electromagnetic wave, at a frequency above the plasma frequency, is given by

$$n_{\mathrm{material}} = 1 - \frac{r_e \lambda^2 \rho_e}{2\pi}, \tag{3.6}$$

where r_e is the classical electron radius, λ the X-ray wavelength, and ρ_e the electron density [150]. Combining Equation 3.5 and 3.6 at θ_c leads to $\theta_c \propto \sqrt{\rho_e}$.

For angles $\theta > \theta_c$, the X-ray beam splits into a reflected beam and a beam transmitted into the material. The transmitted beam can subsequently be reflected or transmitted again at the second interface of the material. Since the refractive index depends on the electron density, a contrast in electron density between the two material is required for the interface to be visible in XRR. The superposition of the two reflected beams produces interference oscillations, known as Kiessig fringes, which can be used to determine the layer thickness. For interference to occur, the difference in the momentum transfer $\Delta|\mathbf{Q}|$ of both beam matches the constructive interference condition due to the difference in path length given by the thickness d of the layer:

$$\Delta|\mathbf{Q}| = \frac{n2\pi}{d}, \tag{3.7}$$

where n is a normal number [150].

The momentum transfer $\mathbf{Q}$ for a single beam is defined as the difference in momentum between the incident and the scattered X-ray, $\mathbf{Q} = \mathbf{k}_{\text{initial}} - \mathbf{k}_{\text{final}}$. Geometrically, the length of this vector in the reflection plane is given by

$$|\mathbf{Q}| = \frac{4\pi}{\lambda} \sin(\theta), \tag{3.8}$$

which directly relates it to the reflection angle θ [150]. According to Eq. 3.7, the angular spacing $\Delta\theta$ between adjacent thickness fringes decreases with increasing layer thickness. Using laboratory-based equipment, layer thicknesses from a few nanometers up to around one hundred nanometers can be measured.

The roughness at each interface influences the ratio of diffusely scattered X-rays to those undergoing specular reflection. The higher the roughness, the lower the reflected intensity and the greater the amount of diffuse scattering. As a result, the intensity ratio between the minima and maxima of the fringes is reduced.

The exact physical model used to simulate an XRR curve for given material parameters with GenX, as well as the algorithm employed to fit this model to experimental data, is described in the program documentation and references [148].

3.6.2. Grazing incident X-ray diffraction

X-ray diffraction (XRD) is used to investigate the atomic structure of crystalline layers, in which the atoms are arranged on a regular lattice with lattice vectors $\mathbf{R}$. Families of parallel lattice planes can be constructed, such that for each family of planes every lattice point $\mathbf{R}$ lies on one of these planes [151]. XRD allows the measurement of the interplanar spacing d between the planes. A useful way to uniquely identify all families of parallel lattice planes in a lattice $\mathbf{R}$ is through its reciprocal lattice $\mathbf{G}$, which is defined by the condition

$$e^{i\mathbf{G}\cdot\mathbf{R}} = 1 \tag{3.9}$$

[151].

Every reciprocal lattice vector $\mathbf{G}$ is a normal vector to a family of parallel planes passing through the lattice points. The length of $\mathbf{G}$ is related to the interplanar spacing d by

$$|\mathbf{G}| = \frac{2\pi n}{d}, \tag{3.10}$$

which corresponds to the spacing d/n between these parallel planes [151]. The shortest reciprocal lattice vector $\mathbf{G}$ in each direction corresponds to the family of planes with $n = 1$, where every plane contains a lattice vector $\mathbf{R}$, thereby directly identifying the lattice distance d [151].

When a crystal is illuminated with a parallelized X-ray beam, each family of atomic lattice planes produces a reflection at a specific angle θ (Figure 3.2b), known as Bragg reflection. Bragg reflections occur when the so-called Laue condition is satisfied, which states that the change in momentum of the X-ray during reflection, $\mathbf{Q} = \mathbf{G}$, equals a reciprocal lattice vector. Combining the Laue condition with Eq.3.10 and Eq.3.8 leads to

$$2d\sin(\theta) = n \cdot \lambda, \tag{3.11}$$

which is known as Bragg's law [152].

To measure the Bragg reflections of a thin layer, XRD is performed under grazing-incidence conditions (GI-XRD). The X-rays are collimated by a Göbel mirror and directed onto the sample at a fixed grazing-incidence angle. This angle must be chosen slightly above the critical angle of total reflection, θ_c, so that, according to Snell's law (Eq. 3.5), the propagation direction of the

X-rays inside the sample is nearly parallel to the surface. This makes the measurement highly surface sensitive and therefore well suited to probe thin layers. To record the intensity of the X-rays reflected from the lattice planes, the detector is scanned along the 2θ angle. To increase the measured intensity, the opening of the silicon strip detector is maximized to $14.325,\text{mm}$, and to improve the signal quality an equatorial Soller is used to filter out divergent X-rays.

In XRD, only those crystallites of the sample contribute to the signal whose lattice-plane normal vectors are oriented such that the incident and diffracted beams satisfy the Bragg condition for reflection from the lattice planes. In GI-XRD, the incident angle θ remains fixed during the measurement while 2θ is scanned. As a result, the lattice-plane normal vectors being probed rotate during the scan, so crystallites with different spatial orientations are measured at different 2θ values. Therefore, GI-XRD is only suitable for highly polycrystalline samples, which contain crystallites with all spatial orientations.

Alternatively, a standard XRD scan, by a 2θ-ω scan, can be conducted, in which the incident angle of the beam ω and the detector angle 2θ are varied simultaneously. In this case, the orientation of the lattice-plane normal vectors being probed does not change during the measurement, and only crystallites of a fixed orientation are measured. To reduce the contribution from crystallites with other orientations, the detector slit opening is minimized, and the spectral profile of the Göbel-mirror-collimated beam is further improved by an additional monochromator. This measurement type is particularly suitable for studying the relationship between an epitaxial grown film and its substrate. However, since this thesis investigates the crystallinity of polycrystalline thin layers, only GI-XRD was used.

3.6.3. Grazing incident total X-ray scattering

The principle of total X-ray scattering is to measure and analyze the scattering of a sample over a wide $\mathbf{Q}$-range. This includes the Bragg peaks, if the sample is crystalline, as well as the diffuse scattering background [153]. To measure at high $|\mathbf{Q}|$ values, according to Equation 3.8, scattering data must be collected up to high angular regions. Most importantly, since $|\mathbf{Q}|$ scales with $1/\lambda$, the X-ray wavelength used must be as short as practical. However, because the cross-section for coherent elastic scattering decreases with increasing X-ray energy, the use of shorter wavelengths is practically limited by the resulting reduction in scattering signal [154]. By using high X-ray intensities available at a beamline together with a 2D X-ray detector, it is possible to measure a wide $\mathbf{Q}$-range of the scattering spectrum within less then a second [155]. This enables the study of temporal dynamics, for example structural changes induced by temperature variations such as crystallization. To achieve surface sensitivity, similar to the GI-XRD method described in the previous section, total X-ray scattering can also be measured at grazing-incidence angles around the angle of total external reflection. This approach even allows the measurement from thin layers only a few nanometers thick [155]. The experimental details of the total X-ray scattering experiments performed are described in Chapter 6.2.3.

The measured intensity $I(\mathbf{Q})$ must be corrected for signals not originating from the sample. This is typically achieved by subtracting a background measurement performed on the bare substrate. Furthermore, from the scattered intensity of the sample, all contributions must be removed that do not arise from single coherent scattering events. These include non-elastic processes such as absorption, as well as elastic but non-coherent scattering contributions, which are described by the Laue monotonic diffuse-scattering term [154]. The remaining coherent intensity, $I_C(\mathbf{Q})$, is then azimuthally integrated and expressed as a function of the magnitude of the momentum transfer vector, also denoted as $I_C(\mathbf{Q})$.

Based on the Born approximation, the scattering amplitude of singly coherently scattered X-rays

$$\Psi(\mathbf{Q}) = \frac{1}{\langle b \rangle} \sum_{\nu} b_\nu e^{i\mathbf{Q}\cdot\mathbf{R}\nu} \tag{3.12}$$

is given by the sum over all atomic positions $\mathbf{R}\nu$, weighted by their scattering strengths b_ν, also referred to as the atomic scattering amplitudes. This expression therefore provides direct access to the real-space atomic arrangement [156]. Because X-rays interact only weakly with matter compared to electrons, the fraction of singly coherently and elastically scattered X-rays is high in the scattering signal. Therefore the scattering of X-rays can be well described by the Born approximation.

The measured intensity $I_C(\mathbf{Q}) \propto |\Psi(\mathbf{Q})|^2$ is related only to the squared magnitude of the scattering amplitude,

$$|\Psi(\mathbf{Q})|^2 = \frac{1}{\langle b \rangle^2} \sum_{\nu,\mu} b_\nu b_\mu e^{i\mathbf{Q}\cdot(\mathbf{R}\nu - \mathbf{R}\mu)}, \tag{3.13}$$

and thus the direct phase information is lost in a standard measurement. Only relative phase differences between the scattering contributions of different atoms can be accessed [156]. This information can be used to determine correlations of atomic distances within the sample, which are described by the atomic pair distribution function (PDF). The PDF provides a probabilistic description of the short-range order, similar to a histogram [153, 157]. Further details on the data correction and PDF calculation are given in Chapter 6.2.3.

3.7. Photoemission based analysis

3.7.1. (X-ray) photoelectron spectroscopy

Photoelectron spectroscopy (PES) is a technique used to study materials by measuring the kinetic energy spectrum of electrons emitted due to photoelectric effect [158]. X-ray photoelectron spectroscopy (XPS) can be used to determine the binding energies of core-level electrons. For this purpose, synchrotron radiation is often employed, or alternatively, smaller laboratory-based equipment may be used. In this work, a Versa Probe 5000 from *Physical Electronics* was used, which employs Al K_α radiation with an energy of 1486 eV. Ultraviolet radiation can also be used, often employing He I with 21.2 eV, for investigations focused on the valence band edge or the work function (UPS) [159].

To capture the emitted photoelectrons, the measurement is carried out in a vacuum chamber, and the electrons are extracted from the sample by an electron optic with a specific extraction voltage. A typical way to measure the kinetic energy is by using a hemispherical analyzer. It consists of two concentrical hemispherical electrodes which, due to their electric bias, force the electrons passing through to follow a deflected trajectory. Only electrons with a kinetic energy equal to the pass energy of the analyzer will traverse it and be counted by a subsequent electron detector [160, 159]. To select electrons of a specific kinetic energy, the extracted electrons can be further accelerated or decelerated. By sweeping this acceleration or deceleration, the entire spectrum of kinetic energies can be measured.

In an experimental setup the sample and the photo-detector are electrically connected, thus the Fermi level within the system are typically assumed to be aligned. Binding energies E_B are then measured in reference to the Fermi level in the material. Thus the energy necessary to remove an electron from the material into vacuum is the sum of its binding energy and the work function of the sample Φ_S. Consequently the kinetic energy of an electron excited by a photon of energy of

$h\nu$ is

$$E_{\mathrm{kin}} = h\nu - \Phi_{\mathrm{S}} - E_{\mathrm{B}}. \tag{3.14}$$

However, the sample is in electric contact with the electron analyzer with the work function Φ_{A}. If the sample is conducting then the Fermi level of sample and analyzer are aligned. Thus the kinetic energy gets effected by difference of the work function, and the kinetic energy measured with the analyzer is

$$E_{\mathrm{kin}} = h\nu - \Phi_{\mathrm{A}} - E_{\mathrm{B}} \tag{3.15}$$

[161].

If the sample is strongly insulating, the Fermi levels of the analyzer and the sample do not align [162]. Moreover, the removal of surface electrons can cause a spatial build-up of charge, which reduces the measured kinetic energy. To compensate for this charge accumulation, an electron flood gun is often used to provide low-energy electrons for charge neutralization. However, the use of a flood gun can lead to spatially inhomogeneous charge compensation. To address this limitation, a dual-beam system is often employed, combining an electron flood gun with a low-energy ion source. The use of ions, often argon, must be considered carefully, as they can affect the surface through damage or reduction [162].

The process of the electron emission can be conceptual separated into three steps [163]:

1. Generation of photoelectron
2. Translation of the electron from the place of generation to the surface of the sample
3. Leaving of the sample surface by overcoming the work function

In the first step, the generation of photoelectrons occurs within a relatively large volume of the sample. However, only those photoelectrons generated close to the sample surface reach the surface in the second step and possess sufficient energy to overcome the work function in the third step.

Particularly valuable for material analysis are electrons, which do not experience inelastic scattering in the second step, since they retain information about the binding energy of specific core electrons.

The depth from which these electrons originate, relative to the sample surface, is characterized by the inelastic mean free path (IMFP, λ_{mf}), which depends strongly on the kinetic energy of the electrons. The IMFP is defined as the path length λ_{mf} over which the electron intensity $I(z)$ decreases to $1/e$ of its initial value [158], described by

$$I(z) = I_0 \exp(-z/\lambda_{\mathrm{mf}}). \tag{3.16}$$

At electron energies up to a few keV, the mean free path is on the order of nanometers or less, making XPS a highly surface-sensitive technique that probes only the first few nanometers of a sample.

The energy dependence of the IMFP has a roughly similar shape for all types of materials, which is referred to as the universal curve [158]. Since the universal curve increases with higher kinetic energy, X-rays of higher photon energy can be used to probe photoelectron generation from deeper regions within the material. Another common approach to access photoelectrons originating from different depths is to vary the take-off angle at which electrons are extracted. Electrons traveling at an angle θ relative to the surface normal have an increased path length of $z \cdot \cos(\theta)$ within the material. Therefore, electrons detected at a take-off angle normal to the sample surface can originate from deeper regions, whereas at shallow take-off angles the detected electrons primarily originate from the near-surface region [164].

Core levels exhibit an energetic splitting due to the coupling of the spin (s) and orbital (l) angular momenta. The two resulting states, $j = l \pm s$, have an intensity ratio determined by their multiplicity, $2j + 1$ [165]. The binding energy of a core electron is influenced by the chemical environment of the atom, a phenomenon known as the chemical shift [166]. In particular, the bonding and the resulting valence the atom affect its core level energy. Generally, a more positive valence state leads to reduced screening of the core electrons, resulting in a higher binding energy, whereas a more negative valence state increases screening and lowers the binding energy. Such changes are especially relevant in the context of memory devices based on the valence change mechanism, which can be studied using this technique [8].

Since binding energies are measured relative to the Fermi level, they can also be used to detect shifts of the Fermi level, if it is aligned with the detector. For example, the position of the Fermi level relative to the valence band edge can be determined by subtracting the measured core-level energy from the measured difference between the core level and the valence band edge, which is independent of the Fermi level position [167].

Using this approach, band bending at a material interface near the surface can be studied through depth-dependent XPS measurements. Depth dependence can be achieved either by varying the take-off angle (as described earlier) [72] or by modifying the thickness of the surface material, for example through successive deposition [167] or etching and measuring.

While only elastically scattered photoelectrons are typically analyzed to study core levels, inelastically scattered electrons can also provide valuable information about a material, depending on the excitation mechanisms. Excitation features can be extrinsic, arising during the movement of the electron through the material, or intrinsic, occurring during the generation of the photoelectron [168, 169]. Characteristic excitation processes lead to specific energy losses, giving rise to so-called satellite peaks in the core-level spectra. Energy loss features can be related to plasmon excitations, leading to plasmon loss peaks. Or excitation in the electronic structure of the atom, for instance, a shake-up peak arises from a discrete electronic excitation accompanying the emission of a core-level electron, while a shake-off process promotes an electron into the valence band, producing a broad tail toward lower kinetic energies. Metals, in particular, exhibit strongly asymmetric peaks due to excitations into the unoccupied states of the conduction band above the Fermi level [161]. In insulators, the onset of inter-band transitions depends on the material's band gap, meaning that the associated energy-loss features can be used to extract information about the band gap.

3.7.2. Photo electron emission microscopy

Photoelectron Emission Microscopy (PEEM) is the spatial analysis of a sample's surface based on the emission of photoelectrons. For this purpose, a PEEM column based on an electrostatic lens system is commonly used [170, 171, 172]. If the extracted electrons are also energetically filtered, PEEM can additionally be used for spatially resolved electron spectroscopy.

In this work, a NanoESCA system from *Scienta Omicron NanoTechnology* and *Focus GmbH* is used [173, 174]. In its PEEM column, the electrons pass through several optical elements and are subsequently energetically filtered by an anti-symmetric tandem arrangement of hemispherical analyzers. Electron extraction in the PEEM column begins with an electrostatic immersion lens. The extractor aperture is positioned very close to the sample surface (1.8 mm), and the sample is immersed in the strong electric field of the anode (12 kV). This field enables the collection of electrons across all emission angles, even those with high kinetic energy. Since the parallel crystal momentum $k_{\parallel}$ is conserved during the photoemission process, this results in a momentum-resolved distribution of photoelectrons in the back focal plane of the objective lens [175]. An aperture placed in this plane can be used to select specific regions of the captured k-space, thereby enhancing image contrast. The electron beam then passes through two stigmators, which

are connected by a transfer lens that corrects aberrations in both k-space and real space. Finally, after the second stigmator, an iris aperture allows the selection of specific real-space regions of the electron image.

In the following projection lens system, the retardation optics reduce the electron energy to match the pass energy range of the subsequent hemispherical analyzer (HSA) and project the beam into the energy analyzer. The energy analyzer is based on an anti-symmetric tandem arrangement of two hemispherical analyzers. This configuration, known as an imaging double energy analyzer (IDEA), enhances the energy resolution compared to a single HSA. For a single HSA, the energy resolution scales with the pass energy but is ultimately limited by the spherical aberration term (α^2), which originates from the angular dispersion of the incoming electrons. In an IDEA the dispersion of the electrons get corrected by the second HSA, nearly canceling the influence of the α^2-term on the energy resolution [174]. With a contrast aperture of 1 mm and a pass energy of 100 eV, the NanoESCA system used here achieves an energy resolution with a full width at half maximum (FWHM) of 0.4 eV.

The NanoESCA can be used to measure work function differences if a UV mercury lamp is employed as photon source [176]. The mercury lamp emits strongly at around 4.9 eV, with photons extending up to 5.3 eV. As a result, photoelectron excitation occurs at energies close to the work function, and this measurement principle is referred to as threshold emission. The electrons emitted with the lowest kinetic energy, measured relative to the Fermi level, can be used to determine the work function of the material, as described in more detail in Chapter 6.5.1. However, the precision of the measured work function is limited by the energy resolution and can be further affected by the high electric field of the extractor lens, which lowers the work function due to the Schottky effect. For the lens configuration used here, this reduction is approximately 0.1 eV [176].

3.8. Optical characterization

3.8.1. Spectrophotometer

A photometer measures the intensity of light, while a spectrophotometer measures the intensity as a function of wavelength. In this work, a Lambda 950 spectrophotometer from *PerkinElmer* was used to measure the reflectance R (in %) and transmittance T (in %) of samples in the ultraviolet, visible, and near-infrared regions (UV-vis-NIR). These data can then be used to analyse the band gap of a material, as described in detail in Chapter 6.5.3.

For the measurements, two different types of light sources were employed. For the visible and infrared regions, a tungsten-halogen lamp was used, which emits continuous blackbody type radiation. For the ultraviolet region, a deuterium discharge lamp serves as light source, which emits a continuous spectrum in the UV range due to dissociation emission [172].

One of the two light sources is selected by a mirror system equipped with an optical filter and subsequently coupled into a double monochromator. The second monochromator effectively suppresses stray light generated in the first, thereby enhancing the spectral purity of the selected light. Each monochromator is based on a grating.

The monochromatic light beam is then rapidly alternated between two beam paths using a system based on an optical chopper and a beam splitter. This setup, known as a dual-beam spectrophotometer, compensates for temporal fluctuations of the light source by alternately measuring the beam passing through the sample and the reference beam [172].

The transmitted or reflected light from the sample, as well as the reference beam, is collected by an integrating sphere and measured by a photodetector. The integrating sphere, also called an Ulbricht sphere, serves to capture both the direct beam and the diffusely scattered light. For transmission measurements, the sample is positioned at the entrance of the integrating sphere, whereas for reflectance measurements, it is positioned at the exit port of the sphere.

3.9. Electrical characterization

Unless noted otherwise, all electrical measurements presented in this thesis were performed with a Keithley 2611A source measure unit from Keithley Instruments, operated as a voltage source while simultaneously recording the device current, with a lower measurable current limit of about 100 pA.

3.10. Elemental analysis

3.10.1. Inductively Coupled Plasma Mass Spectrometry

Elemental analysis of the samples was conducted using inductively coupled plasma mass spectrometry (ICP-MS). This technique combines ionization in an inductively coupled argon plasma with element-selective detection via mass spectrometry. Because the ICP-MS setup used requires the sample to be in solution, the analyzed films were first digested with acid. For the digestion procedures the samples were treated with HCl and H_2O_2 in a 3:1 ratio for 2 hours at 50 °C.

The resulting solutions are then introduced by a peristaltic pump into the nebulizer of the ICP-MS system. In the nebulizer, a high-velocity carrier gas, usually argon, produces a fine mist that enters a spray chamber [177, 178]. From there, the aerosol is transported through the inner tube of a concentric three-tube torch assembly, at the tip of which the plasma is generated by an inductively coupled current produced by a radiofrequency (RF) coil [179, 180]. The plasma is sustained independently of the inflow from the inner tube by an additional argon flow through the outer tube of the torch. The intermediate tube provides an auxiliary argon stream to further shape the plasma.

Within the plasma, which can reach temperatures of up to 10 000 K, the aerosol droplets are vaporized, atomized, and subsequently ionized. Argon, as the main plasma gas, has a relatively high first ionization potential of 15.8 eV compared to most other elements, and can therefore ionize the majority of elements in the periodic table. Elements whose ionization potentials exceed that of argon cannot be analyzed with an argon plasma. The degree of ionization can be estimated by the Saha equation. Under typical plasma conditions ($\approx$ 7500 K), the equation predicts ionization rates above 50 % for elements with first ionization potentials below 10 eV [180]. Most elements have a first ionization potential below 10 eV and a second ionization potential above, thus resulting often in over 90 % first ionization and a low degree of double charged species.

The resulting ion beam is then extracted in the so called interface region and guided into the low-pressure region of the mass spectrometer. The interface consists of two sequential cones, the sample cone and the skimmer cone, which have progressively smaller orifices. The orifice allow the extraction of the central region of the gas flow, which contains the ions. The use of two cones further allows a stepwise reduction of pressure by differential pumping [179, 181]. At the end of the interface, the ions are further separated from the beam of neutral atoms and photons by an electrostatic lens, which directs them along an off-axis trajectory through an additional orifice.

The design of the following mass spectrometric setup differ between the two used ICP-MS systems.

In the Agilent 7900, the ion beam is first guided through an octopole reaction system, where helium is used as a cell gas to reduce interferences in the mass spectrometric signal caused by polyatomic ions. In the presence of helium, the octopole acts as a collision cell. Since polyatomic ions have larger collision cross sections they lose more kinetic energy by the collision. These energetic, reduced ions are subsequently filtered out, a process known as kinetic energy discrimination [182, 183]. Afterwards the remaining ion beam is separated according to its mass-to-charge (m/z) ratio by a quadrupole analyzer and detected by an orthogonally aligned electron multiplier.

Compared to the Agilent 7900, the Agilent 8900 allows for the reduction of isobaric interferences. The system is based on a tandem configuration of quadrupole mass spectrometers with an octopole reaction cell positioned between them. This setup enables the removal of isobaric interferences by treating ions of a specific mass-to-charge ratio by chemical reaction with the cell gas [182, 183]. The ion–molecule reactions can selectively change the mass of the interfering ion or of the analyte. The resulting mass-shifted reactive analyte, or the unreactive analyte freed from interference by the reaction, can then be measured by the second quadrupole and electron multiplier. The reduction of isobaric interferences is particularly advantageous for samples with complex compositions or when strong interferences arise from matrix ions or other highly abundant species. Thus, higher selectivity and improved trace-level detection can be achieved.

In this work, the Agilent 7900 or Agilent 8900 was used depending on availability. To ensure that no systematic differences occurred between the measurements, the octopole of the Agilent 8900 was used only as a collision cell with helium gas, and the first quadrupole was not used for mass-to-charge dependent separation. Thus, the configuration of the Agilent 8900 was similar to that of the Agilent 7900.

4. Large area pulsed laser deposition

The in this Chapter written text was perviously published in *Thin Solid Films* Volume 805, 30 September 2024, with the title “Large area pulsed laser deposition of memristive $Pr_{0.7}Ca_{0.3}MnO_3$ heterostructures for neuromorphic computing”.

4.1. Consideration on the use of large-area PLD

Pulsed laser deposition (PLD) is a well-established technique for the epitaxial deposition of complex metal oxides in academic research [184, 185]. The deposition is typically performed on small samples 1 cm^2 in size [186, 187, 188]. However, PLD has not yet played a significant role in industrial thin film deposition on large wafers [189, 190]. A major issue for large-area deposition is the directional expansion of the plasma plume. Therefore, the effective deposition area is much smaller than a 4" or larger wafer [128]. It is necessary to use a scanning concept that achieves full wafer coverage of the deposited film [190, 191].

Each concept should address ensure a homogeneous ablation from the target material by moving the laser spot over the target surface. This is important to avoid distortions of the laser spot and ensure a homogeneous and reliable deposition. A challenge for the homogeneity of a layer deposited by PLD can be the pollution by droplets formed from molten target material. To prevent the formation of droplets, it is recommended to use dense targets with a sintering density close to the crystalline density [128] and sharply projected laser spots without spatial inhomogeneity of the fluence. Further important for a commercial use of PLD are fast deposition times which fulfill the requirements for an economic production process. Therefore the fluence control must consider the change in the transmission of the laser entrance window, and the laser entrance window must be easily replaceable [192]. The most important challenge in deposition over a full wafer is to stitch together the individual plumes in such a way that the film grows homogeneously across the entire wafer, which requires a strategy for coordinating the relative movement between plume and substrate. This is particularly challenging if the strategy needs to be easily adaptable for different deposition thicknesses, especially when the targeted film thickness is 20 nm or below.

Many different concepts are possible; until today, no single concept is considered the best. Rotating the substrate and scanning the ablation spot over a parallel-positioned target via mirror rotation is popular. The scan range over the target must be well-aligned to the radius of the substrate. Therefore, a homogeneous deposition can be achieved by scanning the laser spot along the target with varying speeds (faster scanning speed towards the center of the substrate) [191, 193, 194, 195]. A problem of this strategy is that the alternation of the projection angle by the mirror rotation changes the spot size on the target [192], which can influence the deposition rate and the stoichiometry [128]. Addressing this issue, there is a modified concept where the scanning of the laser beam happens at a constant projected angle by a translation movement of the beamline and a target with inclined positions towards the substrate surface [196].

However, the concept of two-dimensional scanning with linear movements is the most direct way to achieve a homogeneous deposition on a wafer. A major issue for this strategy is the broadening of the deposition plume as the distance between the target and substrate increases [197]. This broadening occurs in high vacuum due to plume self-interaction and is significantly increased due to scattering processes when a process gas is used. It is a problem for homogeneity since it causes higher deposition rates in the central areas of the wafer than in the edge areas when the

scanning motion doesn't allows much longer movement distances as the wafer is big.

To address the issue of plume broadening in this work, a slit system was used to localize the deposition region, thereby eliminating the need for excessive scanning. The first part of this investigates the effect of the slit system and process gas pressure on plume broadening. This investigation has been used to parameterize simulation software to assess the effectiveness of different movement speeds and to develop strategies for homogeneous deposition, adjustable to a chosen film thickness in the order of 20 nm. In the second part of this chapter, these strategies were used to fabricate area-dependent switching memory cells on a standard 4" Si wafer using the material combination of $Pr_{0.7}Ca_{0.3}MnO_3$ and AlO_x.

4.2. Details of the PLD system

A KrF excimer laser is used with a 100 Hz repetition rate to reduce the process time. The high number of shots for a single deposition (order of 100,000 shots per sample) leads to deposition on the laser entrance window, which causes a relevant change in the optical transmission after a few depositions. This effect is stronger with lower process gas pressure. Two features are installed to handle this issue. The first feature is a thin quartz glass slide mounted inside the chamber in front of the entrance window for protection. These slides are getting exchanged by an in-vacuum working magazine system with space for 10 exchange glass slides. Furthermore, the energy measurement for the fluence control includes the change in the transmission of the glass slides. Therefore, the target gets moved to the side during the energy measurement, and the laser beam leaves the chamber through an additional exit window. This exit window is covered during the deposition.

The laser beam is projected onto the target by the beamline, which is mounted entirely on rails to maintain a constant distance throughout the movement. On the beamline, the beam is first slightly focused by a convex lens to correct for the divergence of the excimer beam. Directly behind the lens is the aperture, which shapes the beam profile rectangular with a size of 22 mm $\times$ 10 mm The shaped beam is then guided by the two mirrors through two further lenses. First, a divergence lens increases the imaginary distance to the aperture, and then a focusing lens directly in front of the chamber entrance window projects the aperture onto the target. The resulting spot size has a rectangular shape of (2.28 - 2.39) mm $\times$ (1.22 - 1.60) mm, with the long side parallel to the cylinder axis, and is taken into account in the fluence control software with an average spot size of 0.034 cm^2.

The laser ablates a ceramic target, and the resulting plasma plume condenses on the sample surface. The used PCMO target had a density of 4.53 g/cm^3 (relative density of 86% [21]), and the used $SrTiO_3$ (STO) target had a density of 5.06 g/cm^3 (relative density of 99% [198]). The PLD system uses a cylindrical target (see Figure 4.1). The deposition process is controlled by two movements: one-dimensional scanning of the substrate and one-dimensional scanning of the laser beam line along the cylindrical surface of the target. The deposition of the full layer is achieved by combining these two movements. Homogeneous ablation of the target surface is achieved by rotating the cylindrical target and combining this with the one-dimensional movement of the laser beam.

To address the issue of plume broadening, a slit system was installed. The two-dimensional scanning consists of movements along two axes. Slits are mounted perpendicular to each axis of motion to confine the plume deposition to the aimed area. One axis is the movement of the substrate itself, which moves behind a fixed slit (Figure 4.1a). The slit is called a "heat shield slit" because it also protects the chamber from thermal radiation during high-temperature deposition. The second axis is the movement of the laser spot over the cylindrical target. The plume is confined along this axis by a slit that moves with the laser spot in the chamber (Figure 4.1b).

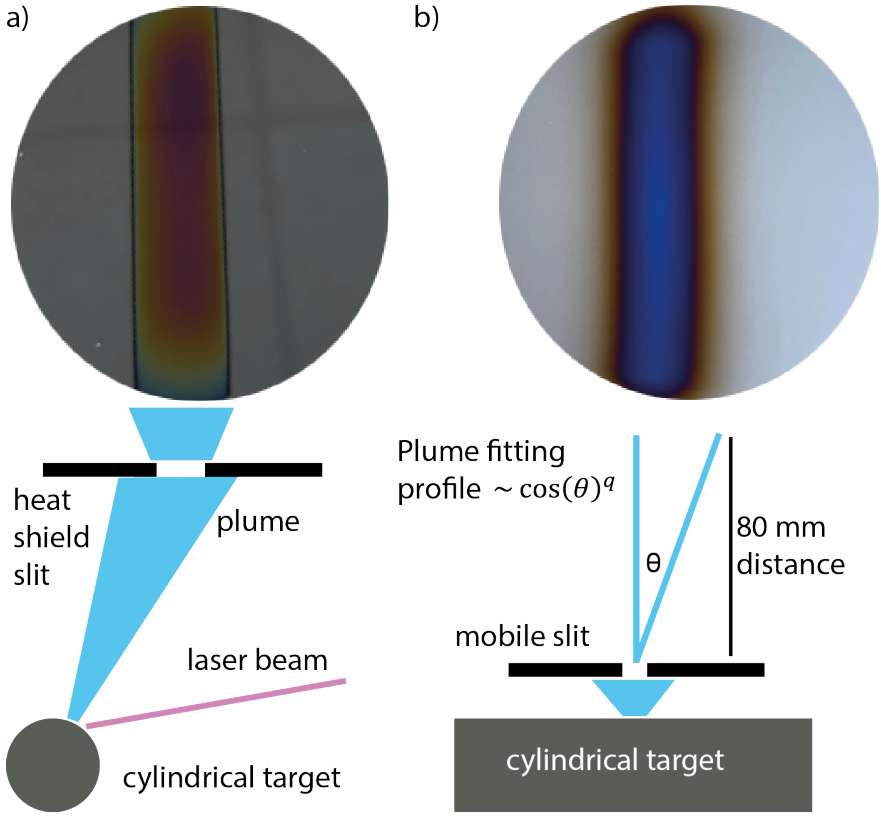

Figure 4.1.: Slit system for 2-dimensional scanning. a) Viewing direction on the cylinder base of the target. Image of a deposited film for exclusive movement of the laser spot, edges given by the heat shield. b) Viewing direction on the cylinder surface of the target. Image of a deposited film for exclusive movement of the substrate, edges given by the mobile slit.

To achieve this, the entire beamline is mounted on rails and moves during the process while maintaining focus.

4.3. Influence of slit system and working pressure

Figure 4.1a shows the image of a deposited film when only the beamline is moving. The edges are defined by the static slit, which is close to the substrate and therefore produces sharp edges. Figure 4.1b) shows an image of a deposited film when only the substrate is moved. The edges given by the moving slit close to the target are diffuse. As this slit is further away from the substrate, the confinement function is less pronounced. To tune the deposition, we investigated the influence of the slit further away from the substrate on the deposition profile, as its confinement function is less effective. First, the influence of slit width and oxygen pressure on the deposition rate was investigated. STO, as standard complex oxide material, was used as the target material to increase the applicability of our investigations to other complex oxides. Figure 4.2d shows that the deposition rates, determined by X-ray reflectivity measurements (XRR), are similar for most slit sizes. A noticeable decrease in deposition rate is observed for a slit width of 3.5 mm, which approaches the laser spot width of 2.5 mm. It is also evident that the deposition rate decreases at higher pressures, with vanishing rates above 5 Pa.

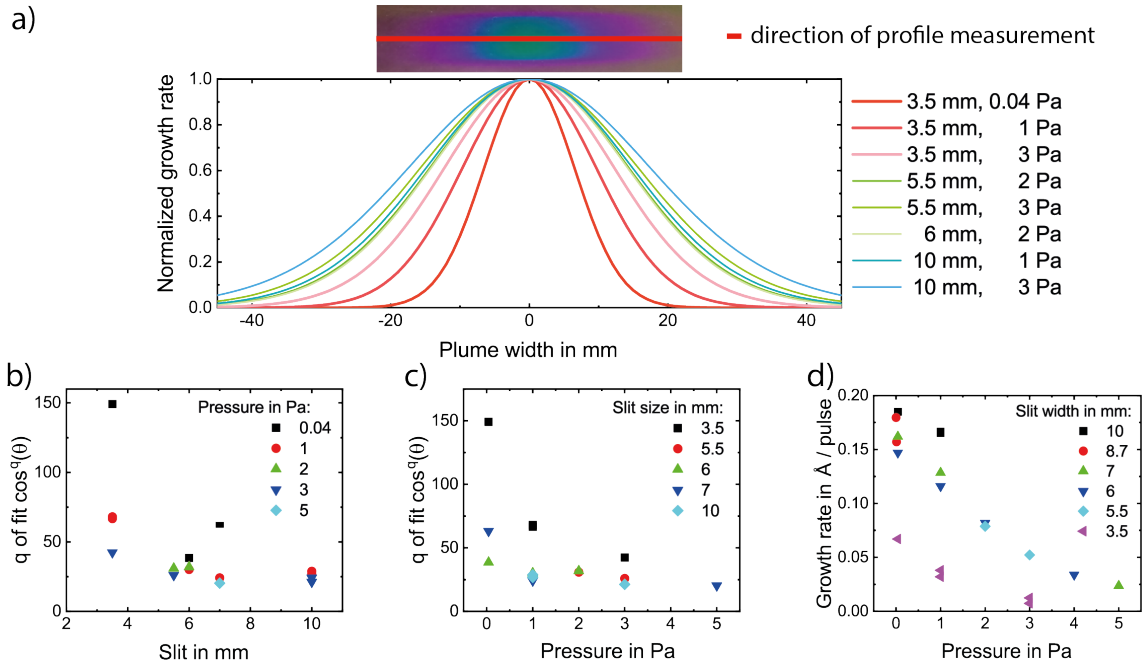

Figure 4.2.: Deposition rate in dependency of the slit width and the pressure and fitting of the deposition profile. a) Fitted $\cos(\theta)^q$ functions of the STO deposition profiles (measured by XRR). b+c) Fitted q values in dependency of the b) slit width variation and the c) O_2 process gas pressure. d) Maximum STO growth rate in dependency of slit width and pressure.

4.4. Parameterization of the simulation software

Using the knowledge of the pressure range of interest, we then characterized the deposition profiles of STO for different slit widths at different pressures with XRR and fitted them with the function $\cos(a + \tan^{-1}\frac{x}{80\,\mathrm{mm}})^q$ where a and q are the fitting parameter and $\tan^{-1}\frac{x}{80\,\mathrm{mm}}$ the angle θ for the used substrate- target distance of 80 mm, see Figure 4.2a, c, d. These profiles were then integrated into simulation software from the company *SURFACE*, which simulates deposition over the entire wafer for selected motion velocities Figure 4.3a, c. The simulation is a Python-based grid calculation. The development of the simulation program and the characterization of the STO layer were carried out by Marc Pohlmann from *SURFACE* as part of the NEUROTEC project collaboration. For each laser pulse, the positions of all motors will be calculated based on their velocities. On a width equal to the defined slit size around the resulting motor position, the deposition rate profile for the respective pressure and slit size is summed up on the grid. The result is a height distribution, either relative or absolute, depending on whether the deposition profile is given as normalized or nm/laser pulse.

4.5. Development of the simulation strategies for PCMO

The general configurations of the system in Section 4.3 and the software in Section 4.4 have been made using STO as a prototypical complex oxide material. It can be assumed that the general influence of slit size and process pressure on the deposition rate and deposition profile is similar for different oxides. The general configuration for STO and the specific development of the deposition strategies for PCMO ensure that the system is configured to be easily adaptable to different materials.

The software was used to develop strategies to achieve homogeneous deposition for PCMO

by selecting an appropriate combination of movement speeds. Since the difficulty of achieving homogeneity increases as the films get thinner, the strategies were developed for a typical layer thickness of 20 nm. Once a working strategy is established for a thin film, it is easier to adapt it to a thicker film.

Two strategies were developed. The most straightforward strategy (called here “strategy one”) involves moving the beamline quickly while moving the substrate slowly. Therefore, the simulation was conducted with the parameters (target length 98 mm, substrate length 106 mm, beamline velocity 20 mm/sec, target velocity 0.1 mm/sec, heat shield 20 mm, target distance 80 mm, q = 400, laser 100 Hz, and 2100 s). This simulation led to a low standard deviation of the thickness divided by the mean thickness of 0.07 %, taken and analyzed within the marked circle of Figure 4.3, which is lower than that of the second strategy shown in Figure 4.3c.

To verify this strategy, a deposition was conducted with parameters according to the simulation and a fluence of 2.5 J/cm^2 and 1 Pa O_2 as process gas pressure. The uniform growth of PCMO was then verified by spatially resolved XRR measurements along two orthogonal axes across the wafer, as presented in Figure 4.3b.

To determine the deposition profile, fitting of the XRR measurements was carried out at each position, as exemplarily illustrated in Figure 4.4. The fitting procedure was carried out using the software GenX 3.6.22 [148]. The multilayer stack was modeled with two layers, consisting of PCMO and SiO_2. For the lower SiO_2 layer, a density of 2.65 g/cm^3 was assumed. The fitting parameters were the interface roughness, surface roughness, PCMO density, and layer thickness. The count intensity was manually adjusted based on the count rate at total reflection. The fit was primarily optimized for the layer thickness by aligning the oscillation period. The measurement was conducted on a D8 diffractometer from *Bruker*, employing a Cu K-alpha source and Bragg-Brentano geometry. A 2 mm circular aperture was used to spatially restrict the beam.

A disadvantage of this deposition strategy is that only multiples of the minimum thickness can be deposited. In the case of Figure 4.3b, the deposition time was twice the running time of the substrate movement in one direction. Therefore, the minimum thickness for this process parameter is half of the thickness obtained. The minimum thickness is therefore slightly below 10 nm and cannot be arbitrarily reduced by increasing the substrate speed. If the substrate speed is too high, inhomogeneous thickness distributions will result due to the larger gaps between the stitched individual plume profiles.

To address the first strategic problem, we used the simulation software to develop combinations of fast beamline and substrate movements for a defined number of laser pulses that result in homogeneous deposition. An example of such a combination is given by the simulation shown in Figure 4.3c, employing the following parameters: target length 98 mm, substrate length 106 mm, beamline speed 5 mm/sec, substrate speed 20 mm/sec, heat shield 20 mm, target distance 80 mm, q = 400, laser 100 Hz, and 2000 s. However, the standard deviation of the thickness divided by the average thickness, taken from the marked circle, is 1.5 % and thus higher than that of the near-perfect simulation for strategy one (Figure 4.3a). The experimental verification for the homogeneous deposition using these movement combinations is shown in Figure 4.3d, by spatially resolved XRR measurements along two orthogonal axes across the wafer. The deposition parameters were chosen according to the simulation while using a fluence of 2.5 J/cm^2 and a process gas pressure of 1 Pa O_2. However, it is important to note that the movement speed must be adjusted for different numbers of shots and the corresponding film thicknesses.

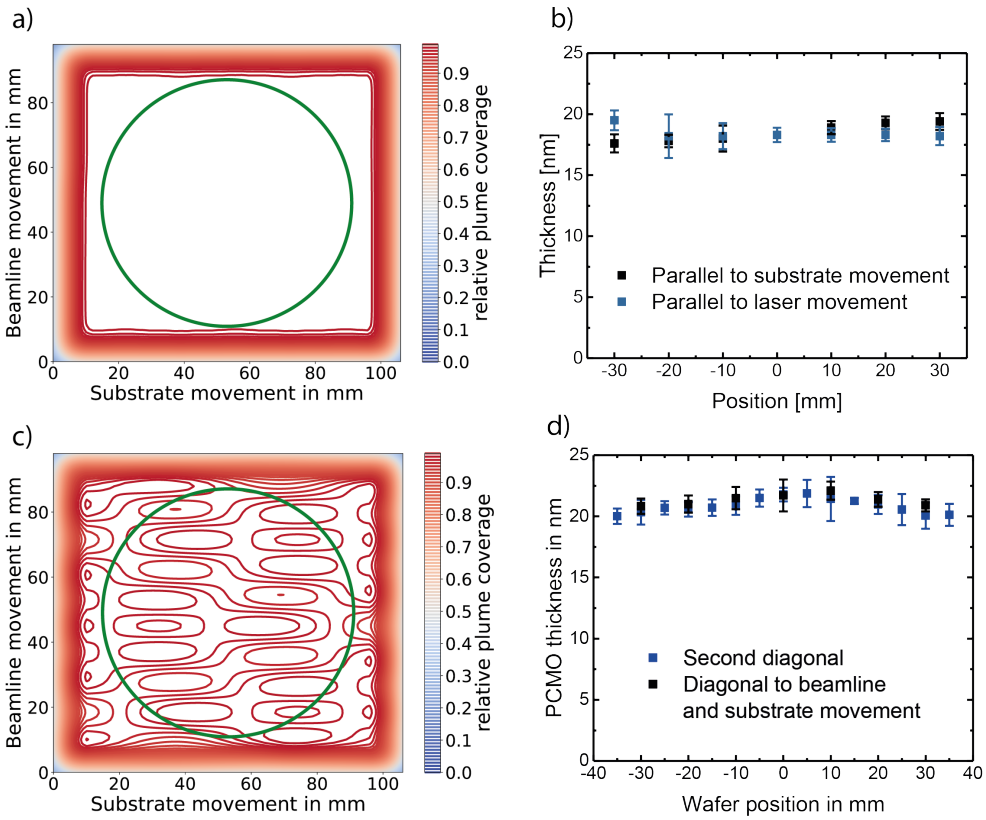

Figure 4.3.: Simulated deposition profiles a) and c) and corresponding measured deposition profiles b) and d). Figure a) and b) illustrate the incremental movement strategy, in which the beamline moves quickly while the substrate moves slowly. Figure c) and d) depict a dynamic movement strategy, where both axes move rapidly using an appropriate combination of movement speeds.

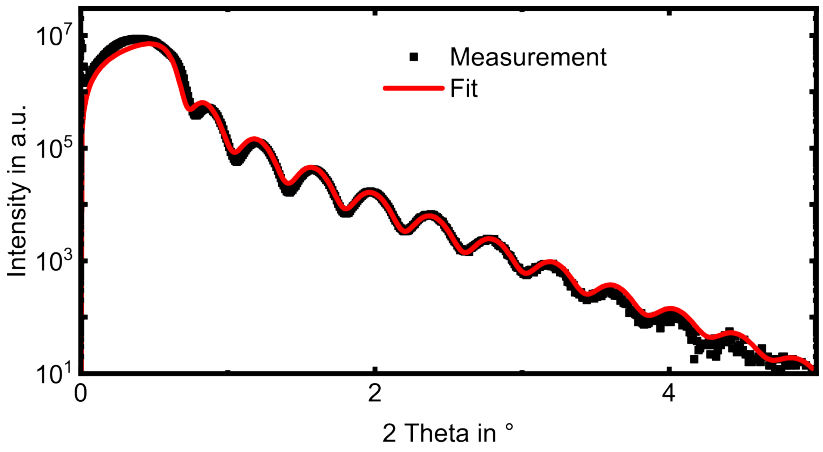

Figure 4.4.: Example of the fitting of XRR-data, as done for Figure 4.3 b) and d). The XRR data shown are from Figure 4.33d (measurement: second diagonal at 20 mm). The fitting led to the following material parameters (PCMO thickness: 21.0 nm, surface roughness: 0.6 nm, interface roughness: 0.7 nm, density: 4.6 g/cm^3).

4.6. PCMO stoichiometry

After developing the deposition process, the dependence of film stoichiometry on the deposition parameters was systematically analyzed. To assess the film stoichiometry, the films were dissolved from either the whole wafers or 1 cm $\times$ 1 cm diced pieces using an acid digestion procedure, as described in Chapter 3.10.1. The resulting solutions were subsequently analyzed by inductively coupled plasma mass spectrometry (ICP-MS), calibrated against an elemental standard.

To evaluate the influence of the fluence on the cation stoichiometry, depositions were performed without the slit system. Each deposition was conducted at an O_2 process gas pressure of 1 Pa with 500,000 laser shots. For the subsequent analysis, the whole wafer was used to dissolve the deposited material, thus the stoichiometry shown in Figure 4.5a represents an average over the full wafer. As shown in Figure 4.5a, the cation ratio exhibited only a weak dependence of the fluence. Nevertheless, the absolute amount of deposited material increased with increasing fluence, consistent with the expectation that higher fluence ablates more material from the target.

Furthermore, the homogeneity of the stoichiometry for the developed process with slit system was investigated for the deposition of PCMO on a substrate at room temperature (Figure 4.6a–c) and at 400 °C (Figure 4.6d–f) at O_2 process gas pressures of 0.7 Pa, 1 Pa, and 2 Pa. Each deposition was conducted at a fluence of 2.5 J/cm^2 with 212,000 laser shots. To examine variations in the cation stoichiometry, the wafer was diced into 1 cm $\times$ 1 cm pieces, and pieces along a line through the wafer center were analyzed. For Figure 4.6b, two orthogonal lines intersecting at the wafer center were investigated.

Figure 4.6 shows that the stoichiometry in the central region of the wafer is very homogeneous. A comparison between depositions at room temperature and at 400 °C indicates that the substrate temperature has only a minor effect on the stoichiometry. By contrast, for both temperatures the O_2 process pressure exhibits a strong influence. With increasing pressure, the deposited stoichiometry deviates more strongly from that of the target. This deviation can be explained by enhanced scattering of the ablation plume with the background gas, which affects the ionic species differently. The data clearly show that the relative ratio of Pr increases with pressure. This can be attributed to the fact that the trajectory of the relatively heavier Pr atoms (average atomic mass 141 u) is less affected by scattering compared to the trajectories of the lighter Ca and Mn atoms (average atomic masses 40 u and 55 u, respectively).

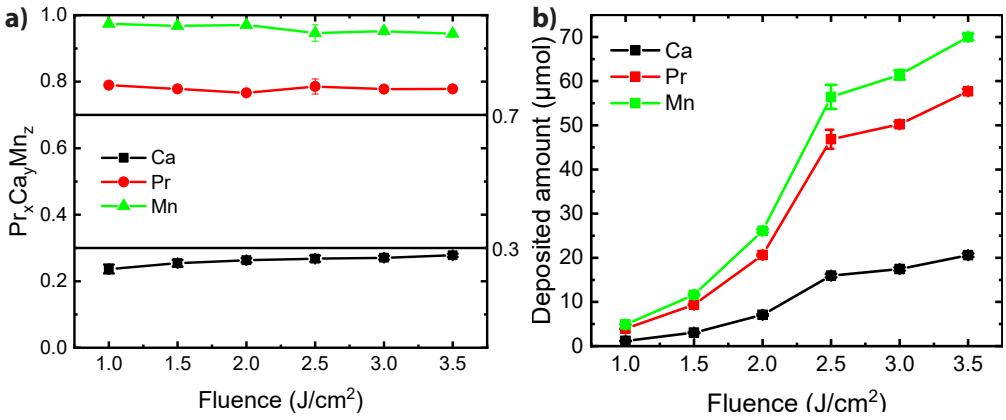

Figure 4.5.: a) Average cation stoichiometry on a 4" wafer as a function of fluence. b) Amount of deposited and digested cations as a function of fluence.

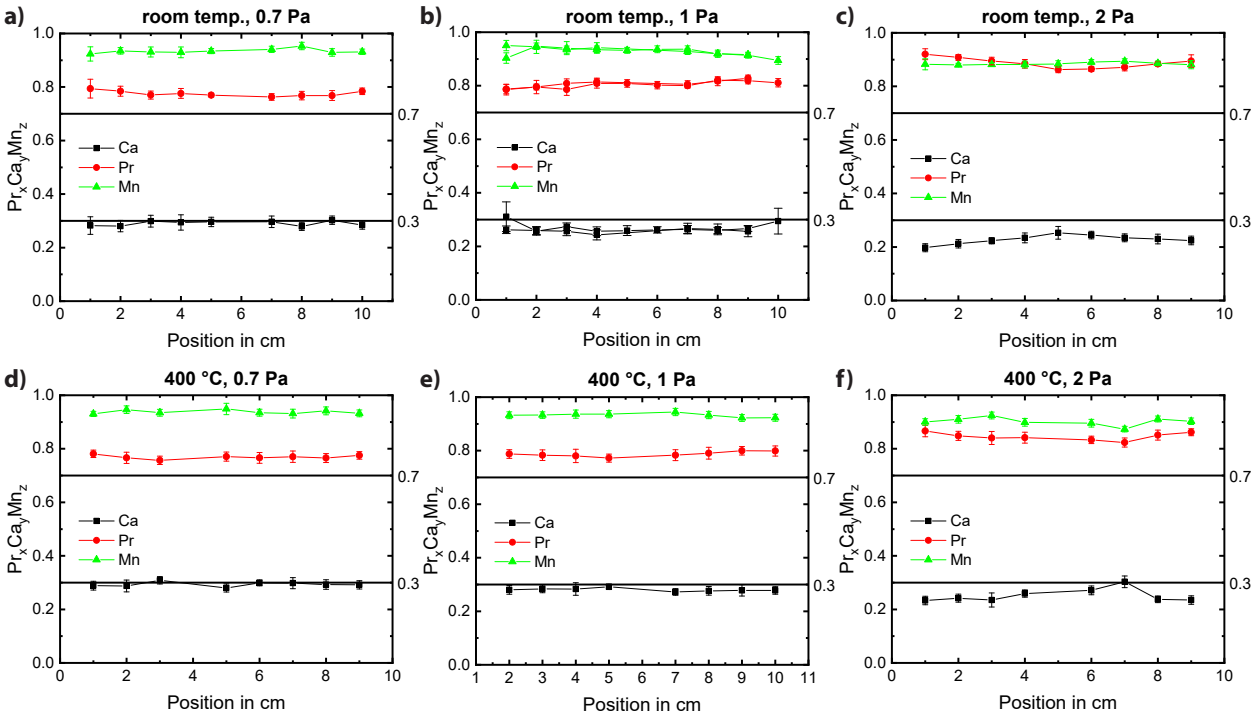

Figure 4.6.: Homogeneity of the cation stoichiometry across the wafer for deposition at room temperature a) till c) and at 400 ℃ d) till f). The stoichiometry was measured at oxygen process gas pressures of 0.7 Pa in a) and d), 1 Pa in b) and e), and 2 Pa in c) and f).

5. Devices based on low-conductivity amorphous PCMO

The text written in this Chapter was previously published in *Thin Solid Films* , Volume 805, 30 September 2024, with the title “Large area pulsed laser deposition of memristive $Pr_{0.7}Ca_{0.3}MnO_3$ heterostructures for neuromorphic computing”.

5.1. Interfaces and PCMO Stoichiometry

The homogeneous deposition process developed in the previous chapter for a 4" wafer was used to realize PCMO-based memristive devices, of which the schematic cross section is shown in Figure 5.1c. Therefore, the PCMO was deposited on the Pt coated thermally oxidized 4” Si Wafer with the following stack: 20 nm Pt/ 5 nm Ta/ 430 nm SiO_2/Si. The deposition parameters were: 2.5 J/cm^2 fluence, 1 Pa O_2 process gas pressure, 20 mm heat slit opening, 4 mm target slit opening, 100 Hz laser repetition rate, 100 rpm target-rotation, beamline movement from 4 to 104 mm at 20 mm/sec, substrate movement in step mode with a 0.25 mm step size at each turning point of the beamline, and background pressure 10^{-5} Pa.

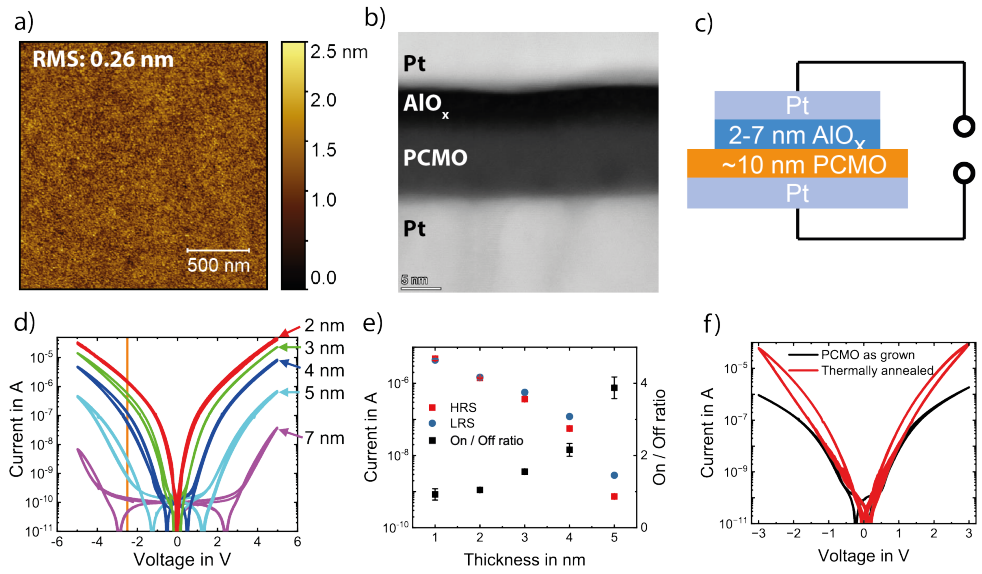

Figure 5.1.: a) AFM scan of about 10 nm PCMO deposited at 1 Pa O_2 on the Pt bottom electrode before dicing and stripping b) HAADF-STEM of the device cross-section with thermally treated PCMO and 5 nm AlO_x. c) Schematic device cross section. d) AlO_x thickness dependence of IV curves of 50 µm $\times$ 50 µm devices with non-annealed PCMO e) HRS, LRS and On/Off ratio extracted from d) at -2.5 V f) Comparison between 3 nm AlO_x device (50 µm $\times$ 50 µm) with and without thermal treatment

All the devices shown in this section are from the same wafer, deposited with the movement strategy two (Figure 4.3c+d) and by 50,000 shots, which led to a PCMO layer of around 10 nm,

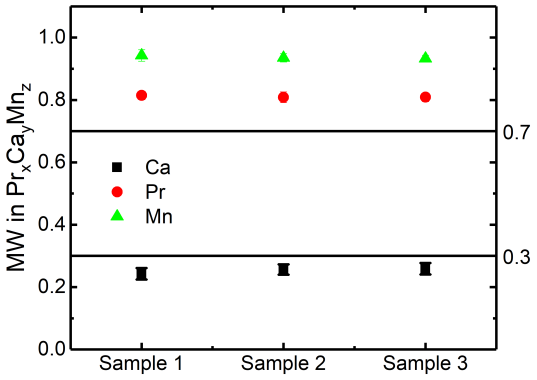

Figure 5.2.: Stoichiometry measurement of PCMO by ICP-MS.

as can be seen in the HAADF-STEM measurement of the cross-section of a device with thermally treated PCMO and 5 nm AlO_x(Figure 5.1b).

Further, inductively coupled plasma mass spectrometry (ICP-MS) was used to measure the stoichiometry of a similarly parallel processed wafer (same pressure, fluence, slit settings), with 212,000 laser shots to achieve a higher layer thickness. Therefore, the wafer was diced into 1 cm $\times$ 1 cm pieces, and three neighboring pieces from the homogeneous region were analyzed. To access the layer for the ICP-MS, it was dissolved by acid digestion through cooking for 2 hours at 323 K in 3 ml HNO_3 and 1 ml H_2O_2. Three aliquots in 20:1 and 10:1 dilution were taken from each sample for analysis. The ICP-MS was performed on an ICP-MS 8900 from *Agilent Technologies* by comparison with element standards. This analysis showed a homogeneous stoichiometry for neighboring pieces with average values of $Pr_{0.81}Ca_{0.25}Mn_{0.94}$ (Figure 5.2).

Since the switching effect occurs at the PCMO/AlO_x interface, a focus of the fabrication was to achieve a smooth interface between PCMO/AlO_x and AlO_x/Pt. Therefore, both PCMO and AlO_x must possess low surface roughness. Atomic force microscopy (AFM) showed that the PCMO surface roughness decreases with the oxygen process during the PLD (RMS values [0.2 nm, 0.3 nm, 2.9 nm, 8.3 nm] for [without process gas, 1 Pa, 4 Pa, 10 Pa], background pressure 10^{-5} Pa). The 1 Pa process was chosen for its smooth surfaces. An AFM scan of about 10 nm PCMO deposited at 1 Pa O_2 on the Pt bottom electrode before dicing and stripping is shown in Figure 5.1a.

The well-defined interfaces of the whole device stack can be seen in the high-angle annular dark-field scanning transmission electron microscope (HAADF-STEM) images (Figure 5.1b), where the signal is mainly due to Rutherford scattering from the sample. The HAADF-STEM cross-section shows a device with thermally treated PCMO and 5 nm AlO_x. The platinum electrodes appear in light gray because they exhibit the strongest Rutherford scattering due to the high atomic number of Pt (Z(Pt) = 78). The PCMO and the AlO_x are sandwiched in between. The PCMO is visible in darker gray (Z(Pr) = 59, Z(Mn) = 25, Z(Ca) = 20), while the AlO_x does not show strong scattering due to the low atomic number of its constituents (Z(O) = 8, Z(Al) = 13) and is therefore black.

5.2. Aluminum oxide sub-stoichiometry

The RF sputter deposition of aluminum oxide in a reactive gas atmosphere (3:2 (Ar:O_2) flow rate mixture) resulted in smooth oxide layers (RMS 0.2 nm - Figure 5.3e). The sputter deposition (Chapter 3.1.2) was done in a reactive gas atmosphere at 2 Pa with a gas mixture of argon and oxygen (3:2 (Ar: O_2) flow rate mixture) using alternating current (RF magnetron at 200 W), with a target substrate distance of around 10 mm and a sputtering time of 45 s.

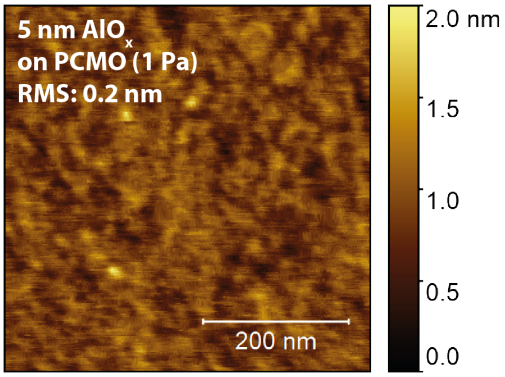

Figure 5.3.: Atomic force microscopy images show the surface of the 5 nm AlO_x sputter deposited on the, in Section 4.5 used, PCMO deposited at 1 Pa on Pt.

To investigate the oxygen stoichiometry of the AlO_x layer, XPS measurements were conducted on the Al 2p state (Figure 5.4 a and c) and on the O 1s state (Figure 5.4 b and d). Therefore, 5 nm AlO_x was directly sputtered onto thermally treated PCMO and then transferred directly from the sputter chamber to the XPS chamber under ultra-high vacuum conditions. The XPS analysis (Chapter 3.7.1) was performed with a PHI 5000 Versa Probe, using a monochromatic Al Kα X-ray source for photoelectron excitation, and an argon gun along with an electron gun for charge neutralization. The hemispherical analyzer used a pass energy of 187.85 eV for the survey scan of Figure 5.4 a and c, and 23.5 eV for the Al 2p peak scans of Figure 5.4 b and d. All spectra are from the same point and have been checked for reproducibility at a second point on the sample surface. Figure 5.4 a and b were taken at a detector angle of 80° from the surface plane and are therefore more depth sensitive than the spectra of Figure 5.4 c and d, which were taken at a surface sensitive angle of 30°.

X-ray photoelectron spectroscopy (XPS) on the AlO_x surface shows plasmonic loss features of the Al 2s and Al 2p peaks, as well as a mixed contribution of metal and oxide peaks at the Al 2p level (Figure 5.4).

For the data analysis, the program CasaXPS Version 2.3.24PR.0 was used. All spectra had been charge corrected by setting the aliphatic carbon peak to 284.8 eV. To fit the background, a Shirley background was used.

The metallic peaks had been fitted with an asymmetric peak shape of ST(1.3)LA(1,1.63,143) as recommended by [199]. The same peak shape was used to identify the asymmetric plasmon peak in the survey scans.

The oxide peaks have been fitted with GL(30), a symmetric product function of Gaussian and Lorentzian contributions, with a mixing ratio of 70:30. The following constraints were used for fitting the Al 2p spectra in Figure 5.4 b and d. As expected from the spin-orbit coupling, the area ratio for the 1/2 and 3/2 metal peaks and oxide peaks has been constrained to a 1:2 ratio. The FWHM of the corresponding multiplets is constrained to be equal. Furthermore, the energy difference of both multiplets is assumed to be 0.44 eV, as recommended by [199]. In Figure 5.4 a and c, plasmonic excitations can be identified, which are associated with electronic oscillation in the conduction band [200], and therefore are a sign of metallic contribution.

The peak fitting on the Al 2p spectra shows an increase in the oxide peak for the surface sensitive measurement, from a signal area contribution of Figure 5.4 b 23% at an 80° take-off angle to Figure 5.4 d 34% at 30°. The increased oxygen content at the surface could be explained by an additional oxidation reaction in the reactive gas atmosphere at the sample surface after the sputter deposition. The AlO_x is therefore considered a suboxide.

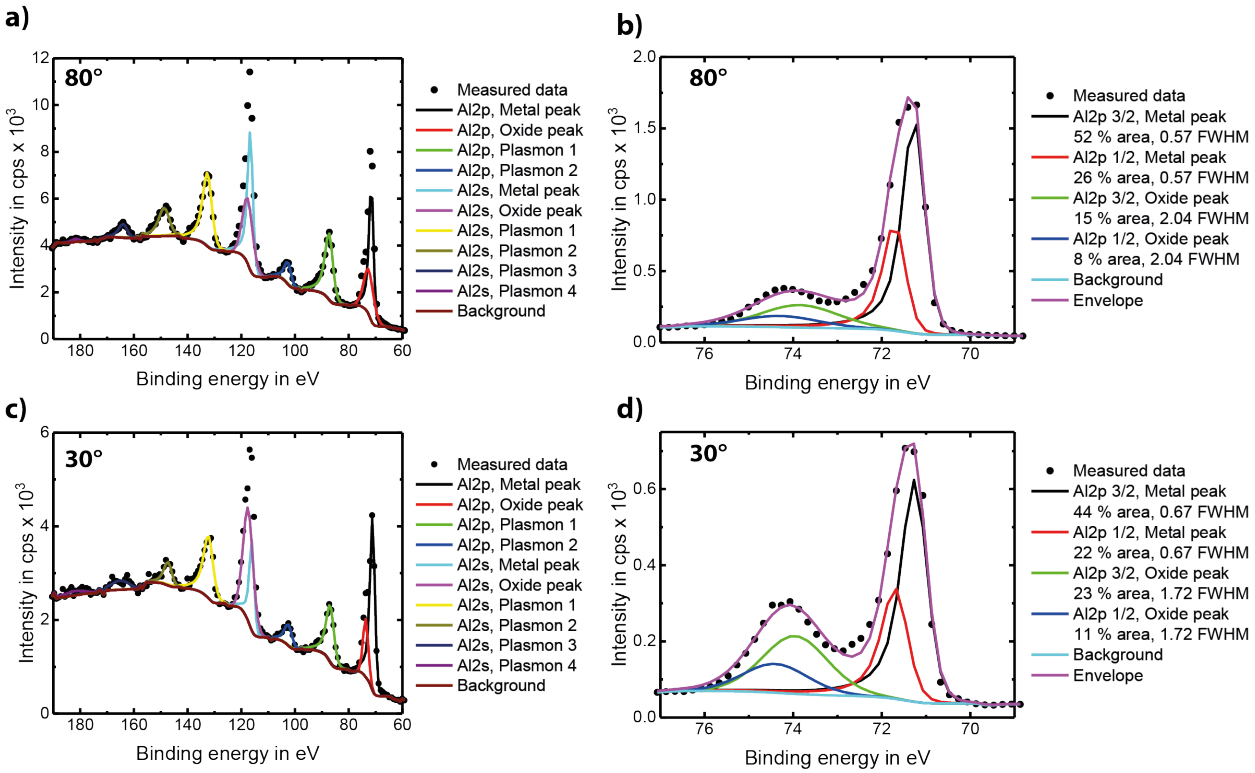

Figure 5.4.: XPS-spectra of 5 nm sputtered AlO_x on c-PCMO of the Al 2s level a) and c) and the Al 2p level at a more bulk-sensitive take-off angle of 80° in a) and b) and a more surface sensitive take-off angle of 30° in c and d.

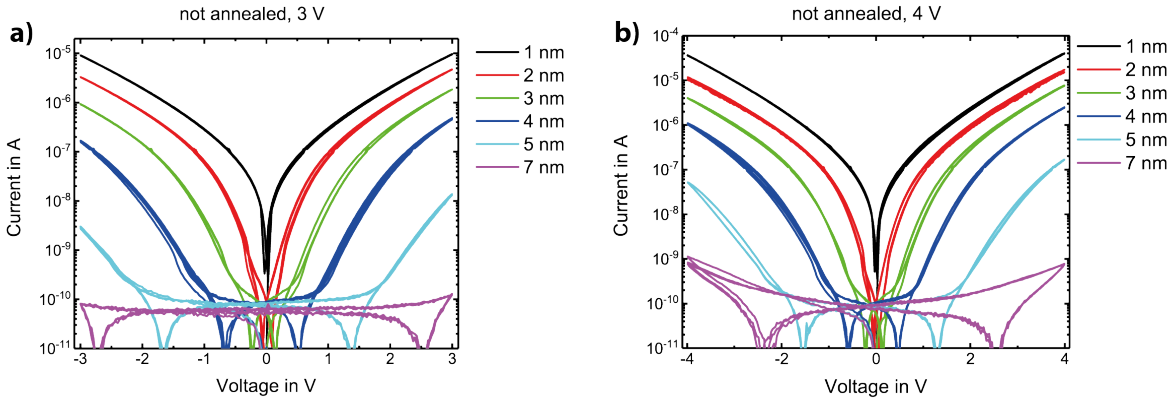

Figure 5.5.: AlO_x thickness dependence of $I-V$ loops for the not annealed PCMO devices with a pad size of 50 µm $\times$ 50 µm for a maximal applied sweeping voltage of a) 3 V and b) 4 V. The $I-V$ loops were measured with stepping rates of 30 mV and holding times of 20 ms at each voltage step, which led to an effective sweep rate of 1.5 V/s.

5.3. Device characterization

Figure 5.1d presents the current-voltage ($I-V$) characteristics of the devices as a function of the AlO_x layer thickness. Figure 5.1e displays the mean current values of the high-resistance state (HRS) and low-resistance state (LRS), determined from the $I-V$ curves in Figure 5.1d at the orange-indicated voltage of -2.5 V, along with the corresponding on/off ratio. The 7 nm sample is omitted because its charging is too large for readout at 2.5 V.

The $I-V$ curve exhibits hysteresis at an oxide thickness of 3 nm. The ratio of the current of the low resistive state (LRS) to the high resistive state (HRS) increases with increasing AlO_x thickness (Figure 5.4e) from 2 nm AlO_x (1.07 ± 0.13) over 3 nm (1.53 ± 0.19) and 4 nm (2.20 ± 0.42) up to 5 nm (3.90 ± 0.89) until the resistance becomes too high and charging dominates, as seen for the 7 nm layer. Sweep voltages of 5 V are necessary to clearly observe hysteresis, as evident from the comparison with the I-V characteristics measured with maximum sweep voltages of 3 V and 4 V in Figure 5.5a and b. A 3 V sweep does not produce any hysteresis, and the I-V opening that appears at 4 V is negligibly small.

Figure 5.6 shows the normalized decay of the LRS of the 5 nm AlO_x sample, measured on two devices with a (50 µm $\times$ 50 µm) pad. After different waiting times, the values were extracted at -3.2 V from $I-V$ sweeps. The device was set to the LRS for each time tested by three consecutive 5 V sweeps. The reference for the HRS is measured after the device has been set to the HRS by three consecutive +5 V sweeps. This retention measurement showed that the LRS is stable for 6 minutes. It shows serious decay after 1 hour and 13 minutes, and nearly complete decay after 21 hours.

Additionally, the endurance of the IV-cycling was evaluated. Figure 5.7 shows the $I-V$ loops of a sample with 5 nm AlO_x and amorphous PCMO. The first 100 cycles a) show a constant on/off ratio, while the HRS and LRS slowly increase. b) shows all 583 cycles, with device failure occurring after 579 cycles. The degradation of the devices led to a continuous increase in resistance until the LRS and HRS were indistinguishable. The graph was compiled from four measurement sets — cycles 1 to 100, 101 to 200, 201 to 400, and 401 to 583. Since the $I-V$ loops have charging contributions during sweeping, small discontinuities can be seen at the merging points (cycles 101, 201, and 401). All The $I-V$ loops were done without holding time at the voltage steps and with a step width of 100 mV to reduce degradation by shortening the measurement time. The pure measurement time of the Keithley 2611A source meter, delayed by communication with a

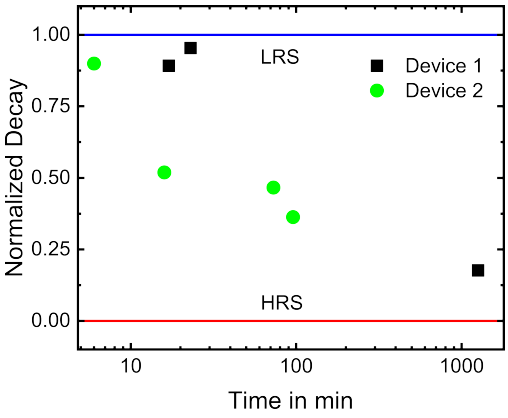

Figure 5.6.: The normalized decay of the LRS was measured on two devices with a (50 µm × 50 µm) pad, 5 nm AlO_x, and PCMO without thermal treatment.

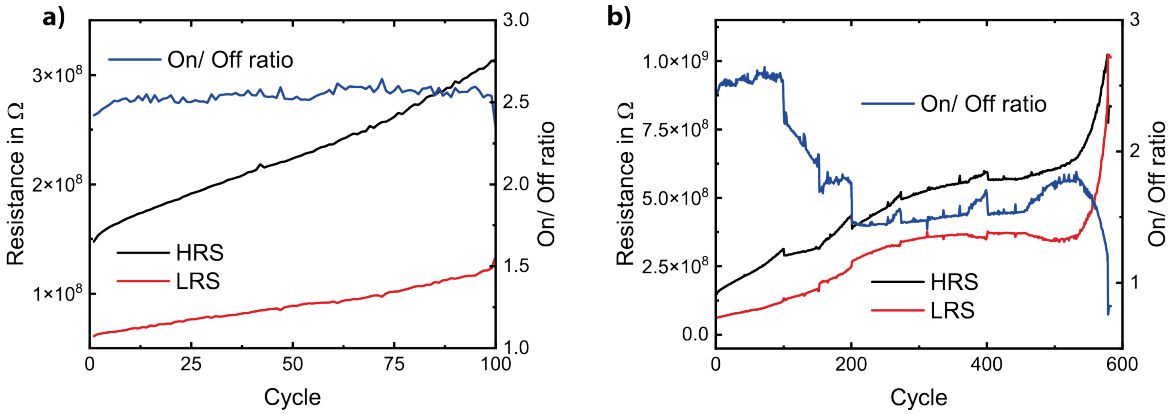

Figure 5.7.: Endurance characterization via I–V loops for the sample with a 5 nm AlO_x layer and amorphous PCMO, recorded at a read-out voltage of -4 V. a) presents the first 100 cycles, while b) displays all 583 cycles, with device failure occurring after 579 cycles. The complete dataset was compiled from four consecutive measurement sets: cycles 1–100, 101–200, 201–400, and 401–583.

LabView user interface, resulted in a sweep rate of around 3.3 V/s. The values were extracted from the $I - V$ loops at -4 V.

The reproducibility of the $I - V$ loops was shown by the measurement of the device to device variation presented in Figure 5.8. Therefore, the device-to-device variation was measured for ten different devices with (50 µm × 50 µm) pads, 5 nm AlO_x, and amorphous PCMO. Figure 5.8 a shows the comparison of the $I - V$ loops for one cycle per device, which was initialized by at least one previous cycle. Figure 5.8 shows the percentiles of the cumulative probability of the current plot of the HRS and LRS extracted from Figure 5.8 a at the voltage marked in orange. The double logarithmic reciprocal y scale was chosen in the style of a Weibull plot. The approximation of the percentiles was done using the Blom method. This analysis shows a clear separation of the HRS and the LRS.

All these devices in Figure 5.1d) have no thermal treatment of the PCMO and are therefore compatible with the backend of line processing in standard CMOS technology.

Further thermal treatment at 923 K for 2 minutes of the as-deposited amorphous PCMO causes crystallization, as shown by GI-XRD measurements in Figure 5.9. The measurements were conducted on 95 nm PCMO on Pt before and after thermal annealing for 2 minutes at 923 K in N_2.

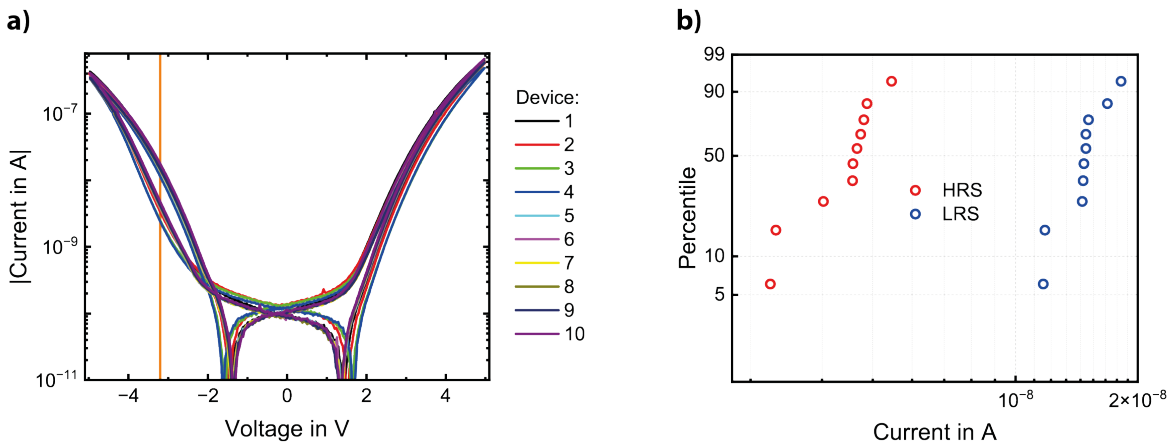

Figure 5.8.: Device-to-device variation measured on ten different devices with (50 µm × 50 µm) pad, 5 nm AlO_x, and amorphous PCMO. a) Comparison of the $I - V$ loops, with one cycle per device. b) quantile probability plot of the HRS and LRS extracted from a) at the voltage marked in orange.

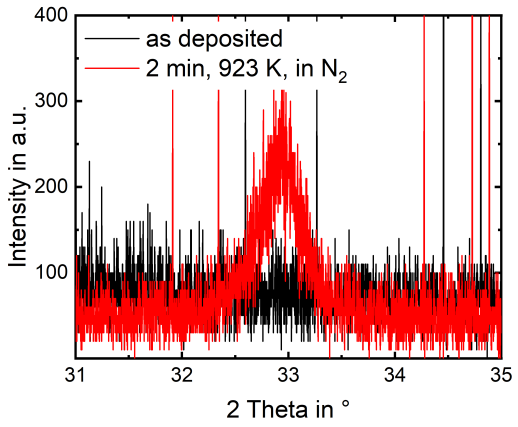

Figure 5.9.: GI-XRD measurement of 95 nm PCMO on Pt before and after thermal annealing for 2 minutes at 923 K in N_2.

The data clearly show the appearance of a Bragg reflection and, therefore, the crystallization of the previous amorphous PCMO layer. The broad peak covers, in the case of a perfect crystalline PCMO with orthorhombic symmetry (space group Pnma (62)), the (200), (121), (121), (12$\bar{1}$), (121), and (002) orientations [201, 26, 21]. In pseudocubic notation, this represents the (110) orientation. The measurements have been done around these peaks because they have the highest structure factor $|F|$. The measurement was done with a Bruker D8 diffractometer with a Cu K-alpha source and Bragg-Brentano geometry. The constant incidence angle ω was set to 0.4°. Crystallization of PCMO reduces the resistance and switching voltage and increases the ratio between the LRS and HRS, as can be seen in Figure 5.1f.

Both types of devices, with amorphous and crystalline PCMO, show area-dependent scaling of the HRS and LRS, as studied in Figure 5.10. Figure 5.10 a and c show the $I - V$ loops (each 3 cycles) for different pad sizes (20 µm × 20 µm), (50 µm × 50 µm), and (100 µm × 100 µm). Figure 5.10 a shows the $I - V$ loop of a sample without thermal treatment of the PCMO and with 5 nm AlO_x. Figure 5.10 c displays the $I - V$ loops of thermally treated (2 min at 923 K in N_2) PCMO with

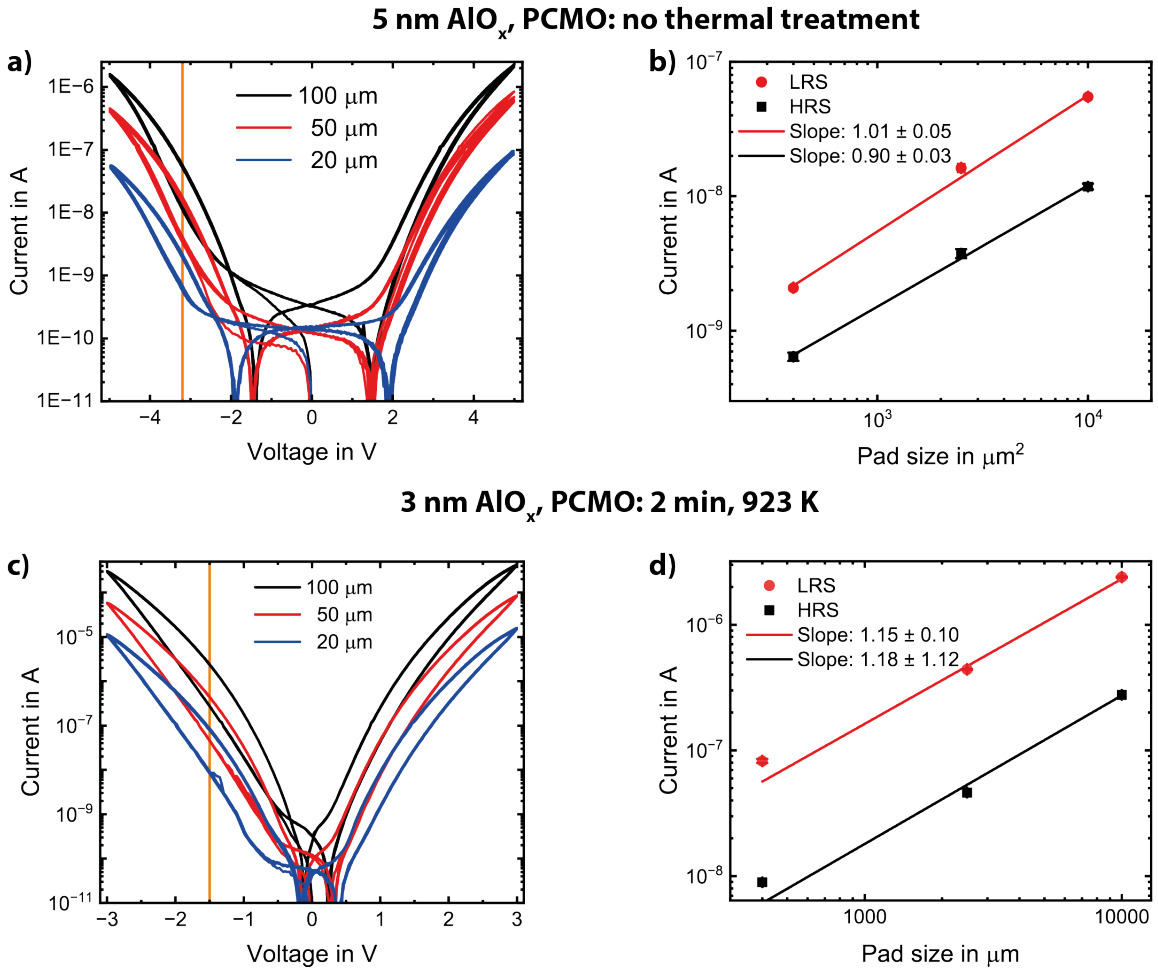

Figure 5.10.: a) and c) are the $I-V$ loops (each 3 cycles) for different pad sizes (20 µm $\times$ 20 µm), (50 µm $\times$ 50 µm), and (100 µm $\times$ 100 µm). a) Shows the $I-V$ loop of a sample without thermal treatment of the PCMO and with 5 nm AlO_x. and c) displays the $I-V$ loops of thermally treated (2 min, at 923 K in N_2) PCMO with 3 nm AlO_x. b) and d) plot the current at the HRS and LRS from the $I-V$ loops of a) and c), read out at the orange-marked voltage.

3 nm AlO_x.

Figure 5.10b and d plot the HRS and LRS from the $I-V$ loops of a and c. The values are taken at the orange-marked voltages. The linear fit in the double logarithmic plot checks the area dependence, with the fitting results of the slope written in the legend. As can be seen in the double logarithmic current-area plot (Figure 5.10). The slope of the linear fit is close to 1, which verifies the linear scaling of the current with the area.

To better understand the effect of the thermal treatment on the switching and to investigate the possibility of a device with pronounced hysteresis and CMOS compatible PCMO deposition, the next chapter compares in detail three different types of PCMO and the resulting devices. The three different types of PCMO are: PCMO deposited at the CMOS compatibility limit of 400 °C, PCMO deposited at room temperature, and thermally treated polycrystalline PCMO.

6. Devices based on highly conductive amorphous PCMO: a comparative study

The text written in this chapter is published as the following paper [3].

6.1. Overview

In the following, the properties of two different types of amorphous PCMO, grown at room temperature and at 400 °C, were investigated and compared with those of polycrystalline PCMO. To understand the differences in resistance, the atomic structure, particularly the short-range order, was examined using grazing incidence X-ray scattering.

All three types of PCMO were integrated into Pt/AlO_x/PCMO/Pt heterostructures, with the AlO_x thickness systematically varied from 2 nm to 5 nm, and their memristive properties were subsequently investigated. Additional experimental details are provided in Chapter 3.4. The resulting $I-V$ curves were analyzed to identify the underlying conduction mechanisms.

Furthermore, band diagrams of the memristive heterostructures were calculated and used to interpret the different conduction mechanisms and the asymmetry observed in the $I-V$ curves. For these calculations, the band gap and work function of all three PCMO types were measured. Finally, finite-element simulations based on the $I-V$ curves were used to investigate the electric field distribution within the device. These simulations accounted for the nonlinear dependence of resistance on the electric field, aiming to explain the memristive effect as a function of AlO_x thickness and PCMO resistance.

For the study of PCMO properties, PCMO was deposited either on fused silica or on a Pt bottom electrode on a Si wafer. The experimental details are described in Chapter 3.4. The PCMO sample batch deposited on Pt was used for in-situ GI-XRD in Figure 6.2. It was also used for PEEM measurements in Figure 6.9, for DC conductivity measurements in Figure 6.4 and for STS measurements in Figure 6.11. The PCMO sample batch deposited on fused silica was used for synchrotron measurements in Figure 6.3, PDF analysis (Figure 6.5) and for band gap determination by UV/Vis spectroscopy (Figure 6.10).

6.2. Structural analysis and crystallinity

6.2.1. Surface morphology and density change by crystallization of PCMO

The change of the surface morphology, after the crystallizing annealing treatment, can be seen by comparing the AFM-images of a-PCMO and c-PCMO in Figure 6.1a. The polycrystalline PCMO exhibit many grains, which may be crystal grains forming a network of grain boundaries. The grain size increases with increasing PCMO film thickness (Figure 6.1a). The formation of a granular morphology is consistent with the relatively short annealing time of 2 minutes, which kinetically allows only the growth of numerous small crystallites. Furthermore, XRR measurements (Figure 6.1b) show that the crystallization process is associated with an increase in the total reflection angle, which corresponds to an increase in density.

The corresponding film shrinkage with film thickness increases approximately with film thickness. This can be seen from the thickness measurements (Figure 6.1c) made with different mea-

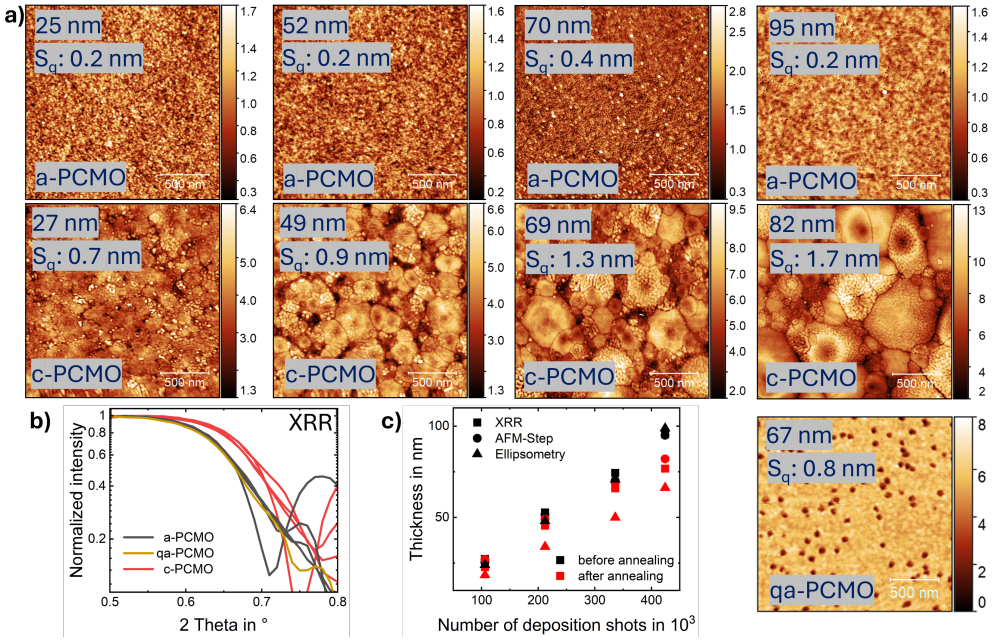

Figure 6.1.: a) Atomic Force Microscopy (AFM) images (scale in nm) of amorphous and polycrystalline PCMO depending on PCMO thickness. The c-PCMO shows a distinct crystallite morphology with increasing crystallite size with thickness. The qa-PCMO shows pinholes on its surface. b) X-ray reflectivity (XRR) scans of the samples show the increase in total reflection angle with crystallization. c) AFM step measurements, XRR measurements and ellipsometry measurements show an increasing thickness reduction upon annealing with increasing PCMO thickness.

surement methods. The different methods give different thickness values with the same trend of increasing thickness reduction with thicker PCMO layers.

Local AFM step measurements were performed at a lift-off edge between PCMO and Pt. XRR fitting of the multilayer stack was performed using the GenX program [148]. The fitting of the ellipsometry measurements was performed assuming a Tauc-Lorentz model for the PCMO.

6.2.2. GI-XRD measurements and in-situ crystallization temperature

Grazing incidence X-ray diffraction (GI-XRD) was performed using a Bruker D8 to investigate the crystallinity. The angle of incidence was set slightly above the angle of total reflection. The c-PCMO GI-XRD spectrum is shown in Figure 6.2a and agrees well with the calculated reference of crystalline PCMO obtained in VESTA (ICSD-56634 [201]). For the investigation of the crystallization temperature, the strongest Bragg reflection, occuring at about 33° of the pseudo-cubic (110) orientation, was selected (Figure 6.2a).

Figure 6.2b compares the GI-XRD of qa-PCMO, a-PCMO and c-PCMO at 33°. Neither a-PCMO nor qa-PCMO show Bragg reflections (Figure 6.2b). In contrast, c-PCMO shows a Bragg reflection. To determine the crystallization temperature of PCMO, GI-XRD with in-situ annealing was performed in an N_2 environment. Bragg reflections begin to appear between 540 ℃ and 560 ℃ (Figure 6.2c), which is consistent with the results of GI-XRD on a-, qa-, and c-PCMO.

6.2.3. Total X-ray scattering

The GI-XRD results were reproduced by total X-ray scattering measurements (Figure 6.3) collected using the grazing-incidence diffraction and scattering setup provided by DESY Photon Sci-

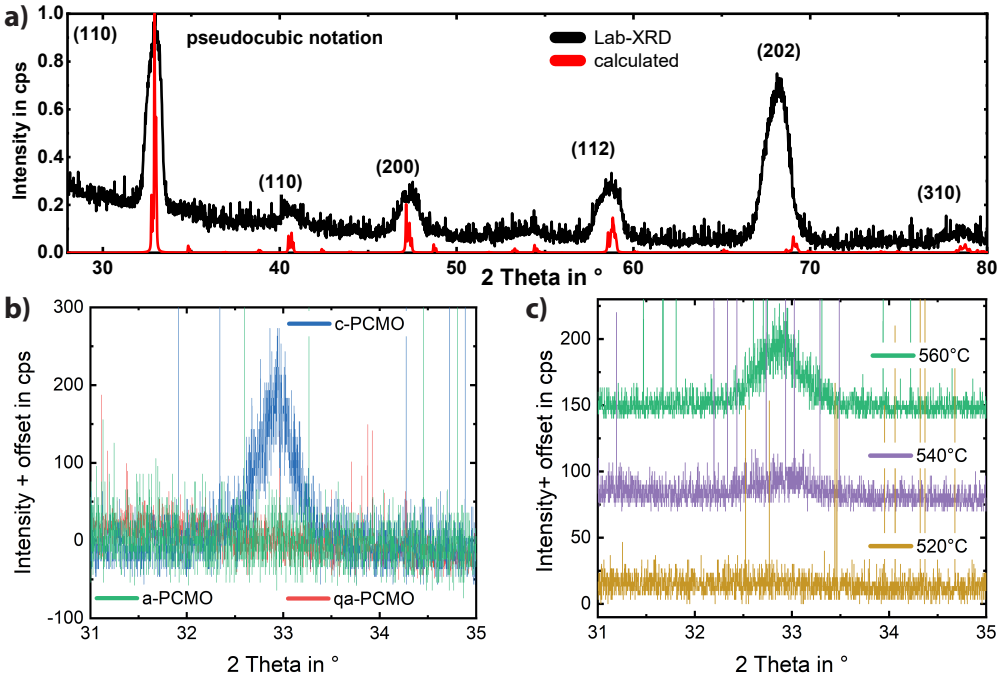

Figure 6.2.: a) GI-XRD spectrum of c-PCMO obtained with laboratory equipment (BrukerD8). For comparison, the theoretical powder pattern of c-PCMO is plotted. The broad Bragg reflections are assigned according to the pseudo-cubic perovskite notation. This spectrum was measured after in-situ annealing (Figure c) up to 860 ℃. b) GI-XRD comparison around 2θ of 33 ° of 23 ℃ and 400 ℃ deposited PCMO and thermally annealed PCMO. c) GI-XRD with in-situ annealing in N_2 with a heating ramp of 300 ℃/min. A pre-scan heating time of 10 min and a scan time of 10 min were used for each scan.

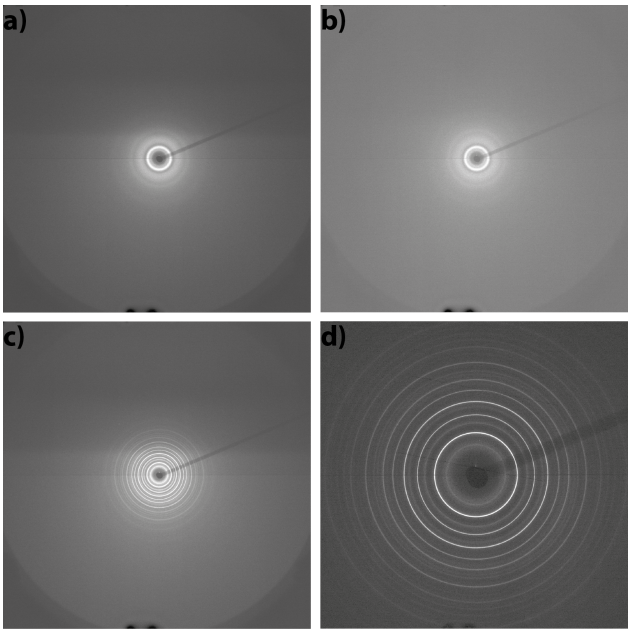

Figure 6.3.: 2D real-space grazing incidence X-ray scattering of PCMO on fused silica was performed using a 100 keV X-ray beam at DESY-PETRA III. Figures a, b, and c show the high Q-range scattering data (up to 25 Å^{-1}) for a-PCMO (a), qa-PCMO (b), and c-PCMO (c), used for the PDF calculation. Figure d presents higher-resolution scattering data, focusing on the Bragg reflection of c-PCMO, with Q values up to 8 Å^{-1}.

ence and carried out at PETRA III - P07, experimental hutch (EH2) [155]. Ann-Christin Dippel, Philipp Glaevecke, and Olof Gutowski provided assistance during the experiments. The measurements were carried out as part of this PhD project during beamtime (I-20230316) allocated to Hassan Sultani, under the supervision of Susanne Hoffmann Eifert.

The PCMO deposition process and annealing treatment were identical, and amorphous fused silica was used as substrate. The high-energy X-rays used (103.4 keV) correspond to a wavelength of 0.12 Å and were focused to a beamsize of 2 µm $\times$ 30 µm. By using high energy X-rays, a large Q-range can be accessed, allowing the calculation of the reduced pair distribution function (PDF) $G(r)$. The scattering signal was recorded with a Varex XRD4343 2D detector with a pixel pitch of 150 µm with 0.5 s acquisition time per image.

Two types of measurements were performed. The high Q measurements (Figure 6.3 a, b and c) capture both a low Q region of Bragg reflections as well as a high Q region with diffuse scattering from short range order. These data are then combined and used in the PDF analysis, which provides near-order information. For a comprehensive study of the Bragg reflections, low-Q measurements were conducted (Figure 6.3 d). To perform the high Q-range PDF analysis, a short sample to detector distance of 395 mm was used, resulting in Q_{maxinst} = 25 Å^{-1}. The low Q range measurements were done with a distance of 1345 mm and a corresponding Q_{maxinst} = 8 Å^{-1}.

The high Q measurements of qa-PCMO, a-PCMO and c-PCMO (Figure 6.3 a, b and c) show no Bragg reflection in the case of qa-PCMO and a-PCMO, in contrast to c-PCMO, confirming the laboratory based results shown in Figure 6.2b. This rules out the presence of small nanocrystallites in qa-PCMO that are not visible with a laboratory X-ray source. The high-Q (Figure 6.3 c) and low-Q (Figure 6.3 d) measurements on c-PCMO show the presence of highly circular and homogeneous Debye Scherrer rings. It can therefore be concluded that c-PCMO is highly polycrystalline with no observable preference for a particular lattice orientation.

6.2.4. Calculation of the pair distribution function

The pair distribution function $G(r)$ was calculated with the xPDFsuite software [202, 203, 204], from the total X-ray scattering data (Figure 6.5a). The calculations were conducted in collaboration with Hassan Sultani as part of this PhD project. In a first step, the coherent scattering intensity $I_c(Q)$ was determined from the measured intensity $I_m(Q)$. For this purpose, the measured intensity of the fused silica, which serves as a reference for the background signal, was subtracted. xPDFsuite then uses an algorithm to calculate the $a(Q)$ and $b(Q)$ parameters to account for multiplicative and additive corrections to the intensity.

$$I_m(Q) = a(Q)I_c(Q) + b(Q). \tag{6.1}$$

For this algorithm the tuning parameter R_{poly} is set to 0.98 Å and a maximum Q value of the instrument of $Q_{\mathrm{maxinst}} = 25\,\text{Å}^{-1}$ is considered a[203].

Subsequently, the total scattering structure function

$$S(Q) = \frac{I_c(Q) - \langle f(Q)^2\rangle + \langle f(Q)\rangle^2}{\langle f(Q)\rangle^2} \tag{6.2}$$

was calculated by considering the atomic scattering factor $f(Q)$ averaged over the atomic composition of $Pr_{0.7}Ca_{0.3}MnO_3$. Then the reduced pair distribution function

$$G(r) = \frac{2}{\pi}\int_{Q_{\mathrm{min}}}^{Q_{\mathrm{max}}} F(Q)\sin(Qr)dQ \tag{6.3}$$

was calculated as the Fourier transform of the reduced structure function

$$F(Q) = Q(S(Q) - 1). \tag{6.4}$$

Hereby, a lower limit of 0.1 Å^{-1} was chosen for the Fourier integral to exclude low-Q data affected by the beam stop. The upper Q_{max} limit of 14 Å^{-1} of the Fourier integral was selected as a compromise, set at a level that allows for an optimal r-space resolution while avoiding the influence of high-frequency noise in $G(r)$.

To compare the calculated $G(r)$ (Figure 6.5b) with the $G(r)$ of an ideal crystal, a simulation was calculated for a crystallographic file (ICSD database element 56634 [201]). The simulation was performed using the PDFgui tool from xPDFsuite with $Q_{\mathrm{max}} = 14\text{Å}^{-1}$ as for the PDF calculation and a spacing of 0.01 Å. For this simulation, experiment related impreciseness were considered to make the simulated $G(r)$ comparable with the calculated $G(r)$.

The experimental Q-space resolution leads to a damping Q_{damp} of the calculated $G(r)$ with increasing r as well as to a broadening Q_{broad} of the peak shapes with increasing r. These effects have been experimentally quantified by Dippel et al. [155] for a ceria reference sample under the assumption of a Gaussian peak profile. Following their recommendation for the $G(r)$ simulation with *PDFgui* for the setup of 395 mm detector-sample distance, the damping was considered by $Q_{\mathrm{damp}} = 0.03\,\text{Å}^{-1}$ and the broadening by $Q_{\mathrm{broad}} = 0.05\,\text{Å}^{-1}$.

6.3. DC conductivity and atomic structure

To investigate the potential benefits of amorphous PCMO, three different types of PCMO were studied, two of which are amorphous. All samples were deposited by pulsed laser deposition, as described in Section 3.4. The two amorphous types were deposited below the measured crystallization temperature of 560 °C (Section 6.2.2): one at room temperature (a-PCMO) and

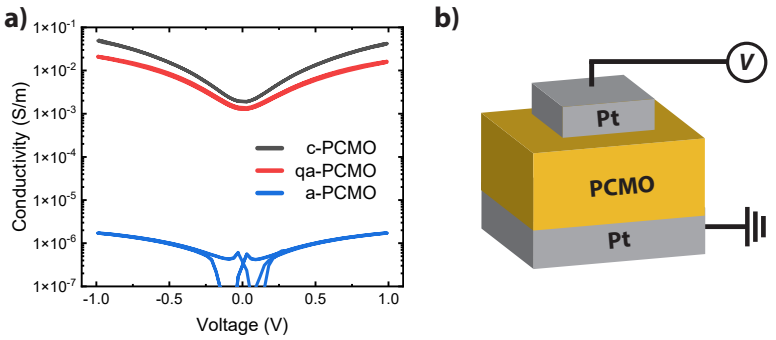

Figure 6.4.: a) DC conductivity of three types of PCMO: a-PCMO deposited at room temperature, c-PCMO deposited at room temperature and subsequently annealed, and qa-PCMO deposited at 400 °C. b) The conductivity was measured using the illustrated stack configuration. The Pt top electrode had a size of 50 µm $\times$ 50 µm and the thickness of the PCMO was 69 nm for c-PCMO, 70 nm for a-PCMO and 67 nm for qa-PCMO.

the other at the CMOS-compatibility limit of 400 °C (qa-PCMO). For comparison, polycrystalline PCMO (c-PCMO) was used, obtained by thermally annealing PCMO at 650 °C for 2 minutes. The PCMO used for this process was deposited at room temperature.

Direct current (DC) conductivity measurements (Figure 6.4) showed that the conductivity of qa-PCMO is up to four orders of magnitude higher than that of a-PCMO deposited at room temperature, and nearly as high as that of c-PCMO.

Further two-dimensional scattering images (discussed in more detail in the Experimental Section, Figure 6.3) confirmed the high degree of polycrystallinity in thermally annealed PCMO, as evidenced by homogeneous Debye Scherrer rings without any preferred orientation.

6.3.1. MnO_6 octahedron as local bonding unit and its network

The X-ray total scattering measurements, up to high Q (Figure 6.5a), were used to calculate the reduced pair distribution function (PDF) $G(r)$ (Figure 6.5b), with the atomic distance r, as described in Section 6.2.4, to obtain information about the atomic short-range order in the materials. By comparing the observed bond distances with those expected from the PCMO unit cell, we identified the MnO_6 octahedron as the local bonding unit, as discussed below.

The calculated $G(r)$ (Figure 6.5b) shows a long-range order of the atomic correlation distances for c-PCMO in its full calculation range of 30 Å. In contrast, the $G(r)$ of a-PCMO and qa-PCMO exhibit only a short-range order of up to 10-15 Å. Furthermore, the $G(r)$ of c-PCMO shows strong similarities with the simulated pair distribution function (PDF) for perfectly crystalline PCMO.

A more comprehensive analysis of the small Å region of the $G(r)$ bond distance correlation structure of c-, a-, and qa-PCMO is shown in Figure 6.5c. The peaks observed in the c-PCMO structure were assigned to the corresponding bond distances of crystalline PCMO (ICSD-56634 [201]) by manually comparing the bond distances in the unit cell (Figure 6.5d and e), using the crystallographic visualization software VESTA 3.5.7. The O-O bonds were excluded from consideration due to the relatively low atomic form factor of the oxygen anion, which results in weak scattering intensity. Figure 6.5c shows that the direct Mn-O (Manganese-Oxygen) and A-O (A-site-Oxygen) bonds are visible in the $G(r)$ of all PCMO configurations. Also the A-O distance is similar to the one observed and expected for c-PCMO.

The clear Mn-O bond peak provides evidence that the local bonding unit Mn-O_6 of manganese, surrounded by an oxygen octahedron, can be used to describe the local structure of a-PCMO and qa-PCMO. The octahedral configuration for Mn^{3+} is particularly advantageous due to its large ionic radius [205], which, according to Shannon, is 0.645 Å in a high-spin configuration and 0.58 Å

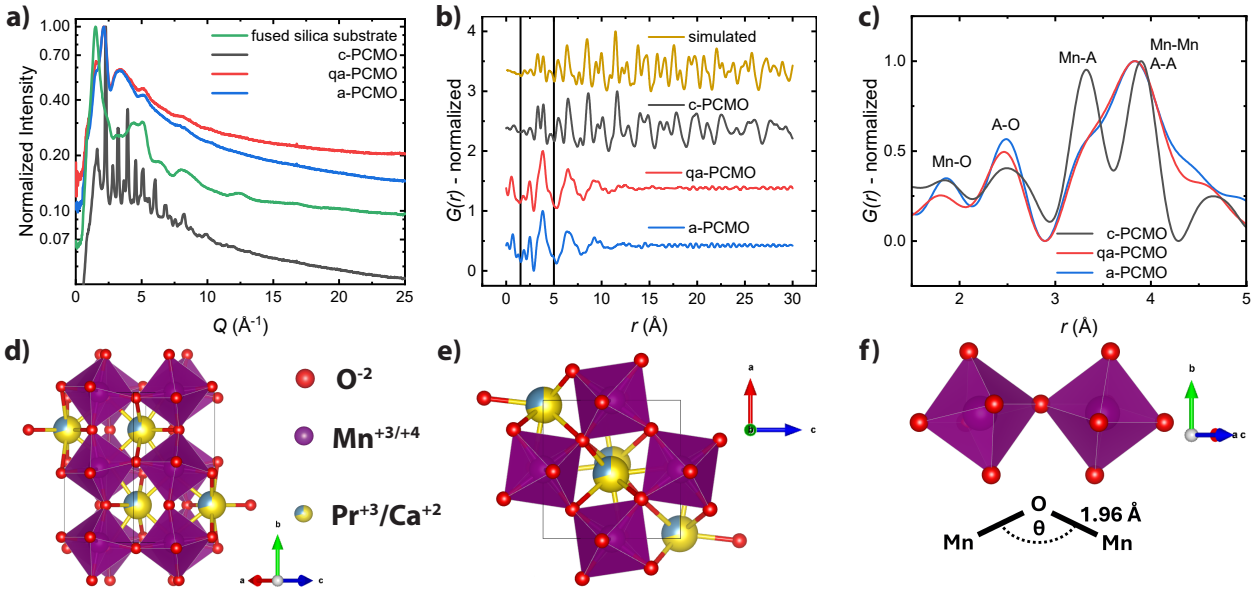

Figure 6.5.: a) Azimuthal integration of the high-Q X-ray scattering (Figure 6.3). b) Reduced pair distribution function $G(r)$, calculated from a), and the simulated curve of an ideal PCMO crystal (ICSD-56634 [201]). All $G(r)$ values have been normalized to their highest peaks and arbitrarily shifted for graphical purposes. c) A magnified renormalized comparison of the PDFs of qa-PCMO, c-PCMO and a-PCMO with the assignment of bond distances. d) Unit cell of $Pr_{0.7}Ca_{0.3}MnO_3$, viewed from the $[\bar{1}0\bar{1}]$ direction. e) PCMO unit cell from the [010] direction. f) Two Mn-O_6 octahedra from the PCMO unit cell, which are bonded at a vertex with a 156° angle and have a Mn-O distance of 1.96 Å. Figure d), e) and f) were generated with the VESTA 3.5.7 software and are based on the ICSD-56634 database item, which is based on Radelli et al. [201].

in a low-spin configuration [206], whereby Mn^{3+} usually appears in high-spin configuration due to the strong Hund's coupling [205].

Moreover, for the Mn^{4+} valence with smaller ionic radius, the octahedral configuration is advantageous due to the increased energetic benefit of an octahedral crystal field splitting for a $3d^3$ orbital configuration compared to a tetragonal crystal field splitting. Therefore, Mn^{4+} are usually found in the octahedral configuration [205].

The next layer bonding distances of the A-side cation A-A (theoretically between 3.8 Å and 3.9 Å) and manganese Mn-Mn (theoretically between 3.8 Å and 3.9 Å) and Mn-A (theoretically between 3.1 Å and 3.3 Å) are clearly distinguishable in the $G(r)$ of crystalline PCMO. However, in a-PCMO and qa-PCMO, the peaks corresponding to the Mn-Mn and A-A distances are significantly broadened to the extent that they overlap with the Mn-A peak. The broadening of the Mn-Mn and A-A peaks can be attributed to changes in the bond angle and bond distances. The broad peak leads to the conclusion that the assumed Mn-O_6 octahedra as local bonding units are randomly ordered and tilted with respect to each other.

Based on this, we propose that the atomic structure consists of a disordered network with broadly distributed Mn-O-Mn bond angles. With this structural picture in mind, we attempt to understand the origin of the strong conductivity differences between amorphous PCMO and quasi-amorphous PCMO.

The conductivity σ of qa-PCMO is around a third of that of c-PCMO, while the conductivity of a-PCMO is up to four orders of magnitude lower. To investigate this difference, the conductivity

$$\sigma = e\rho\mu \tag{6.5}$$

can be factorized into the charge carrier density ρ, the mobility μ and the elementary charge e.

The charge carrier density in crystalline PCMO is determined by the manganese valency, and the charge transport can be described by Jahn-Teller-based polarons, which are localized charge carriers [34, 53, 81]. The polaronic description is based on the movement of the e_g electron, which is formed in the octahedral crystal field by the surrounding oxygen anions around the Mn^{3+} cation and is associated with the Jahn-Teller distortion. The amount of e_g electrons depends on the amount of Mn^{3+} cations, which are controlled by the Ca content. For the used $Pr_{0.7}Ca_{0.3}MnO_3$ with an assumed mass density ρ_m of 6.2 g/cm^3 [21] the formal hole density ρ_h can be calculated from the ratio

$$\rho_h = \frac{\rho_\mathrm{m}}{M} * N_A * 0.3 \tag{6.6}$$

with the molar mass M of PCMO and Avogadro constant N_A. Thus ρ_h is $5.5{\cdot}10^{21}$/cm^3. From this perspective, the formal charge carrier density depends mainly on the stoichiometry. Since the conductivity depends linearly on ρ (Equation 6.5), only a strong variation would explain the strong conductivity difference of up to $9{\cdot}10^3$ between room temperature and 400 °C deposited amorphous PCMO.

Alternatively, the conductivity difference could be explained by a strong variation in the electronic mobility μ. It can be assumed that the charge carriers move along the network of MnO_6 octahedra, formed by bonds between the directional Mn e_g orbitals and the directional Oxygen 2p orbitals. The overlap of these orbitals is strongly influenced by the Mn-O-Mn bond angle α, as shown in Figure 6.5f. It is known that, in the crystalline mixed-valence manganite system $A_{0.7}A'_{0.3}MnO_3$, the bandwidth of the one-electron e_g band decreases with increasing tilting of the Mn-O-Mn bond angle θ [207]. This was also experimentally demonstrated by Hwang et al. [23], who varied the bond angle in an $A_{0.7}A'_{0.3}MnO_3$ system by tuning the tolerance factor through isovalent doping. Hwang et al. [23] observed a continuous increase in the Curie temperature for the formation of the ferromagnetic metallic phase, attributed to double exchange, and an increase in room-temperature conductivity as the Mn-O-Mn bond angle α becomes less tilted.

It is also well known that, within the framework of the tight-binding model, the matrix element for electron hopping between two MnO_6 octahedra depends on the bond angle θ. According to the Slater-Koster parametrization, the band swith varies with $\cos^2(\theta)$ [207].

For crystalline PCMO, the strong tilting of its bond angle—about 156° [201]—is considered to be the reason for its narrow bandwidth and the strong influence of the Jahn-Teller distortion on electronic mobility, due to localization by polaronic formation [53]. The electronic mobility of epitaxial $Pr_{0.64}Ca_{0.36}MnO_3$ is about 0.015 cm^2/Vs [81] at room temperature.

Considering the strong influence of the bond angle on the mobility [23, 207], conduction through the bond network formed by MnO_6 octahedra can be described within the framework of percolation theory, where a significant change in conductivity can be explained by the formation of volume-spanning percolation clusters [208].

Therefore, we assume that the local bonding configuration controls the probability p of electron hopping, and that this bond angle distribution differs between a-PCMO and qa-PCMO. A simplified way to estimate a representative value for p would be to calculate the ratio of Mn-O-Mn bonds that are larger than the bond angle in crystalline PCMO, which is 156°. In percolation networks, a percolation threshold p_c exists. If $p < p_c$, then the percolation clusters formed within the PCMO layer remain finite in size. When $p > p_c$, the cluster size becomes theoretically infinite, occupying a subset of the bond network within the entire film [208]. We propose that $p < p_c$ for a-PCMO and $p > p_c$ for qa-PCMO respectively. Since conductivity can drastically change when p crosses the percolation threshold, even small variations in the local bonding configuration could lead to significant changes in electronic mobility; thus, this approach would be suitable to explain the large differences in conductivity between the two types of (quasi-)amorphous PCMO.

In the framework of percolation theory, this conductivity change is considered a second-order phase transition. The percolation probability P, defined as the probability that a MnO_6 octahedron is part of the global cluster, serves as the order parameter. Thus, P vanishes for $p < p_c$ and follows a non-trivial power law for $p > p_c$ [208]."

To refer to the possible structural origin of these conductivity differences, namely the orientational ordering of local bonding units without translational symmetry, we labeled the PCMO deposited at 400 °C as quasi-amorphous. This terminology is used in reference to literature [209], where the term was applied to titanates and zirconates, exhibiting pyro- and piezoelectric properties from orientationally ordered but spatially disordered Ti-O_6 octahedra, forming a random network with local dipole moments.

6.4. Electrical characterisation and conduction mechanism of the memristive devices

6.4.1. *I-V* characteristics and resistive switching

The three different types of PCMO were integrated into devices based on Pt/AlO_x/PCMO/Pt heterostructures, as described in detail in Section 3.4. The corresponding $I-V$ curves for each AlO_x thickness, depending on the PCMO type, are shown in Figure 6.6a-d.

Overall, the $I-V$ characteristics reveal that a-PCMO devices exhibit the lowest on/off ratio and begin to switch at an AlO_x thickness of 4 nm. In contrast, qa-PCMO devices display the highest on/off ratio at an AlO_x thickness of 3 nm, which decreases with increasing oxide thickness. Meanwhile, c-PCMO devices show switching behavior at AlO_x thicknesses of 3 nm and above, achieving their maximum on/off ratio at 5 nm.

Further, for all thicknesses, a consistent trend is observed: the current is highest for c-PCMO (shown in gray), lowest for a-PCMO (shown in blue), and intermediate for devices based on qa-PCMO (shown in red). This trend is not caused by the resistance of the PCMO layers, which follow

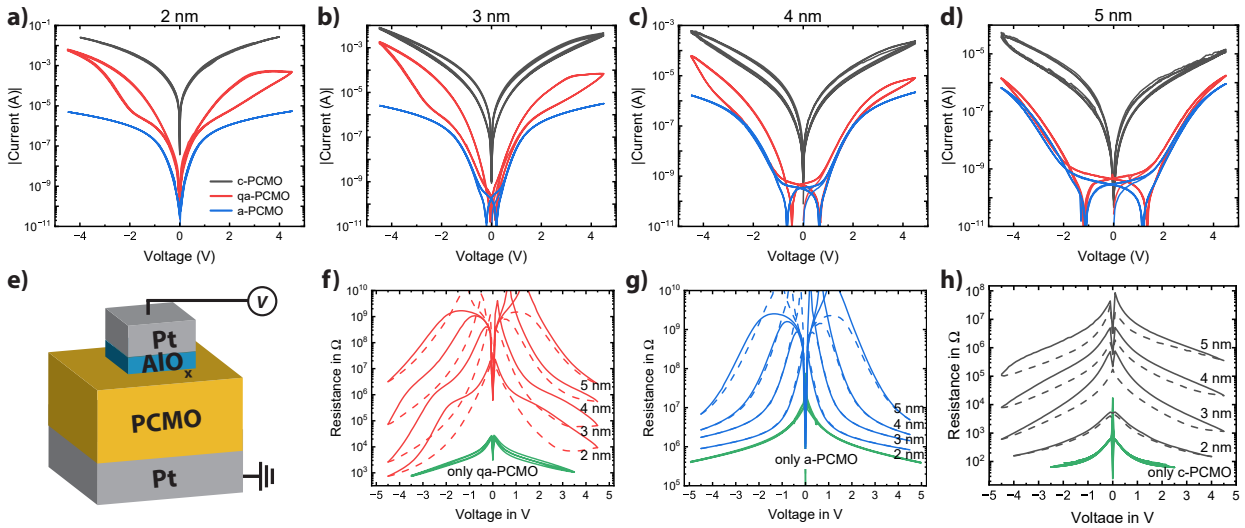

Figure 6.6.: a), b), c), and d) show the dependence of the $I-V$ characteristics of the memristive devices on the PCMO types (grey: c-PCMO, red: qa-PCMO, and blue: a-PCMO) for different AlO_x thicknesses: a) 2 nm, b) 3 nm, c) 4 nm, and d) 5 nm. The schematic structure and the polarity of the bias on the 100 µm x 100 µm pad structure, is drawn in e). The PCMO thickness was approximately 70 nm in all cases. f), g), and h) show the dependence of the $R-V$ characteristics on the AlO_x thicknesses, along with a comparison to the resistance of the pure PCMO layer, for the different PCMO types: f) qa-PCMO, g) a-PCMO, and h) c-PCMO. In each $R-V$ curve, the HRS is shown with a solid line and the LRS with a dashed line.

the same order, since the resistance of the PCMO layer is much lower than the device resistance, as shown in Figure 6.6f, g, and h.

These figures show the thickness dependence of the $R-V$ characteristics for all three PCMO types: quasi-amorphous (f), amorphous (g), and crystalline (h), separated into the HRS (solid) and the LRS (dashed). The $R-V$ characteristics for different thicknesses are stacked with roughly similar spacings in this semi-logarithmic plot, indicating a roughly exponential increase in the tunnel resistance through the AlO_x with increasing thickness.

Furthermore, Figure 6.6 shows that increasing the AlO_x thickness leads to a convergence of resistance values across all device types. As indicated by the scale, devices with a 2 nm AlO_x layer exhibit resistance differences of up to four orders of magnitude, while those with 5 nm AlO_x show differences of less than two orders of magnitude. Especially, the current level of qa-PCMO devices in the HRS becomes similar to that of a-PCMO devices as the AlO_x thickness increases (Figure 6.6).

However, the resistances do not fully converge for 5 nm AlO_x, with c-PCMO still showing a substantially higher current. Since the cause of these resistance differences does not lie in the intrinsic resistance of the individual PCMO layers, other factors must be considered. One possible explanation is that the growth of AlO_x may vary depending on the underlying surface morphology of the PCMO (Figure 6.1, discussed in Section 6.2.1). A clear correlation can be observed between the surface roughness of the PCMO and the current levels of the devices, particularly for the relatively rough c-PCMO morphology.

Further, as indicated by the differences in the shape of the $I-V$ characteristics and the size of the on/off ratio, variations in the conduction mechanisms across the Pt/AlO_x/PCMO heterostructure must also be considered. This effect may result from variations in the oxygen vacancy exchange during switching, caused by the different PCMO types, or from changes in band alignment in the heterostructures induced by the different PCMO types.

6.4.2. Conduction type and asymmetry

To investigate the conduction mechanisms, the shape of the $\log(R_{\text{device}})$-V characteristics was fitted using two different functions, allowing the behavior to be categorized into two distinct types of conduction.

One identified conduction type exhibits a $\log(R_{\text{device}}) = \frac{a}{V} + b$ dependence, as represented by the blue fits in Figure 6.7a and 6.8, where a and b are fitting parameters. This $\frac{1}{E}$ field dependence is characteristic of tunneling through a triangular potential barrier formed by band bending under a high electric field. The $\frac{1}{E}$ term originates from the field-dependent narrowing of the triangular barrier, which affects the Wentzel-Kramers-Brillouin (WKB) integral that determines the tunneling probability. This field dependence can be observed for Fowler- Nordheim tunneling in the case of direct tunneling, but it may also describe trap-assisted tunneling under high electric fields [210, 211].

The second identified conduction type is described by $\log(R_{\text{device}}) = a\sqrt{|V|} + b$, as represented by the green fits in Figure 6.7c and 6.8, where a and b are fitting parameters. A $\sqrt{E}$ field dependence is commonly associated with thermal emission processes such as Schottky or Poole-Frenkel emission. In the case of Schottky emission, the $\sqrt{E}$ behavior arises from the field-induced lowering of the emission barrier at the electrode, due to the combined effect of image charge and the applied electric field. For Poole-Frenkel emission, the $\sqrt{E}$ dependence results from the electric field lowering the Coulombic potential of a trap level [210, 211].

Fitting the $\log(R_{\text{device}})$-V characteristics showed that conduction in a-PCMO-based devices can be well described by a $\frac{1}{V}$-type behavior across both resistive states and all AlO_x thicknesses (Figure 6.7a). In contrast, c-PCMO-based devices (Figure 6.7c) exhibit a $\sqrt{|V|}$-type conduction for both resistive states and all AlO_x thicknesses.

The asymmetry of the R-V characteristics with respect to voltage polarity was also analyzed. Therefore, for both the HRS and LRS separately, the resistance was plotted against the absolute voltage $|V|$. The color between the two curves indicates which polarity results in a higher resistance—green (Figure 6.7d) for positive and blue (Figure 6.7b) for negative. Low-voltage regions, which are affected by charging effects, were excluded from the graphical analysis.

The bias was applied to the Pt electrode at the AlO_x interface, as shown in Figure 6.6e. It was found that the two different conduction types correlate with the two different types of asymmetry. For a-PCMO, which exhibits $\frac{1}{V}$-type conduction, the resistance is lower under positive bias on the top electrode (Figure 6.7b), whereas for c-PCMO, which shows $\sqrt{|V|}$-type conduction, the resistance is lower under negative bias on the top electrode (Figure 6.7d).

The $\log(R_{\text{device}})$-V characteristics (Figure 6.8) of qa-PCMO shows a mixed picture. The devices exhibit a $\frac{1}{V}$-type conduction and lower resistance under positive bias on the top electrode—similar to a-PCMO—in the HRS for all AlO_x thicknesses and in the LRS for 5 nm AlO_x. High-voltage regions in the HRS, where the resistance state is influenced by switching, show the opposite asymmetry and were excluded from the graph. The LRS of devices with 2, 3, and 4 nm AlO_x shows a $\sqrt{|V|}$-type conduction and lower resistance under negative bias on the top electrode, similar to the devices based on c-PCMO.

Therefore, a correlation between conduction type and asymmetry is found. For a analysis of this behavior, the band alignment of the heterostructures is calculated in the next Section.

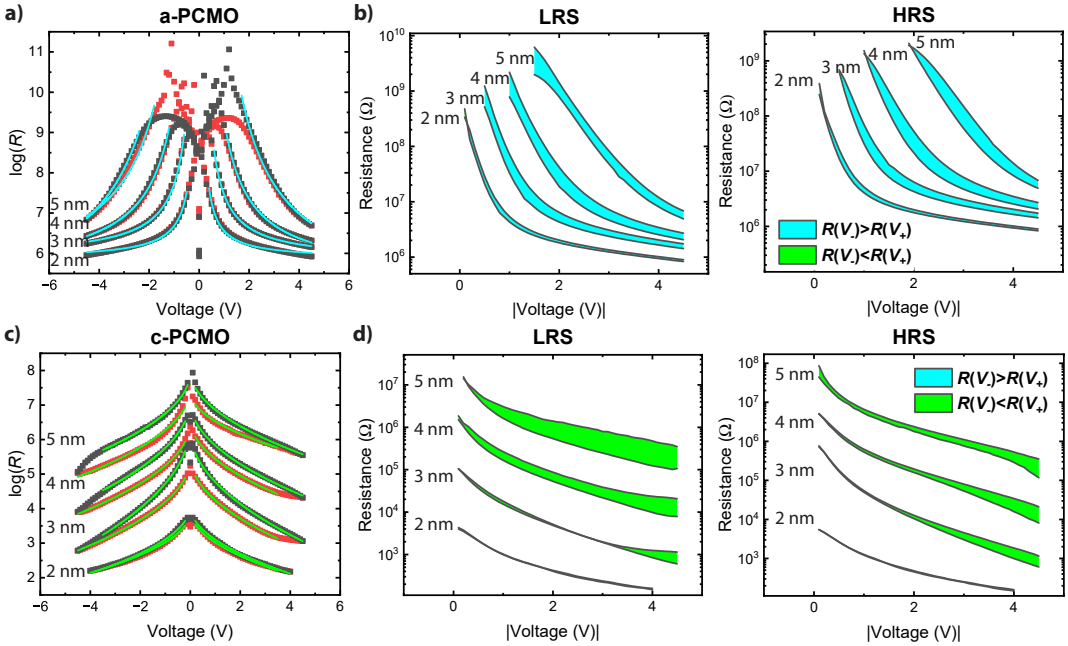

Figure 6.7.: a) Shows the fitting of the $\log(R_{\text{device}}) - V$ characteristic of a-PCMO devices using $\log(R_{\text{device}}) = \frac{a}{|V|} + b$, shown in blue for both resistive states (HRS in grey, LRS in red) and for all AlO_x thicknesses. b) Analyzes the asymmetry of the $R - V$ characteristic of the a-PCMO devices at different bias polarities, separately for the LRS and HRS. The color between the two resistance curves indicates whether the resistance is higher when a positive bias $R(V_+)$ (green) or a negative bias $R(V_-)$ (blue) is applied to the Pt electrode at the AlO_x interface. c) Shows the fitting of the $\log(R_{\text{device}}) - V$ characteristic of c-PCMO devices using $\log(R_{\text{device}}) = a\sqrt{|V|} + b$, shown in green. d) Analyzes the asymmetry of the c-PCMO devices.

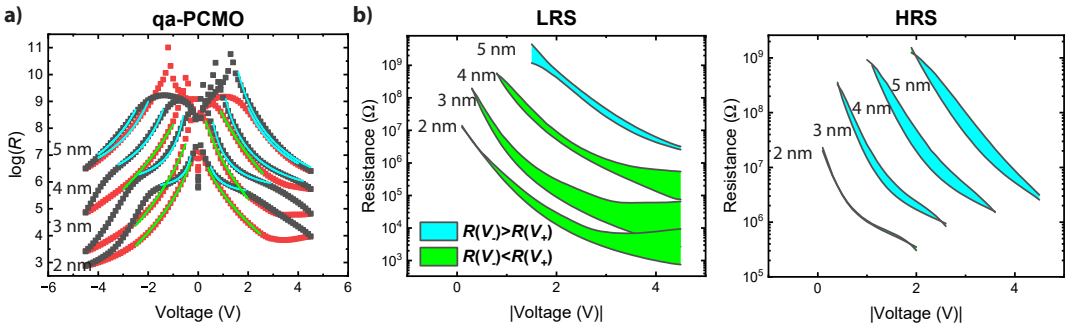

Figure 6.8.: a) Shows the fitting of the $\log(R_{\text{device}}) - V$ characteristic of qa-PCMO devices using $\log(R_{\text{device}}) = \frac{a}{|V|} + b$ (blue) for the HRS of all AlO_x thicknesses and the 5 nm LRS. The green fitting shows $\log(R_{\text{device}}) = a\sqrt{|V|} + b$ for all LRS states, except for 5 nm AlO_x. b) Analyzes the asymmetry of the $R - V$ characteristic of the a-PCMO devices at different bias polarities, separately for the LRS and HRS. The color between the two resistance curves indicates whether the resistance is higher when a positive bias $R(V_+)$ (green) or a negative bias $R(V_-)$ (blue) is applied to the Pt electrode at the AlO_x interface.

6.5. Band alignment and asymmetry

To better understand the reasons for the different conduction types and their connection to asymmetry, we aim to calculate the band alignment of these three types of heterostructures. Therefore, the work function and the band gap of the different types of PCMO were measured.

6.5.1. Work function determination by threshold emission spectroscopy

A photoelectron emission microscope (PEEM) was used to measure the spatially resolved energy spectra of the emitted photoelectrons (see Figure 6.9). The measurements were performed in collaboration with Kalle Goß as part of this PhD project. Thus by using a mercury lamp, the work function of a-, qa- and c-PCMO could be determined by means of threshold emission spectroscopy. The PEEM measurements were performed with a NanoESCA from *Scienta Omicron GmbH* (entrance slit 1 mm, pass energy 100 eV).

A-PCMO (70 nm), c-PCMO (69 nm) and qa-PCMO (67 nm) were deposited on a Pt bottom electrode. Subsequently, a Pt top electrode was deposited using a shadow mask technique. The deposited top electrodes have an approximately square shape with side lengths of about 10-15 µm (see Figure 6.9).

The Pt bottom electrode was directly connected to the sample holder to align the Fermi level of the detector and the sample. To correct the effect of surface charge, the obtained photoelectron spectra of PCMO were charge corrected by the photoelectron spectra of the floating Pt top electrode, which should have an equivalent electric potential.

Photoelectron generation was achieved by using a mercury lamp. To avoid the influence of potential surface inhomogeneities in the Pt, the PEEM spectra were averaged from a rectangular area extracted from the central region of the Pt top electrode, as shown in Figure 6.9. For PCMO, spectra were extracted from four rectangular areas surrounding the central Pt pad to account for inhomogeneities in the electron optics. These rectangular regions were spaced a few micrometers from the Pt pad to minimize the effects of noise from the Pt. The four measurements for each PCMO configuration and the corresponding Pt reference are then normalized and plotted.

The spatial inhomogeneity of the electron optics can be evaluated by comparing the four averaged intensities and is found to be approximately 0.2 eV for both qa-PCMO and c-PCMO, and 0.1 eV for a-PCMO. Since the energy resolution, with a FWHM of 0.4 eV (Chapter 3.7.2), is more limiting than this measured spatial variation in the electron optics, 0.4 eV is used as uncertainty in the work fucntion measurement.

The x-axis of the PEEM spectra depicts the difference between the photon energy of the mercury lamp, represented by $h\nu$, and the binding energy, represented by E_{bin}. The binding energy is defined in reference to the Fermi level, assuming that the Fermi level of the sample and detector are aligned by the connection with the bottom electrode.

The energy scale of the x-axis, according to the conservation of energy, is equal to

$$h\nu - E_{\mathrm{bin}} = E_{\mathrm{k}} + \Phi_{\mathrm{s}}, \tag{6.7}$$

where Φ_{s} is the work function of the sample and E_{k} is the kinetic energy of the electron. For the sample with the insulating a-PCMO, a shift of 0.1 eV towards higher $h\nu - E_{\mathrm{bin}}$ was measured in the Pt reference spectra, probably due to charging. The spectra were charge corrected to the highest photon energy of 5.3 eV.

As can be seen in Figure 6.9, the highest energy values correspond to the maximum energy of the photon source. The lowest energy value corresponds to electrons with a kinetic energy of 0 eV, which includes the secondary electron cutoff. If the kinetic energy is $E_{\mathrm{k}} = 0$ eV, then the value of the x-scale directly represents the work function of the material (Equation 6.7). This values were increased by 0.1 eV to consider the eletric field induced reduction, as described in Chapter

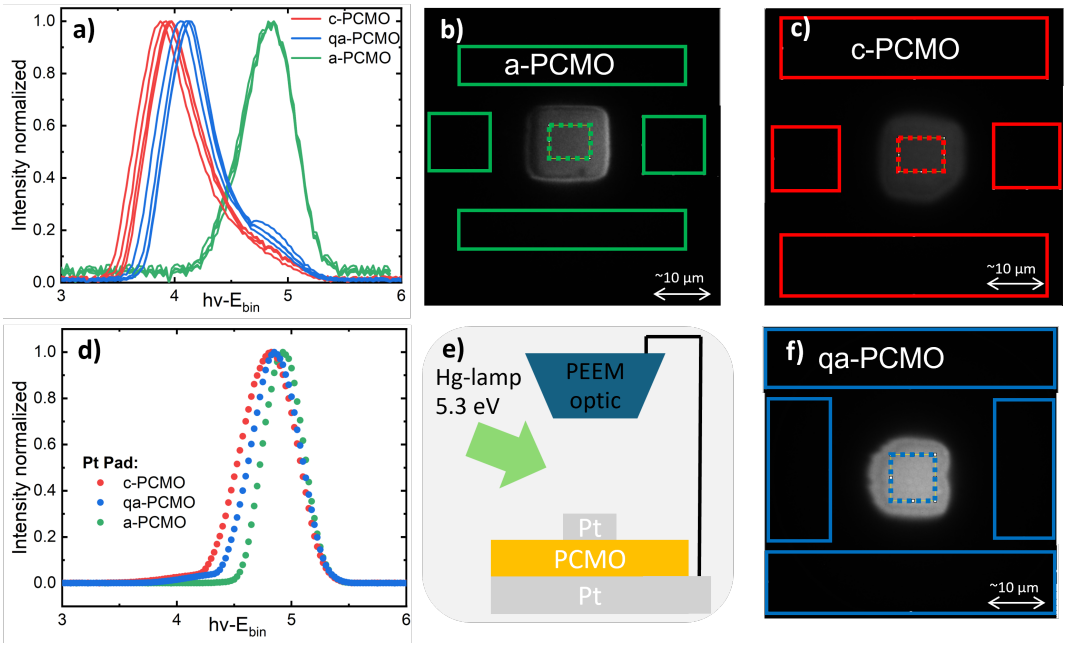

Figure 6.9.: The PEEM images presented here show the three PCMO samples (Figure b: a-PCMO, Figure c: c-PCMO and Figure f: qa-PCMO) and the deposited Pt top electrode. As shown in the accompanying schematic (Figure e), the samples are electrically grounded via the bottom Pt electrode. The data show the energy distribution of photoelectrons emitted from the Pt electrode (Figure d) as well as from the surrounding PCMO (Figure a).

3.7.2. Linear extrapolation of the secondary electron cutoff gives the averaged work functions summarized in Table 6.1.

6.5.2. Work function comparison

Work function values of the different PCMO types were determined by threshold photoelectron spectroscopy, as described in Section 6.5.1, and are listed in Table 6.1. We found that the work functions of c-PCMO and qa-PCMO are similar and lower than that of a-PCMO. The measured work functions were used to determine the valence band position in the band alignment calculations in Section 6.5.4, reflecting the relative differences between the various types of PCMO. A comparison of the determined values with the literature is limited as references are not available for amorphous PCMO at the time of this work. For crystalline PCMO, the available literature values typically refer to highly crystalline, often epitaxial grown samples. Moreover, the electronic structure at the surface of epitaxial grown PCMO is not necessarily comparable to the work function measured on a short-time post-annealed, highly polycrystalline PCMO surface. However, the direct measurements of the work function of epitaxial grown PCMO by Kelvin probe measurements [64] (Chapter 2.1.6) show values which are at least 0.6 eV higher than the measured value for c-PCMO. This work function difference could be caused by a oxygen reduction at the surface, during PEEM measurements due to the ultra-high vacuum and UV light illumination. DFT calculations on the work function of PCMO [65] showed that surficial oxygen reduction decreases the work function. Reducing conditions are also relevant at the active switching interface during device integration of PCMO with AlO_x, where the high thermodynamic potential of aluminum oxide can cause a reduction of PCMO during deposition [2]. Thus, using the low work function for subsequent band alignment calculations of PCMO/AlO_x interfaces is justified.

Table 6.1.: Work function values of the three different types of PCMO were determined from the secondary electron cutoff, measured using threshold emission in a photoelectron emission microscope. Band gap values of the three different types of PCMO were determined from the absorption edge (shown in Figure 6.10), as measured by UV/Vis reflection and transmission spectroscopy.

Material:	Work function (eV)	Band gap (eV)
c-PCMO	3.6 ± 0.4	0.6 ± 0.1
qa-PCMO	3.8 ± 0.4	2.0 ± 0.1
a-PCMO	4.4 ± 0.4	2.2 ± 0.1

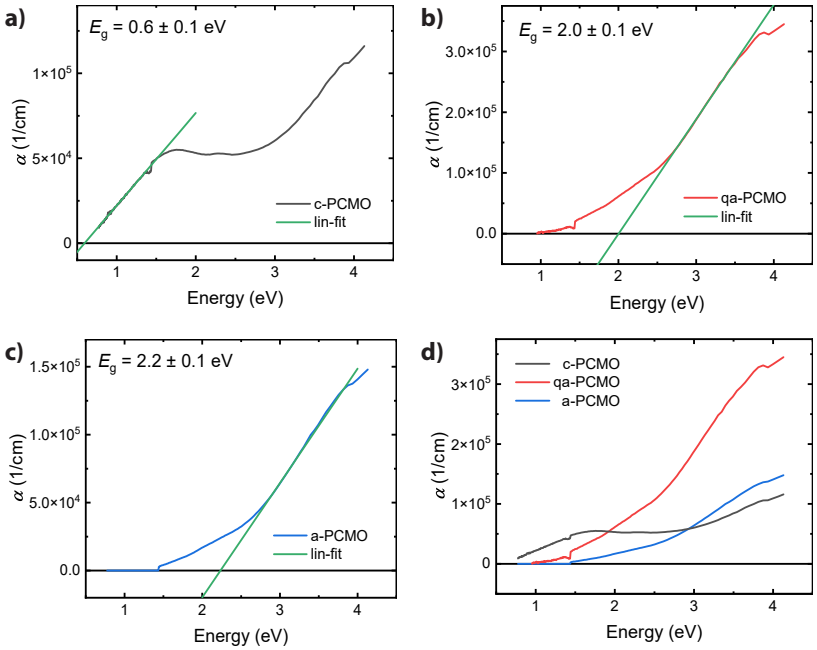

Figure 6.10.: All Figures show the normalized relative absorption coefficient α of PCMO as a function of photon energy. The band gap is determined by linear fitting in a), b), and c), for c-PCMO, qa-PCMO, and a-PCMO, respectively. In d), the spectra of a-PCMO, qa-PCMO, and c-PCMO are compared.

6.5.3. Band gap determination by UV/Vis and STS

PCMO was deposited on transparent fused silica to allow the measurement of transmission (T, in %) and reflection (R, in %). Measurements were performed with a LAMBDA 950 spectrophotometer from *PerkinElmer* (in a spectra range from 1600 to 300 nm) coupled to an integrating sphere. The measurements were carried out in collaboration with Karsten Bittkau as part of this PhD project. Combining transmission (T) and reflection (R), and assuming a Lambert-Beer decay, yields the following relation with the thickness d and the absorption coefficient α:

$$T = (1 - R)e^{-\alpha d}. \tag{6.8}$$

The α absorption spectra were plotted against photon energy (see Figure 6.10). The band gap was determined by linear fitting of the main absorption edges. The tails of the absorption edges of a-PCMO and qa-PCMO can be considered as Urbach tails, as is typical for amorphous materials [212]. Therefore, they were excluded from the band gap determination.

Scanning tunneling spectroscopy (STS) measurements were performed on a-PCMO, qa-PCMO,

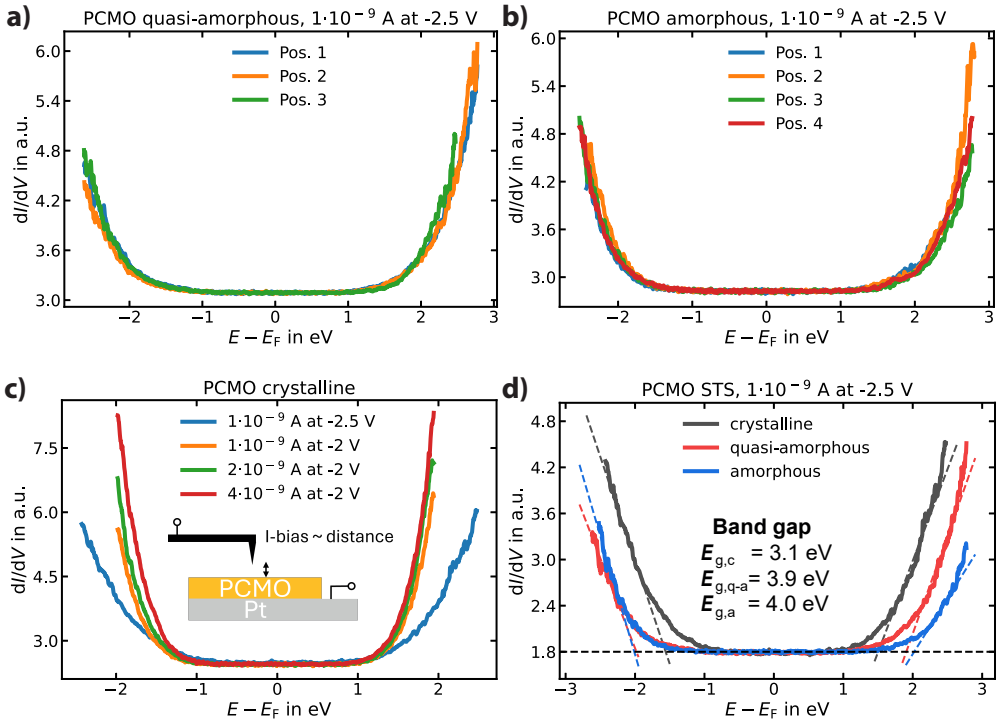

Figure 6.11.: dI/d$V - V$ curves of a) qa-PCMO and b) a-PCMO illustrating the spatial reproducibility. c) shows the dependence of the dI/d$V - V$ curves on the tip-sample distance for c-PCMO. The distance is adjusted according to the schematic drawing inset in d), either by changing the tunnel current for a constant bias or by changing the bias for a constant current. d) A comparison of the differential conductance of the STS measurement on c-PCMO, a-PCMO, and qa-PCMO is presented. Band edges were determined by linear extrapolation of the valence and conduction band edges.

and c-PCMO deposited on Pt. The measurements were carried out in collaboration with Yen-Po Liu as part of this PhD project. The platinum electrode, which serves as the bottom electrode, was electrically connected to the sample STM holder, which was biased for tunneling measurements.

The STS measurements were performed with a LT-STM from *CreaTEC* operating at 5 K in UHV. The energy potential for STS is calibrated using the surface state of surface reconstructed Au (111) single crystal around -400 mV. In order to achieve stable tunneling on such high band gap materials, the tungsten tip of the STM was conditioned on the Au crystal with a high bias voltage of about +2.35 V and a tunnel current setpoint in the order of $5 \cdot 10^{-10}$A.

The differential conductance (dI/dV) was recorded in parallel with the tunnel current using a lock-in amplifier modulating the DC bias with an AC signal at a frequency of 383 Hz and a nominal peak-to-peak amplitude of 100 mV. The lock-in amplifier is operated in automatic phase lock mode, resulting in an arbitrary offset of the dI/dV signal in the measurement.

The measurements shown are the result of an averaging process that combines five spectra to reduce the noise level. To ensure a stable and reproducible STS, the measurements are performed repeatedly with the same voltage and current setpoint for multiple regions on each sample. This approach excludes surface inhomogeneities and ensures reproducibility, as shown in Figure 6.11a and b.

The tip-sample distance is defined in relation to the tunneling parameters. For example, a higher tunneling current setpoint at a fixed bias would result in a shorter distance, and vice versa. Additional measurements with varying tip-sample distances are performed by varying the bias voltage or bias current (see Figure 6.11c). The results of these measurements show a slight

Table 6.2.: Valence band edge, conduction band edge and resulting band gap relative to the Fermi level as determined by scanning tunneling spectroscopy. Δ_{gap} is the increase in band gap measured by STS compared to the band gap measured by UV/Vis. Δ_{WF} is the theoretical contact potential between W-tip with an assumed work function of 4.5 eV and PCMO with a work function determined by PEEM. All values are in eV.

	STS (eV)			UV/Vis (eV)	Δ (eV)	Δ (eV)
	VB-edge	CB-edge	Band gap	Band gap	gap	WF
c-PCMO	-1.6	1.5	3.1	0.6	2.5	0.9
qa-PCMO	-2.0	1.9	3.9	2.0	1.9	0.7
a-PCMO	-2.0	2.0	4.0	2.2	1.8	0.1

decrease in band gap with decreasing tip-sample distance. Furthermore, no in-gap state is seen even for short tip-sample distances.

Figure 6.11 shows the differential conductance of c-PCMO, a-PCMO, and qa-PCMO. The valence band (VB) edge and the conductance band (CB) edge were determined by linear extrapolation of the band edges and their intersection with the linear approximation of the differential conductance within the band gap. The determined band edges and corresponding band gaps are summarized in the Table 6.2.

The band edges are very symmetrical in the differential conductance spectrum, indicating that the Fermi level is in the center of the band gap. This phenomenon could be explained by the dopant states frozen-out and the surface states caused Fermi level pinning. Since the thermal energy at 5 K is about 0.4 meV, which is much lower than the polaron binding or activation energy [53], the hole-doped polaronic states can be frozen-out, thus shifting the Fermi level to the center of the band gap. Additionally, also the presence of surface states could cause Fermi level pinning in the center of the band gap.

The measured STS band gaps show the same relative trends as the UV/Vis measurements. The band gap of a- and qa-PCMO is about 1 eV larger than that of c-PCMO. In addition, the band gap of qa-PCMO is observed to be slightly smaller (0.1 eV) than that of a-PCMO. However, the band gaps measured by STS are significantly larger than those measured by UV/Vis. The increases Δ_{gap} are 2.5 eV for c-PCMO, 1.9 eV for qa-PCMO and 1.8 eV for a-PCMO (see Table 6.2). The absolute increase in band gap Δ_{gap} can be attributed to the following factors:

1. Tip Induced Band Bending (TIBB).
2. Differences between the surface electronic state measured by STS and the bulk electronic state measured by UV/VIS.
3. A change in band gap with temperature.

To evaluate the influence of the tip-sample interaction on the band gap measured by STS, simulations were performed using the SEMITIP software by R. M. Feenstra [213, 214]. From SEMITIP the Uni3 simulation was used to evaluate the effect of tip distance and the Uni1 model was used for geometry independent 1d simulations. The material parameters for the PCMO were assumed to be a dielectric constant of 30 [69] and an effective mass of $69 \cdot m_e$. The effective mass was estimated by the Drude model, using a mobility of 0.015 cm^2/Vs [81] and a scattering frequency equal to the phonon mode controlling polaron formation of 17 THz [44]. TIBB simulations show asymmetry depending on the contact potential. Since, as discussed above, no contact potential dependence was observed due to potential Fermi level pinning by surface states, but no further details about these states are known, for simplicity the contact potential and the surface state density were set to zero for TIBB simulations to obtain symmetric TIBB and to evaluate the effect of other parameters.

Assuming that TIBB contributes to Δ_{gap} by varying the acceptor or donor concentration in the simulation model, the following trends emerge. Assuming strong hole doping based on the formal calcium hole doping of $5.3{\cdot}10^{21}/\mathrm{cm}^3$ (Section 6.3.1), TIBB would be insignificant. Further, assuming weak hole doping, TIBB would be strongly asymmetric, neither of which was observed. Only an extremely low carrier density would explain the strongly symmetric TIBB, which can be explained by a freeze-out of the carriers. However, some observed trends are not fully consistent with what would be expected for TIBB. TIBB generally increases with shorter tip-sample distances, while Figure 6.11 shows an opposite trend. This can be explained by an increase in state sensitivity for shorter tip-sample distances [215], compensating the effect on TIBB. Furthermore, the highest Δ_{gap} was observed for crystalline PCMO, which has the lowest band gap, even though TIBB is expected to increase with band gap. A discrepancy between bulk and surface electronic states may contribute to this behavior. The transition from a crystalline bulk to an amorphous surface could account for the observed increase in band gap.

In addition, the band gap increase can be caused by the low measurement temperature of 5 K, as reported in the literature. Epitaxial or bulk crystalline PCMO forms an insulating charge-ordered state below 240 K, which forms an antiferromagnetic order and associated charge ordering below a Neel temperature of 170 K. The charge ordering is accompanied by the formation of a pseudo-gap as measured in STS, e.g. by Singh et al. [216] or Kar and Raychaudhuri [217]. The measured pseudo-gap is 0.3 eV at 78 K and decreases with temperature. However, this literature has measured the pseudo-gap in highly crystalline PCMO and explained it with the formation of a charge-ordered antiferromagnetic state, and the formation of magnetic or charge long-range order is not possible for amorphous materials.

The band gaps of all three types of PCMO were determined by UV/Vis spectroscopy and are listed in Table 6.1. The band gaps of qa-PCMO and a-PCMO are similar and larger than that of c-PCMO. This trend was confirmed by scanning tunneling spectroscopy at low temperatures (5 K). Even lower band gap values have been reported in the literature for epitaxial PCMO (see [53] and [45]). However, absorption behavior at lower energy values was not investigated in this study due to the limitations of the measurement range, which spanned from 0.8 eV to 4.1 eV.

Furthermore, the pronounced granular polycrystalline nature of c-PCMO, with its grain boundaries and possible amorphous regions, may have influenced the measured transmission, complicating direct comparison with epitaxial PCMO. Nevertheless, the relative differences in the band gaps among c-PCMO, a-PCMO, and qa-PCMO are evident.

The measured band gaps were further used to determine the conduction band position for the band bending calculations. However, the exact band gap values do not significantly impact our analysis, as the majority charge carriers are located in the valence band, whose position in the band diagram is defined by the work function.

6.5.4. Band alignment

To calculate the band alignment of the three different heterostructures, the positions of the valence and conduction band edges were assumed as shown in Figure 6.12a. Due to its high Ca doping and the resulting mixed valence of manganese, $Pr_{0.7}Ca_{0.3}MnO_3$ is expected to have a hole concentration of $5.5{\cdot}10^{21}/\mathrm{cm}^3$, as discussed in Section 6.3.1. Assuming that the holes lie directly at the valence band edge, thereby shifting the Fermi level to that position, the measured work function can be directly used to determine the valence band edge in Figure 6.12a. The position of the conduction band edge was then calculated using the measured band gap as the energy difference.

The conduction band edge of Pt was estimated using a literature value for the effective work function, measured specifically at the interface with sputtered aluminum oxide [218].

The conduction and valence band edges of aluminum oxide were estimated using literature

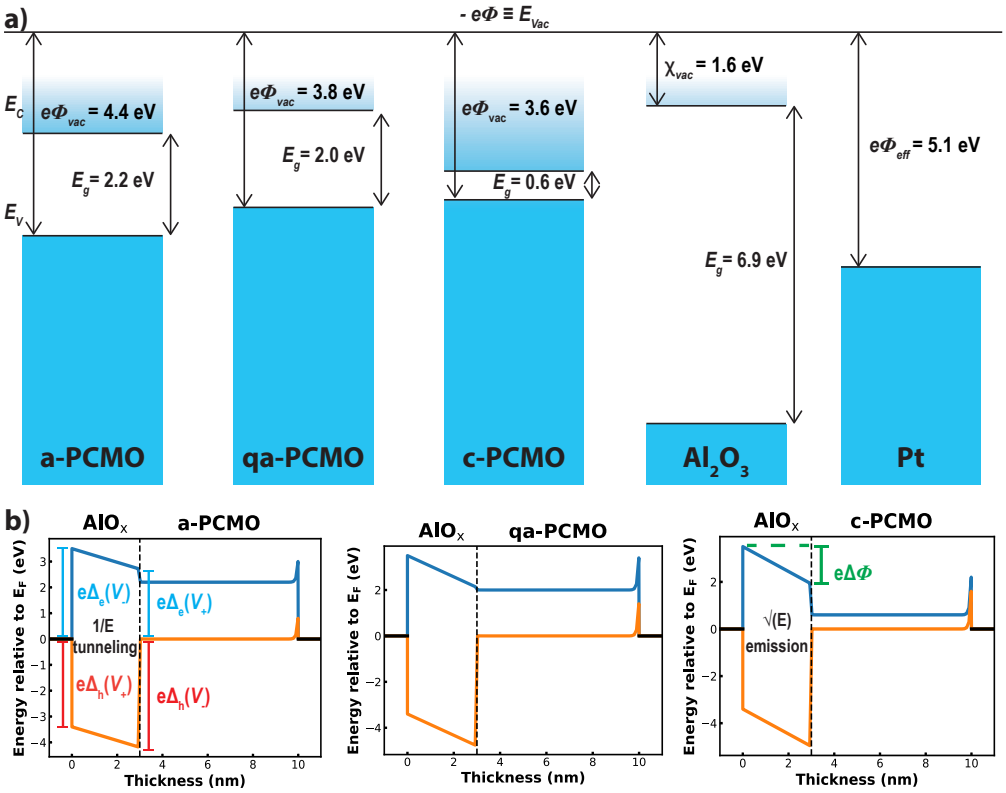

Figure 6.12.: **a)** Comparison of the electronic structures of the materials involved in the PCMO devices. This study determined the band gap and work function of a-, qa-, and c-PCMO. The electron affinity and band gap of aluminum oxide were obtained from Lewandkow et al. [218]. The effective work function of Pt on aluminum oxide was taken from [219]. **b)** The resulting band alignment of the Pt/AlO_x/PCMO/Pt devices was determined for all three PCMO device types, and the influence of the built-in voltage on the asymmetry of the conduction mechanisms is illustrated.

values for the electron affinity and band gap, based on measurements of sputtered amorphous aluminum oxide [218].

The one-dimensional Poisson equation

$$\frac{\mathrm{d}^2\Phi(x)}{\mathrm{d}x^2} = -\frac{\rho(x,\Phi(x))}{\epsilon} \tag{6.9}$$

was used to calculate the band alignment via the electric potential, Φ. Here, ρ is the charge density and ϵ is the permittivity of the oxides. The $e\Phi_{\mathrm{vac}}$ work function of the two platinum electrodes, which are assumed to be perfect conductors, was used as Dirichlet boundary conditions to solve this ordinary differential equation for $\Phi(x)$ in the $AlOx_x$/PCMO region. For the calculations, a Python-based model was used, which was developed by Clemens Wittberg within his master's thesis and adapted in close collaboration for this material system.

The assumed permittivities are $30\,\epsilon_0$ for PCMO [69] and $10\,\epsilon_0$ for AlO_x [220]. The Poisson equation was separated into a system of two first-order ordinary differential equations and solved using the SciPy function solve_bvp [221], while accounting for the continuity of the electric displacement field $\epsilon_{\mathrm{AlO_x}} E_{\mathrm{AlO_x}} = \epsilon_{\mathrm{PCMO}} E_{\mathrm{PCMO}}$ at the PCMO/$AlOx_x$ interface.

The charge carrier $\rho(x,\Phi(x))$ depends on the height of the Fermi level via the integral of the Fermi-Dirac distribution over the density of states (DOS) of the material. The details of the implementation for $\rho(x,\Phi(x))$ are described in Section 6.5.5. For AlO_x, the DOS of the conduction and valence bands is based on simplified parabolic band approximations using the effective mass

of the charge carriers. The effective electron and hole masses in the AlO_x were assumed to be $0.4{\cdot}m_e$ [222] and $7.5{\cdot}m_e$ [223], respectively.

For PCMO, the DOS is mainly controlled by the high hole density at the valence band edge. The parabolic band approximation was parameterized with an effective mass of 69 m_e. This value was estimated using the Drude model, assuming a mobility of 0.015 cm^2/Vs [81] and a scattering frequency equal to that of the phonon mode controlling polaron formation (17 THz) [44]. However, this assumption has little impact on the calculated band bending, as the charge carrier density in PCMO is primarily determined by its hole doping.

The calculated band alignment for all three types of PCMO devices is shown in Figure 6.12b. A representative AlO_x thickness of 3 nm was used, and, purely for graphical purposes, a 7 nm-thick PCMO layer was chosen. Thicker PCMO layers would not further affect the band alignment, as the space charge zones are much smaler then the PCMO layer thickness.

The calculated band diagrams (Figure 6.12b) show band bending at both PCMO interfaces due to the built-in potential with the Pt electrode, which is 1.6 V for c-PCMO, 1.4 V for qa-PCMO, and 0.8 V for a-PCMO. At the active switching interface (AlO_x/PCMO), in all cases, nearly the entire built-in potential drops across the AlO_x. This behavior arises from the requirement that the normal component of the electric displacement field must be continuous. Since the hole concentration in PCMO is high, the band bending directly at the PCMO interface can already exhibit high curvature, thereby causing a strong voltage drop $\Delta\Phi$ across the AlO_x.

On the other side of the PCMO, at the Pt/PCMO interface, the built-in potential induces a hole accumulation region within the PCMO for all types. However, this region is not further considered in the subsequent analysis of the heterostructure's conduction behavior, as the PCMO/Pt contact is known to behave ohmic [2]. The negligible influence of this accumulation region is due to its extremely thin width (approximately 0.5 nm), which results from the high hole concentration in PCMO.

6.5.5. Density of states for the band alignment model

The charge carrier density $\rho(x, \Phi(x))$, as integrated in the Python based model, consists of the integral of the Fermi-Dirac distribution f, evaluating the contributions from the density of states (DOS) of the acceptors g_a, the donors g_d, and from the DOS given by the parabolic band approximation for the valence band $g_{\mathrm{v-band}}$ and the conduction band $g_{\mathrm{c-band}}$, as follows:

$$\begin{aligned}\rho(x,\Phi(x)) =& e\int_0^{E_\mathrm{g}} dE\, g_\mathrm{d}(E_\mathrm{V}(\Phi(x))+E)[1-f(E_\mathrm{V}(\Phi(x))+E,T)] \\ &- e\int_0^{E_\mathrm{g}} dE\, g_\mathrm{a}(E_\mathrm{V}(\Phi(x))+E) f(E_\mathrm{V}(\Phi(x))+E,T) \\ &+ e\int_0^{\infty} dE\, g_{\mathrm{v-band}}(-E)[1-f(E_\mathrm{V}(\Phi(x))-E,T)] \\ &- e\int_{E_\mathrm{g}}^{\infty} dE\, g_{\mathrm{c-band}}(E-E_\mathrm{g}) f(E_\mathrm{V}(\Phi(x))+E,T).\end{aligned} \tag{6.10}$$

The VBM $E_\mathrm{V}(\Phi(x))$ can be calculated via

$$E_\mathrm{V}(\Phi(x)) = e\Phi(x) + e\phi_\mathrm{m} - e\chi_\mathrm{oxide} - E_\mathrm{g} \tag{6.11}$$

for the metal work function ϕ_m, the oxide electron affinity χ_oxide and band gap E_g.

The electron DOS for electrons with an effective mass m_e^* in the parabolic conduction band are

given by

$$g_{\mathrm{c-band}}(E) = \begin{cases} \frac{1}{2\pi^2}\left(\frac{2m_e^*}{\hbar^2}\right)^{3/2}\sqrt{E}, & \text{if } E \geq 0 \equiv E_{\mathrm{C}}, \\ 0, & \text{if } E < 0 \equiv E_{\mathrm{C}}. \end{cases} \tag{6.12}$$

and equivalently

$$g_{\mathrm{v-band}}(E) = \begin{cases} \frac{1}{2\pi^2}\left(\frac{2m_h^*}{\hbar^2}\right)^{3/2}\sqrt{E}, & \text{if } E \leq 0 \equiv E_{\mathrm{V}}, \\ 0, & \text{if } E > 0 \equiv E_{\mathrm{V}}. \end{cases} \tag{6.13}$$

the DOS for holes with an effective mass m_h^* in the parabolic valance band.

Lastly

$$f(E,T) = \frac{1}{1+\exp\left(\frac{E-E_{\mathrm{F}}}{k_B T}\right)} \tag{6.14}$$

denotes the the Fermi-Dirac distribution $f(E_{\mathrm{V}}(\Phi(x)) + E, T)$ for a temperature T and the Fermi level E_{F}.

6.5.6. Discussion of band alignment, conduction type and asymmetry

The band alignment calculation in Figure 6.12b can be used to interpret the correlation between conduction type and asymmetry found in Section 6.4.2.

The observed $\frac{1}{V}$ conduction behavior was attributed to tunneling through a triangular potential barrier, with the barrier height governing the tunneling current [210, 211]. Since the majority charge carriers are considered to be holes, the relevant barrier heights, $\Delta(V^-)$ and $\Delta(V^+)$, are referenced to the valence band edge of AlO_x, as illustrated in Figure 6.12b.

If a negative voltage V^- is applied to the top electrode, the resulting barrier height $\Delta(V^-)$ is given by the difference between the PCMO work function and the valence band edge of AlO_x. For the reverse direction, when a positive voltage V^+ is applied, the barrier height is given by the difference between the Pt work function and the valence band edge of AlO_x ($\Delta(V^+)$). Since Figure 6.12b shows that $\Delta(V^-) > \Delta(V^+)$ for all PCMO types, this asymmetry can account for the observed $R(V^-) > R(V^+)$ behavior associated with the $\frac{1}{V}$ conduction mechanism.

The observed $\sqrt{|V|}$ conduction behavior can be attributed to Poole-Frenkel emission, in which the characteristic $\sqrt{E}$ dependence arises from the electric field-induced lowering of the Coulombic emission barrier associated with a trap, or to Schottky emission [210, 211]. The applied voltages V^- and V^+ are modified by the built-in potential $\Delta\Phi$ across the AlO_x, resulting in effective voltages of $|V^-| + \Delta\Phi$ and $|V^+| - \Delta\Phi$, respectively, as illustrated in Figure 6.12b. This results in an asymmetry, as $|V^-| + \Delta\Phi > |V^+| - \Delta\Phi$, which explains the observed resistance asymmetry $R(V^-) < R(V^+)$ associated with this conduction behavior.

The same conclusion between asymmetry and *I-V* characteristics can also be drawn for electron transport, where the barrier Δ_e leads to the same conclusion for the inverse direction of charge transport.

A possible reason for this change in conduction type in qa-PCMO could be a more significant change in trap density in AlO_x during switching, compared to c-PCMO. In the LRS, the trap density is high, enabling Poole-Frenkel emission, while in the HRS, the trap density is too low for Poole-Frenkel emission to occur. Since this vacancy exchange, and thus the change in trap density, can be expected to be more significant closer to the PCMO interface, this could also explain why no change in conduction mechanism occurs in the device with the thickest AlO_x layer of 5 nm..

6.5.7. Literature comparison

To place this work in the context of existing research, Table 6.3 summarizes publications that either study the c-PCMO / AlO_x system or analyze devices based on amorphous PCMO. Comparing this work with the literature shows that none of these papers provide a calculation of the band diagram of the devices and interpret it consistently with the asymmetry of the I-V loops and the transport mechanism. Furthermore, none of these papers have shown or analyzed the increased conductivity of amorphous PCMO deposited at 400 °C. Also, the investigated literature lacks a proper analysis of the influence of the AlO_x thickness, since the AlO_x is mostly not directly deposited but is formed after the deposition of an Al contact electrode. Many studies in the literature also do not examine the underlying conduction mechanisms, and in those that do, often describe the charge transport across the defective interfacial AlO_x by Poole–Frenkel emission. Furthermore, the change in the conduction mechanism during switching is also observed in the literature.

Many papers misidentify PCMO conduction as space charge limited current (SCLC). SCLC assumes current reduction by space charge from injected carriers [224, 86], but PCMO's very high intrinsic carrier density, due to its mixed valency, makes this mechanism inappropriate. Transport in crystalline PCMO is instead well described by polaronic conduction [34, 2]. For amorphous PCMO, no transport model is firmly established. Several studies attribute conduction to SCLC (Table 6.3) while reporting high carrier densities.

Table 6.3.: Literature comparison with other PCMO/AlOx based devices.

Stack	Switching interface	PCMO morphology	CMOS compatible fabrication	Switching type	Switching Voltage	Conduction mechanism	Ref.
Pt/ PCMO/ ITO	Pt/PCMO interface claimed	amorphous	yes	area-dependent	set: 1.3 to 1.8 V, reset -1.35 to -1.85) V	SCLC	[114]
Pt/ PCMO/ TiN	Pt/PCMO interface claimed	amorphous	yes	area-dependent	set: 0.94 V, reset -1.3 V	SCLC	[110]
ITO/ZnO/ PCMO/ ITO	ZnO deposited	amorphous	yes	filamentary	set: -2.0 to -2.6 V, reset 2.0 to 2.3 V	SCLC	[113]
Ti/ PCMO/ Pt	Ti deposited and TiO_x formed	mixture crystalline and amorphous	yes	filamentary	set: -11 to -19) V, reset 10 to 17 V	not studied	[109]
Al/ AlO_x/ PCMO/ Pt	Al deposited and AlO_x formed	crystalline	no	bipolar	set: -4 V, reset +4 V	not studied	[225]
Pt/ Al/ AlO_x/ PCMO/ Pt	Al deposited and AlO_x formed	crystalline PCMO, amorphous interface	yes	bipolar	set: -3 V, reset +3 V	not studied	[14, 226]
Al/ AlO_x/ PCMO/ Pt	Al deposited and AlO_x formed	crystalline PCMO, amorphous interface	yes	bipolar	set: -3 V, reset +3 V	not studied	[15]
W/ PCMO/ Pt	W tip for measurement	crystalline	no	filamentary	set: $\sim$-3 V, reset 3.5 V	not studied	[127]
W/ PCMO/ Pt	W tip for measurement	amorphous	yes	unipolar	set: up to 14 V, reset 2-3 V	not studied	[127]
Pt/ Al/ AlO_x/ PCMO/ Pt	Al deposited, AlO_x formed	crystalline	no	area-dependent	set: -3 V, reset 2.2 V	not studied	[12]
Al/ AlO_x/ Mo / PCMO/ Pt	Al+Mo deposited, AlO_x, MoO_x formed	crystalline	not provided	area-dependent	set: -5 V, reset 3 V	not studied	[93]
Pt/ AlO_x/ TiN PCMO/ Pt	not provided	crystalline	no	area-dependent	set: -5 to -3 V, reset 2 to 5 V	not studied	[93, 227]
Al/ AlO_x/ PCMO/ Pt	Al deposited, AlO_x formed	crystalline	no	bipolar	set: -6 to -3 V, reset 3 to 6 V	HRS: Poole-Frenkel, LRS: SCLC	[228]
W/ Al/ AlO_x/ PCMO/ Pt	Al deposited, AlO_x formed	not provided	not provided	area-dependent	set: -3.5 V, reset 3.5 V	HRS: Poole-Frenkel, LRS: SCLC	[229]
Pt/ Al/ PCMO/ Pt	Al deposited, AlO_x formed	crystalline	no	area-dependent	set: -4 to -3.8 V, reset 2.5 to 2.6 V	AlO_x: Poole-Frenkel, PCMO: polaron hopping	[72]

6.6. Field distribution and on/off ratio

To further understand the switching process, it is essential to consider the ionic movement of vacancies. According to the Mott-Gurney law [2], the ionic drift velocity depends non-linearly on the electric field strength. Therefore, the influence of electric field strength on the resulting on/off ratio is analyzed in the following Section.

To investigate the voltage division within the memristive heterostructure, the non-linear dependence of conductivity on the electric field must be taken into account for both materials. Therefore, the conductivity σ of PCMO and AlO_x was implemented using a highly simplified exponential model:

$$\sigma = \alpha_{1,2} \cdot \exp(\beta_{1,2} \cdot E) \tag{6.15}$$

as employed by Gutsche et al. [72] in their study of the AlO_x/PCMO system. Here, $\alpha_{1,2}$ and $\beta_{1,2}$ are material-specific fitting parameters.

To investigate the spatial distribution of the electric field within this material model through $I-V$ characterization, a simulation model was developed using the COMSOL Multiphysics framework. The development of the COMSOL model was carried out by Iliyas Dossayev in close collaboration as part of this PhD project.

This model is based on solving the one-dimensional steady-state continuity equation for electric current using the finite element method while accounting for the spatially and field-dependent electrical conductivity. The continuity equation (Equation 6.16) governing steady-state electric current (Equation 6.17) is given by:

$$\nabla \cdot J = 0 \tag{6.16}$$

$$J = \sigma E, \quad \text{with} \quad E = -\nabla V \tag{6.17}$$

where J denotes the current density, E the electric field, and V the electric potential.

Using this model, the material-specific parameters $\alpha_{1,2}$ and $\beta_{1,2}$ were determined by fitting the simulated $I-V$ characteristics to the measurements of the single PCMO layers and their corresponding device types, as described in detail in Section 6.6.1.

The model was used to investigate the influence of the electric field strength in the AlO_x on the SET process, during which oxygen ions in the AlO_x are pushed into the PCMO by the electric field. Therefore, for each device type individually, the variation of the electric field within the AlO_x as a function of its thickness is shown in Figure 6.13. The electric field was therefore extracted from the HRS before the SET process, at -2.5 V, the highest voltage within the limits of the material fitting, providing the field distribution prior to switching.

Interestingly, the variation of the electric field with AlO_x thickness differs between device types. For qa-PCMO, the electric field decreases with increasing AlO_x thickness—as would be expected if the entire voltage drop occurs across the AlO_x and the field dependence of the resistance is neglected. In that case, the electric field in AlO_x is given by $E_{\mathrm{AlO_x}} = \frac{V_{\mathrm{AlO_x}}}{d}$, which scales inversely with the oxide thickness d. A-PCMO and c-PCMO (besides 5 nm) show the opposite behavior, with an increase in the electric field as the aluminum oxide thickness increases.

The electric field strength is further analyzed by its effect on the switching process, as reflected in the resulting on/off ratio. Since the on/off ratio strongly depends on the voltage at which the LRS and HRS are compared in the $I-V$ characteristic, it cannot be represented by a single value. Instead, Figure 6.13 shows the on/off ratio of the $I-V$ characteristic at every voltage.

The analysis shows, for each device type, a correlation between the increase in electric field within AlO_x and the increase in on/off ratio, confirming that the electric field in AlO_x drives oxygen ion migration during the SET process. To visually highlight this correlation, the aluminum oxide thicknesses that follow the trend are marked with stars in their on/off ratio characteristics, either at the voltage corresponding to the maximum on/off ratio or, if no such maximum exists, at a pre-switching voltage.

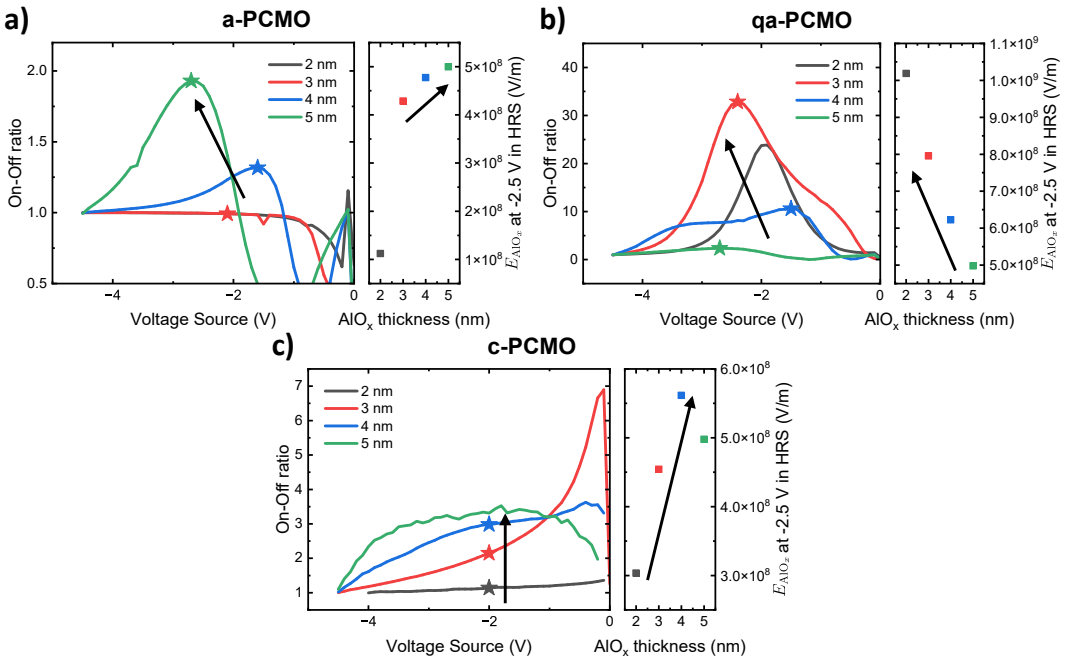

Figure 6.13.: Correlation between the on/off ratio of a) a-PCMO, b) qa-PCMO, and c) c-PCMO devices and the electric field in AlO_x at -2.5 V in the HRS, as a function of AlO_x thickness. To visually highlight this correlation, the curves that follow the trend are marked with stars in their on/off ratio characteristics, either at the voltage corresponding to the maximum on/off ratio, or, if no such maximum exists, at a pre-switching voltage.

For a-PCMO (Figure 6.13a), this correlation is particularly evident. It explains the opening of the $I - V$ loop at higher AlO_x thicknesses, where the increased resistance leads to a larger voltage drop across the AlO_x layer.

For qa-PCMO (Figure 6.13b), the decrease in E_{AlO_x} correlates well with the decrease in on/off ratio for 3, 4, and 5 nm AlO_x. The 2 nm device can be excluded from the analysis since the readout voltage of -2.5 V is already above the switching voltage, as can be seen in Figure 6.14a.

For c-PCMO devices, the enhanced electric field (Figure 6.13c) arising from the increase in AlO_x thickness from 2 nm to 4 nm, and the associated increase in resistance, promotes more pronounced oxygen vacancy migration during the resistive switching process. This, in turn, results in an increased ON/OFF ratio (Figure 6.13d), which can be attributed to enhanced Poole–Frenkel emission in the LRS. When the AlO_x thickness is further increased to 5 nm, the effective field strength is reduced, causing the ON/OFF ratio to saturate.

While the model effectively reproduces the experimental $I - V$ characteristics (see Section 6.6.1), it has limitations. The observed correlation between the electric field in AlO_x and the on/off ratio is intriguing but raises concerns of circular reasoning, as the model is based on fitting the same $I - V$ data it aims to explain. This risk is reduced by the fact that each resistive state is assigned its own set of material parameters, and conclusions are drawn across different branches of the $I - V$ loop, not within the same state. Notably, the model captures key trends in the on/off ratio without including time-dependent kinetics. The fact that this is possible with a time-independent model suggests that the ionic movement is mainly field-driven since temperature-accelerated kinetics exhibit strong time dependence [8].

Table 6.4.: Fitted α and β values of PCMO single layers.

Material	α **(S/m)**	β **(m/V)**
a-PCMO	2.08e-6	2.57e-8
qa-PCMO	1.21e-4	2.28e-8
c-PCMO	1.73e-3	3.23e-8

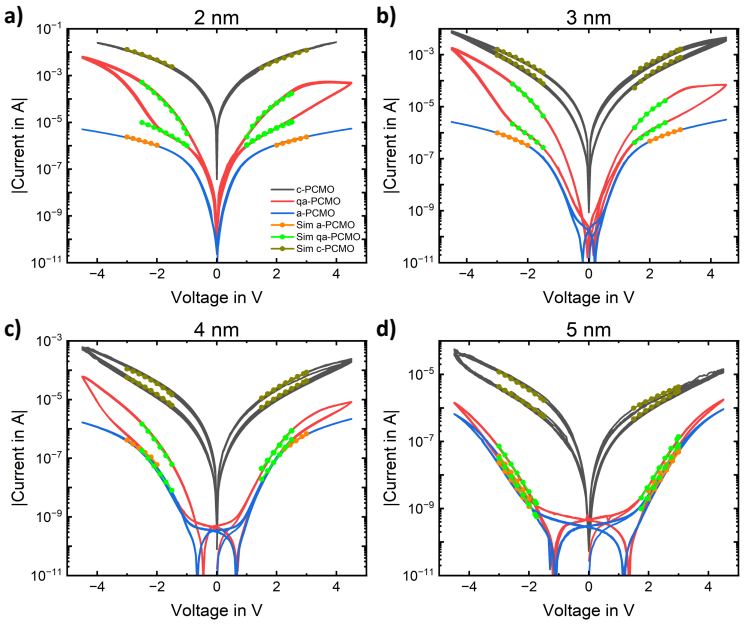

Figure 6.14.: Fitted $I - V$ characteristics using the material model for non-linear resistances.

6.6.1. Parametrization of non-linear resistance model

The material parameters $\alpha_{1,2}$ and $\beta_{1,2}$ for the non-linear resistance model were determined by Iliyas Dossayev by fitting the $I - V$ characteristic of the COMSOL model described in Section 6.6 to the $I - V$ characteristics measured at the single PCMO layers and their various device types.

The fitting process was initiated using the single PCMO layer resistances shown in Figure 6.6 f, g, and h. Data in the voltage range of 1.5 V to 5 V were used to determine the field-dependent conductivity parameters α and β shown in Table 6.4. The values extracted from the single-layer structures were subsequently used as initial constraints in modeling the complete multilayer device.

In fitting the complete stack, the α and β parameters associated with the tunnel oxide were treated as free variables to account for intrinsic variability in growth and conduction mechanisms. The α and β parameters corresponding to the PCMO layers were allowed to vary within one order of magnitude of their single-layer values.

The voltage range selected for the fitting process is between 1.5 V and 3 V, as shown in Figure 6.13. The upper voltage boundary was chosen to be as high as possible so that the model can extrapolate the electric field at switching voltages without already being in a voltage region where switching happens and, thus, conductivity is influenced by ionic mobility. The simulated $I - V$ characteristics based on the fitting model match the experimental data well, as shown in Figure 6.14. The resulting parameters for α and β are presented in Tables 6.5 and 6.6, respectively.

Table 6.5.: Fitted α values of PCMO and AlO_x from the device characteristics as a function of AlO_x thickness.

Values of α (S/m)								
nm	**PCMO**				**AlO_x**			
	LRS +	LRS -	HRS +	HRS -	LRS +	LRS -	HRS +	HRS -
a-PCMO:								
2	2.08E-06	2.08E-06			2.54E-09	2.54E-09		
3	2.01E-06	2.02E-06			2.50E-11	2.50E-11		
4	7.42E-07	7.49E-07			3.88E-10	2.13E-10		
5	7.44E-06	9.45E-06	1.35E-05	1.49E-05	3.73E-12	2.58E-12	1.53E-12	1.52E-12
qa-PCMO:								
2	2.32E-04	4.64E-04	1.21E-04	1.21E-04	7.09E-11	1.35E-09	6.14E-08	5.63E-08
3	1.21E-04	1.21E-04	8.06E-05	1.21E-04	5.51E-10	2.00E-12	5.81E-09	2.67E-09
4	1.21E-04	1.21E-04	8.06E-05	1.21E-04	2.49E-10	1.06E-10	4.46E-11	2.00E-11
5	1.21E-04	1.20E-04	1.21E-04	1.21E-04	3.28E-12	1.32E-12	4.85E-13	4.85E-13
c-PCMO:								
2	1.07E-02	1.04E-02			4.08E-08	6.52E-08		
3	1.41E-03	1.41E-03	1.4E-03	1.4E-03	1.07E-10	1.07E-10	1.71E-10	1.67E-10
4	1.12E-03	7.37E-04	1.11E-03	7.09E-04	5.46E-07	2.74E-07	3.57E-07	3.05E-07
5	1.41E-03	1.41E-03	1.41E-03	1.41E-03	1.50E-07	1.52E-07	4.63E-08	4.69E-08

Table 6.6.: Fitted β values of PCMO and AlO_x from the device characteristics as a function of AlO_x thickness.

Values of β (m/V)								
nm	**PCMO**				**AlO_x**			
	LRS +	LRS -	HRS +	HRS -	LRS +	LRS -	HRS +	HRS -
a-PCMO:								
2	2.67E-08	2.67E-08			5.60E-08	5.60E-08		
3	3.08E-08	3.08E-08			2.70E-08	2.01E-08		
4	1.28E-07	1.27E-07			1.18E-08	1.09E-08		
5	2.57E-08	2.57E-08	2.57E-08	2.57E-08	1.35E-08	1.31E-08	1.44E-08	1.31E-08
qa-PCMO:								
2	2.28E-08	2.22E-08	8.59E-08	1.71E-07	2.78E-09	2.78E-09	1.89E-08	1.30E-08
3	1.25E-08	2.22E-08	4.36E-08	1.11E-07	4.66E-09	5.29E-09	1.35E-08	2.89E-08
4	1.25E-08	2.28E-08	2.28E-08	2.22E-08	1.08E-08	1.06E-08	1.03E-08	1.16E-08
5	2.28E-08	2.28E-08	2.28E-08	2.22E-08	1.55E-08	1.40E-08	1.48E-08	1.37E-08
c-PCMO:								
2	3.86E-08	3.86E-08			3.04E-08	3.49E-08		
3	4.76E-08	4.76E-08	4.79E-08	4.85E-08	4.78E-08	4.69E-08	2.75E-08	3.06E-08
4	4.76E-08	1.73E-08	4.76E-08	4.71E-08	4.88E-09	8.00E-09	4.47E-09	5.53E-09
5	4.70E-08	4.70E-08	4.72E-08	4.67E-08	2.61E-09	4.37E-09	4.08E-09	4.59E-09

6.7. Discussion of the PCMO and aluminum oxide interaction during switching

It is well known in the literature that the resistive switching in the PCMO/ AlO_x heterostructures arises from oxygen vacancy exchange between the PCMO and the AlO_x [2]. This is consistent with the observed bipolar switching. A negative bias applied to the Pt/AlO_x top electrode leads to an increase in oxygen vacancy concentration within AlO_x, where they cause defect states within its band gap [230, 231, 232], which decrease the resistance by increasing transport via Poole-Frenkel emission or trap-assisted tunneling (Figure 6.12b).

Therefore, the amount of oxygen vacancies in AlO_x is higher in the LRS and lower in the HRS, while the opposite is true for the PCMO. In PCMO, the vacancies can have the opposite effect on the resistance, which increases by interrupting the Mn-O-Mn bonds. However, this effect is only well documented in the literature for crystalline PCMO [2]. Thus, the resistance response of both materials can be complementary to the movement of oxygen vacancies through the switching [226].

Since our analysis of the AlO_x thickness dependence (Section 6.4) showed that the overall device resistance is predominantly governed by transport through the AlO_x layer, we can conclude that variations in the PCMO resistance play only a minor role in the total resistance change of the device.

However, the PCMO affects the conduction mechanism in the AlO_x by modifying the number of vacancies present in the AlO_x. One influence is its effect on the electric field distribution, as shown in Section 6.6, which drives vacancy migration and thereby affects the number of vacancies displaced during a switching event. Another influence of the PCMO occurs in the AlO_x during the initial growth. As shown by the in-situ transfer XPS measurements of Section 5.2, AlO_x grown on the rough surface of c-PCMO shows a high oxygen vacancy concentration.

This high vacancy concentration could be the reason why the transport through the AlO_x for c-PCMO devices shows Poole-Frenkel emission in the HRS and LRS (Figure 6.7), while qa-PCMO devices show this transport mechanism only in the LRS (Figure 6.8) due to the increase in vacancies in the AlO_x caused by the switching. Since this vacancy exchange can be expected to be more significant closer to the PCMO interface, but the electron transport happens across the full AlO_x, this can explain the missing change of conduction mechanism for a thicker AlO_x of 5 nm.

Another effect of the PCMO on the transport across the AlO_x originates from its electronic structure, especially its work function, which influences the band bending (Figure 6.12b) and thus determines which defect levels are available for tunneling and affects the emission barriers. The fact that only qa-PCMO devices, and not a-PCMO devices, show changes in the LRS from tunneling to Poole-Frenkel emission could be due to the differences in work function. While qa-PCMO and c-PCMO have similar work functions, the work function of a-PCMO is higher (Section 6.5.2).

Since the c-PCMO devices with Poole–Frenkel emission have the highest conductivity of all (Figure 6.6), and the change to Poole-Frenkel emission results in a high conductivity increase for qa-PCMO, we conclude that Poole–Frenkel emission leads to higher conductivity as a tunneling process. Further, this change in the conduction mechanism also leads to the highest ON/OFF ratio. In a-PCMO/ AlO_x and c-PCMO/ AlO_x devices, switching modulates the magnitude of the current without altering the underlying conduction mechanism, which shows a lower ON/OFF ratio than the qa-PCMO/ AlO_x devices, where the transport mechanism changes. From a device performance perspective, this suggests that switching-induced changes in conduction mechanisms may be more beneficial than merely modulating a fixed transport process.

7. Conclusion and outlook

The following conclusion and outlook are based on the papers [1, 2, 3].

7.1. Conclusion

In Chapter 4, a process for the homogeneous pulsed laser deposition of PCMO on a 4-inch wafer was developed. Therefore, simulation software was used to model the deposition profiles for different substrate movement strategies. Using this approach, two movement strategies were identified that resulted in homogeneous deposition. One strategy involves moving the beamline quickly while moving the substrate slowly, which showed the highest homogeneity in the simulation. The other strategy is to move both the beamline and the substrate quickly while finding an appropriate combination of both speeds for a given number of laser shots. Both strategies were experimentally verified, producing a homogeneous thin film of PCMO on 4" wafers.

With the developed LAPLD process, PCMO/AlO_x-based devices with well-defined, smooth interfaces were produced. The devices show area-dependent resistive switching for both amorphous and polycrystalline PCMO. The influence of the aluminum oxide thickness on the switching shows that the IV loop starts to exhibit a hysteresis for AlO_x thicknesses $\geq$ 3 nm. An increase in AlO_x thickness leads to an increase in resistance and capacitive charging. An additional thermal treatment reduces the resistance and switching voltage and increases the ratio between low and high resistive states. Devices without thermal treatment of the PCMO are compatible with the back-end-of-line processing (BEOL) of standard CMOS technology

Chapter 5 gives a comprehensive investigation of resistive switching in memristive devices based on amorphous, quasi-amorphous, and crystalline PCMO. Deposition at 400 ℃ leads to a resistance reduction of up to four orders of magnitude compared to deposition at room temperature while still preserving the amorphous structure. Structural analysis confirms the presence of short-range order, and a percolation model based on a disordered Mn-O_6 octahedral network is proposed to explain the differences in resistance. All three types of PCMO were integrated into Pt/AlO_x/PCMO/Pt heterostructures with AlO_x thicknesses from 2-5 nm, and their memristive behavior was studied via $I-V$ analysis. a-PCMO devices showed weak switching with $\log(R) \propto 1/E$-like conduction. qa-PCMO devices exhibited the highest on/off ratios, transitioning from $\log(R) \propto 1/E$ in HRS to $\log(R) \propto \sqrt{E}$ in LRS. c-PCMO devices had the highest current levels, dominated by $\log(R) \propto \sqrt{E}$-like conduction. The device characterization revealed that qa-PCMO/AlO_x heterostructures exhibit an enhanced on/off ratio compared to devices based on fully amorphous PCMO.

Using PEEM, UV/Vis spectroscopy, and STS, the work function and band gap of a-, qa-, and c-PCMO were measured. The obtained values were used to construct band diagrams for each PCMO type. This enabled a direct correlation between the observed conduction mechanisms in the $I-V$ characteristics, the asymmetry in the $I-V$ loops, and the underlying band alignments, allowing for a consistent interpretation of the switching behavior across different device types.

Simulations based on fitted $I-V$ curves show that the type of PCMO strongly influences the electric field distribution within the AlO_x tunnel barrier. This increase in field strength, which depends on the AlO_x thickness, correlates with a higher on/off ratio.

Overall, this work advances both the development of materials and the fundamental understanding of disordered PCMO systems, establishing qa-PCMO as a promising candidate for area-dependent memristive devices. Furthermore, it paves the way for future research on potential

advantages of area-dependent devices based on amorphous materials. Given that PCMO is one of the most technologically advanced material systems for area-dependent switching [2], these results have the potential to influence the technological development of area-dependent devices.

7.2. Outlook

Building on the findings of this thesis, the next steps outlined below are necessary to further explore the potential benefits of devices based on amorphous PCMO and further develop this device technology.

An important open question for the use of qa-PCMO in industrial relevant memory cells, is whether the area-dependent scaling of amorphous PCMO continues down to the nanoscale and if the resulting resistance range can be utilized for memory cells. If the resistance is too high at the nanoscale, the read-out current could become too low to be usable in a memory device. Further it has to be addressed whether amorphous PCMO exhibits improved scaling than polycrystalline PCMO, owing to its more homogeneous atomic structure and potentially reduced influence from grain boundaries and related effects.

Another potential benefits of qa-PCMO, which has to be investigated is, whether it offers enhanced stability against defect formation during device processing steps, particularly those involving high-energy or chemically aggressive techniques such as dry etching. If the amorphous structure improves the material's resilience to interface damage, this could provide a technological advantage over its polycrystalline counterpart. Thus qa-PCMO could enable improved reproducibility in integrated device stacks.

In order to further advance this technology and to quantify its potential as a competitive memory technology, research into the reliability of qa-PCMO-based devices will be required. In particular, endurance and retention must be assessed after CMOS integration. These studies should be based on a statistical evaluation of a large number of devices to ensure meaningful conclusions. This analysis would further contribute to the development of variability-aware compact models that allow reliable circuit simulations.

Another important question concerns the switching speeds achievable with qa-PCMO and whether nanosecond-scale operation is possible. Answering this will be essential to judge the suitability for high-speed non-volatile memory applications. Detailed studies of the switching kinetics could also provide deeper insights into the mechanisms of oxygen vacancy exchange and the roles of field acceleration and thermal effects. In PCMO device stacks, the lack of Joule heating, which enables gradual switching, can be accompanied by reduced switching speed, poorer retention and more pronounced read disturbance. This trade-off could be resolved by tailored stacking of materials or interface engineering to confine the field drop to the position where fast ion movement is required. Further, alternative material combinations for the qa-PCMO heterostructure may help reduce switching voltages. There is a lot of room for improvement with respect to the choice of material stacks for improved device performance.

To investigate the potential of qa-PCMO in neuromorphic computing, its performance in gradual multilevel switching must be evaluated. In this context, the influence of read-disturb effects should also be examined. Furthermore, programming algorithms need to be developed to optimize multilevel switching, to increase the retention of states and to improve the endurance.

Finally, it remains unclear how oxygen vacancies affect electronic transport and modify the band structure in detail, both in polycrystalline and amorphous PCMO. Extended DFT modeling could provide valuable insights; however, this is particularly challenging for amorphous atomic arrangements.

8. Acknowledgements

The results of this PhD thesis were made possible by a wide variety of experimental techniques and computational simulations, which required strong collaboration.

The following collaborations were essential for the experimental work:

The development of the deposition processes on the large-area pulsed laser deposition system was carried out in collaboration with *SURFACE systems + technology GmbH & Co. KG*, which built the system within the framework of the NEUROTEC project. The characterization of the effect of the slit system on STO deposition for use in the simulation software was carried out by Marc Pohlmann from *SURFACE*. Further collaboration on the LAPLD system was conducted with Zoe Moos and Zhenhao Liu. Many of the PCMO depositions at 400 °C, together with the analysis of film thickness and surface morphology by AFM and subsequent device fabrication, were carried out by Zhenhao Liu as part of his master's thesis, which was directly supervised within the framework of this PhD project.

The total X-ray scattering measurements were collected using the grazing-incidence diffraction and scattering setup provided by DESY Photon Science and carried out at PETRA III (P07, Experimental Hutch EH2). Assistance during the experiments was provided by Ann-Christin Dippel, Philipp Glaevecke, and Olof Gutowski. The measurements were performed in collaboration during beamtime (I-20230316) allocated to Hassan Sultani, under the supervision of Susanne Hoffmann-Eifert.

The photoelectron emission microscopy was performed by and in collaboration with Kalle Goß.

The spectrophotometer measurements were carried out in collaboration with Karsten Bittkau.

The STEM measurements of the PCMO devices were conducted by Pengfei Cao under the supervision of Joachim P. Mayer.

For the theoretical considerations and modeling, the following collaborations were essential:

The literature review was conducted in collaboration with Zoe Moos, Alexander Gutsche, Stephan Menzel, and Regina Dittmann.

The development of the simulation program for large-area pulsed laser deposition was carried out by Marc Pohlmann from *SURFACE systems + technology GmbH & Co. KG*.

The Python-based model used to calculate the band alignment was developed by Clemens Wittberg within the framework of his master's thesis and was adapted for the PCMO-based devices in close collaboration.

The development of the COMSOL model to analyze the field distribution in the PCMO devices, as well as the fitting of the $I-V$ characteristics to determine the material parameters, was carried out in close collaboration with Iliyas Dossayev, under the supervision of Stephan Menzel.

Further acknowledgments are due for the following:

The supervision of this PhD project, together with insightful discussions, helpful feedback, and stimulating input, was provided by Regina Dittmann.

The foundation on which this PhD project was built stems from the PhD project of Alexander Gutsche, who also provided a helpful introduction to the field and to the experimental methods used.

Additional thanks go to the remaining technical, scientific, and administrative staff of PGI-7 for their valuable cooperation and insightful discussions.

This work was funded by the Federal Ministry of Education and Research project NEUROTEC (grant No. 16ES1133K), NEUROTEC-II (grant No. 16ME0398K) and NeuroSys (03ZU1106AB)

(grant No. 03ZU1106AA – phase I, 03ZU2106AB – phase II) as part of the initiative Clusters4Future.

It is further declared that the AI tools ChatGPT and DeepL Write were used to improve the grammar and wording of the text in this work.

References

[1] M. Buczek et al. “Large area pulsed laser deposition of memristive $Pr_{0.7}Ca_{0.3}MnO_3$ heterostructures for neuromorphic computing”. In: *Thin Solid Films* 805 (Sept. 2024), p. 140499. ISSN: 0040-6090. DOI: 10.1016/j.tsf.2024.140499.

[2] Max Buczek et al. “$Pr_{1-x}Ca_xMnO_3$-Based Memristive Heterostructures: Basic Mechanisms and Applications”. In: *Chemical Reviews* (June 2025). ISSN: 0009-2665. DOI: 10.1021/acs.chemrev.4c00813.

[3] Max Buczek et al. “Amorphous, Highly Conductive Pr0.7Ca0.3MnO3 for Area-Dependent Resistive Switching AlOx Bilayer Devices”. In: *Advanced Electronic Materials* (Sept. 2026), e00556. ISSN: 2199-160X. DOI: 10.1002/aelm.202500556.

[4] Catherine D. Schuman et al. “Opportunities for neuromorphic computing algorithms and applications”. In: *Nature Computational Science* 2.1 (Jan. 2022), pp. 10–19. ISSN: 2662-8457. DOI: 10.1038/s43588-021-00184-y.

[5] Fernando Aguirre et al. “Hardware implementation of memristor-based artificial neural networks”. In: *Nature Communications 2024 15:1* 15.1 (Mar. 2024), pp. 1–40. ISSN: 2041-1723. DOI: 10.1038/s41467-024-45670-9.

[6] Yi Huang et al. “Memristor-based hardware accelerators for artificial intelligence”. In: *Nature Reviews Electrical Engineering* 1.5 (May 2024), pp. 286–299. ISSN: 2948-1201. DOI: 10.1038/s44287-024-00037-6.

[7] Dennis V. Christensen et al. “2022 roadmap on neuromorphic computing and engineering”. In: *Neuromorphic Computing and Engineering* 2.2 (2022). ISSN: 26344386. DOI: 10.1088/2634-4386/ac4a83.

[8] Regina Dittmann, Stephan Menzel, and Rainer Waser. “Nanoionic memristive phenomena in metal oxides: the valence change mechanism”. In: *Advances in Physics* 70.2 (Apr. 2021), pp. 155–349. ISSN: 0001-8732. DOI: 10.1080/00018732.2022.2084006.

[9] S. Bagdzevicius et al. “Interface-Type Resistive Switching in Perovskite Materials”. In: *Resistive Switching: Oxide Materials, Mechanisms, Devices and Operations*. Ed. by Jennifer Rupp, Daniele Ielmini, and Ilia Valov. Cham: Springer International Publishing, 2022, pp. 235–287. ISBN: 978-3-030-42424-4. DOI: 10.1007/978-3-030-42424-4_11.

[10] Stephan Menzel et al. “Physics of the Switching Kinetics in Resistive Memories”. In: *Advanced Functional Materials* 25.40 (Oct. 2015), pp. 6306–6325. ISSN: 1616-3028. DOI: 10.1002/ADFM.201500825.

[11] Stephan Menzel et al. “Origin of the Ultra-nonlinear Switching Kinetics in Oxide-Based Resistive Switches”. In: *Advanced Functional Materials* 21.23 (Dec. 2011), pp. 4487–4492. ISSN: 1616-3028. DOI: 10.1002/ADFM.201101117.

[12] Alexander Gutsche et al. “Exploring Area-Dependent $Pr_{0.7}Ca_{0.3}MnO_3$-Based Memristive Devices as Synapses in Spiking and Artificial Neural Networks”. In: *Frontiers in Neuroscience* Volume 15 - 2021 (2021). ISSN: 1662-453X. DOI: 10.3389/fnins.2021.661261.

[13] Akihito Sawa and Rene Meyer. “Interface-Type Switching”. en. In: *Resistive Switching*. John Wiley & Sons, Ltd, 2016, pp. 457–482. ISBN: 978-3-527-68087-0. DOI: 10.1002/9783527680870.ch16.

[14] Zhaoliang Liao et al. “Electroforming and endurance behavior of Al/$Pr_{0.7}Ca_{0.3}MnO_3$/Pt devices”. In: *Applied Physics Letters* 99.11 (Sept. 2011), p. 113506. ISSN: 00036951. DOI: 10.1063/1.3638059.

[15] Z. L. Liao et al. “Categorization of resistive switching of metal- $Pr_{0.7}Ca_{0.3}MnO_3$ -metal devices”. In: *Applied Physics Letters* 94.25 (June 2009), p. 253503. ISSN: 00036951. DOI: 10.1063/1.3159471.

[16] A. Asamitsu et al. “Current switching of resistive states in magnetoresistive manganites”. In: *Nature 1997 388:6637* 388.6637 (1997), pp. 50–52. ISSN: 1476-4687. DOI: 10.1038/40363.

[17] Roger A. De Souza. “Ion Transport in Metal Oxides”. In: *Resistive Switching*. John Wiley & Sons, Ltd, June 2016, pp. 125–164. ISBN: 978-3-527-68087-0. DOI: 10.1002/9783527680870.ch5.

[18] A Schulman, H Huhtinen, and P Paturi. “Manganite memristive devices: recent progress and emerging opportunities”. In: *Journal of Physics D: Applied Physics* 57.42 (July 2024), p. 422001. ISSN: 0022-3727. DOI: 10.1088/1361-6463/ad6575.

[19] Daeseok Lee and Hyunsang Hwang. “$Pr_{0.7}Ca_{0.3}MnO_3$ (PCMO)-Based Synaptic Devices”. In: *Neuro-inspired Computing Using Resistive Synaptic Devices*. Ed. by Shimeng Yu. Cham: Springer International Publishing, 2017, pp. 53–71. ISBN: 978-3-319-54313-0. DOI: 10.1007/978-3-319-54313-0_3.

[20] *4DS Memory investor hub*. URL: https://announcements.4dsmemory.com/announcements.

[21] C. Pithan et al. “Oxygen nonstoichiometry and electrical transport properties of $Pr_{1-x}Ca_xMnO_3$ ceramics”. In: *Journal of the European Ceramic Society* 42.15 (Dec. 2022), pp. 7049–7062. ISSN: 0955-2219. DOI: 10.1016/j.jeurceramsoc.2022.08.006.

[22] Elbio Dagotto, Takashi Hotta, and Adriana Moreo. “Colossal magnetoresistant materials: the key role of phase separation”. In: *Physics Reports* 344.1 (2001), pp. 1–153. ISSN: 0370-1573. DOI: https://doi.org/10.1016/S0370-1573(00)00121-6.

[23] H. Y. Hwang et al. “Lattice Effects on the Magnetoresistance in Doped $LaMnO_3$”. In: *Physical Review Letters* 75.5 (July 1995), pp. 914–917. DOI: 10.1103/PhysRevLett.75.914.

[24] H. Y. Hwang et al. “Pressure effects on the magnetoresistance in doped manganese perovskites”. In: *Physical Review B* 52.21 (Dec. 1995), p. 15046. ISSN: 01631829. DOI: 10.1103/PhysRevB.52.15046.

[25] R. D. Shannon. “Revised effective ionic radii and systematic studies of interatomic distances in halides and chalcogenides”. In: *Acta Cryst.* A32.5 (Sept. 1976), pp. 751–767. ISSN: 0567-7394. DOI: 10.1107/S0567739476001551.

[26] A. T. Kozakov et al. “Valence state of cations in manganites $Pr_{1-x}Ca_xMnO_3$ (0.3 <= x <= 0.5) from X-ray diffraction and X-ray photoelectron spectroscopy”. In: *Journal of Alloys and Compounds* 740 (Apr. 2018), pp. 132–142. ISSN: 0925-8388. DOI: 10.1016/J.JALLCOM.2018.01.002.

[27] P. W. Anderson and H. Hasegawa. “Considerations on Double Exchange”. In: *Physical Review* 100.2 (Oct. 1955), p. 675. ISSN: 0031899X. DOI: 10.1103/PhysRev.100.675.

[28] J. M. D. Coey, M. Viret, and S. von Molnár. “Mixed-valence manganites”. In: *Advances in Physics* 48.2 (Mar. 1999), pp. 167–293. ISSN: 0001-8732. DOI: 10.1080/000187399243455.

[29] Y. Tomioka et al. “Magnetic-field-induced metal-insulator phenomena in $Pr_{1-x}Ca_xMnO_3$ with controlled charge-ordering instability”. In: *Phys. Rev. B* 53.4 (1996), R1689–R1692. DOI: 10.1103/PhysRevB.53.R1689.

[30] B. Kressdorf et al. “Orbital-order phase transition in $Pr_{1-x}Ca_xMnO_3$ probed by photovoltaics”. In: *Physical Review B* 103.23 (June 2021), p. 235122. ISSN: 24699969. DOI: 10.1103/PhysRevB.103.235122.

[31] Doon Gibbs et al. “X-ray resonant scattering studies of orbital and charge ordering in $Pr_{1-x}Ca_xMnO_3$”. In: *Physical Review B* 64.19 (Oct. 2001), p. 195133. ISSN: 1550235X. DOI: 10.1103/PhysRevB.64.195133.

[32] Z. Jirák et al. “Neutron diffraction study of $Pr_{1-x}Ca_xMnO_3$ perovskites”. In: *Journal of Magnetism and Magnetic Materials* 53.1-2 (Nov. 1985), pp. 153–166. ISSN: 0304-8853. DOI: 10.1016/0304-8853(85)90144-1.

[33] Benedikt Ifland et al. “Current–voltage characteristics of manganite–titanite perovskite junctions”. In: *Beilstein Journal of Nanotechnology 6:152* 6.1 (July 2015), pp. 1467–1484. ISSN: 2190-4286. DOI: 10.3762/BJNANO.6.152.

[34] S Schramm, J Hoffmann, and Ch Jooss. “Transport and ordering of polarons in CER manganites PrCaMnO”. In: *Journal of Physics: Condensed Matter* 20.39 (Sept. 2008), p. 395231. ISSN: 0953-8984. DOI: 10.1088/0953-8984/20/39/395231.

[35] Ch Jooss et al. “Polaron melting and ordering as key mechanisms for colossal resistance effects in manganites”. In: *Proceedings of the National Academy of Sciences of the United States of America* 104.34 (Aug. 2007), pp. 13597–13602. ISSN: 00278424. DOI: 10.1073/PNAS.0702748104.

[36] M. Scherff et al. “Interplay of cross-plane polaronic transport and resistive switching in Pt–$Pr_{0.67}Ca_{0.33}MnO_3$–Pt heterostructures”. In: *New Journal of Physics* 15.10 (2013), p. 103008. ISSN: 1367-2630. DOI: 10.1088/1367-2630/15/10/103008.

[37] Stephanie Raabe et al. “In situ electrochemical electron microscopy study of oxygen evolution activity of doped manganite perovskites”. In: *Advanced Functional Materials* 22.16 (Aug. 2012), pp. 3378–3388. ISSN: 1616301X. DOI: 10.1002/ADFM.201103173.

[38] Mohsen Sotoudeh et al. “Electronic structure of $Pr_{1-x}Ca_xMnO_3$”. In: *Physical Review B* 95 (2017), p. 235150. DOI: 10.1103/PhysRevB.95.235150.

[39] P. A. Cox. *Transition Metal Oxides. An Introduction to their Electronic Structure and Properties*. Ed. by J. S. Rowlinson et al. Vol. 105. Oxford University Press, 1992. DOI: 10.1002/ange.19931050352.

[40] G. Zampieri et al. “XPS and XAS spectra of $CaMnO_3$ and $LaMnO_3$”. In: *Physica B: Condensed Matter* 320.1-4 (July 2002), pp. 51–55. ISSN: 0921-4526. DOI: 10.1016/S0921-4526(02)00618-X.

[41] Shashank V. Inge et al. “Accurate prediction of migration barrier of oxygen vacancy in Formula Presented and Formula Presented: Explaining experimental results with density functional theory”. In: *Physical Review B* 108.3 (July 2023), p. 035114. ISSN: 24699969. DOI: 10.1103/PhysRevB.108.035114.

[42] J. H. Jung et al. “Determination of electronic band structures of $CaMnO_3$ and $LaMnO_3$ using optical-conductivity analyses”. In: *Phys. Rev. B* 55 (1997), p. 15489. DOI: 10.1103/PhysRevB.55.15489.

[43] Hong Sub Lee et al. “A new route to the Mott-Hubbard metal-insulator transition: Strong correlations effects in $Pr_{0.7}Ca_{0.3}MnO_3$”. In: *Scientific Reports 2013 3:1* 3.1 (Apr. 2013), pp. 1–5. ISSN: 2045-2322. DOI: 10.1038/srep01704.

[44] Matteo Rini et al. “Control of the electronic phase of a manganite by mode-selective vibrational excitation”. In: *Nature* 449.7158 (Sept. 2007), pp. 72–74. ISSN: 1476-4687. DOI: 10.1038/nature06119.

[45] S. Asanuma et al. “Relationship between resistive switching characteristics and band diagrams of Ti/$Pr_{1-x}Ca_xMnO_3$ junctions”. In: *Physical Review B* 80.23 (Dec. 2009), p. 235113. DOI: 10.1103/PhysRevB.80.235113.

[46] A. Sawa et al. “Highly rectifying $Pr_{0.7}Ca_{0.3}MnO_3$/$SrTi_{0.9998}Nb_{0.0002}O_3$ p-n junction”. In: *Applied Physics Letters* 86.11 (Mar. 2005), pp. 1–3. ISSN: 00036951. DOI: 10.1063/1.1883336.

[47] Robert R. Heikes and Roland W. Ure Jr. *Thermoelectricity: science and engineering*. Interscience Publishers, Inc., 1961. DOI: 10.1021/ja00863a051.

[48] Partha Sarathi Mondal et al. “Possible Existence of Two Charge-Ordered Phases in $Pr_{1-x}Ca_xMnO_3$ for 0.40 <= x <= 0.50”. In: *Journal of the Physical Society of Japan* 83.6 (May 2014), p. 064709. ISSN: 13474073. DOI: 10.7566/JPSJ.83.064709.

[49] Shigeki Yamada et al. “Thermopower in $Pr_{1-x}Ca_xMnO_3$”. In: *Journal of the Physical Society of Japan* 69.5 (Nov. 2000), pp. 1278–1281. ISSN: 00319015. DOI: 10.1143/JPSJ.69.1278.

[50] G. Venkataiah, Y. Kalyana Lakshmi, and P. Venugopal Reddy. “Thermopower studies of $Pr_{0.67}D_{0.33}MnO_3$ manganite system”. In: *Journal of Physics D: Applied Physics* 40.3 (2007), p. 721. ISSN: 0022-3727. DOI: 10.1088/0022-3727/40/3/005.

[51] A. S. Alexandrov and P. E. Kornilovitch. “Mobile Small Polaron”. In: *Phys. Rev. Lett.* 82.4 (1999), pp. 807–810. DOI: 10.1103/PhysRevLett.82.807.

[52] I. G. Austin and N. F. Mott. “Polarons in Crystalline and Non-crystalline Materials”. In: *Advances in Physics* 18.71 (Jan. 1969), pp. 41–102. ISSN: 14606976. DOI: 10.1080/00018736900101267.

[53] S. Mildner et al. “Temperature- and doping-dependent optical absorption in the small-polaron system $Pr_{1-x}Ca_xMnO_3$”. In: *Physical Review B* 92.3 (July 2015), p. 035145. DOI: 10.1103/PhysRevB.92.035145.

[54] T. Holstein. “Studies of polaron motion: Part I. The molecular-crystal model”. In: *Annals of Physics* 8.3 (Nov. 1959), pp. 325–342. ISSN: 0003-4916. DOI: 10.1016/0003-4916(59)90002-8.

[55] D. Feinberg, S. Ciuchi, and F. de Pasquale. “Squeezing phenomena in interacting electron-phonon systems”. In: *International Journal of Modern Physics B* 04.07n08 (June 1990), pp. 1317–1367. ISSN: 0217-9792. DOI: 10.1142/S0217979290000656.

[56] T. Holstein. “Studies of Polaron Motion: Part II. The “Small” Polaron”. In: *Annals of Physics* 281.1-2 (Apr. 2000), pp. 725–773. ISSN: 0003-4916. DOI: 10.1006/APHY.2000.6021.

[57] Y. M. Xie et al. “Effects of interaction and disorder on polarons in colossal resistance manganite $Pr_{0.68}Ca_{0.32}MnO_3$ thin films”. In: *Materials Research Express* 1 (2014), p. 46403. DOI: 10.1088/2053-1591/1/4/046403.

[58] A. V. Boris et al. “Infrared optical properties of $La_{0.7}Ca_{0.3}MnO_3$ epitaxial films”. In: *Journal of Applied Physics* 81.8 (Apr. 1997), pp. 5756–5758. ISSN: 0021-8979. DOI: 10.1063/1.364716.

[59] Anja Herpers. “Electrical characterization of manganite and titanate heterostructures”. PhD Thesis. RWTH Aachen, 2014. ISBN: 978-3-89336-948-5. URL: https://juser.fz-juelich.de/record/152080.

[60] Y. B. Nian et al. “Evidence for an oxygen diffusion model for the electric pulse induced resistance change effect in transition-metal oxides”. In: *Physical Review Letters* 98.14 (Apr. 2007), p. 146403. ISSN: 00319007. DOI: 10.1103/PhysRevLett.98.146403.

[61] Zhaoliang Liao et al. “Evidence for electric-field-driven migration and diffusion of oxygen vacancies in $Pr_{0.7}Ca_{0.3}MnO_3$”. In: *Journal of Applied Physics* 111.11 (June 2012), p. 114506. ISSN: 00218979. DOI: 10.1063/1.4724333.

[62] Ch Jooss et al. “Electric pulse induced resistance change effect in manganites due to polaron localization at the metal-oxide interfacial region”. In: *Physical Review B* 77.13 (Apr. 2008), p. 132409. DOI: 10.1103/PhysRevB.77.132409.

[63] *Tunnel RRAM - Device Features and 1R True Cross-Point Implementation*. IFF - FZ Jülich, Mar. 2013.

[64] D. W. Reagor et al. “Work function of the mixed-valent manganese perovskites”. In: *Journal of Applied Physics* 95.12 (June 2004), pp. 7971–7975. ISSN: 0021-8979. DOI: 10.1063/1.1737802.

[65] Lei Bi, Sumeet C. Pandey, and Nirmal Ramaswamy. “Determination of effective work function of $Pr_{0.7}Ca_{0.3}MnO_3$ and Pt films on ZrO_x using terraced-oxide method”. In: *Applied Physics Letters* 103.3 (July 2013), p. 033516. ISSN: 0003-6951. DOI: 10.1063/1.4816004.

[66] A. Sawa et al. “Fermi level shift in $La_{1-x}Sr_xMO_3$ (M=Mn, Fe, Co, and Ni) probed by Schottky-like heteroepitaxial junctions with $SrTi_{0.99}Nb_{0.01}O_3$”. In: *Appl. Phys. Lett* 90.25 (June 2007), p. 252102. DOI: 10.1063/1.2749431.

[67] Francesco Borgatti et al. “Chemical insight into electroforming of resistive switching manganite heterostructures”. en. In: *Nanoscale* 5.9 (Apr. 2013), pp. 3954–3960. ISSN: 2040-3372. DOI: 10.1039/C3NR00106G.

[68] Zhigao Sheng et al. “Dynamics of multiple phases in a colossal-magnetoresistive manganite as revealed by dielectric spectroscopy”. In: *Nature Communications 2012 3:1* 3.1 (July 2012), pp. 1–6. ISSN: 2041-1723. DOI: 10.1038/ncomms1943.

[69] N. Biškup et al. “Origin of the colossal dielectric response of $Pr_{0.6}Ca_{0.4}MnO_3$”. In: *Physical Review B* 72.2 (July 2005), p. 024115. DOI: 10.1103/PhysRevB.72.024115.

[70] Hae-Geon Lee. *Chemical thermodynamics for metals and materials*. Imperial College Press, 1999. ISBN: 1-911298-89-5. DOI: 10.1142/p152.

[71] Shinichi Shirasaki et al. “Defect structure and oxygen diffusion in undoped and La-doped polycrystalline barium titanate”. In: *The Journal of Chemical Physics* 73.9 (1980), pp. 4640–4645. ISSN: 0021-9606. DOI: 10.1063/1.440654.

[72] Alexander Gutsche et al. “Disentangling ionic and electronic contributions to the switching dynamics of memristive $Pr_{0.7}Ca_{0.3}MnO_3$/Al devices by employing a two-resistor model”. In: *Physical Review Materials* 6.9 (Sept. 2022), p. 095002. DOI: 10.1103/PhysRevMaterials.6.095002.

[73] Keiji Shono et al. “Origin of negative differential resistance observed on bipolar resistance switching device with Ti/$Pr_{0.7}Ca_{0.3}MnO_3$/Pt structure”. In: *Applied Physics Express* 1.5 (May 2008), pp. 0550021–0550023. ISSN: 18820778. DOI: 10.1143/APEX.1.055002.

[74] Anja Herpers et al. “Spectroscopic Proof of the Correlation between Redox-State and Charge-Carrier Transport at the Interface of Resistively Switching Ti/PCMO Devices”. In: *Advanced Materials* 26.17 (2014), pp. 2730–2735. ISSN: 1521-4095. DOI: 10.1002/adma.201304054.

[75] H. Kaji et al. “Effect of electrode and interface oxide on the property of ReRAM composed of $Pr_{0.7}Ca_{0.3}MnO_3$”. In: *IOP Conference Series: Materials Science and Engineering* 8.1 (2010), p. 012032. ISSN: 1757-899X. DOI: 10.1088/1757-899X/8/1/012032.

[76] Alexander Gutsche. “Area-dependent resistive switching in PCMO-based memristive devices”. PhD Thesis. Rheinisch-Westfälische Technische Hochschule Aachen, 2023. DOI: DOI:10.18154/RWTH-2023-07951.

[77] Kibong Moon et al. “Resistive-switching analogue memory device for neuromorphic application”. In: *2014 Silicon Nanoelectronics Workshop, SNW 2014* (Dec. 2015). DOI: 10.1109/SNW.2014.7348602.

[78] Kyungjoon Baek et al. “In situ TEM observation on the interface-type resistive switching by electrochemical redox reactions at a TiN/PCMO interface”. en. In: *Nanoscale* 9.2 (2017), pp. 582–593. DOI: 10.1039/C6NR06293H.

[79] Jürgen Smoliner. *Grundlagen der Halbleiterphysik*. 2nd ed. Springer Berlin Heidelberg, 2020. DOI: 10.1007/978-3-662-60654-4.

[80] T. Meyer. “Structural and Electronic Investigation of Strongly Correlated Transition Metal Oxide Perovskite Thin Films and Interfaces using In-situ Transmission Electron Microscopy”. PhD Thesis. Georg-August-University Göttingen, Sept. 2020. DOI: 10.53846/GOEDISS-8815.

[81] Gesine Saucke et al. “Polaron absorption for photovoltaic energy conversion in a manganite-titanate pn heterojunction”. In: *Physical Review B - Condensed Matter and Materials Physics* 85.16 (Apr. 2012), p. 165315. ISSN: 10980121. DOI: https://doi.org/10.1103/PhysRevB.85.165315.

[82] T. Meyer et al. “High-resolution Scanning Transmission EBIC Analysis of Misfit Dislocations at Perovskite pn-Heterojunctions”. In: *IOP Publishing* 1190.1 (2019), p. 012009. DOI: 10.1088/1742-6596/1190/1/012009.

[83] Rene Meyer et al. “Oxide dual-layer memory element for scalable non-volatile cross-point memory technology”. In: *9th Annual Non-Volatile Memory Technology Symposium, NVMTS*. 2008, pp. 1–5. ISBN: 978-1-4244-2411-5. DOI: 10.1109/NVMT.2008.4731194.

[84] Benedikt Arndt et al. “Spectroscopic Indications of Tunnel Barrier Charging as the Switching Mechanism in Memristive Devices”. In: *Advanced Functional Materials* 27.45 (Dec. 2017), p. 1702282. ISSN: 1616-3028. DOI: 10.1002/ADFM.201702282.

[85] John G. Simmons. “Electric Tunnel Effect between Dissimilar Electrodes Separated by a Thin Insulating Film”. In: *Journal of Applied Physics* 34.9 (Sept. 1963), pp. 2581–2590. ISSN: 0021-8979. DOI: 10.1063/1.1729774.

[86] Carsten Funck and Stephan Menzel. “Comprehensive Model of Electron Conduction in Oxide-Based Memristive Devices”. In: *ACS Applied Electronic Materials* 3.9 (Sept. 2021), pp. 3674–3692. ISSN: 26376113. DOI: 10.1021/acsaelm.1c00398.

[87] Mau Phon et al. “Current transport mechanism in trapped oxides: A generalized trap-assisted tunneling model”. In: *Journal of Applied Physics* 86.3 (Aug. 1999), pp. 1488–1491. ISSN: 0021-8979. DOI: 10.1063/1.370918.

[88] S. Lashkare et al. “PCMO RRAM for Integrate-and-Fire Neuron in Spiking Neural Networks”. In: *IEEE Electron Device Letters* 39.4 (Apr. 2018), pp. 484–487. ISSN: 07413106. DOI: 10.1109/LED.2018.2805822.

[89] I. Chakraborty et al. “Space Charge Limited Current with Self-heating in $Pr_{0.7}Ca_{0.3}MnO_3$ based RRAM”. May 2016. URL: https://arxiv.org/abs/1605.08755v1.

[90] I. Chakraborty et al. “Materials parameter extraction using analytical models in PCMO based RRAM”. In: *Device Research Conference - Conference Digest, DRC*. Vol. 2015-August. Institute of Electrical and Electronics Engineers Inc., Aug. 2015, pp. 87–88. ISBN: 978-1-4673-8134-5. DOI: 10.1109/DRC.2015.7175568.

[91] Masayuki Fujimoto et al. “Resistive switching properties of high crystallinity and low-resistance $Pr_{0.7}Ca_{0.3}MnO_3$ thin film with point-contacted Ag electrodes”. In: *Applied Physics Letters* 91.22 (Nov. 2007), p. 223504. ISSN: 00036951. DOI: 10.1063/1.2816124.

[92] T. Harada et al. “Trap-controlled space-charge-limited current mechanism in resistance switching at Al/$Pr_{0.7}Ca_{0.3}MnO_3$ interface”. In: *Applied Physics Letters* 92.22 (June 2008), p. 222113. ISSN: 0003-6951. DOI: 10.1063/1.2938049.

[93] Kibong Moon et al. “Bidirectional non-filamentary RRAM as an analog neuromorphic synapse, Part I: Al/Mo/$Pr_{0.7}Ca_{0.3}MnO_3$ material improvements and device measurements”. In: *IEEE Journal of the Electron Devices Society* 6.1 (2018), pp. 146–155. ISSN: 21686734. DOI: 10.1109/JEDS.2017.2780275.

[94] Sangsu Park et al. “A nitrogen-treated memristive device for tunable electronic synapses”. In: *Semiconductor Science and Technology* 29.10 (Sept. 2014), p. 104006. ISSN: 0268-1242. DOI: 10.1088/0268-1242/29/10/104006.

[95] Christopher Linderälv, Anders Lindman, and Paul Erhart. “A Unifying Perspective on Oxygen Vacancies in Wide Band Gap Oxides”. In: *The Journal of Physical Chemistry Letters* 9.1 (Jan. 2018), pp. 222–228. DOI: 10.1021/acs.jpclett.7b03028.

[96] Benedikt Johannes Arndt. “Resistive switching in $Pr_{1-x}Ca_xMnO_3$YSZ: conclusive model and switching kinetics”. PhD Thesis. RWTH Aachen University, 2022. DOI: 10.18154/RWTH-2022-02791.

[97] Peter Lackner et al. “Using photoelectron spectroscopy to observe oxygen spillover to zirconia”. In: *Physical Chemistry Chemical Physics* 21.32 (Aug. 2019), pp. 17613–17620. ISSN: 1463-9084. DOI: 10.1039/C9CP03322J.

[98] Stefano Fabris, Anthony T. Paxton, and Michael W. Finnis. “A stabilization mechanism of zirconia based on oxygen vacancies only”. In: *Acta Materialia* 50.20 (2002), pp. 5171–5178. ISSN: 1359-6454. DOI: https://doi.org/10.1016/S1359-6454(02)00385-3.

[99] Hong Jiang et al. “Electronic band structure of zirconia and hafnia polymorphs from the GW perspective”. In: *Physical Review B* 81.8 (Feb. 2010), p. 85119. DOI: 10.1103/PhysRevB.81.085119.

[100] Thomas Götsch et al. “Spectroscopic investigation of the electronic structure of yttria-stabilized zirconia”. In: *Physical Review Materials* 2.3 (Mar. 2018), p. 35801. DOI: 10.1103/PhysRevMaterials.2.035801.

[101] David W. McComb. “Bonding and electronic structure in zirconia pseudopolymorphs investigated by electron energy-loss spectroscopy”. In: *Physical Review B* 54.10 (Sept. 1996), pp. 7094–7102. DOI: 10.1103/PhysRevB.54.7094.

[102] S. Ostanin et al. “Effect of relaxation on the oxygen K-edge electron energy-loss near-edge structure in yttria-stabilized zirconia”. In: *Physical Review B* 62.22 (Dec. 2000), pp. 14728–14735. DOI: 10.1103/PhysRevB.62.14728.

[103] Nils Sommer, Regina Dittmann, and Stephan Menzel. “Effect of Oxygen Exchange between Two Oxide Layers of a Memristive Bilayer Valence-Change Memory Cell on the Switching Polarity”. In: *PHYSICAL REVIEW APPLIED* 19 (2023), p. 44084. DOI: 10.1103/PhysRevApplied.19.044084.

[104] M. Scherff et al. “Polarity reversal in bipolar resistive switching in $Pr_{0.7}Ca_{0.3}MnO_3$ noble metal sandwich structures”. In: *Journal of Applied Physics* 110.4 (Aug. 2011), p. 043718. ISSN: 0021-8979. DOI: 10.1063/1.3610429.

[105] Thilo Kramer et al. “Developing an in situ environmental TEM set up for investigations of resistive switching mechanisms in Pt-$Pr_{1-x}Ca_xMnO_{3-\(\delta\)}$-Pt sandwich structures”. In: *Ultramicroscopy* 184 (2018), pp. 61–70. ISSN: 0304-3991. DOI: https://doi.org/10.1016/j.ultramic.2017.08.012.

[106] Vivek Saraswat et al. “Reaction-Drift Model for Switching Transients in $Pr_{0.7}Ca_{0.3}MnO_3$-Based Resistive RAM”. In: *IEEE Transactions on Electron Devices* 67.9 (Sept. 2020), pp. 3610–3617. ISSN: 15579646. DOI: 10.1109/TED.2020.3011387.

[107] Akihito Sawa. “Resistive switching in transition metal oxides”. In: *Materials Today* 11.6 (June 2008), pp. 28–36. ISSN: 1369-7021. DOI: 10.1016/S1369-7021(08)70119-6.

[108] Ting Zhang et al. “Interface-related switching behaviors of amorphous $Pr_{0.67}Sr_{0.33}MnO_3$-based memory cells”. en. In: *Chinese Physics B* 21.10 (Oct. 2012), p. 107304. ISSN: 1674-1056. DOI: 10.1088/1674-1056/21/10/107304.

[109] Naoki Kanegami, Yusuke Nishi, and Tsunenobu Kimoto. “Unique resistive switching phenomena exhibiting both filament-type and interface-type switching in Ti/$Pr_{0.7}Ca_{0.3}MnO_3$ /Pt ReRAM cells”. In: *Applied Physics Letters* 116.1 (Jan. 2020), p. 013501. ISSN: 0003-6951. DOI: 10.1063/1.5131090.

[110] Tae-Geun Seong et al. “Effect of Oxygen Pressure on the Resistive Switching Behavior of Amorphous $Pr_{0.7}Ca_{0.3}MnO_3$ Films”. en. In: *ECS Solid State Letters* 2.4 (Jan. 2013), P35. ISSN: 2162-8750. DOI: 10.1149/2.004304ssl.

[111] Hiroshi Yamamoto et al. “Correlation between degree of crystallinity and transition field in electric or magnetic field-induced insulator–metal transition of $Pr_{0.5}Ca_{0.5}MnO_3$ thin films”. In: *Solid State Communications* 142.1 (Apr. 2007), pp. 28–31. ISSN: 0038-1098. DOI: 10.1016/j.ssc.2007.01.042.

[112] Tae-Geun Seong et al. “Unipolar resistive switching properties of amorphous $Pr_{0.7}Ca_{0.3}MnO_3$ films grown on a Pt/Ti/SiO_2/Si substrate”. In: *Current Applied Physics* 14.4 (Apr. 2014), pp. 538–542. ISSN: 1567-1739. DOI: 10.1016/j.cap.2014.01.012.

[113] R. Zhang et al. “Transparent amorphous memory cell: A bipolar resistive switching in ZnO/$Pr_{0.7}Ca_{0.3}MnO_3$/ITO for invisible electronics application”. In: *Journal of Non-Crystalline Solids* 406 (Dec. 2014), pp. 102–106. ISSN: 0022-3093. DOI: 10.1016/j.jnoncrysol.2014.09.055.

[114] Tae-Geun Seong et al. “Resistive switching properties of amorphous $Pr_{0.7}Ca_{0.3}MnO_3$ films grown on indium tin oxide/glass substrate using pulsed laser deposition method”. In: *Applied Physics Letters* 100.21 (May 2012), p. 212111. ISSN: 0003-6951. DOI: 10.1063/1.4722797.

[115] Daeseok Lee et al. “Trade-off between number of conductance states and variability of conductance change in $Pr_{0.7}Ca_{0.3}MnO_3$-based synapse device”. In: *Applied Physics Letters* 106.11 (Mar. 2015), p. 113701. ISSN: 00036951. DOI: 10.1063/1.4915924.

[116] A. Wahl et al. “Magnetic contributions to the low-temperature specific heat of the ferromagnetic insulator $Pr_{0.8}Ca_{0.2}MnO_3$”. In: *The European Physical Journal B - Condensed Matter and Complex Systems* 26.2 (2002), pp. 135–140. ISSN: 1434-6036. DOI: 10.1140/epjb/e20020074.

[117] Rainer Waser et al. “Redox-Based Resistive Switching Memories – Nanoionic Mechanisms, Prospects, and Challenges”. In: *Advanced Materials* 21.25-26 (July 2009), pp. 2632–2663. ISSN: 1521-4095. DOI: 10.1002/ADMA.200900375.

[118] R. Dittmann et al. “Engineering the kinetics of redox-based memristive devices for neuromorphic computing”. In: *2023 International Electron Devices Meeting (IEDM)*. Dec. 2023, pp. 1–4. DOI: 10.1109/IEDM45741.2023.10413803.

[119] N. Panwar et al. “Self-Heating during submicrosecond Current Transients in $Pr_{0.7}Ca_{0.3}MnO_3$-Based RRAM”. In: *IEEE Transactions on Electron Devices* 64.1 (Jan. 2017), pp. 137–144. ISSN: 00189383. DOI: 10.1109/TED.2016.2632712.

[120] Kibong Moon et al. “Analog synapse device with 5-b MLC and improved data retention for neuromorphic system”. In: *IEEE Electron Device Letters* 37.8 (Aug. 2016), pp. 1067–1070. ISSN: 07413106. DOI: 10.1109/LED.2016.2583545.

[121] P. Kumbhare and U. Ganguly. “Ionic Transport Barrier Tuning by Composition in $Pr_{1-x}Ca_xMnO_3$-Based Selector-Less RRAM and Its Effect on Memory Performance”. In: *IEEE Transactions on Electron Devices* 65.6 (June 2018), pp. 2479–2484. ISSN: 00189383. DOI: 10.1109/TED.2018.2827420.

[122] Chuljun Lee et al. “Improved On-chip Training Efficiency at Elevated Temperature and Excellent Inference Accuracy with Retention (> 10^8s) of $Pr_{0.7}Ca_{0.3}MnO_{3-x}$ ECRAM Synapse Device for Hardware Neural Network”. In: *IEEE International Electron Devices Meeting (IEDM)*. Vol. 2021-December. Institute of Electrical and Electronics Engineers Inc., 2021, pp. 12.3.1–12.3.4. ISBN: 978-1-6654-2572-8. DOI: 10.1109/IEDM19574.2021.9720597.

[123] Shashank V. Inge et al. “Understanding and Predicting the Activation Energy of Oxygen Migration in $Pr_{0.5}Ca_{0.5}MnO$: A DFT study”. In: *8th IEEE Electron Devices Technology & Manufacturing Conference (EDTM)*. Institute of Electrical and Electronics Engineers Inc., 2024, pp. 1–3. ISBN: 979-8-3503-7152-9. DOI: 10.1109/EDTM58488.2024.10511856.

[124] Stefan Wiefels et al. “Reliability Aspects of 28 nm BEOL-Integrated Resistive Switching Random Access Memory”. In: *Physica Status Solidi (A) Applications and Materials Science* 221.22 (Nov. 2023), p. 2300401. ISSN: 18626319. DOI: 10.1002/PSSA.202300401.

[125] Gang Jian-Lei et al. “Clockwise vs Counter-Clockwise I-V Hysteresis of Point-Contact Metal-Tip/$Pr_{0.7}Ca_{0.3}MnO_3$/Pt Devices”. en. In: *Chinese Physics Letters* 27.2 (Feb. 2010), p. 027301. ISSN: 0256-307X. DOI: 10.1088/0256-307X/27/2/027301.

[126] D. S. Kim et al. “Resistive switching characteristics of $Pr_{0.7}Ca_{0.3}MnO_3$ thin films grown on glass substrates by pulsed laser deposition”. In: *Thin Solid Films* 515.4 (Dec. 2006), pp. 2573–2576. ISSN: 0040-6090. DOI: 10.1016/j.tsf.2006.08.011.

[127] Neeraj Panwar et al. “Effect of morphological change on unipolar and bipolar switching characteristics in $Pr_{0.7}Ca_{0.3}MnO_3$ based RRAM”. In: *Materials Research Society Symposium Proceedings* 1729.1 (Apr. 2015), pp. 47–52. ISSN: 02729172. DOI: 10.1557/OPL.2015.192.

[128] Nick A. Shepelin et al. “A practical guide to pulsed laser deposition”. In: *Chemical Society Reviews* 52.7 (Apr. 2023), pp. 2294–2321. ISSN: 14604744. DOI: 10.1039/D2CS00938B.

[129] Hans H. Gatzen, Volker Saile, and Jürg Leuthold. “Deposition Technologies”. In: *Micro and Nano Fabrication: Tools and Processes*. Ed. by Hans H. Gatzen, Volker Saile, and Jürg Leuthold. Berlin, Heidelberg: Springer Berlin Heidelberg, 2015, pp. 65–203. ISBN: 978-3-662-44395-8. DOI: 10.1007/978-3-662-44395-8_3.

[130] D. Depla, S. Mahieu, and J.E. Greene. “Chapter 5 - Sputter Deposition Processes”. In: *Handbook of Deposition Technologies for Films and Coatings (Third Edition)*. Ed. by Peter M. Martin. Boston: William Andrew Publishing, Jan. 2010, pp. 253–296. ISBN: 978-0-8155-2031-3. DOI: 10.1016/B978-0-8155-2031-3.00005-3.

[131] Annemie Bogaerts, Ivan Kolev, and Guy Buyle. “Modeling of the Magnetron Discharge”. In: *Reactive Sputter Deposition*. Ed. by Diederik Depla and Stijn Mahieu. Berlin, Heidelberg: Springer Berlin Heidelberg, 2008, pp. 61–130. ISBN: 978-3-540-76664-3. DOI: 10.1007/978-3-540-76664-3_3.

[132] Christian Koch. *Fotolithografie: Grundlagen der Mikrostrukturierung*. Ed. by Titus J. Rinke and Christian Koch. Ulm: MicroChemicals, 2017. ISBN: 978-3-9818782-0-2.

[133] Hans H. Gatzen, Volker Saile, and Jürg Leuthold. “Lithography”. In: *Micro and Nano Fabrication: Tools and Processes*. Ed. by Hans H. Gatzen, Volker Saile, and Jürg Leuthold. Berlin, Heidelberg: Springer Berlin Heidelberg, 2015, pp. 313–395. ISBN: 978-3-662-44395-8. DOI: 10.1007/978-3-662-44395-8_6.

[134] Zheng Cui. “Optical Lithography”. In: *Nanofabrication: Principles, Capabilities and Limits*. Ed. by Zheng Cui. Cham: Springer International Publishing, 2024, pp. 9–81. ISBN: 978-3-031-62546-6. DOI: 10.1007/978-3-031-62546-6_2.

[135] Sami Franssila. “Etching”. In: *Introduction to Microfabrication*. Sept. 2010, pp. 127–141. ISBN: 978-1-119-99041-3. DOI: 10.1002/9781119990413.ch11.

[136] Hans H. Gatzen, Volker Saile, and Jürg Leuthold. “Etching Technologies”. In: *Micro and Nano Fabrication: Tools and Processes*. Ed. by Hans H. Gatzen, Volker Saile, and Jürg Leuthold. Berlin, Heidelberg: Springer Berlin Heidelberg, 2015, pp. 205–272. ISBN: 978-3-662-44395-8. DOI: 10.1007/978-3-662-44395-8_4.

[137] Peter Eaton and Paul West. *Atomic Force Microscopy*. Oxford University Press, Mar. 2010. ISBN: 978-0-19-957045-4. DOI: 10.1093/acprof:oso/9780199570454.001.0001.

[138] Bert Voigtländer. “Introduction”. In: *Atomic Force Microscopy*. Ed. by Bert Voigtländer. Cham: Springer International Publishing, 2019, pp. 1–13. ISBN: 978-3-030-13654-3. DOI: 10.1007/978-3-030-13654-3_1.

[139] Bert Voigtländer. “Forces Between Tip and Sample”. In: *Atomic Force Microscopy*. Ed. by Bert Voigtländer. Cham: Springer International Publishing, 2019, pp. 161–176. ISBN: 978-3-030-13654-3. DOI: 10.1007/978-3-030-13654-3_10.

[140] Bert Voigtländer. “Cantilevers and Detection Methods in Atomic Force Microscopy”. In: *Atomic Force Microscopy*. Ed. by Bert Voigtländer. Cham: Springer International Publishing, 2019, pp. 177–197. ISBN: 978-3-030-13654-3. DOI: 10.1007/978-3-030-13654-3_11.

[141] Bert Voigtländer. “Technical Aspects of Scanning Probe Microscopy”. In: *Scanning Probe Microscopy: Atomic Force Microscopy and Scanning Tunneling Microscopy*. Ed. by Bert Voigtländer. Berlin, Heidelberg: Springer Berlin Heidelberg, 2015, pp. 31–63. ISBN: 978-3-662-45240-0. DOI: 10.1007/978-3-662-45240-0_3.

[142] Bert Voigtländer. “Static Atomic Force Microscopy”. In: *Atomic Force Microscopy*. Ed. by Bert Voigtländer. Cham: Springer International Publishing, 2019, pp. 199–208. ISBN: 978-3-030-13654-3. DOI: 10.1007/978-3-030-13654-3_12.

[143] Bert Voigtländer. “Amplitude Modulation (AM) Mode in Dynamic Atomic Force Microscopy”. In: *Atomic Force Microscopy*. Ed. by Bert Voigtländer. Cham: Springer International Publishing, 2019, pp. 209–229. ISBN: 978-3-030-13654-3. DOI: 10.1007/978-3-030-13654-3_13.

[144] Bert Voigtländer. “Intermittent Contact Mode/Tapping Mode”. In: *Atomic Force Microscopy*. Ed. by Bert Voigtländer. Cham: Springer International Publishing, 2019, pp. 231–253. ISBN: 978-3-030-13654-3. DOI: 10.1007/978-3-030-13654-3_14.

[145] Bert Voigtländer. “Scanning Tunneling Microscopy”. In: *Scanning Probe Microscopy: Atomic Force Microscopy and Scanning Tunneling Microscopy*. Ed. by Bert Voigtländer. Berlin, Heidelberg: Springer Berlin Heidelberg, 2015, pp. 279–308. ISBN: 978-3-662-45240-0. DOI: 10.1007/978-3-662-45240-0_20.

[146] Bert Voigtländer. “Electronics for Scanning Probe Microscopy”. In: *Scanning Probe Microscopy: Atomic Force Microscopy and Scanning Tunneling Microscopy*. Ed. by Bert Voigtländer. Berlin, Heidelberg: Springer Berlin Heidelberg, 2015, pp. 77–99. ISBN: 978-3-662-45240-0. DOI: 10.1007/978-3-662-45240-0_5.

[147] Bert Voigtländer. “Scanning Tunneling Spectroscopy (STS)”. In: *Scanning Probe Microscopy: Atomic Force Microscopy and Scanning Tunneling Microscopy*. Ed. by Bert Voigtländer. Berlin, Heidelberg: Springer Berlin Heidelberg, 2015, pp. 309–334. ISBN: 978-3-662-45240-0. DOI: 10.1007/978-3-662-45240-0_21.

[148] Artur Glavic and Matts Björck. “GenX 3: The latest generation of an established tool”. In: *Journal of Applied Crystallography* 55.4 (Aug. 2022), pp. 1063–1071. ISSN: 1600-5767. DOI: 10.1107/S1600576722006653.

[149] Wolfgang Demtröder. “Elektromagnetische Wellen in Materie”. In: *Experimentalphysik 2: Elektrizität und Optik*. Ed. by Wolfgang Demtröder. Berlin, Heidelberg: Springer Berlin Heidelberg, 2017, pp. 209–248. ISBN: 978-3-662-55790-7. DOI: 10.1007/978-3-662-55790-7_8.

[150] A. Gibaud, M. S. Chebil, and T. Beuvier. “X-Ray Reflectivity”. In: *Surface Science Techniques*. Ed. by Gianangelo Bracco and Bodil Holst. Berlin, Heidelberg: Springer Berlin Heidelberg, 2013, pp. 191–216. ISBN: 978-3-642-34243-1. DOI: 10.1007/978-3-642-34243-1_7.

[151] Steven H. Simon. *The Oxford Solid State Basics*. First edition. Oxford University Press, 2013. ISBN: 978-0-19-968077-1.

[152] Yoshio Waseda, Eiichiro Matsubara, and Kozo Shinoda. “Scattering and Diffraction”. In: *X-Ray Diffraction Crystallography: Introduction, Examples and Solved Problems*. Ed. by Yoshio Waseda, Eiichiro Matsubara, and Kozo Shinoda. Berlin, Heidelberg: Springer Berlin Heidelberg, 2011, pp. 67–106. ISBN: 978-3-642-16635-8. DOI: 10.1007/978-3-642-16635-8_3.

[153] Egami Takeshi and Simon J.L. Billinge. “Chapter 1 - Structure of Complex Materials”. In: *Pergamon Materials Series*. Ed. by Takeshi Egami and Simon J.L. Billinge. Vol. 16. Pergamon, Jan. 2012, pp. 1–25. DOI: 10.1016/B978-0-08-097133-9.00001-0.

[154] Egami Takeshi and Simon J.L. Billinge. “Chapter 5 - Data Collection Analysis”. In: *Pergamon Materials Series*. Ed. by Takeshi Egami and Simon J.L. Billinge. Vol. 16. Pergamon, Jan. 2012, pp. 159–257. DOI: 10.1016/B978-0-08-097133-9.00005-8.

[155] A. C. Dippel et al. “Local atomic structure of thin and ultrathin films via rapid high-energy X-ray total scattering at grazing incidence”. In: *IUCrJ* 6 (2019), pp. 290–298. ISSN: 2052-2525. DOI: 10.1107/S2052252519000514.

[156] Egami Takeshi and Simon J.L. Billinge. “Chapter 2 - Crystallographic Analysis of Complex Materials”. In: *Pergamon Materials Series*. Ed. by Takeshi Egami and Simon J.L. Billinge. Vol. 16. Pergamon, Jan. 2012, pp. 27–54. DOI: 10.1016/B978-0-08-097133-9.00002-2.

[157] Egami Takeshi and Simon J.L. Billinge. “Chapter 3 - The Method of Total Scattering and Atomic Pair Distribution Function Analysis”. In: *Pergamon Materials Series*. Ed. by Takeshi Egami and Simon J.L. Billinge. Vol. 16. Pergamon, Jan. 2012, pp. 55–111. DOI: 10.1016/B978-0-08-097133-9.00003-4.

[158] Stefan Hüfner. “Introduction and Basic Principles”. In: *Photoelectron Spectroscopy: Principles and Applications*. Ed. by Stefan Hüfner. Berlin, Heidelberg: Springer Berlin Heidelberg, 2003, pp. 1–60. ISBN: 978-3-662-09280-4. DOI: 10.1007/978-3-662-09280-4_1.

[159] Shigemasa Suga, Akira Sekiyama, and Christian Tusche. “Instrumentation and Methodology”. In: *Photoelectron Spectroscopy: Bulk and Surface Electronic Structures*. Ed. by Shigemasa Suga, Akira Sekiyama, and Christian Tusche. Cham: Springer International Publishing, 2021, pp. 51–109. ISBN: 978-3-030-64073-6. DOI: 10.1007/978-3-030-64073-6_3.

[160] Siegfried Hofmann. “Instrumentation”. In: *Auger- and X-Ray Photoelectron Spectroscopy in Materials Science: A User-Oriented Guide*. Ed. by Siegfried Hofmann. Berlin, Heidelberg: Springer Berlin Heidelberg, 2013, pp. 11–41. ISBN: 978-3-642-27381-0. DOI: 10.1007/978-3-642-27381-0_2.

[161] Siegfried Hofmann. “Qualitative Analysis (Principle and Spectral Interpretation)”. In: *Auger- and X-Ray Photoelectron Spectroscopy in Materials Science: A User-Oriented Guide*. Ed. by Siegfried Hofmann. Berlin, Heidelberg: Springer Berlin Heidelberg, 2013, pp. 43–76. ISBN: 978-3-642-27381-0. DOI: 10.1007/978-3-642-27381-0_3.

[162] Donald R. Baer et al. “XPS guide: Charge neutralization and binding energy referencing for insulating samples”. In: *Journal of Vacuum Science & Technology A* 38.3 (Apr. 2020), p. 031204. ISSN: 0734-2101. DOI: 10.1116/6.0000057.

[163] Shigemasa Suga, Akira Sekiyama, and Christian Tusche. “Theoretical Background”. In: *Photoelectron Spectroscopy: Bulk and Surface Electronic Structures*. Ed. by Shigemasa Suga, Akira Sekiyama, and Christian Tusche. Cham: Springer International Publishing, 2021, pp. 9–49. ISBN: 978-3-030-64073-6. DOI: 10.1007/978-3-030-64073-6_2.

[164] Shigemasa Suga, Akira Sekiyama, and Christian Tusche. “Bulk and Surface Sensitivity of Photoelectron Spectroscopy”. In: *Photoelectron Spectroscopy: Bulk and Surface Electronic Structures*. Ed. by Shigemasa Suga, Akira Sekiyama, and Christian Tusche. Cham: Springer International Publishing, 2021, pp. 111–118. ISBN: 978-3-030-64073-6. DOI: 10.1007/978-3-030-64073-6_4.

[165] Ankita Mathur, Ravinder Kaushik, and Aditi Halder. “Application of X-Ray Photoelectron Spectroscopy in Materials for Energy Conversion and Environmental Remediation”. In: *Modern Techniques of Spectroscopy: Basics, Instrumentation, and Applications*. Ed. by Dheeraj Kumar Singh, Manik Pradhan, and Arnulf Materny. Singapore: Springer Singapore, 2021, pp. 411–430. ISBN: 978-981-336-084-6. DOI: 10.1007/978-981-33-6084-6_16.

[166] Stefan Hüfner. “Core Levels and Final States”. In: *Photoelectron Spectroscopy: Principles and Applications*. Ed. by Stefan Hüfner. Berlin, Heidelberg: Springer Berlin Heidelberg, 2003, pp. 61–107. ISBN: 978-3-662-09280-4. DOI: 10.1007/978-3-662-09280-4_2.

[167] Jonas Deuermeier. “Origins of limited electrical performance of polycrystalline Cu2O thin-film transistors”. en. PhD Thesis. Darmstadt: Technische Universität Darmstadt, Mar. 2017. DOI: 10.26083/tuprints-00005915.

[168] Stefan Hüfner. “Charge-Excitation Final States: Satellites”. In: *Photoelectron Spectroscopy: Principles and Applications*. Ed. by Stefan Hüfner. Berlin, Heidelberg: Springer Berlin Heidelberg, 2003, pp. 109–172. ISBN: 978-3-662-09280-4. DOI: 10.1007/978-3-662-09280-4_3.

[169] Stefan Hüfner. “Continuous Satellites and Plasmon Satellites: XPS Photoemission in Nearly Free Electron Systems”. In: *Photoelectron Spectroscopy: Principles and Applications*. Ed. by Stefan Hüfner. Berlin, Heidelberg: Springer Berlin Heidelberg, 2003, pp. 173–209. ISBN: 978-3-662-09280-4. DOI: 10.1007/978-3-662-09280-4_4.

[170] Jun Feng and Andreas Scholl. “Photoemission Electron Microscopy (PEEM)”. In: *Science of Microscopy*. Ed. by Peter W. Hawkes and John C. H. Spence. New York, NY: Springer New York, 2007, pp. 657–695. ISBN: 978-0-387-49762-4. DOI: 10.1007/978-0-387-49762-4_9.

[171] Claus M Schneider and Gerd Schönhense. “Investigating surface magnetism by means of photoexcitation electron emission microscopy”. In: *Reports on Progress in Physics* 65.12 (Nov. 2002), p. 1785. ISSN: 0034-4885. DOI: 10.1088/0034-4885/65/12/202.

[172] Tevfik Onur Menteş and Andrea Locatelli. “Angle-resolved X-ray photoemission electron microscopy”. In: *Photoelectron microscopy, Time resolved pump-probe PES* 185.10 (Oct. 2012), pp. 323–329. ISSN: 0368-2048. DOI: 10.1016/j.elspec.2012.07.007.

[173] O. Renault et al. “Energy-filtered XPEEM with NanoESCA using synchrotron and laboratory X-ray sources: Principles and first demonstrated results”. In: *Proceedings of the Fifth International Conference on LEEM/PEEM* 601.20 (Oct. 2007), pp. 4727–4732. ISSN: 0039-6028. DOI: 10.1016/j.susc.2007.05.061.

[174] M Escher et al. “NanoESCA: a novel energy filter for imaging x-ray photoemission spectroscopy”. In: *Journal of Physics: Condensed Matter* 17.16 (Apr. 2005), S1329. ISSN: 0953-8984. DOI: 10.1088/0953-8984/17/16/004.

[175] Shigemasa Suga, Akira Sekiyama, and Christian Tusche. “Momentum Microscopy”. In: *Photoelectron Spectroscopy: Bulk and Surface Electronic Structures*. Ed. by Shigemasa Suga, Akira Sekiyama, and Christian Tusche. Cham: Springer International Publishing, 2021, pp. 351–416. ISBN: 978-3-030-64073-6. DOI: 10.1007/978-3-030-64073-6_11.

[176] Olivier Renault et al. “Energy-filtered PEEM imaging of polycrystalline Cu surfaces with work function contrast and high lateral resolution”. In: *e-Journal of Surface Science and Nanotechnology* 4 (2006), pp. 431–434. DOI: 10.1380/ejssnt.2006.431.

[177] José L. Todoli and Frank Vanhaecke. “Liquid Sample Introduction and Electrothermal Vaporisation for ICP-MS: Fundamentals and Applications”. In: *Inductively Coupled Plasma Mass Spectrometry Handbook*. Sept. 2005, pp. 182–227. ISBN: 978-1-4443-0546-3. DOI: 10.1002/9781444305463.ch5.

[178] Howard E. Taylor. “Chapter 5 - Sample Introduction”. In: *Inductively Coupled Plasma-Mass Spectrometry*. Ed. by Howard E. Taylor. San Diego: Academic Press, Jan. 2001, pp. 53–90. ISBN: 978-0-12-683865-7. DOI: 10.1016/B978-012683865-7/50005-3.

[179] Steve J. Hill, Andy Fisher, and Martin Liezers. “Plasma Generation, Ion Sampling and Focusing”. In: *Inductively Coupled Plasma Mass Spectrometry Handbook*. Sept. 2005, pp. 1–25. ISBN: 978-1-4443-0546-3. DOI: 10.1002/9781444305463.ch1.

[180] Howard E. Taylor. “Chapter 3 - Inductively Coupled Plasmas”. In: *Inductively Coupled Plasma-Mass Spectrometry*. Ed. by Howard E. Taylor. San Diego: Academic Press, Jan. 2001, pp. 15–27. ISBN: 978-0-12-683865-7. DOI: 10.1016/B978-012683865-7/50003-X.

[181] Howard E. Taylor. “Chapter 4 - Instrumentation”. In: *Inductively Coupled Plasma-Mass Spectrometry*. Ed. by Howard E. Taylor. San Diego: Academic Press, Jan. 2001, pp. 29–51. ISBN: 978-0-12-683865-7. DOI: 10.1016/B978-012683865-7/50004-1.

[182] Gregory K. Koyanagi, Diethard K. Bohme, and Dmitry R. Bandura. “Collision and Reaction Cells”. In: *Inductively Coupled Plasma Mass Spectrometry Handbook*. Sept. 2005, pp. 336–384. ISBN: 978-1-4443-0546-3. DOI: 10.1002/9781444305463.ch8.

[183] Howard E. Taylor. “Chapter 8 - Interferences”. In: *Inductively Coupled Plasma-Mass Spectrometry*. Ed. by Howard E. Taylor. San Diego: Academic Press, Jan. 2001, pp. 125–142. ISBN: 978-0-12-683865-7. DOI: 10.1016/B978-012683865-7/50008-9.

[184] Yao Lei et al. “Ferroelectric and flexible barrier resistive switching of epitaxial BiFeO3 films studied by temperature-dependent current and capacitance spectroscopy”. In: *Journal of Materials Science: Materials in Electronics* 27.8 (Aug. 2016), pp. 7927–7932. ISSN: 1573-482X. DOI: 10.1007/s10854-016-4784-y.

[185] M. Coll et al. “Towards Oxide Electronics: a Roadmap”. In: *Applied Surface Science* 482 (July 2019), pp. 1–93. ISSN: 0169-4332. DOI: 10.1016/J.APSUSC.2019.03.312.

[186] Y. Z. Chen et al. “A high-mobility two-dimensional electron gas at the spinel/perovskite interface of \[\gamma \]-Al_2O_3/$SrTiO_3$”. In: *Nature Communications 2013 4:1* 4.1 (Jan. 2013), pp. 1–6. ISSN: 2041-1723. DOI: 10.1038/ncomms2394.

[187] Matjaž Spreitzer et al. “Pulsed laser deposition of $SrTiO_3$ on a H-terminated Si substrate”. In: *Journal of Materials Chemistry C* 1.34 (Aug. 2013), pp. 5216–5222. ISSN: 20507534. DOI: 10.1039/C3TC30913D.

[188] Christoph Baeumer et al. “Quantifying redox-induced Schottky barrier variations in memristive devices via in operando spectromicroscopy with graphene electrodes”. In: *Nature Communications 2016 7:1* 7.1 (Aug. 2016), pp. 1–7. ISSN: 2041-1723. DOI: 10.1038/ncomms12398.

[189] Vikram Sivakumar et al. “Pulsed laser deposition in Twente: from research tool towards industrial deposition”. In: *Journal of Physics D: Applied Physics* 47.3 (Dec. 2013), p. 034006. ISSN: 0022-3727. DOI: 10.1088/0022-3727/47/3/034006.

[190] James A. Greer. “History and current status of commercial pulsed laser deposition equipment”. In: *Journal of Physics D: Applied Physics* 47.3 (Dec. 2013), p. 034005. ISSN: 0022-3727. DOI: 10.1088/0022-3727/47/3/034005.

[191] J. A. Greer, ; M. D. Tabat, and M. D. Tabat. “Large-area pulsed laser deposition: Techniques and applications”. In: *Journal of Vacuum Science & Technology A* 13.3 (May 1995), pp. 1175–1181. ISSN: 0734-2101. DOI: 10.1116/1.579857.

[192] J. A. Greer, M. D. Tabat, and C. Lu. “Future trends for large-area pulsed laser deposition”. In: *Nuclear Instruments and Methods in Physics Research Section B: Beam Interactions with Materials and Atoms* 121.1-4 (Jan. 1997), pp. 357–362. ISSN: 0168-583X. DOI: 10.1016/S0168-583X(96)00434-X.

[193] N. Pryds et al. “Thickness determination of large-area films of yttria-stabilized zirconia produced by pulsed laser deposition”. In: *Applied Surface Science* 252.13 (Apr. 2006), pp. 4882–4885. ISSN: 0169-4332. DOI: 10.1016/J.APSUSC.2005.07.145.

[194] S. Boughaba et al. “Ultrathin Ta2O5 films produced by large-area pulsed laser deposition”. In: *Thin Solid Films* 371.1-2 (Aug. 2000), pp. 119–125. ISSN: 0040-6090. DOI: 10.1016/S0040-6090(00)00982-2.

[195] Zakhar Vakulov et al. “Towards scalable large-area pulsed laser deposition”. In: *Materials* 14.17 (Sept. 2021), p. 4854. ISSN: 19961944. DOI: 10.3390/ma14174854.

[196] Shigeki Sakai et al. “Large-area pulsed-laser deposition of dielectric and ferroelectric thin films”. In: *Journal of Vacuum Science & Technology A* 25.4 (July 2007), pp. 903–907. ISSN: 0734-2101. DOI: 10.1116/1.2748808.

[197] Alejandro Ojeda-G-P et al. “Angular distribution of species in pulsed laser deposition of $La_xCa_{1-x}MnO_3$”. In: *Applied Surface Science* 336 (May 2015), pp. 150–156. ISSN: 0169-4332. DOI: 10.1016/J.APSUSC.2014.10.089.

[198] Luís Amaral, Ana M. R. Senos, and Paula M. Vilarinho. “Sintering kinetic studies in nonstoichiometric strontium titanate ceramics”. In: *Materials Research Bulletin* 44.2 (Feb. 2009), pp. 263–270. ISSN: 0025-5408. DOI: 10.1016/J.MATERRESBULL.2008.06.002.

[199] Alvaro J. Lizarbe et al. “Insight note: X-ray photoelectron spectroscopy (XPS) peak fitting of the Al 2p peak from electrically isolated aluminum foil with an oxide layer”. In: *Surface and Interface Analysis* 55.9 (Sept. 2023), pp. 651–657. ISSN: 10969918. DOI: 10.1002/SIA.7238.

[200] Jolm F. Moulder et al. *Handbook of X-ray photoelectron spectroscopy*. Physical Electronics, 1992. ISBN: 978-0-9627026-2-4.

[201] P. G. Radaelli et al. “Structural effects on the magnetic and transport properties of perovskite $A_{1-x}A'_xMnO_3$ (x=0.25, 0.30)”. In: *Phys. Rev. B* 56.13 (Oct. 1997), pp. 8265–8276. DOI: 10.1103/PhysRevB.56.8265.

[202] Xiaohao Yang et al. *xPDFsuite: an end-to-end software solution for high throughput pair distribution function transformation, visualization and analysis*. 2015. URL: https://arxiv.org/abs/1402.3163.

[203] P. Juhás et al. “PDFgetX3: a rapid and highly automatable program for processing powder diffraction data into total scattering pair distribution functions”. In: *Journal of Applied Crystallography* 46.2 (Apr. 2013), pp. 560–566. DOI: 10.1107/S0021889813005190.

[204] Egami Takeshi and Simon J.L. Billinge. “Chapter 4 - Total Scattering Experiments”. In: *Pergamon Materials Series*. Ed. by Takeshi Egami and Simon J.L. Billinge. Vol. 16. Pergamon, Jan. 2012, pp. 113–158. DOI: 10.1016/B978-0-08-097133-9.00004-6.

[205] Erwin Riedel and Christoph Janiak. *Anorganische Chemie*. De Gruyter, 2011. ISBN: 978-3-11-022567-9. DOI: 10.1515/9783110225679.

[206] Ahmer A. B. Baloch et al. “Extending Shannon’s ionic radii database using machine learning”. In: *Physical Review Materials* 5.4 (Apr. 2021), p. 043804. DOI: 10.1103/PhysRevMaterials.5.043804.

[207] Masatoshi Imada, Atsushi Fujimori, and Yoshinori Tokura. “Metal-insulator transitions”. In: *Reviews of Modern Physics* 70.4 (Oct. 1998), pp. 1039–1263. DOI: 10.1103/RevModPhys.70.1039.

[208] J.P. Clerc et al. “The electrical conductivity of binary disordered systems, percolation clusters, fractals and related models”. In: *Advances in Physics* 39.3 (June 1990), pp. 191–309. ISSN: 0001-8732. DOI: 10.1080/00018739000101501.

[209] Ellen Wachtel and Igor Lubomirsky. “Quasi-Amorphous Inorganic Thin Films: Non-Crystalline Polar Phases”. In: *Advanced Materials* 22.23 (2010), pp. 2485–2493. DOI: https://doi.org/10.1002/adma.200903232.

[210] Ee Wah Lim and Razali Ismail. “Conduction Mechanism of Valence Change Resistive Switching Memory: A Survey”. en. In: *Electronics* 4.3 (Sept. 2015), pp. 586–613. ISSN: 2079-9292. DOI: 10.3390/electronics4030586.

[211] Fu-Chien Chiu. “A Review on Conduction Mechanisms in Dielectric Films”. en. In: *Advances in Materials Science and Engineering* 2014.1 (2014), p. 578168. ISSN: 1687-8442. DOI: 10.1155/2014/578168.

[212] Menglin Li, Peng Huang, and Haizheng Zhong. “Current Understanding of Band-Edge Properties of Halide Perovskites: Urbach Tail, Rashba Splitting, and Exciton Binding Energy”. In: *The Journal of Physical Chemistry Letters* 14.6 (Feb. 2023), pp. 1592–1603. DOI: 10.1021/acs.jpclett.2c03525.

[213] Y. Dong et al. “Band offsets of InGaP/GaAs heterojunctions by scanning tunneling spectroscopy”. In: *Journal of Applied Physics* 103.7 (Apr. 2008), p. 073704. ISSN: 0021-8979. DOI: 10.1063/1.2902828.

[214] R M Feenstra et al. “Influence of tip-induced band bending on tunnelling spectra of semiconductor surfaces”. en. In: *Nanotechnology* 18.4 (Dec. 2006), p. 044015. ISSN: 0957-4484. DOI: 10.1088/0957-4484/18/4/044015.

[215] Niclas Schmidt et al. “In-Gap States of HfO_2 Nanoislands Driven by Crystal Nucleation: Implications for Resistive Random-Access Memory Devices”. In: *ACS Applied Nano Materials* 6.1 (Jan. 2023), pp. 148–159. DOI: 10.1021/acsanm.2c04165.

[216] Udai Raj Singh et al. “Evidence of mobile carriers with charge-ordering gap in epitaxial $P_{0.625}Ca_{0.375}MnO_3$ thin films”. In: *Phys. Rev. B* 81.15 (Apr. 2010), p. 155120. DOI: 10.1103/PhysRevB.81.155120.

[217] Sohini Kar and A. K. Raychaudhuri. “Localized reversible nanoscale phase separation in $Pr_{0.63}Ca_{0.37}MnO_3$ single crystal using a scanning tunneling microscope tip”. In: *Applied Physics Letters* 91.14 (Oct. 2007), p. 143124. ISSN: 0003-6951. DOI: 10.1063/1.2794795.

[218] Rafał Lewandków et al. “Interface formation of Al_2O_3 on n-GaN(0001): Photoelectron spectroscopy studies”. en. In: *Surface and Interface Analysis* 53.1 (2021), pp. 118–124. ISSN: 1096-9918. DOI: 10.1002/sia.6886.

[219] Christoph Henkel et al. “Atomic layer-deposited platinum in high-k/metal gate stacks”. en. In: *Semiconductor Science and Technology* 24.12 (Nov. 2009), p. 125013. ISSN: 0268-1242. DOI: 10.1088/0268-1242/24/12/125013.

[220] V. A. Pustovarov et al. “Oxygen vacancy in Al_2O_3: Photoluminescence study and first-principle simulation”. In: *Thin Solid Films* 519.19 (2011), pp. 6319–6322. ISSN: 0040-6090. DOI: https://doi.org/10.1016/j.tsf.2011.04.014.

[221] Pauli Virtanen et al. “SciPy 1.0: fundamental algorithms for scientific computing in Python”. In: *Nature Methods* 17.3 (Mar. 2020), pp. 261–272. ISSN: 1548-7105. DOI: 10.1038/s41592-019-0686-2.

[222] Sang Yong No et al. “Property Changes of Aluminum Oxide Thin Films Deposited by Atomic Layer Deposition under Photon Radiation”. In: *Journal of The Electrochemical Society* 153.6 (Apr. 2006), F87. ISSN: 1945-7111. DOI: 10.1149/1.2186179.

[223] T. V. Perevalov, V. A. Gritsenko, and V. V. Kaichev. “Electronic structure of aluminum oxide: ab initio simulations of alpha and gamma phases and comparison with experiment for amorphous films”. In: *Eur. Phys. J. Appl. Phys.* 52.3 (Dec. 2010). DOI: 10.1051/epjap/2010159.

[224] S.M. Sze and K.K. Ng. “Physics and Properties of Semiconductors—A Review”. In: *Physics of Semiconductor Devices*. Wiley, Oct. 2006, pp. 5–75. ISBN: 978-0-470-06832-8. DOI: 10.1002/9780470068328.ch1.

[225] Song-Lin Li et al. “Resistive switching properties in oxygen-deficient $Pr_{0.7}Ca_{0.3}MnO_3$ junctions with active Al top electrodes”. In: *Journal of Applied Physics* 105.3 (Feb. 2009), p. 033710. ISSN: 0021-8979. DOI: 10.1063/1.3073987.

[226] Song-Lin Li et al. “A Metal Oxide Heterostructure for Resistive Random Access Memory Devices”. In: *Chinese Physics Letters* 30.4 (Apr. 2013), p. 047701. ISSN: 0256-307X. DOI: 10.1088/0256-307X/30/4/047701.

[227] Sangsu Park et al. “Electronic system with memristive synapses for pattern recognition”. In: *Scientific Reports* 5.1 (May 2015), pp. 1–9. ISSN: 2045-2322. DOI: 10.1038/srep10123.

[228] Song-Lin Li et al. “Resistive switching properties and low resistance state relaxation in Al/$Pr_{0.7}Ca_{0.3}MnO_3$/Pt junctions”. In: *Journal of Physics D: Applied Physics* 42.4 (2009), p. 045411. ISSN: 0022-3727. DOI: 10.1088/0022-3727/42/4/045411.

[229] S. Park et al. “RRAM-based synapse for neuromorphic system with pattern recognition function”. In: *International Electron Devices Meeting*. IEEE, Dec. 2012, pp. 10.2.1–10.2.4. ISBN: 978-1-4673-4870-6. DOI: 10.1109/IEDM.2012.6479016.

[230] D. Liu, S. J. Clark, and J. Robertson. “Oxygen vacancy levels and electron transport in Al_2O_3”. In: *Applied Physics Letters* 96.3 (Jan. 2010), p. 032905. ISSN: 0003-6951. DOI: 10.1063/1.3293440.

[231] M. A. Korotin and E. Z. Kurmaev. “Electronic Structure of Aluminum Oxide with Oxygen Vacancies”. In: *Physics of Metals and Metallography* 119.8 (Aug. 2018), pp. 707–712. ISSN: 1555-6190. DOI: 10.1134/S0031918X18080069.

[232] Jack Strand and Alexander L. Shluger. “On the Structure of Oxygen Deficient Amorphous Oxide Films”. In: *Advanced Science* 11.8 (Feb. 2024), p. 2306243. ISSN: 2198-3844. DOI: 10.1002/advs.202306243.

Band / Volume 296
Structural and Magnetic Properties of Biocompatible Iron Oxide Nanoparticles for Medical Applications
A. Nasser (2025), xii, 140 pp
ISBN: 978-3-95806-837-7

Band / Volume 297
Metabolic engineering of *Pseudomonas taiwanensis* for the improved production of styrene
J. Rönitz (2025), XII, 147 pp
ISBN: 978-3-95806-841-4

Band / Volume 298
Elucidation of anti-viral strategies in *Streptomyces*
B. U. Rackow (2025), xii, 148 pp
ISBN: 978-3-95806-842-1

Band / Volume 299
Ab initio investigations of spin-orbit functionalized graphene
D. Mazhjoo (2025), 163 pp
ISBN: 978-3-95806-847-6

Band / Volume 300
3D neural implants for* in vivo *applications
M. Jung (2025), xvi, 215 pp
ISBN: 978-3-95806-852-0

Band / Volume 301
Phonons in Magnetic Systems by means of Density- Functional Perturbation Theory
A. Neukirchen (2025), xviii, 195 pp
ISBN: 978-3-95806-853-7

Band / Volume 302
Optimal control and machine learning of quantum device dynamics
F. Preti (2025), iv, 211 pp
ISBN: 978-3-95806-856-8

Band / Volume 303
Development of a New, Miniaturized and Flexible Temperature Sensor
S. Hamacher (2025), XXII, 153 pp
ISBN: 978-3-95806-863-6

Band / Volume 304
Investigation of spin current generated THz transients in materials with high spin-orbit coupling
S. Heidtfeld (2026), viii, 112, v pp
ISBN: 978-3-95806-893-3

Schriften des Forschungszentrums Jülich
Reihe Schlüsseltechnologien / Key Technologies

Band / Volume 305
Structural and Electronic Characterization of MBE-grown Topological Insulator Thin Films
X. Hou (2026), iv, 168 pp
ISBN: 978-3-95806-918-3 (Print)
ISBN: 978-3-95806-919-0 (E-Book)

Band / Volume 306
***In Situ* Biasing Off-Axis Electron Holography and Electron Beam Induced Current Microscopy for the Electrical Investigation of p-n Junctions in High-Efficiency III-V Multi-Junction Solar Cells**
V. Mergner (2026), XXXII, 259 pp
ISBN: 978-3-95806-924-4 (Print)
ISBN: 978-3-95806-925-1 (E-Book)

Band / Volume 307
Engineering of *Pseudomonas taiwanensis* for production of chorismate-derived secondary metabolites
F. Kofler (2026), XIV, 141 pp
ISBN: 978-3-95806-968-8 (Print)
ISBN: 978-3-95806-969-5 (E-Book)

Band / Volume 308
Neutron Scattering – Lectures
edited by I. Apanasenko, S. Förster, K. Friese, E. Kentzinger, M. Kruteva, M. Zobel, R. Zorn (2026), ca. 383 pp
ISBN: 978-3-95806-986-2 (Print)
ISBN: 978-3-95806-987-9 (E-Book)

Band / Volume 309
Metal-free chemical vapor deposition of single-layer graphene and hexagonal boron nitride films on c-plane sapphire for electronic devices
Z. Wang (2026), xiii, 206 pp
ISBN: 978-3-95806-992-3 (Print)
ISBN: 978-3-95806-993-0 (E-Book)

Band / Volume 310
BEOL-Compatible Area-Dependent Memristive Devices from Wafer-Scale Pulsed Laser Deposited Amorphous $Pr_{0.7}Ca_{0.3}MnO_3$
M. Buczek (2026), x, 146 pp
ISBN 978-3-69367-002-6 (Print)
ISBN 978-3-69367-003-3 (E-Book)

Weitere ***Schriften des Verlags im Forschungszentrum Jülich*** unter
http://wwwzb1.fz-juelich.de/verlagextern1/index.asp

Schlüsseltechnologien / Key Technologies
Band / Volume 310
ISBN 978-3-69367-002-6

Mitglied der Helmholtz-Gemeinschaft

JÜLICH
Forschungszentrum